Formazanate Ir(III)/Pt(II) Complexes and Their Derivatives

by
Ge Mu

A dissertation submitted to the Department of Chemistry,
University of Houston
in partial fulfillment of the requirements for the degree of

Doctor of Philosophy

in Chemistry

Chair of Committee: Prof. Thomas Teets

Committee Member: Prof. Allan Jacobson

Committee Member: Prof. Judy Wu

Committee Member: Prof. Melissa Zastrow

Committee Member: Prof. Eric Van Caemelbecke

University of Houston
August 2020

Acknowledgments

The Ph.D. program in Department of Chemistry at University of Houston is a fantastic experience to my life after my five years of research in organometallics and inorganic chemistry. The very first person I want to thank is Prof. Thomas Teets. It was my pleasure to be accepted and start my Ph.D. life in Prof. Teets group, from where I started to learn how to solve scientific problems systematically as a rookie and was encouraged to expand the properties of formazanate complexes to some new areas later in direction of constructive suggestion from him. He always supported me to try some new ideas which might not succeed eventually and guaranteed that I stepped on the right route instead of getting lost. I also need to appreciate Prof. Wu and Zhili Wen who offered me a big help in my research especially in aspects of DFT calculation and explanation of unique optical and redox properties of my complexes. In addition, I enjoyed the devoted teaching from Prof. Wu and Prof. Jacobson that their classes always gave me great motivation to learn about unknowns. Originating from these outstanding chemistry researchers, I have been able to approach and meet extraordinary people at University of Houston.

Members in our research group provided me opportunities to learn from different people with different cultures. Dr. Evanta Kabir shared her experiences and techniques in synthetic chemistry and characterization wholeheartedly, which help to facilitate my management of latter independent projects. Dr. Hanah Na influenced me a lot for her hard-working and inspirational personality. I enjoyed working with Dr. Kusun Choung along with his dedication and knowledgeable synthetic skills. Dr. Yanyu Wu, Dr. Po-Ni Lai and Dr. Jonghwa Shon

helped me a lot about my research with crucial suggestions and were always available when I was seeking some help. Chenggang Jiang also helped me a lot in synthesis and purification of products.

I also want to give my acknowledgement to my friends in Houston. Hao Li was my roommate for two years and I could never forget the yummy Chinese courses he cooked. Dr. Haina Jia, Dr. Dawei Xiao and Dr. Zhongzheng Cai helped me a lot in accommodation and the starting of research at UH. Besides, I want to thank Qinxuan Wang, Yanxin Chen, Muxin Qiao and Haowen Zhao, who always kept me accompany, treated me as a family member and shared happiness among us. My girlfriend, Danlei Xiang, always encouraged me and shared individual progress to each other. Lastly, I want to acknowledge my parents for their absolute support spiritually, physically and financially for the five years and their optimism and toughness inspired me to overcome any obstacles in my research and my life.

ABSTRACT

Formazanates, the monoanionic form of formazans with a 1,2,4,5-tetraazapentadienyl (NNCNN) core, have become a well-known redox-active ligand class in recent years and the two additional nitrogen atoms in the backbone provide formazanates with more accessible redox properties and stronger absorption, due to the more stabilized LUMOs, compared with structural analogue β-diketiminates and thus, greatly expand the redox chemistry of formazanates. The massive attention on the coordination chemistry of formazanates is because of their ligand-based redox process, which may facilitate multielectron redox behaviors, bond activations, and excited-state charge separation. A variety of formazanate complexes of many main group metal and first- and second-row transition metals have been established, highlighting the chelating behaviors of formazanate ligands as well as their unique magnetic and photoluminescent properties. Our group focuses on the coordination chemistry of formazanate with third row transition metals and their derivatives, exhibiting strong absorption in visible region as well as multiple accessible redox potenials.

We found a new route for preparation of homoleptic azo-iminate Pt(II) complexes via hydrogenative cleavage of formazans, involving the proton-coupled electrons transfer to the formazanate, with two ligand radicals paired in the delocalized HOMO. Further research indicated that the irreversible first oxidation is accompanied with protonation.

A new class of bis-cyclometalated Ir(III) formazanate complexes were also prepared with different configurations and in most cases the “open form” were major products. However, different coordination modes minimally impact the orbital energies, with similar absorption and redox behaviors for both isomers.

In addition, a new route for the preparation of azo-triazolide Ir(III) complexes was found via cyclization of 3-cyanodiarylformazanate ligands when we tried to increase the steric profile of the substituents. These rearranged complexes share similar orbital structures with formazanate congeners but have a blue-shift in absorption due to the major transition being (HOMO−1)→LUMO.

We further expanded the coordination chemistry of formazanates and a series of dinuclear formazanate Ir(III)/Pt(II) complexes were obtained with different coordination modes. Ir (III) and Pt(II) displayed different preferences on coordinating sites of 4-pyridylformazanates. Some dinuclear compounds showed distinctly red-shifted absorption and a smaller HOMO–LUMO gap compared to others.

.

TABLE OF CONTENTS

List of Tables

List of Figures

List of Schemes

List of Charts

1 Chapter One Redox-active Formazans in Coordination Chemistry

1.1 Introduction

Nitrogen-rich redox-active molecules have been prominent among series of non-innocent ligands and their representative examples, such as diimines [1] and 1,2,4,5-tetrazines,[2] have been intensively studied over many years in the fields of basic coordination chemistry,[3] bioinorganic chemistry,[4] and catalysis.[5,6] Complexes of redox-active ligands have ligand-centered frontier orbitals, typically of π symmetry, that facilitate multielectron redox behaviors,[7] bond activation,[8] and charge separation[9] in the excited-state enabled by adding or removing electrons from redox-active ligands. Formazans (NNCNN), a class of nitrogen-rich, highly-colored redox-active compounds, have been known since late 1800s and studied more closely since 1940s.[10,11] The two additional nitrogen atoms greatly expand the absorption and redox properties of formazans relative to the structural analogue β-diketimine. Their intense colors and redox-chemistry that originates from the backbone have led to their widespread application as dyes mainly in cell biology for quantitative measurement of cell viability. NAD(P)H-dependent cellular oxidoreductases, reflecting the number of viable cells, are capable of reducing the tetrazolium dye MTT to its insoluble formazans,[12,13] and precursors to other stable redox-active compounds like verdazyls,[14–16] with reactions of formazans and formaldehyde in the presence of base and following oxidation in air. (Chart 1.1)

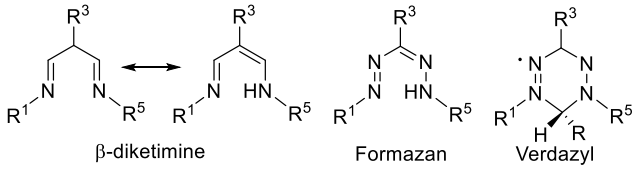

Chart 1.1 Structures of β-diketimine, formazan, and verdazyl compounds.

The facile synthetic chemistry of formazans allows modulation of properties through structural variation. The most general methods use the reaction of diazonium salts with substrates with activated carbon functionalities like hydrozones, and asymmetric formazans could also be accessed with different substituents

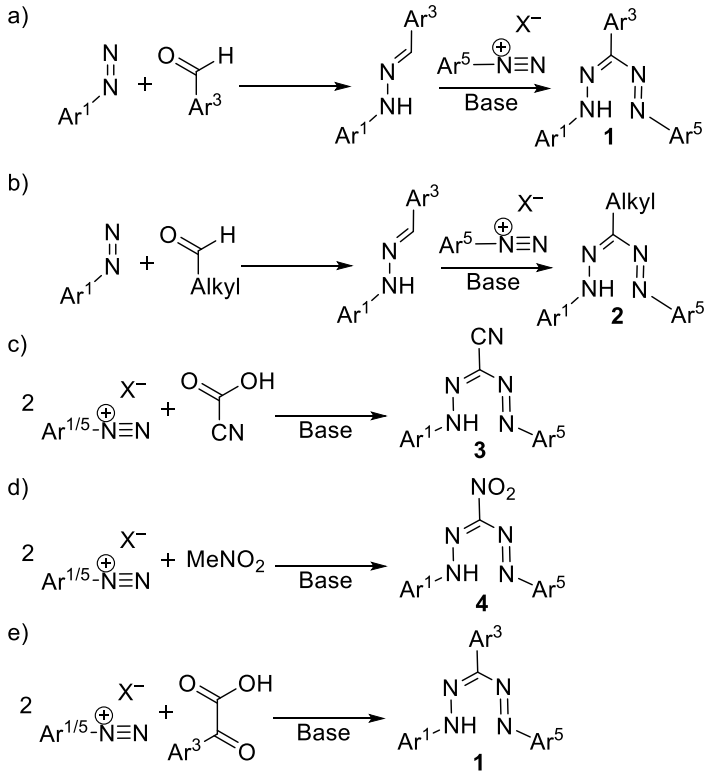

Scheme 1.1 Common routes for the synthesis of formazans.

on R^1 / R^5 positions[17] while, alternatively, coupling two equiv. diazonium salts with compounds containing activated methylene yield symmetric formazans in some cases

(Scheme 1.1).[18,19] The major concerns in the preparation of formazans focus on the stabilities of the requisite diazonium salts especially when sterically demanding substituents are introduced. The substituents on R^3 position may induce structural isomerization, namely, the bulky alkyl and aryl group tend to favor the "closed" form whereas for congeners with relatively small substituents on R^3 (e.g., H, Me, CN), the configuration of either "open" or "linear" form could be adopted (Figure 1.1). The identities of isomers correlate with the color of formazans with "closed" form always exhibiting blood red while "open" and "linear" congeners show orange color.[20]

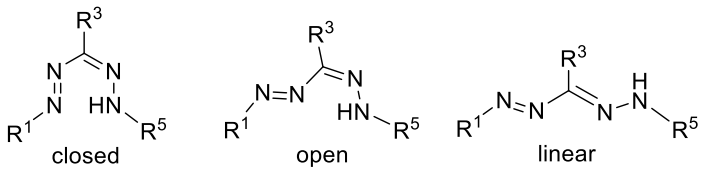

Figure 1.1 Three configurations of formazans

1.2 Formazanate Coordination Chemistry

The coordination chemistry of formazans, however, has not been further studied compared with other well-established nitrogen-rich redox-active ligands.[21–23] Formazanates, the monoanionic form of formazans, feature the abilities to engage in both oxidative and reductive redox behaviors with the presence of high-lying HOMO and low-lying LUMO of π symmetry. Both HOMO and LUMO are mainly composed of orbitals centered on the backbone of formazanate (NNCNN) (Figure 1.2).[20] Formazanates with diverse substitution patterns, like the π-conjugated aromatic N–Ar^1/Ar^5 groups, leads to rational tuning of electron structures and the LUMO is always π-anti-bonding between the four nitrogen in the framework and present a nodal plane that goes though C–R^3 fragment, suggesting that

variation on R^3 position has little effect on the energy of the LUMO. Thus, formazanate complexes are always expected to ligand-centered and readily to engage in ligand-based reductions due to the low-lying LUMO.[5,6] In addition, electronic transitions occur in the visible range of the spectrum with both absorption and emission properties of

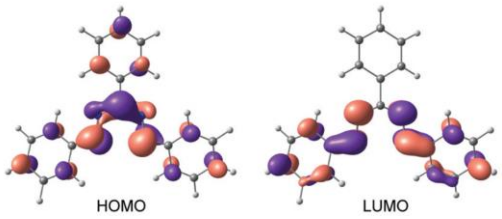

Figure 1.2 Frontier orbitals of triphenylformazanate ligand in "closed"form chelating mode, calculated using density functional theory (B3LYP/6-31G(d)).[20] Chem. Soc. Rev. 2020, 49 (1), 85–113 – Published by the Royal Society of Chemistry

formazanate complexes are tunable by modifying the ligands structures. Moreover, coordinative flexibility resulting from isomerization of formazanates allows the formation of "linear" (four-member ring), "open" (five-member ring) and "closed" (six-member ring) forms with different biting angles, which could effectively relieve the steric effect and optimize the coordination environment (Figure 1.3). And based on previous study, for both "closed" form and "linear" form complexes, the π electrons tend to be delocalized on the entire backbone of formazanate ligands with bond distances between that of single and double bonds of respective atoms while for "open" form congeners, however, the metrical parameters indicate that the π electrons prefer to be localized on certain bonds in the backbone of formazanate ligands.

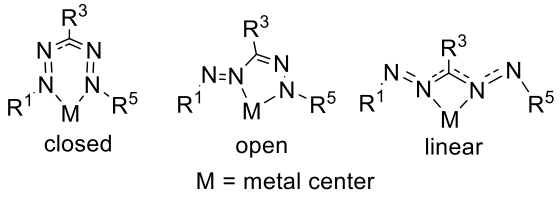

Figure 1.3 Common coordination modes of formazanate ligands in coordination compounds.

A variety of formazanate complexes of many main group metals and first- and second-row transition metals have been described and their work demonstrate the versatile coordination chemistry of formazanate ligands and provide significant insights into photophysical and redox properties of these complexes.

1.2.1 Complexes with Alkali Metals (Na, K)

The deprotonation of formazans with strong alkali metal bases like NaH or KH has been shown to cleanly generate the corresponding alkali metal formazanate salts.[24] (Scheme 1.2) In most cases, either "open" or "linear" form bidentate products are accessible because of the backbone allowing either terminal or internal nitrogen atoms to chelate with the metal center. And for their related complexes, π electrons are always delocalized on the formazanate framework with almost equivalent N–N and C–N bond distances within the ligand core from metrical parameters. Besides, cation exchange could be facilitated with configurations still intact, leaving the formazanate alkali metal salts as potential precursors for the transfer of formazanate ligands to other main group or transition metals via salt metathesis reactions.[25,26]

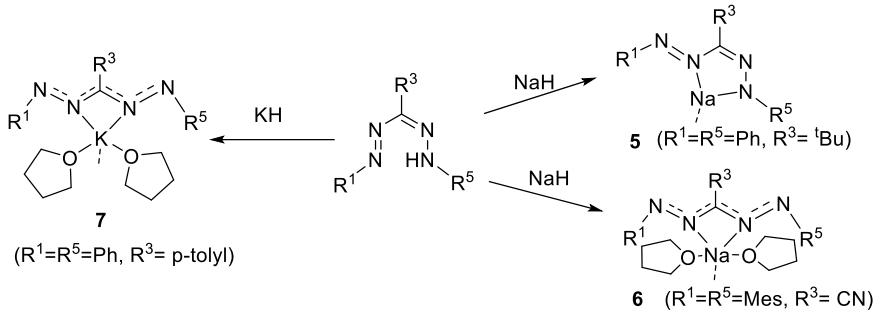

Scheme 1.2 Synthetic routes of some formazante complexes with alkali metals.

However, the introduction of C_6F_5 on R^3 position may disrupt the formation of formazanate alkali metal salts and the nucleophilic formazanates evolve and rearrange to form cyclized products, arylazoindazoles as a mixture of regioisomers, instead of simply deprotonation (Scheme 1.2), and the abnormal products have exhibited unique photoconversion as well as fatigue resistance.[27]

1.2.2 Complexes with Group 13 Metals (B, Al, Ga, In)

Arguably the adducts of boron complexes are the biggest family of formazanate chelating compounds over the past two decades since Hicks and co-workers first managed to convert triarylformazans to verdazyl radical anions which are stable enough to be characterized by UV-vis absorption (λ_{max} ~ 740 nm) and EPR spectroscopy (broad isotropic signal, g ~2.00).[28] This work set the starting point for later research of coordination chemistry of formazanate with boron and their related applications.

The introduction of boron difluoride (BF_2^+) chelates shed a new light on the coordination chemistry of formazanates. The first examples of BF_2 formazanate complexes were prepared from the corresponding homoleptic Zn(II) complexes[29] (Scheme 1.3a) and these compounds could be electrochemically reduced in two steps to the related radical anions and dianions

with structural rigidity and stability associated with the BF_2^+ fragment. Alternative synthetic routes involve the conversion of 3-cyanoformazans to BF_2^+ complexes by heating toluene solutions containing excess NEt_3 and BF_3•OEt_2 at 80 °C overnight[30,31] (Scheme 1.3b) and later the synthetic route was applied to 3-nitroformazans as well and both 3-cyano and 3-nitro compounds were examples of formazanate dyes with decent photoluminescence.[31,32]

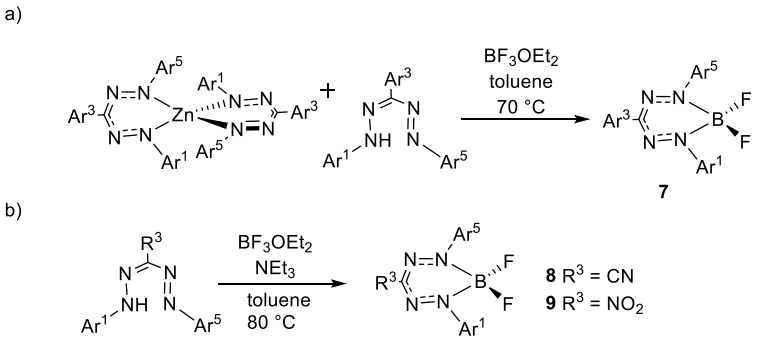

Scheme 1.3 Synthetic routes of some formazante BF_2^+ complexes.

The optoelectronic properties of BF_2 formazanate complexes have been systematically investigated with the variation of R^1, R^3 and R^5 substituents(see Chart 1.2).[29–31,33,34] Figure 1.4 shows the HOMO and LUMO calculated by DFT and both orbitals are highly delocalized over the formazanate framework and N-aryl substituents for most complexes but the R^3 position contributes the crucial part to only HOMO due to the nodal plane in LUMOs.[32] Based on this,

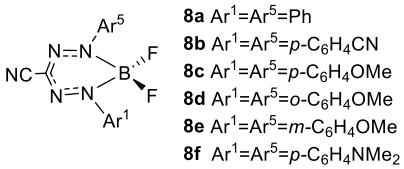

Chart 1.2 Some representative 3-cyanoformazanate BF_2^+ complexes.

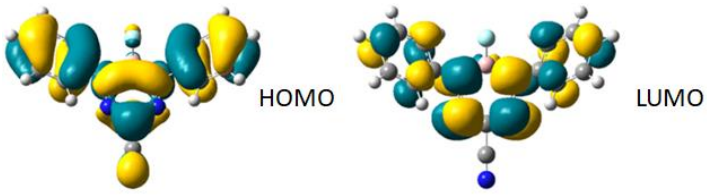

Figure 1.4 HOMO and LUMO for complex **8a**, calculated in toluene solution.[32] Adapted with permission from J. Org. Chem. 2015, 80 (10), 5226–5235. Copyright 2015 American Chemical Society.

properties like electrochemical reduction involving merely LUMOs are generally influenced by the variation at N-aryl substituents, while the variation of R^3 position is important for properties involving both HOMO and LUMO, like absorption and photoluminescence.[32] Also, the substituents at the *para* positions are likely to impact the properties of the BF_2^+ formazanate complexes with significant orbital density at the *para* positions of each aryl ring.[31] For most cases, BF_2^+ formazanate complexes possess highly delocalized π-electron systems on the backbones with low-energy λ_{max} and λ_{PL} values and large stokes shift, shown in Table 1.1. Compared with **8a**, the introduction of *p*-cyanophenyl substituents on R^1/R^5 positions in **8b** leads to the distinct anodic shift of both reduction potentials. And the red-shift in both absorption and emission of **8b** related to **8a** may result from the increase in the size of π-electron system with the addition of cyano groups. In contrast, **8c**, with electron-donating *p*-methoxyphenyl substituents, yields both red-shifted absorption and emission spectra compared with other BF_2^+ formazanate complexes attributed to the donor-acceptor electronic structure and the lone pair electrons from oxygen could be involved in the delocalization of π-electron system to extend the planar structure, also confirmed by the aggregation characteristics in THF solution with aggregation-caused quenching observed due to the π-π

stacking.[35] However, the change from *p*-methoxyphenyl in **8c** to *o*-methoxyphenyl in **8d** results in dramatic change in both photophysical and aggregation behaviors because of the sterically-driven twisting of N-aryl substituents out of the plane of formazanate backbone and the twisting leads to the observation of aggregation-induced emission enhancement (AIEE) on the addition of H_2O to THF soluton.[35] The *m*-substituted compound **8e** had properties intermediate of its *o*- and *p*-isomers.[36] When changing the N-aryl substituents to the strongly electron-donating *p*-dimethylaminophenyl groups, **8f** displays near-infrared photoluminescence and distinct cathodic shift of both reduction waves related to others, attributed to the strong electron donation from nitrogen lone pair and evidence of quinoidal character (N-C bonds with significant double bond character) were observed in crystal structures.[34]

Table 1.1 Optoelectronic properties of 3-cyanoformazanate BF_2 complexes

	λ_{max}[a] (nm)	λ_{PL}[a] (nm)	Φ_{PL}[a]	E_{red1}[b] (V vs Fc^+/Fc)	E_{red2}[b] (V vs Fc^+/Fc)
8a	502	586	0.15	−0.53	−1.68
8b	515	598	0.14	−0.21	−1.25
8c	572	656	0.77	−0.68	−1.82
8d	467	592	0.05	−0.73	−1.88
8e	525	635	0.13	−0.50	−1.62
8f	728	834	0.08	−1.02	−2.05

[a] Recorded in toluene. [b] Recorded in CH_3CN

Boron difluoride formazanate complexes are also used for the subsequent preparations of polynuclear complexes. This type of assembly was reported in two different works by the Gilroy group, one where the normal BF_2^+ formazanate adduct with a 2-pyridyl group on R^3 position (**10**) could work as the bidentate metalloligand to chelate with nickel (**11**), leaving their photophysical and redox properties largely altered (Scheme 1.4a)[37] and the other about a

suite of BF_2^+ formazanate complexes conjugated to platinum acetylide complex (**12a/b**) via aryl acetylene groups on formazanate periphery (Scheme 1.4b).[38]

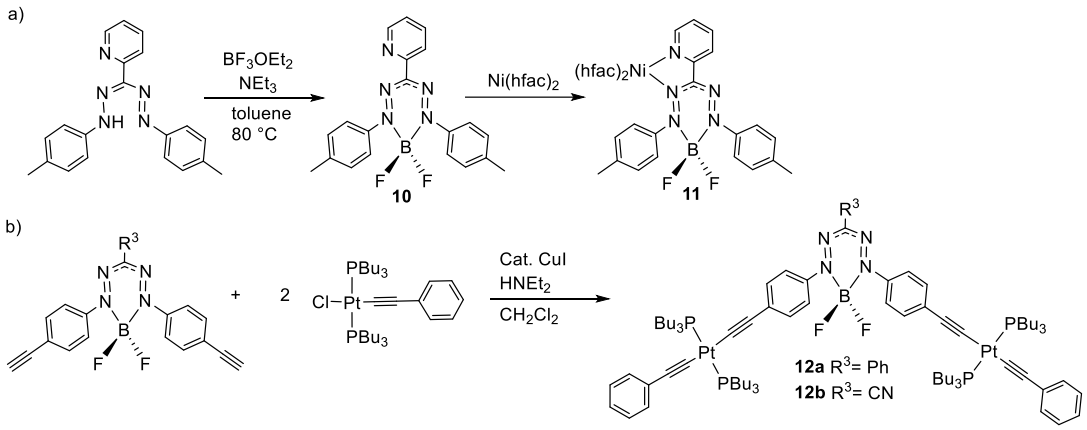

Scheme 1.4 Synthesis of dinuclear BF_2 formazanate adduct with nickel (**a**) and polynuclear BF_2 formazanate adduct with platinum (**b**)

Formazanate complexes of other group 13 metals have received rare attention compared with boron complexes. Tetrahedral complexes could be successfully accessed since Sundermeyer group prepared first heavy group 13 complexes of formazanatets by stirring the related MMe_3 (M= Al, Ga, In) species with triarylformazan ligands in toluene and they always display low-energy absorption with large molar extinction coefficients.[39] For six-coordinate aluminum complexes, they could be prepared by heating formazan with $Al(OiPr)_3$ and phosphine oxide ligand in toluene solution and feature the low-energy absorption and emission and their redox behaviors are always irreversible.[40]

Considering the strong absorption and bio-compatibility of formazans and their extensive use in cell-viability assays,[12,13] BF_2^+ formazanate complexes have been applied as cell-imaging agents in biological areas. **8c** was firstly selected in the research with its relatively high quantum yields in photoluminescence. It could be accumulated in hydrophobic cell

cytoplasm when fibroblast cells are treated with its DMSO-containing solutions. But when the N-aryl substituents are replaced by hydrophilic groups, they could promote the cellular uptake of the BF_2^+ formazanate compounds and enhance the accumulation in cells.[41] These research findings indicate potential impact from structural variation of BF_2^+ formazanate complexes on cell-imaging and therapeutic agents. Besides, BF_2^+ formazanates are always competitive candidates for electrochemiluminescence (ECL) due to their outstanding photophysical and redox properties and **8c** has a maximum ECL efficiency as high as 450%, the highest among BF_2^+ formazanates. For some non-emissive BF_2^+ formazanate complexes (**9**), they could be applied as pH sensor with critical increase in fluorescence quanum yield up to a maximum 18%.[37] Moreover, they could also be brought in functional polymers associating with organic electronics, which, in return, could tune the electron structures with extended π-electron system and enhance the absorption and photoluminescence and induce more accessible redox behaviors.[42]

1.2.3 Complexes with first-row transition metals (Mn, Fe, Co, Ni, Cu & Zn)

Formazanate complexes with first-row transition metals have been intensively investigated for their unique and outstanding properties. Early work shows the treatment of Fe(III) salts with formazans leads to the formation of low-spin octahedral Fe(II) complexes in most cases(Scheme 1.5a).[43,44] Later, the Hicks group found low-spin Fe(III) complexes with a trianionic N_2O_2-based formazanate scaffold could be obtained by salt metathesis of the in-situ-generated Na salt of the tetradentate formazanate with $FeCl_3$; two pyridine ligands bound trans to each other to meet an octahedral coordination geometry(Scheme 1.5b).[45] And their reduction to Fe(II) species was disrupted with the anionic O-donor groups.

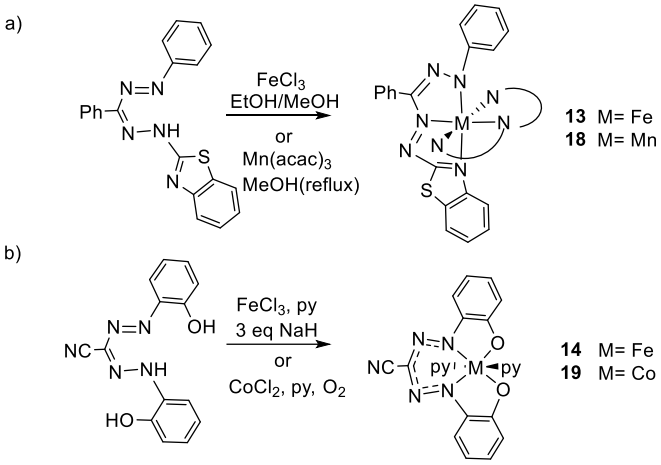

Scheme 1.5 Synthetic routes of some formazante Fe(II)/Mn(II)(**a**) and Fe(III)/Co(III)(**b**) complexes.

The Otten group reported homoleptic formazanate Fe(II) complexes **15** via salt metathesis in 2016 and the absence of additional ligands leaves a tetrahedral coordination around the iron center of the complex(Scheme 1.6).[25] It features a temperature-dependent equilibrium between a diamagnetic state (S=0) at low temperature and a paramagnet (S=2) at high temperature, confirmed by NMR and UV-vis absorption (Figure 1.5). The unusual spin-crossover behavior results from π-backdonation from the d^6 metal center to the low-lying formazanate π-anti-bonding orbitals, which leads to an energy-ordering of the d-orbital manifold of a 2-over-3 splitting. Its reduction peaks at −1.21 V and −2.01 V make the reduced species accessible with the help of Na/ Hg as reducing agents and is best formulated as a low-spin (*S*=1/2) Fe(I) complex with closed-shell formazanate ligands.

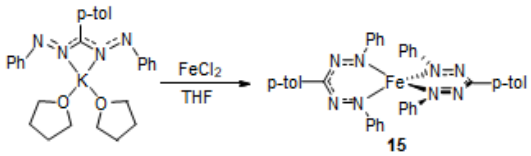

Scheme 1.6 Synthesis of bis(formazanate) Fe(II) complex **15**

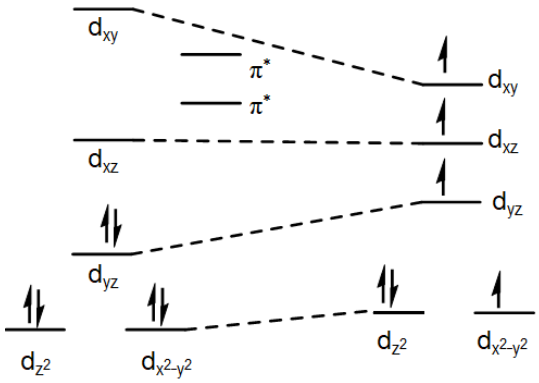

Figure 1.5 Molecular orbital diagram for complex **15** in the LS (S=0) state and the HS (S=2) state. Orbitals shown are obtained from a restricted closed-shell DFT calculation.[25]

The Holland group have also explored and further expanded the redox-active formazanate Fe(II) complexes. The THF adduct of monoformazanate iron amide **16** was used to prepare dimeric metallacycles **17** in which the formazanate chelates in the "open" form leaving a terminal nitrogen atom to bridge another Fe center with alkali metals as conter-cations (Scheme 1.7).[46] The reactivity of complex **16** (or THF adduct **16-THF**) towards CO_2 was examined with formation of isocyanate from a low temperature reaction.

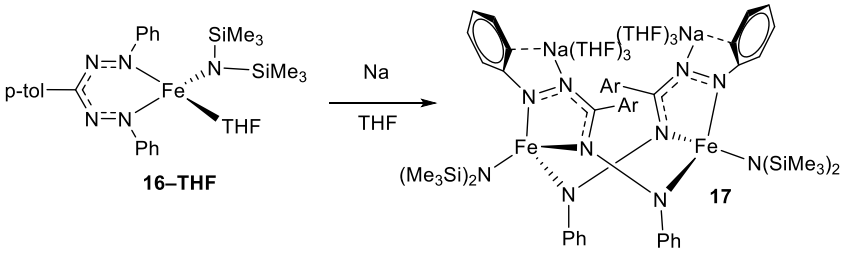

Scheme 1.7 Synthesis of dimeric formazanate Fe(II) metallacycle.

The combination of formazanate with Mn(II) has been reported only once by Brown group[44] (Scheme 1.5a), with the formazanate ligand of **18** preferring tridentate coordination to the Mn metal center in the low-spin Mn(II) complex and associate with other benzothiazolyl substituent to meet the octahedral coordination geometry. The Hicks group first reported

related Co(III) complex **19** with a tetradentate cyanoformazante ligand via salt metathesis and air oxidation (Scheme 1.5b).[45]

Nickel complexes with formazanate have been deeply investigated with detailed insight of structures and relevant properties since 2000. A series of symmetrical homoleptic bis-(triphenylformazanate) nickel(II) complexes with "closed" form chelation were prepared by the Vatsadze group(Scheme 1.8a).[47] They have square planar coordination geometries with the metal ion always out of the plane of formazanate backbone to minimize the steric effect from N-aryl substituents and could work as metalloligands with the introduction of pyridine substituents in supramolecular chemistry. A suite of bis(formazanate) Ni(II) complexes with various hetroaromatic substituents prepared by the Zaidman group were applied in catalysis of ethylene oligomerization. The Hicks group also found that the cyano and nitro group at R^3 position of formazan might induce the production of ill-defined polynuclear formazanate complexes when small N-aryl substituents are available (Scheme 1.8c) while only monoformazanate nickel hydroxide is prepared with sterically more demanding substituents (Scheme 1.8b).

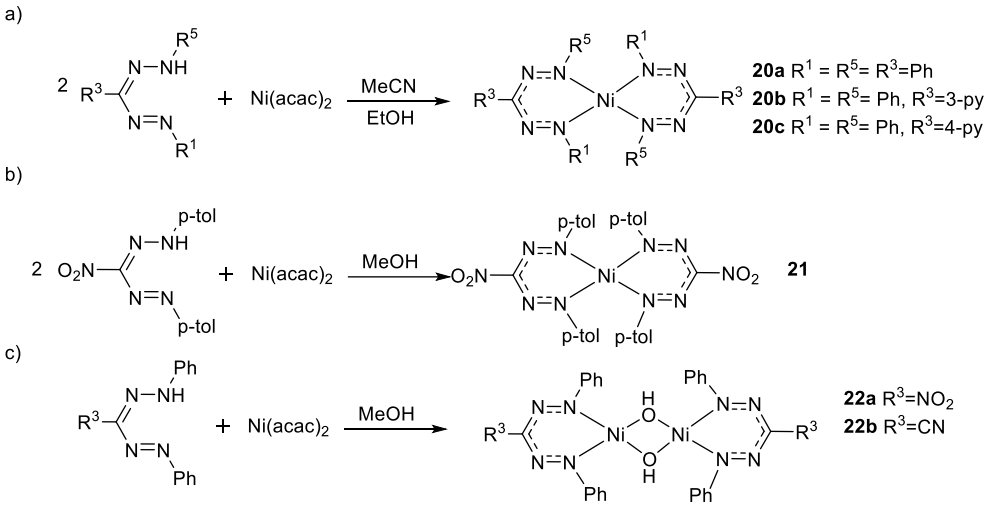

Scheme 1.8 Synthesis of homoleptic mononuclear nickel (II) complexes (**a** & **b**) and polynuclear complex (**c**).

The Hicks group is also the pioneer in the exploration of formazanate complexes with copper, and a pseudo-five-coordinate tetradentate formazanate Cu(II) complex was prepared with additional methoxy groups on the N-aryl positions (Scheme1.9a) and the unpaired electron in the d orbital of Cu(II) center (*S*=1/2) is confirmed by magnetic and spectroscopic data.[45] It was also reported that the formazanate ligand could be involved in the Cu(I) - mediated dioxygen activation. Hicks and Tolman prepared a mononuclear Cu(I) complex **24** with sterically demanding 3-nitroformazanate and the reaction of **24** with O_2 afforded the bis(μ-hydroxo) dinuclear copper(II) complex **25.**[48,49] (Scheme1.9b)

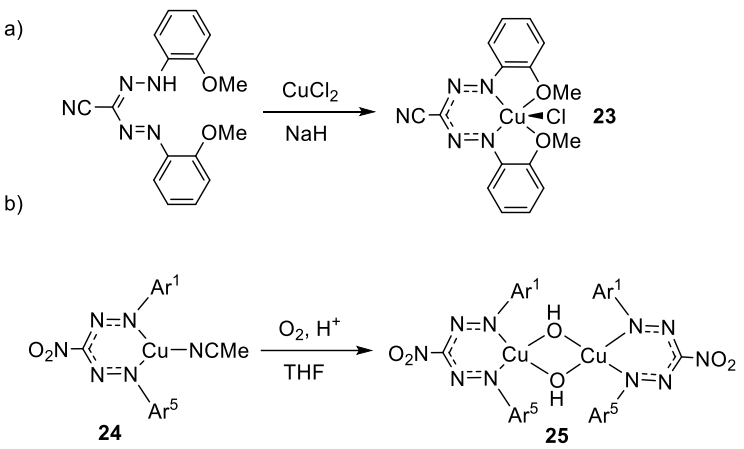

Scheme 1.9 Synthesis of formazanate Cu(II) complex (**a**) and their application in Cu(I) - mediated dioxygen activation (**b**)

Better insight of the combination of formazanate with zinc has been provided with a long history in the spectrophotometric quantification of zinc ions[50] and their ability to function as electron-reservoirs stands out among formazanates with other metals. A series of bis(formazanate) Zn(II) complexes were prepared via protonolysis of $ZnMe_2$ by the Otten group (Scheme 1.10).[26] The reduction potentials of **26a** reside at around −1.31/−1.55 V corresponding to redox-couples **26a**$^{0/-}$ and **26a**$^{-/2-}$ while a cathodic shift could be observed for both reduction peaks of **26b** attributed to the electron-donating *tert*-butyl group. Their related one- and two-electron reduction species could be afforded with additional Na/Hg reducing agents and Na^+ could interact with the nitrogen in the formazanate backbones. For one-electron reduced products, the two formazanate ligands around the zinc center are different with one maintained like the previous neutral starting materials (**26b**) but the other a dianionic radical, demonstrated by crystal structure of **26b**$^{2-}$. With further reduction to the dianionic product, both ligands are dianionic radicals, featuring typical low-energy absorptions($\lambda > 750$ nm). Besides, Gilroy group found these formazanate zinc complexes could be further reduced

at a more negative potential (−2.5 V) and all five different oxidation states (from neutral **26b** to **26b**$^{4-}$) are accessible regardless of the stabilities of the highly reduced species.

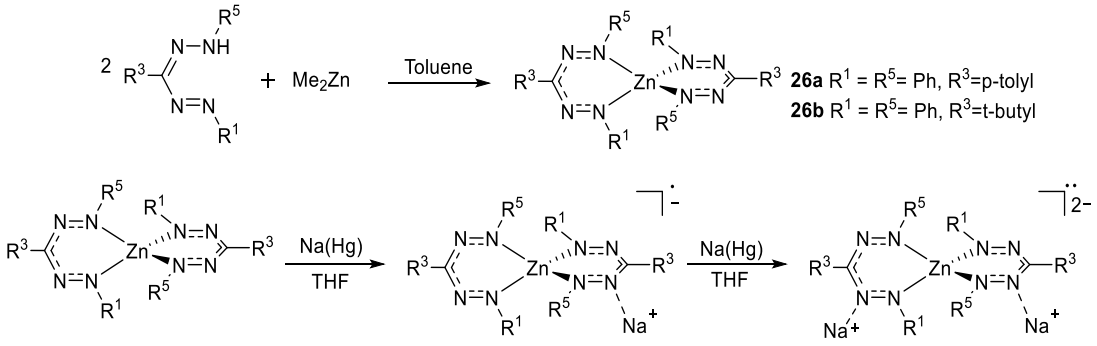

Scheme 1.10 Synthesis of bis(formazanate) zinc complexes and corresponding radical anions and dianions.

1.2.4 Complexes with other transition metals (Ru, Os, Pd)

Formazanate complexes with the heavier elements of group 8 (Ru, Os) are not intensively focused but there is still some progress in this area. Formazanate Ru complexes with some co-ligands like bipyridine or 2-phenylazopyridine were reported by Lahiri group and these studies laid the foundation for evaluation of the redox-noninnocence of formazanate ligands via experiments of spectroelectrochemistry with oxidation and reduction reactions and also provide the first evidence that formazanate ligand can still chelate with metals in its radical form with extended range of oxidation states.[51]

Palladium complexes were firstly reported in 2008, with a square planar coordination geometry chelated by 3-nitroformazanate and fluorinated acetylacetonate ligands, and the irreversible reduction waves in electrochemistry convinced researchers of the instability of their radical anions/dianions(Scheme 1.11a).[52] Later, the Lipunova group reported a new class of chloro-bridged dimeric palladium complexes and even the metal–metal bond between

two Pd centers could form after treatment with ammonium (Scheme 1.11b).[53]

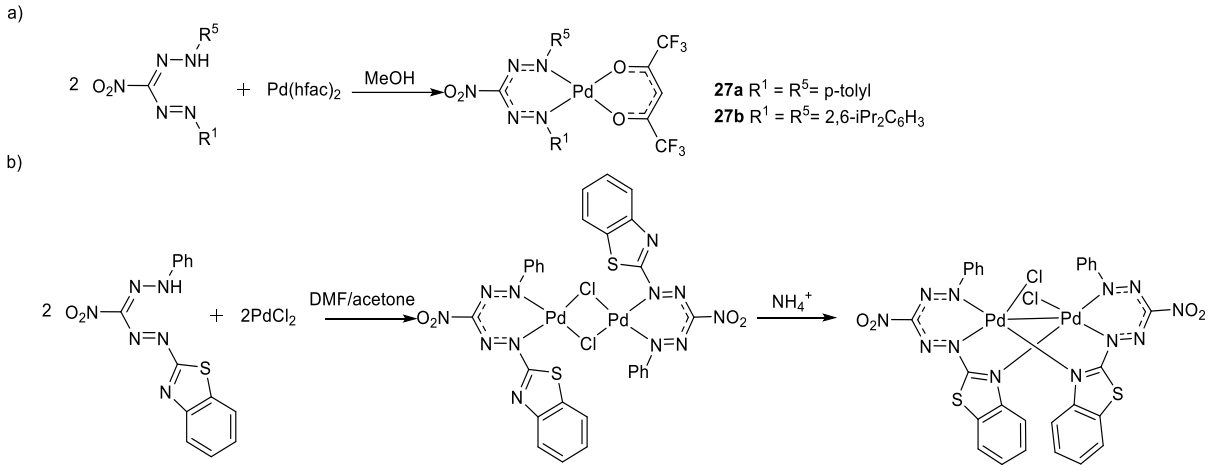

Scheme 1.11 Synthesis of 3-nitroformazanate Pd complex with fluorinated acetylacetonate (**a**) and dinuclear Pd complexes(**b**).

1.2.5 Previous work of our group

Considering previous research on formazanate complexes with main group and first- and second-row transition metals, we expand the coordination chemistry of formazans to the third-row transition metals and focus on their properties of strong absorption in visible region and multiple accessible redox behaviors. The first series of heteroleptic formazanate complexes with platinum reported by us were prepared via metathesis reactions of chloro-bridged dimer with triarylformazans in the presence of base and the product are always the traditional "closed" form chelating mode, confirmed by crystal structures(Scheme 1.12).[54] With the variation of formazanates and cyclometalated C^N ligands with different steric and electronic effects, the reaction always works with decent yields (47%–90%) with their major absorption at 650 nm (with phenyl ring at R^3 position) or 600 nm (without phenyl ring at R^3 position),

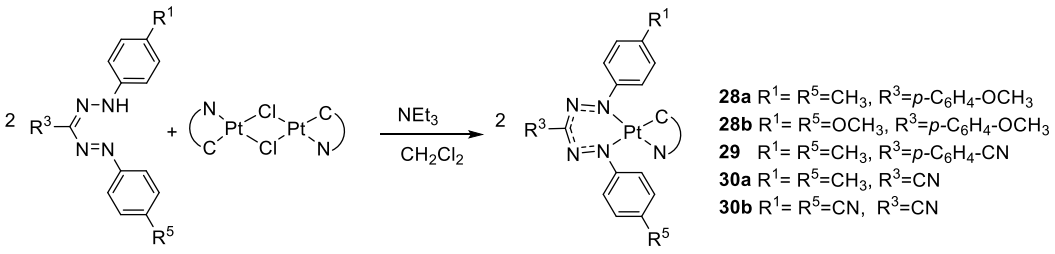

Scheme 1.12 Synthesis of cyclometalated formazanate Pt complexes.

resulting from the formazanate ligand-center $\pi \rightarrow \pi^*$ transition with minimum character of metal-to-ligand charge transfer (MLCT). The obvious red shift of complex **29** compared with **30a**/**b** is attributed to the phenyl ring at R^3 position which could extend the conjugated system of formazanate backbone efficiently.[55] Their redox behaviors are always unique with three reduction peaks, two reversible from the formazanate backbones and one irreversible between them of the Pt–C^N based reduction.

1.3 Brief description of research progress included in the dissertation

Given our previous knowledge and experience in the coordination chemistry of formazans, herein, we continue to focus on their coordination chemistry with the third-row transition metals and expand their photophysical and redox properties as well as their potential involvement in the preparation of some unique metal compounds via rearrangement of formazanate ligands.

We found a new route for preparation of homoleptic azo-iminate Pt(II) complexes via hydrogenative cleavage of formazans, involving the proton-coupled electron transfer to formazanate, and two radical electrons could paired and stabilized in the HOMO with delocalization of π electrons on both ligand frameworks, confirmed by crystal structures and

DFT calculations. Further research indicated that the irreversible first oxidation is accompanied with protonation.[56]

A new class of bis-cyclometalated Ir(III) formazanate complexes were also prepared with two different chelating modes (“open” and “ closed” form) and in most cases the “open” form were major products. However, different coordination modes minimally impact the orbital energy and similar absorption and redox behaviors.[57]

In addition, a new route for the preparation of nitrogen-rich azo-triazolide Ir(III) complexes was discovered via cyclization of 3-cyanodiarylformazanate ligands when we tried to introduce some sterically demanding substituents, but they still share similar orbital structures and redox behaviors with their formazanate congeners. That said, there is a distinct blue-shift in absorption compared with formazanate compounds due to the major transition not from HOMO→LUMO, as is typical in formazanate compounds, but from (HOMO−1)→LUMO (azo-triazolide compounds), with clear evidence from electrochemistry and DFT calculations.[58]

Then, we tried to further highlight and expand the coordination chemistry of formazanates to polynuclear compounds with the introduction of 2- and 4-pyridyl substituents on R^3 position of formazans. A series of dinuclear flexidentate formazanate Ir(III)/Pt(II) complexes were obtained with different coordination modes, reflecting different coordination preferences of 4-pyridylformazanates for Ir(III) and Pt(II) metal centers. Only Pt(II) complexes are available for 3–(2-pyridyl)formazanate. Their UV-vis absorption could be impacted exclusively by the coordination on the backbone of formazanate and some of abnormal-chelating dinuclear compounds showed distinct red-shift absorption compared with others

with a smaller HOMO-LUMO gap whereas the only dimeric metallacycle prepared exhibits a unique absorption at around 510 nm, resulting from the separation of two intense absorption after mixing of two same excited states.[59]

2 Chapter Two Homoleptic Platinum Azo-iminate Complexes via Hydrogenative Cleavage of Formazans

2.1 Introduction

Redox-active ligands have been intensely studied over many years in the contexts of basic coordination chemistry,[2,3,26] bioinorganic chemistry,[4] and catalysis.[5,6] Complexes of redox-active ligands include ligand-centered frontier orbitals, typically of π symmetry, that facilitate multi-electron redox reactivity,[7] bond activation chemistry,[8] and excited-state charge separation[9] enabled by adding or removing electrons from the redox-active ligand. There are many categories of redox-active ligands that have emerged, and one which has received some attention are azo-oximates (Scheme 2.1), which have been coordinated to most late transition metals[60–62] and also used to assemble polymetallic structures.[63–66] As shown in Scheme 1, $3H^+/2e^-$ proton-coupled reduction of azo-oximates can generate azo-imines, which can be further reduced by one additional electron to form 5-π-electron, radical anion azoiminates. This transformation has been observed in palladium[67] and iridium complexes,[68] applying ascorbic acid or sodium borohydride to provide the reducing equivalents, and in rhenium complexes[69] via oxygen-atom transfer to the metal or a phosphine acceptor.

Scheme 2.1 The conversion from azo-oximate to azo-iminate.

Despite the long-standing interest in azo-imine and azo-iminate redox-active ligands, there is no rational synthesis available for this ligand class, and templated syntheses starting with azo-oximates are not general across all transition metals, hence the sparse reports. As an example, whereas homoleptic palladium complexes of azo-iminates can be prepared by reduction of azo-oximates,[67] analogous reactions with isostructural platinum complexes results in proton-coupled electron transfer to the ligand but no N–O bond cleavage.[70] These observations motivate continued pursuits of alternative methods for preparing azo-oximate complexes, to expand the coordination chemistry of these ligands to other transition metal systems.

In this chapter, we show that platinum azo-iminate complexes, which were not accessible using azo-oximate precursors, can instead be prepared from triarylformazan precursors. Triarylformazans are an important class of redox-active ligand in their own right,[26,31,40,49] receiving considerable recent attention as supporting ligands for transition metal compounds and for their redox activity and optical properties. Recent work has also begun to characterize the chemical noninnocence of formazans, where reduction of formazanate complexes is sometimes accompanied by bond rearrangements.[27,71,72] The new mode of reactivity described here, templated, reductive cleavage of formazanates to form azo-iminates, further highlights the redox and chemical reactivity of formazanates and gives access to a new class of compounds.

2.2 Results and Discussion

2.2.1 Synthesis

Scheme 2.2 shows the synthesis of the four homoleptic platinum azo-iminate compounds described here. In an attempt to prepare homoleptic platinum formazanate complexes, free triarylformazans (**Fza**–**Fzd**) were treated with the common platinum(II) precursor *cis*-$Pt(DMSO)_2Cl_2$[73] in refluxing methanol with excess sodium carbonate present. Instead of the

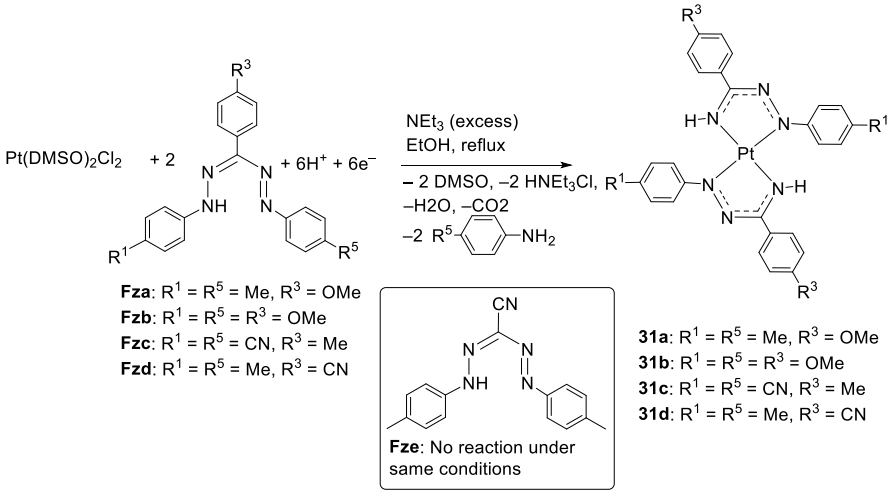

Scheme 2.2 Synthetic route of platinum azo-iminate complexes.

expected bis(formazanate) products, bis(azo-iminate) complexes **31a**–**31d** were formed instead as major products, releasing the respective substituted aniline as a byproduct. The reaction operates with a variety of triarylformazans, tolerating both electron-donating (Me or OMe) and electron-donating substituents at either the site of N=N bond cleavage (R^1/R^5) or at the central position of the backbone (R^3). Under these conditions, modest yields of 27–40% were obtained and when replacing methanol with higher-boiling ethanol, no improvement in

yields was detected but the combination of ethanol with triethylamine, the more soluble but slightly stronger base, induced higher yields of products (60–73%).

Although a detailed mechanism is still not apparent, there are some evidence consistent with the notion that the reduction of chelating formazanate accounts for the rearrangement and formation of **31a**–**31d**. The alcohol solvents are presumably the source of electrons and protons for the cleavage reaction, supported by the observation that no reaction was observed when triarylformazans and *cis*-$Pt(DMSO)_2Cl_2$ are combined in refluxing CH_2Cl_2 with NEt_3 as the base. In our previous work on heteroleptic platinum formazanate complexes,[54,55] formazans were not reduced under the similar conditions when chelating cyclometalated platinum precursors, suggesting the reduction of formazans in the presence of Pt(II) complexes depends on the nature of platinum precursors. We also set some intermediate checkpoints and only unreacted formazans and related products **31a**–**31d** were detected with no evidence for any formazan degradation products or formazanate complexes, indicating the high stability of formazan under the reaction conditions. We have not investigated many Pt precursors, but we observed the low yields of **31a**/**b** (13%/18%) when $Pt(dtbbpy)Cl_2$ (dtbbpy = 4,4'-di-tert-butyl-2,2'-bypyridine) was treated with formazans with excess Na_2CO_3. Table 2.1 summarizes a variety of reactions and conditions during the optimization of the reaction describe in Scheme 2.2, consistent with the idea that alcohol solvent offer both protons and electrons to coordinated formazanate ligands for the formation of azo-iminate compounds. Interestingly, 3-cyanodiarylformazan **Fze** (Scheme 2.2) does not react, and under the same conditions as used for the synthesis of **31a**–**31d** only unreacted starting material was recovered. The related NMR data are shown in Fiqure S1–S8 in appendix.

Table 2.1 Summary of reactions and conditions used to prepare platinum azo-iminate complexes.

Reagents	Conditions	Outcomes
cis-Pt(DMSO)$_2$Cl$_2$+**Fza**–**Fzd+**Na$_2$CO$_3$	Methanol, reflux, 36h	Formation of **31a**–**31d** with isolated yields of 36%(**31a**), 40%(**31b**), 33%(**31c**) and 27%(**31d**)
cis-Pt(DMSO)$_2$Cl$_2$+**Fzb**&**Fzc**+Na$_2$CO$_3$	Ethanol, reflux, 36h	Formation of **31b**&**31c** with isolated yields of 42%(**31b**) and 33%(**31c**)
cis-Pt(DMSO)$_2$Cl$_2$+**Fza**–**Fzd**+NEt$_3$	Ethanol, reflux, 36h	Formation of 31a–31d with isolated yields of 63%(**31a**), 73%(**31b**), 66%(**31c**) and 60%(**31d**)
cis-Pt(DMSO)$_2$Cl$_2$+**Fza**–**Fzd**+NEt$_3$	CH$_2$Cl$_2$, reflux, 36h	No reaction
Pt(bpy)Cl$_2$+**Fza**&**Fzb**+Na$_2$CO$_3$ (bpy = 2,2'-bipyridine)	Methanol/Ethanol, reflux, 36h	No reaction
Pt(dtbbpy)Cl$_2$+**Fza**&**Fzb**+Na$_2$CO$_3$ (dtbbpy = 4,4'di-tert-butyl-2,2'-bipyridine)	Methanol, reflux, 36h	Formation of **31a**&**31b** with isolated yields of 13%(**31a**) and 18%(**31b**)

2.2.2 X-ray Crystallography

The structures of **31a**–**31d** were confirmed by single-crystal X-ray diffraction and are shown in Figure 2.1, with refinement data summarized in Table 2.2. In all cases the two azo-imine ligands are situated in a trans arrangement, and the imine N–H hydrogen atoms were located in the difference map in each case and refined with an affixed distance of 0.88 Å. The crystal structures are consistent with electronic structures best described as formally Pt(II) with two 5-π-electron monoanionic azo-iminate ligands. The structures are rigorously planar; the sums of the bond angles about the Pt center are exactly 360° in each case with deviations

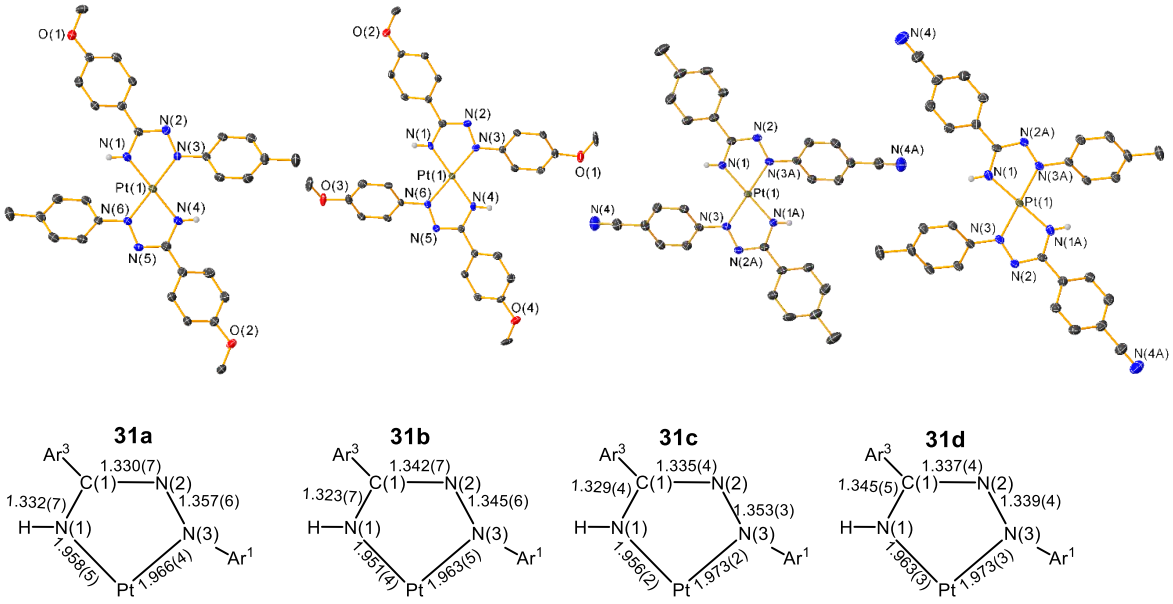

Figure 2.1 X-ray crystal structure of complexes **31a–31d**, with ellipsoids shown at the 50% probability level and carbon-bound hydrogen atoms omitted. In the bottom diagrams bond lengths are shown in Å with esd values in parentheses, and only the crystallographically independent distances are provided.

of the platinum centers from the main coordination plane (N1, N3, N4 and N6) ≤ 0.010 Å, consistent with a formally Pt(II) oxidation state. Furthermore, the bond distances of the azo-iminate ligand (see Figures 2.1) are suggestive of a radical anion core. In particular, the N–N bond distances, which range between 1.339(4) Å and 1.361(6) Å across the series of compounds, are significantly longer than the ~1.28 Å distances typically observed in non-radical azo-ligands and consistent with population of an azo-centered π* orbital.[67,68,74] There are no significant variations in the bond lengths and angles in **31a**–**31d**, which differ with respect to the substituents on the aryl positions.

Table 2.2 Summary of X-ray crystallographic data for azo-iminate complexes **31a**–**31d**

	31a•CH_2Cl_2	**31b**•CH_2Cl_2	**31c**	**31d**•2THF
CCDC	1568976	1568977	1568978	1568979
Crystal data				
Chemical formula	$C_{31}H_{32}Cl_2N_6O_2Pt$	$C_{31}H_{32}Cl_2N_6O_4Pt$	$C_{30}H_{24}N_8Pt$	$C_{38}H_{40}N_8O_2Pt$
M_r	786.61	818.61	691.66	835.87
Crystal system, space group	Monoclinic, $P2_1/n$	Monoclinic, $P2_1/n$	Triclinic, $P\bar{1}$	Triclinic, $P\bar{1}$
Temperature (K)	123	123	296	296
a, b, c (Å)	14.4014(15), 7.5559(8), 27.101(3)	14.256(13), 7.461(7), 28.94(3)	5.3187(15), 10.526(3), 12.290(3)	5.7040(17), 10.947(3), 13.848(4)
α, β, γ (°)	90, 91.4939(14), 90	90, 91.835(12), 90	85.152(3), 86.114(3), 86.192(3)	92.091(3), 98.388(3), 93.512(3)
V (Å^3)	2948.0(5)	3077(5)	682.8(3)	852.9(4)
Z	4	4	1	1
μ (mm^{-1})	4.98	4.78	5.17	4.16
Crystal size (mm)	0.33 × 0.12 × 0.05	0.19 × 0.07 × 0.01	0.29 × 0.06 × 0.02	0.39 × 0.18 × 0.04
Data collection				
T_{min}, T_{max}	0.557, 0.746	0.530, 0.746	0.581, 0.746	0.522, 0.746
No. of measured, independent, and observed [$I > 2\sigma(I)$] reflections	14286, 6457, 5140	16934, 6734, 5254	9154, 3123, 3121	10771, 3760, 3758
R_{int}	0.036	0.038	0.032	0.032
$(\sin\theta/\lambda)_{max}$ (Å^{-1})	0.641	0.641	0.651	0.641
Refinement				
$R[F^2 > 2\sigma(F^2)]$, $wR(F^2)$, S	0.040, 0.107, 1.11	0.034, 0.094, 1.07	0.023, 0.048, 1.07	0.027, 0.067, 1.08
No. of reflections	6457	6734	3123	3760
No. of parameters	417	435	182	273
No. of restraints	67	63	1	210
$\Delta\rho_{max}$, $\Delta\rho_{min}$ (e Å^{-3})	1.39, -2.49	1.36, -1.58	0.92, -1.08	1.27, -1.78

2.2.3 UV-vis absorption

The azo-iminate platinum complexes are all highly colored, appearing dark green in solution, in contrast to the free formazan precursors (**Fza–Fzd**), which appear deep red. UV-

vis spectra for the complexes are shown in Figure 2.2, with a summary of the data in Table 2.3. In addition to intense peaks in the UV ($\lambda < 350$ nm) attributed to localized $\pi \rightarrow \pi^*$ transitions of the aryl substituents, an intense absorption beyond 600 nm dominates the spectrum. The wavelengths of the visible absorption maxima span a narrow range of only 19 nm (400 cm^{-1}), between 676 nm (**31a**) and 695 nm (**31c**). These wavelengths are blue-shifted by 45–64 nm (880–1300 cm^{-1}) from a previously characterized unsubstituted Pd(II) bis-azo-iminate complex, which has a peak absorption at 740 nm.[67] This low-energy transition in Pd(II) analogues has been previously assigned to a fully allowed $a_u \rightarrow b_g$ HOMO→LUMO transition, and an identical assignment is proposed for the Pt(II) analogues described here, which is confirmed by DFT calculations described below.

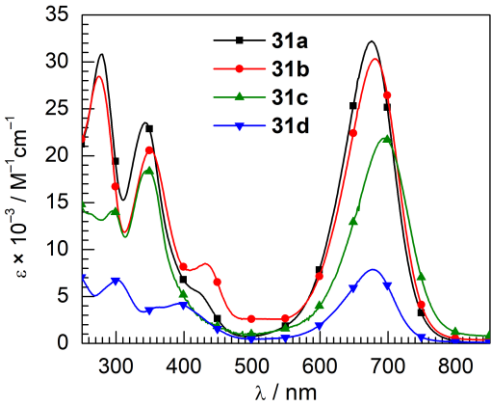

Figure 2.2 Overlaid UV-vis absorption of azo-iminate complexes **31a**–**31d.**

Table 2.3 Summary of UV-vis absorption data. Spectra were recorded in CH_2Cl_2.

	λ / nm (ε × 10^{-3} / $M^{-1}cm^{-1}$)
31a	280 (31), 342 (24), 416 (sh) (5.7), 676 (32)
31b	274 (28), 351 (21), 431 (8.5), 681 (30)
31c	296 (14), 345 (18), 695 (22)
31d	302 (6.7), 364 (3.9), 391 (4.2), 677 (7.9)

The previously described Pd(II) analogues also exhibited substantial ligand-to-metal charge transfer (LMCT) character in their HOMO→LUMO transition,[67] and we also see evidence for some charge-transfer character in complexes **31a**–**31d**. UV-vis spectra were recorded in three solvents of varying polarity (toluene, CH_2Cl_2, and MeOH), and the low-energy band was observed to exhibit measurable solvatochromism in each case. Figure 2.3 displays the overlaid normalized absorption spectra in the three solvents, and Table 2.4 summarizes the observed absorption maxima. The low-energy absorption maximum is the most sensitive to the change in solvent polarity, shifting hypsochromically as the solvent is varied from toluene ($\varepsilon = 2.38$) to dichloromethane ($\varepsilon = 8.93$) to methanol ($\varepsilon = 33.0$).[75] The absorption maximum blue-shifts by only 4–6 nm (87–130 cm^{-1}) when moving from toluene to CH_2Cl_2, but an additional blue shift of 12–16 nm (270–350 cm^{-1}) is noticed when changing the solvent from CH_2Cl_2 to MeOH. These observations are consistent with the notion that the HOMO→LUMO transitions which are primarily azo-iminate-centered also involve significant charge-transfer character.

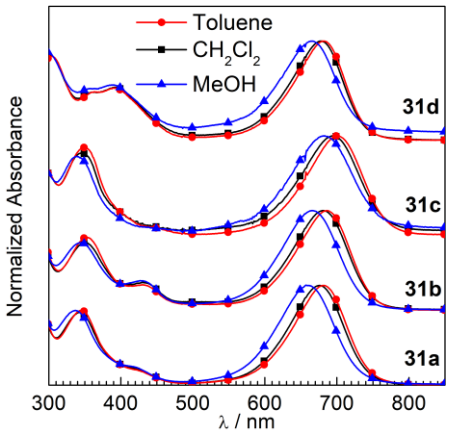

Figure 2.3 Overlaid UV-vis absorption spectra of **31a**–**31d** recorded in different solvents and all spectra were recorded at room temperature and are normalized to thel ow-energy absorption maxima.

Table 2.4 Summary of UV-vis absorption maxima in different solvents.

	λ / nm Toluene→CH_2Cl_2→MeOH
31a	345→342→337, 420→416→412, 682→676→662
31b	352→351→345, 431→431→427, 686→681→665
31c	298→296→295, 349→345→338, 701→695→681,
31d	304→302→299, 364→364→358, 390→391→387, 681→677→665

2.2.4 Electrochemistry

The redox properties of the new complexes were evaluated by cyclic voltammetry, with overlaid voltammograms shown in Figure 2.4 and redox potentials summarized in Table 2.5. Each complex shows two oxidation and two reduction features within the accessible window. The first oxidation is electrochemically irreversible, whereas the second is reversible. In all four cases the first reduction is reversible, and for cyano-substituted complexes **31c** and **31d** the second reduction is also reversible. The potentials of the redox features are responsive to the substitution pattern of the azo-iminate ligand, such that complexes with electron-donating substituents (**31a** and **31b**) are easier to oxidize and more difficult to reduce than the congeners with electron-withdrawing groups (**31c** and **31d**). The redox potentials for complexes **31a** and **31b** are quite similar and replacing the R^1 Me group in **31a** with a second OMe group in **31b** results in a 50–100 mV cathodic shift of the potentials. For example, the reversible reduction in complex **31a** appears at –1.40 V vs. Fc^+/Fc, whereas that for complex **31b** is at –1.45 V. Larger perturbations are achieved with electron-withdrawing cyano substituents, which result in an anodic shift of all redox features. The potentials are most sensitive to incorporation of electron-withdrawing groups at the R^1 azo position, and in complex **31c** the reversible reductions occur at –1.03 and –1.45 V, compared to –1.25 and –

1.85 V for isomeric complex **31d**. The separation between the reduction and oxidation potentials is quite similar in most cases, with a difference of 1.45–1.63 V between the reversible first reduction and the $E_{p,a}$ for the first oxidation, suggesting that the HOMO and LUMO are similarly sensitive to substituent changes and HOMO–LUMO gaps are similar for all complexes. The electrochemical features of these compounds are similar to those reported for an unsubstituted Pd(II) analogue, and in analogy to this previous work we assign both the oxidation and reduction waves to primarily ligand-centered events involving azo-iminate π* orbitals.[67] The high sensitivity of the redox waves to substituents at the azo position is consistent with larger contribution of the azo pπ orbitals to the HOMO and LUMO.

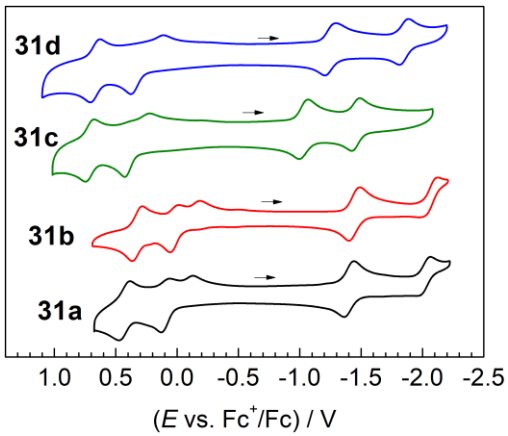

Figure 2.4 Overlaid cyclic voltammograms of complexes **31a**–**31d**, recorded in CH_2Cl_2 with 0.1 M NBu_4PF_6 electrolyte, using a glassy carbon working electrode, platinum wire counter electrode, and silver wire pseudoreference electrode. Potentials were referenced to an internal ferrocene standard, and currents are normalized to bring the plots onto the same scale.

Cyclic voltammograms were also recorded at –60 °C, as representative 31d shown in Figure 2.5. The reduction waves are virtually unperturbed by changing the temperature while the first oxidation is almost reversible, but becomes irreversible rapidly after the second oxidation is processed. At –60 °C the first oxidation becomes completely reversible in

Table 2.5 Summary of electrochemical data of all azo-iminate complexes

	E / V			
	1st Oxidation	**2nd Oxidation[a]**	**1st Reduction[a]**	**2nd Reduction**
31a	+0.07[a]	+0.43	−1.40	−2.07[b]
31b	+0.05[b]	+0.32	−1.45	−2.13[b]
31c	+0.42[b]	+0.71	−1.03	−1.45[a]
31d	+0.38[c]	+0.67	−1.25	−1.85[a]

[a] Reversible peaks. [b] Irreversible peaks. [c] Reversible only at −60 °C

complex **31d** when sweeping only to the first oxidation and allowing a half-wave potential of +0.38 V to be determined for this couple but it remains irreversible at –60 ° when the second oxidation wave is accessed.

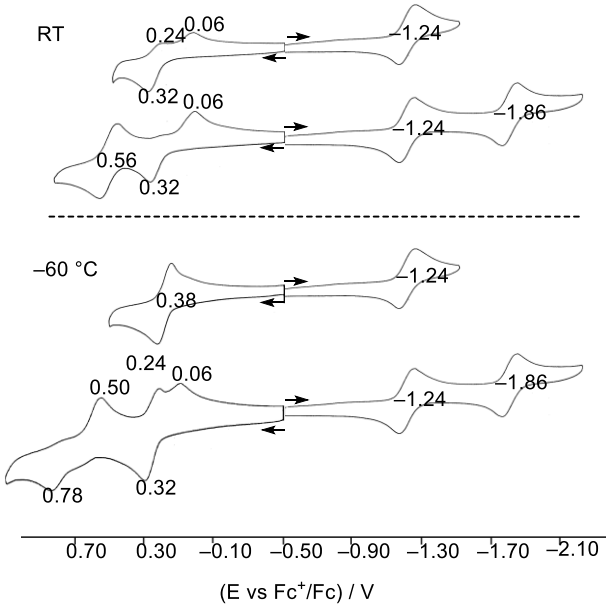

Figure 2.5 Cyclic voltammograms of complex **31d**, recorded at room temperature and −60 °C in CH_2Cl_2. A glassy carbon working electrode, platinum wire counter electrode, and SCE reference electrode were used. Potentials were shifted to the ferrocene scale to match the Figure 2.4.

Further insight into the oxidation waves was obtained by recording voltammograms (anodic sweeps) in the presence of increasing amounts of trifluoroacetic acid (TFA), as shown in Figure 2.6. The first oxidation wave shifts anodically and gradually becomes more reversible

(smaller peak-to-peak separation) as acid is added. The second oxidation wave is unaffected by acid, and in the presence of excess acid (< 500 equiv) the two oxidation waves collapse into one reversible two-electron wave. A plot of $E_{p,a}$ vs. log[H^+], shown in Figure 2.7, has a slope of 138 mV / decade, consistent with a 2-proton process. In addition, when complex **31d** is titrated with acid, distinct changes in the UV-vis absorption spectrum are observed, including a broadening of the low-energy HOMO→LUMO transition and a shift of λ_{max} from 677 to 684 nm, among other changes. All of these data are consistent with an electrochemical mechanism whereby complex **31d** is initially protonated twice by TFA, likely at the unsubstituted nitrogen atoms on the backbone. The first oxidation results in loss of both of

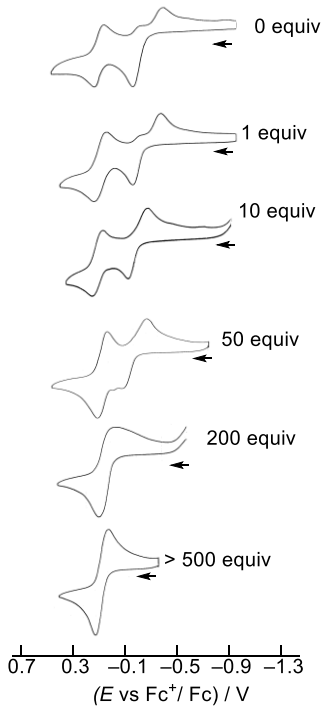

Figure 2.6 Cyclic voltammograms of complex **31d**, with anodic sweeps only, recorded in the presence of increasing amounts of trifluoroacetic acid. The voltammograms were recorded in CH_2Cl_2 with 0.1 M NBu_4PF_6 electrolyte, using a glassy carbon working electrode, platinum wire counter electrode, and SCE reference electrode. Potentials were shifted to the ferrocene scale to match Figure 2.4.

these protons, explaining the acid-dependence of the first oxidation potential, whereas the second oxidation is not coupled with proton loss. At high enough acid concentration, the first oxidation becomes coincident with the second, and a crossover to a two-electron concerted oxidation occurs.

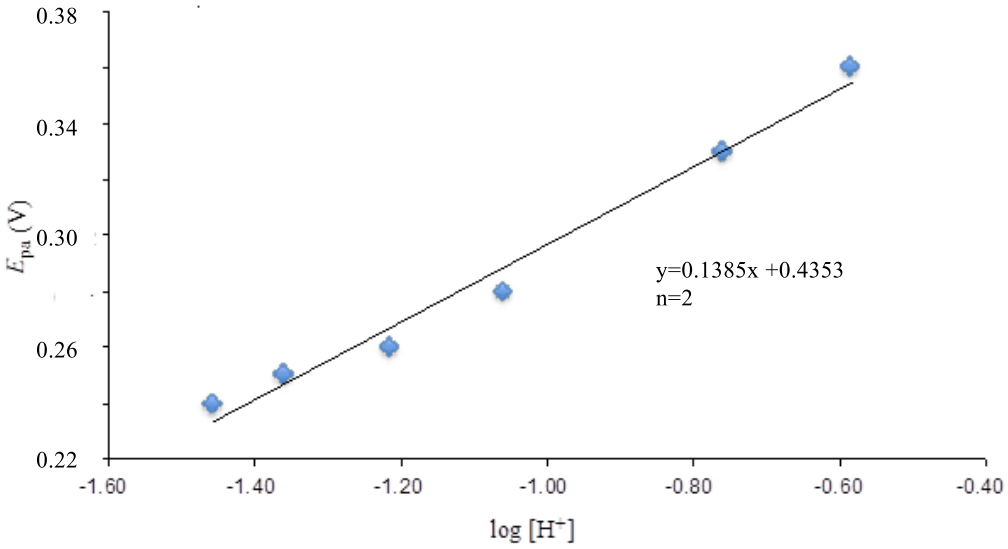

Figure 2.7 Plot of $E_{p,a}$ vs. log [H^+] for the first oxidation wave when complex **31d** is titrated with trifluoroacetic acid.

2.2.5 DFT calculations

Gas-phase DFT computations on complex **31c** were used to evaluate aspects of the frontier orbitals and UV-vis absorption transitions, and they are consistent with the experimental observations described above. The optimized structure is a singlet diradical (S = 0), with a HOMO that is delocalized over both azo-iminate ligands. Figure 2.8 shows plots of the computed HOMO and LUMO orbitals, along with a depiction of the structure in the same orientation. The HOMO and LUMO are mostly comprised of azo-iminate π orbitals, and are very similar to the frontier orbitals of a previously reported, unsubstituted Pd analogue.[67] The

HOMO has a_u symmetry with significant azo N=N antibonding character, consistent with the slightly elongated N=N bonds described above. The LUMO is an out-of-phase, b_g-symmetric combination of the same azo-iminate SALCs found in the HOMO. The major difference between the HOMO and LUMO is the contribution from the platinum center, which totals only 0.31% in the HOMO, but is 12.56% in the LUMO (on the basis of electron density). In

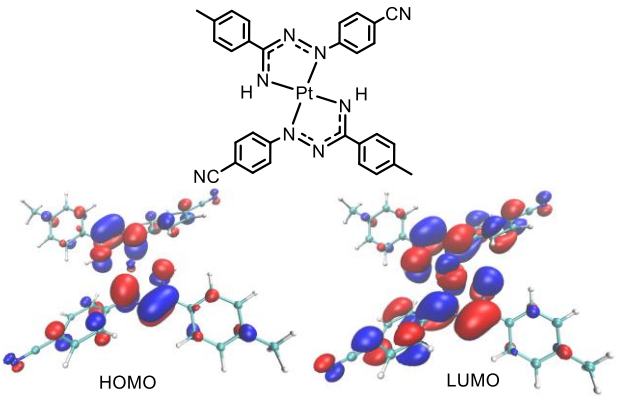

Figure 2.8 Computed HOMO and LUMO plots of complex **31c**

the HOMO, the aryl substituents all contribute nearly equally, consistent with the observation that the first oxidation potentials of **31c** and **31d**, where the electron-withdrawing group is rotated between the two positions, are nearly identical. In contrast, the LUMO has about double the contribution from the *N*-bound aryl groups as from the *C*-bound aryls. This computational observation is also consistent with the electrochemical data, where we observe that placing the electron-withdrawing cyano group at the *N*-aryl position (complex **31c**, E = –1.03 V) perturbs the first reduction potential to a greater extent than when the same substituent is in the other position (complex **31d**, E = –1.25 V). Time-dependent density functional theory was used to evaluate the low-energy UV-vis absorption transition, observed at 695 nm experimentally (CH_2Cl_2). The computed transition occurs at 740 nm with an

oscillator strength of 0.4543, and is exclusively a HOMO→LUMO transition. Given the differential contributions from the platinum atom to the frontier orbitals, this low-energy band is best characterized as primarily a ligand-centered (π→π*) transition with significant ligand-to-metal charge transfer (LMCT) character, in line with the measurable solvatochromism described above.

2.2.6 Spectroelectrochemistry

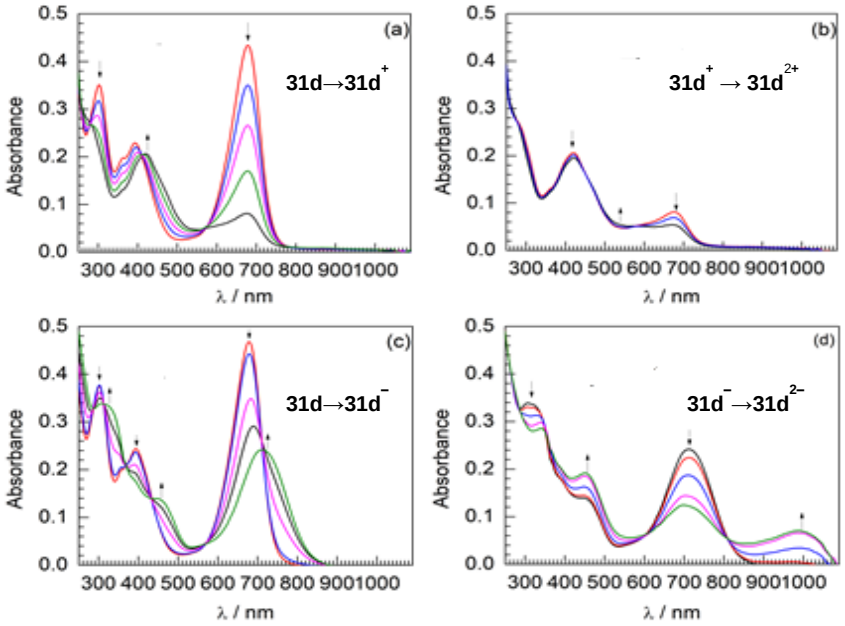

Figure 2.9 UV-vis-NIR spectroelectrochemistry of complex **31d** in CH_2Cl_2 with 0.1 M NBu_4PF_6 electrolyte, showing two successive oxidation (**a** & **b**) and reductions (**c** & **d**). The applied potential was 0.6 V vs. Fc^+/Fc (first oxidation), 1.0 V (second oxidation), –1.4 V (first reduction) and –2.0 V (second reduction).

To further investigate the nature of the oxidized and reduced species, UV-vis spectroelectrochemistry was conducted on complex **31d**. (Figure 2.9) Controlled potential electrolysis was used to generate both the one- and two-electron oxidized and reduced species and clear isobestic points are observed, suggesting the absence of spectral intermediates

during the reactions with only two species inside the solutions. The reduction by two electrons could induce much more significant changes to the absorption profile. The first reduction, which occurs with an applied potential of –1.4 V vs. Fc^{+}/Fc, results in a decrease in intensity with some red shift from 680 nm to 718 nm. In addition, another visible band grows in at 466 nm. This appearance of a split band of the low-energy $\pi \rightarrow \pi^*$ transition is consistent with a ligand-based radical anion being formed, reminiscent of UV-vis spectra of reduced formazanate complexes, either isolated[26] or generated via in situ electrochemical reduction.[76] Upon second reduction, as shown in Figure 2.9d, the band at 466 nm grows in intensity when shifting to 456 nm, and the band at 718 nm diminishes while a new band at 988 nm appears. These spectra are consistent with both reductions being localized on the azo-iminate π system.

2.3 Conclusion

In this work, we show a new route for the preparation of homoleptic platinum azo-iminate complexes. The templated synthesis involves proton-coupled electron transfer to a formazanate which is accompanied by N–N bond cleavage, highlighting the redox and chemical reactivity of formazanates and offering a convenient route to prepare previously unreported platinum complexes. X-ray crystal structure data, cyclic voltammetry, and UV-vis absorption spectroscopy are all consistent with an electronic structure where a formally Pt(II) center is bound by two radical anion azoiminate ligands; the radicals couple in the delocalized HOMO to give diamagnetic singlet diradical species. The electrochemistry and optical properties are dominated by the azo-iminate π system, though some mixing of Pt-centered orbitals perturbs these features from those of previously reported Pd analogues. In future work we aim to develop routes to prepare *heteroleptic* azoiminate complexes, where the ancillary

ligand can further influence the redox and optical properties of the compounds, and also explore applications of these compounds enabled by the accessible ligand-based redox chemistry and strong visible absorption.

2.4 Experimental Section

2.4.1 Materials.

Dry solvents were obtained from a Grubbs Solvent Purification System and degassed with argon. Starting materials and reagents, unless otherwise specified, were obtained from commercial sources and used without further purification. The precursors *cis*-$Pt(DMSO)_2Cl_2$[73] and the formazans **Fza**–**Fzd**[77] were prepared by literature procedures. Tetrabutylammonium hexafluorophosphate ($TBAPF_6$) was recrystallized from hot ethanol and ferrocene was sublimed at ambient pressure before use in electrochemical experiments.

2.4.2 Physical Methods.

^1H and $^{13}C\{^1H\}$ NMR spectra were recorded at room temperature using an ECA-600 NMR spectrometer and are shown in appendix. UV-vis absorption spectra were recorded in screw-capped 1 cm quartz cuvettes using an Agilent Carey 8454 UV-vis spectrophotometer. Cyclic voltammetry (CV) experiments were performed with a CH Instruments 602E potentiostat using a three-electrode system in a nitrogen-filled glove-box or with an EG&G Princeton Applied Research (PAR) 173 potentiostat coupled to an EG&GPAR Model 175 Universal Programmer. Current−voltage curves were recorded on an EG&G PAR R-0151 X−Y recorder. A 3 mm diameter glassy-carbon working electrode and Pt wire counter electrode were used for all cyclic voltammetry experiments; a silver wire pseudo-reference electrode or

a saturated calomel reference electrode (SCE) were used. Measurements were carried out in dichloromethane solution with 0.1 M $TBAPF_6$ as a supporting electrolyte at scan rate of 0.1 V/s. Ferrocene was used as an internal standard when employing a silver wire pseudo-reference, and all potentials were referenced to the ferrocene/ferrocenium couple. Thin-layer UV-vis spectroelectrochemical experiments were performed with a commercially available thin-layer cell purchased from Pine Instruments Inc. Potentials were applied and monitored with an EG&G PAR model 173 potentiostat. High-purity nitrogen from Trigas was used to deoxygenate the solution, and a stream of nitrogen was kept over the solution during each electrochemical and spectroelectrochemical experiment. Bulk purity for all complexes is established by elemental analysis, performed by Atlantic Microlab, Inc. (Norcross, GA). ^{1}H and $^{13}C\{^{1}H\}$ NMR spectra of all compounds are also shown in the Appendix and provide additional evidence for sample purity.

2.4.3 Computational Details.

Geometry optimizations and time-dependent density functional theory (TD-DFT) computations for **31c** were performed in the gas phase at the M06-2X level employing Gaussian09. The 6-211+(g,d) basis set was used for C, H, and N, whereas the Lanl2dz basis set with effective core potential (ECP) was used for Pt. The optimized geometry of **31c** matches well with its crystal structure. TD-DFT computations quantified the HOMO → LUMO transition oscillator strength and composition of the one-electron excitation transition and were carried out at the same level of theory.

2.4.4 X-ray Crystallography Procedures.

Single crystals were grown by vapor diffusion of pentane into concentrated CH_2Cl_2 solutions. Crystals were mounted on a Bruker Apex II three-circle diffractometer using MoKα radiation (λ = 0.71073 Å), conducted by Prof.Teets. The data was collected at 123(2) K and was processed and refined within the APEXII software. Structures were solved by direct methods in SHELXS and refined by standard difference Fourier techniques in the program SHELXL.[78] Carbon-bound hydrogen atoms were placed in calculated positions using the standard riding model and refined isotropically, whereas the N–H hydrogen atoms were located in the difference map, affixed to a distance of 0.88 Å, and also refined isotropically. All non-hydrogen atoms were refined anisotropically. The structure of complexes **31a**, **31b,** and **31d** all contained disordered solvent molecules. Distance restraints (SADI) were used for all 1,2 and 1,3 distances within the disordered parts, and rigid bond restraints SIMU and DELU were employed for the thermal displacement parameters.

2.4.5 Synthesis of complexes

Complex 31a. *cis*-$Pt(DMSO)_2Cl_2$ (30 mg, 0.071 mmol) and **Fza** (51mg, 0.142 mmol) were combined in ethanol (10 mL) with excess triethylamine (0.1 mL), and the mixture was deoxygenated under the protection of N_2. The mixture was refluxed for 36 h and the color changed from purple to dark green. The reaction completion was confirmed by TLC. The ethanol was removed using rotary evaporation and the product was re-dissolved in DCM and purified by column chromatography of Aluminum oxide with an eluent of the mixture of ethyl acetate and hexane (ratio 1:9). The final product was further purified by recrystallization from CH_2Cl_2/pentane. Yield: 31 mg (63%) ^{1}H NMR (600 MHz, $CDCl_3$) δ 7.81 (dd, *J* = 14.7, 8.4

Hz, 8H, ArH), 7.51 (s, 2H, NH), 7.34 (d, *J* = 8.1 Hz, 4H, ArH), 6.94 (d, *J* = 8.8 Hz, 4H, ArH), 3.85 (s, 6H, OCH_3), 2.47 (s, 6H, CH_3). $^{13}C\{^1H\}$ NMR (151 MHz, $CDCl_3$) δ 168.4, 161.0, 153.2, 137.5, 129.8, 128.3, 125.2, 124.1, 114.2, 55.5, 21.3. Anal. Calcd for $C_{30}H_{30}N_6O_2Pt$: C, 51.35, H, 4.31, N, 11.98. Found: C, 51.24, H, 4.38, N, 11.91.

Complex 31b. The title compound was prepared by the general method described above for complex **31a,** using *cis*-$Pt(DMSO)_2Cl_2$ (30 mg, 0.071 mmol) and **Fzb** (56 mg, 0.14 mmol). Yield: 38 mg (73%). ^1H NMR (500 MHz, $CDCl_3$) δ 7.87 (d, *J* = 8.6 Hz, 4H, ArH), 7.83 (d, *J* = 8.5 Hz, 4H, ArH), 7.45 (s, 2H, NH), 7.09 (d, *J* = 7.3 Hz, 4H, ArH), 6.95 (d, *J* = 8.6 Hz, 4H, ArH), 3.93 (s, 6H, OCH_3), 3.85 (s, 6H, OCH_3). $^{13}C\{^1H\}$NMR (151 MHz, $CDCl_3$) δ 168.3, 161.0, 159.4, 149.4, 128.3, 126.3, 124.2, 114.4, 114.2, 55.8, 55.5. Anal. Calcd for $C_{30}H_{30}N_6O_4Pt$: C, 49.11, H, 4.12, N, 11.45. Found: C, 48.84, H, 4.09, N, 11.19.

Complex 31c. The title compound was prepared by the general method described above for complex **31a,** using *cis*-$Pt(DMSO)_2Cl_2$ (30 mg, 0.071 mmol) and **Fzc** (52 mg, 0.14 mmol). Yield: 33 mg (66%). ^1H NMR (600 MHz, DMF-d_7) δ 9.67 (s, 2H, NH), 8.19 (s, 4H, ArH), 8.14 (s, 4H, ArH), 8.10 (s, 4H, ArH), 7.37 (s, 4H, ArH), 2.41 (s, 6H, CH_3). $^{13}C\{^1H\}$ NMR (151 MHz, DMF-d_7) δ 169.8, 157.9, 140.3, 133.4, 129.4, 128.4, 127.9, 127.0, 119.3, 109.5, 20.7. Anal. Calcd for $C_{30}H_{24}N_8Pt$: C, 52.10, H, 3.50, N, 16.20. Found: C, 52.21, H, 3.48, N, 16.35.

Complex 31d. The title compound was prepared by the general method described above for complex **31a,** using *cis*-$Pt(DMSO)_2Cl_2$ (30 mg, 0.071 mmol) and **Fzd** (48 mg, 0.14 mmol). Yield: 30 mg (60%). ^1H NMR (500 MHz, $CDCl_3$) δ 8.01 (s, 4H, ArH), 7.81 (s, 4H, ArH), 7.74 (t, *J* = 8.6 Hz, 4H, ArH), 7.69 (s, 2H, NH), 7.41 (d, *J* = 8.1 Hz, 4H, ArH), 2.50 (s,

6H,CH_3). $^{13}C\{^1H\}$ NMR (151 MHz, $CDCl_3$) δ 152.8, 138.7, 135.1, 133.9, 132.5, 129.8, 127.3, 125.2, 118.6, 113.0, 21.4. Anal. Calcd for $C_{30}H_{24}N_8Pt$: C, 52.10, H, 3.50, N, 16.20. Found: C, 52.03, H, 3.59, N, 16.08.

3 Chapter Three Formazanate Complexes of Bis-Cyclometalated Iridium

3.1 Introduction

The coordination chemistry of formazans, which are a class of chromophoric conjugated organic molecules with a 1,2,4,5-tetraazapentadienyl core, has been long been investigated with transition metals and main group metals. The nitrogen-rich redox active formazans have also been intensively studied in the fields of bioinorganic chemistry[3,4] and catalysis[5,6,79], and a few successful applications have emerged over time in biomedical assays, textile dyes, and colorimetric indicators of cell activity.[10,80–82] The monoanionic form of formazans, formazanates, have become a well-known *N*-chelating ligand class in recent years, structurally analogous to the ubiquitous β-diketiminate ligand class but with redox activity at much more accessible potentials and strong visible absorption, primarily because of LUMOs that are significantly stabilized relative to β-diketiminates.[83–86] The growing interest in formazanate coordination complexes is largely due to the ligand-based redox processes, which can facilitate multielectron redox behavior,[7] bond activation,[8] and excited-state charge separation. In particular, the stabilzed LUMOs in formazanates result in relatively stable reduced products, greatly expanding the redox chemistry of these complexes in small-molecule activation and other contexts.[26,51,87]

Complexes of first-row transition metals with formazanates have been extensively reported,[45,79] including copper complexes which mediate oxygen activation.[48,49] Ligand-based redox chemistry of low-coordinated iron complexes,[46,88,89] and bis-chelated zinc complexes have affirmed the versatility of redox active formazanate ligands.[90,91] Unique magnetic properties were demonstrated in heteroleptic cobalt and bis(formazanate) iron complexes.[25,92] Formazanate complexes of group 14 elements and ruthenium highlight the redox non-innocence of some classes of formazanate complexes.[51,93] Furthermore, boron chelates of formazanates not only exhibit tunable redox properties but are also in many cases photoluminescent,[29,30,32,33,36] finding applications as cell-imaging agents,[36,41] electrochemiluminescence emitters,[94] multifunctional polymers,[42] and precursors to a wide range of BN heterocycles.[90,95]

Despite these numerous examples, coordination complexes of formazans with third-row transition metals remain rare. Dithizonate complexes with a formazan-like core were described where coordination of sulfur to the metal was observed.[96] Complexes of dianionic aryl formazanate ligands which involve o-phenoxy or o-benzoate donors were found to be coordinated in a tridentate fashion with a few heavy transition metals but none of them were extensively characterized or analyzed for further studies.[97–100] Since the strong orbital overlap between radially extended 5d orbitals and the formazanate π system could perturb the inherent redox and optical properties of the formazanates and the 5d metal center could promote formazanate-centered triplet photophysics, our group began investigating and focusing on third-row transition metal complexes of formazanates.

Herein, we describe a diverse set of cyclometalated iridium(III) formazanate complexes. Cyclometalated iridium(III) compounds have been extensively studied in a number of contexts,[101–106] primarily due to their good thermal and photostability, relatively short phosphorescence lifetime, and high photoluminescence quantum yields. Although the synthetic chemistry of cyclometalated iridium(III) formazanates largely parallels that of our previous cyclometalated platinum(II) formanazanate series,[54,55] moving from platinum(II) to iridium(III) give us a chance to assess the different effects of coordination geometry and d-electrons on the structural chemistry, photophysical and redox properties of 5d metal formazanates. We here describe 18 new cyclometalated iridium(III) formazanate complexes of the type $Ir(C\hat{}N)_2$(formazanate) (C^N = cyclometalating ligands) featuring four different cyclometalating ligands and six structurally and electronically varied triaryl- and diarylformaznates. A general synthetic route is presented here and 8 of 18 compounds are structurally characterized by single crystal X-ray diffraction, denoting two coordination modes for the formazanate. The substitution patterns on the formazanate strongly influence the observed ligand-centered redox potentials, with subtle influences from the variety of C^N ligands, suggesting the mixing between iridium d-orbitals and formazanante π orbitals. This work demonstrates that alteration of both the C^N and formazanate ligands offers two layers of control over the redox and optical properties of neutral iridium formazanate complexes.

3.2 Results and Discussion

3.2.1 Synthesis

Scheme 3.1 depicts the general synthetic procedure of the series of 18 heteroleptic cyclometalated iridium formazanate complexes of the type $Ir(C^N)_2$(formazanate). Compounds are numbered based on the identity of the C^N ligand, with the associated letter designating the structure of the formazanate ancillary ligand. Two cyclometalating ligands, 2-phenylpyridine (ppy) and 2-(2,4-difluorophenyl)pyridine (F_2ppy), are paired with all six

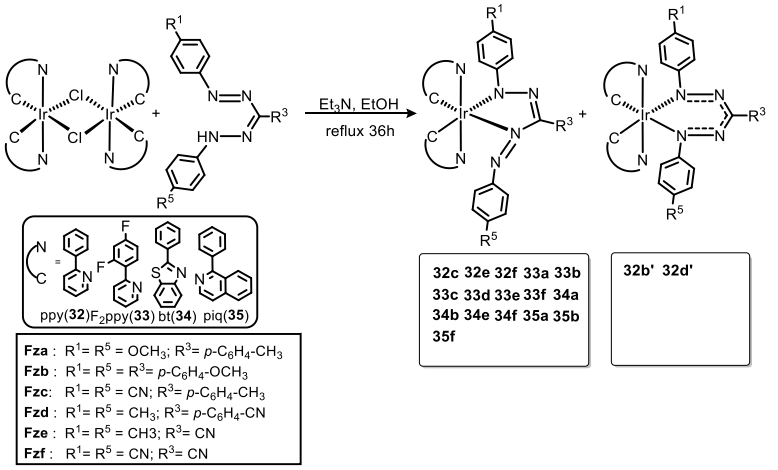

Scheme 3.1 Synthetic route of formazanate Iridium complexes with the major product listed in right boxes.

formazanates studied here (**Fza**–**Fzf**), to produce products **32a–32f** and **33a–33f**, while the other two C^N ligands, 2-phenylbenzothiazole (bt) and 1-phenylisoquinoline(piq), are used to prepare a smaller subset of complexes (**34a**, **34b**, **34e**, **34f**, **35a**, and **35f**). The chloro-bridged dimers $[Ir(C^N)_2(\mu\text{-}Cl)]_2$ are treated with a stoichiometric amount of free formazan in ethanol in the presence of excess triethylamine, by refluxing for 20–36 hours. The reaction always works and tolerates a variety of electronically modified formazans with different

combinations of electron-donating (-CH_3, -OCH_3) and electron-withdrawing (-CN) substituents at either R^1/R^5 or at the central position R^3. Reactions involving triarylformazanates (**Fza–Fzd)** revealed an apparent color change from purple (free formazan) to dark green or blue upon coordination of the formazanate to iridium. In contrast, in reactions involving diaryformazanates (**Fze** & **Fzf**) the color of the product stays the same with the free formazan. The isolated yields vary from 43–80% across the series.

NMR analysis of crude reaction mixtures indicates the possibility of two isomeric products. In particular, some of the complexes with electron-donating substituents on the formazanate, **32a**, **32b**, **34a**, **34b** and **35a**, as well as **32d** (R^3 = *p*-C_6H_4-CN), initially showed the presence of two products in their ^{1}H NMR spectra, one with apparent C_2 symmetry and one with C_1 symmetry. As unequivocally determined by X-ray crystallography (see below), these features are attributed to two different binding modes of the formazanate, one that involves a five-member chelate ring "open" form, binding through the 1- and 4-positions of the formazanate core, and the other the more typical six-member chelate "closed" form, binding through the 1- and 5-positions and denoted by a prime symbol (′). Varying the reaction solvent (dichloromethane, tetrahydrofuran) and temperature did not significantly impact the isomeric ratio, neither did prolonged heating. Chromatographic purification was not effective since both isomers are similar in polarity while recrystallization of the above-mentioned products was generally a good approach with successfully isolation of **34a**, **34b**, and **35a** as the C_1-symmetric "open" form with little amount of the "closed" isomer present. Conversely, for the C^N = ppy series recrystallization resulted in the isolation of **32b′** and **32d′** exclusively as the C_2-symmetric "closed" isomer, whereas **32a** was isolated as a mixture of isomers even after

repeated recrystallization attempts. The remaining triarylformazanate iridium complexes were all isolated in the five-member chelate conformation, as were all diarylformazanate complexes involving **Fze** and **Fzf**. To summarize, 15 of the 18 complexes were purified as the five-member chelate "open" form, whereas only **32b′** and **32d′** were obtained in the "closed" form and **32a** was isolated as a mixture of both isomers. All of the compounds are air and moisture stable and fully characterized by ^{1}H, ^{13}C{^{1}H} and ^{19}F (for **33a–33f**) NMR spectroscopy and elemental analysis, which establish identity and bulk purity. NMR spectroscopy is especially useful for distinguishing the two isomers, with the C_2-symmetric "closed" isomer displaying chemical equivalency of the C^N ligands and the two R^1/R^5 substituents on the formazanate. Related NMR data are shown in Figure S9–S50 in appendix.

3.2.2 X-ray Crystallography

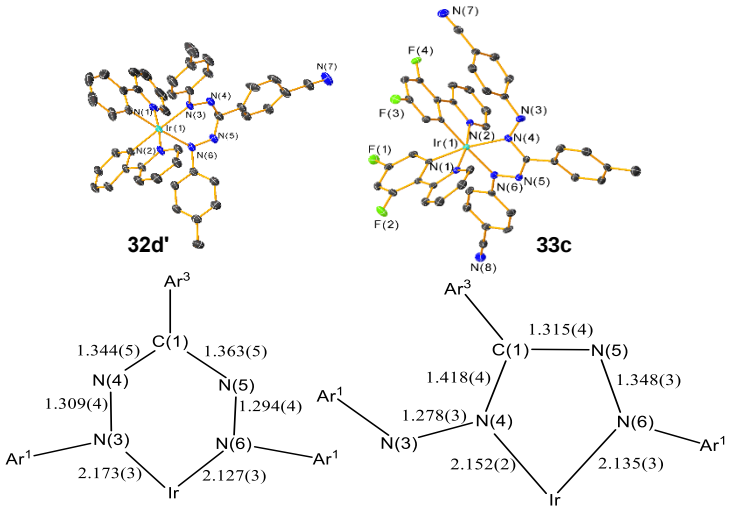

Figure 3.1 X-ray crystal structure of complexes **32d′** ("closed") and **33c** ("open"), with ellipsoids shown at the 50% probability level and hydrogen atoms omitted. The bottom stick diagrams show bond lengths of **32d′** and **33c** in Å, with esd values in parentheses.

Table 3.1 Summary of crystallographic bond distances (Å) and angles (deg) of selected complexes

	32c	**32d′**	**33a**[a]	**33c**	**33d**[b]	**33d′**[b]	**33e**
d (Ir–N3/4)[c]	2.208(8)	2.173(3)	2.161(4)	2.152(2)	2.210(5)	2.142(9)	2.155(6)
d (Ir–N6)	2.119(8)	2.127(3)	2.125(4)	2.135(3)	2.110(3)	2.110(3)	2.103(7)
d (N3–N4)	1.318(11)	1.309(4)	1.313(5)	1.278(3)	1.285(7)	1.325(12)	1.263(11)
d (N4–C1)	1.376(12)	1.344(5)	1.383(5)	1.418(4)	1.400(6)	1.418(10)	1.397(11)
d (N5–C1)	1.333(12)	1.363(5)	1.328(6)	1.315(4)	1.349(5)	1.349(5)	1.314(12)
d (N5–N6)	1.314(11)	1.294(4)	1.313(5)	1.348(3)	1.297(4)	1.297(4)	1.304(8)
∠N(3/4)–Ir–N(6)[d]	74.1(3)	82.45(11)	74.53(14)	74.45(9)	70.50(15)	94.5(3)	75.6(3)

[a] Average of two crystallographically independent molecules. [b] Both isomers disordered in the same crystal structure. [c] Formazanate Ir–N distance. Relevant distance is Ir–N3 for "closed" isomers **32d′** and **33d′**, and Ir–N4 for the rest. [d] Formazanate N–Ir–N chelate angle. Relevant angle is ∠N(3)–Ir–N(6) for "closed" isomers **32d′** and **33d′**, and ∠N(4)–Ir–N(6) for the rest.

The structures of **32c, 32d′, 33a, 33b, 33c, 33d′, 33e, 34a,** and **35a** were confirmed by single-crystal X-ray diffraction, with representative **32d′** and **33c** shown in Figure 3.1. Formazanate bond lengths and angles are summarized in Table 3.1 with refinement details collected in Tables 3.2 and 3.3. The iridium metal center resides in the center of distorted octahedral coordination geometry with two C^N ligands and one formazanate. In all cases, the nitrogen atoms of C^N ligands are in a trans position relative to each other. The Ir–C bond distances (2.014(4)–2.033(4) Å) and Ir–N bond distances involving the C^N ligands (2.036(4)–2.091(8) Å) of all complexes are similar to those of the previously reported cyclometalated Ir complexes.[101,103] Complex **32d′** crystallized with the formazanate exclusively in the six-membered chelate "closed" form, whereas in **33d** both isomers were present, modeled as a two-part disorder with 71% of the "open" form (**33d**) and 29% of the "closed" form (**33d′**). As shown in Table 3.1 and Figure 3.1, the binding mode of the formazanate ("open" vs. "closed") has little influence on the Ir–N (formazanate) bond distances, which range between 2.103(7) and 2.210(5) Å and are significantly longer than those in other formazanate chelate complexes (1.809–2.090 Å).[51,54,55,90,91,107,108] The different

Table 3.2 Summary of crystallographic data of **32d′**, **32c and 33a.**

	32d′·0.5CH_2Cl_2	**32c**·CH_2Cl_2	**33a**
CCDC	191336	191337	191338
Crystal data			
Chemical formula	$C_{44.50}H_{35}ClIrN_7$	$C_{45}H_{33}Cl_2IrN_8$	$C_{44}H_{33}F_4IrN_6O$
M_r	895.44	948.89	929.96
Crystal system, space group	Monoclinic, $P2_1/c$	Triclinic, $P\bar{1}$	Monoclinic, $P2_1/c$
a, b, c (Å)	8.3278 (11), 13.6396 (18), 32.927 (4)	7.800 (4), 13.666 (7), 19.338 (10)	13.819 (2), 17.291 (3), 31.180 (5)
α, β, γ (°)	90, 94.820 (2), 90	94.197 (6), 100.672 (6), 100.065 (6)	90, 99.037 (2), 90
V (Å^3)	3726.9 (9)	1982.6 (18)	7358 (2)
Z	4	2	8
μ (mm^{-1})	3.70	3.55	3.70
Crystal size (mm)	0.25 × 0.12 × 0.05	0.25 × 0.10 × 0.08	0.39 × 0.14 × 0.12
Data collection			
T_{min}, T_{max}	0.553, 0.746	0.602, 0.745	0.510, 0.746
No. of measured, independent and observed [$I > 2\sigma(I)$] reflections	21621, 8442, 7359	22406, 7691, 7169	42064, 16616, 15080
R_{int}	0.020	0.036	0.019
$(\sin\theta/\lambda)_{max}$ (Å^{-1})	0.649	0.617	0.649
Refinement			
$R[F^2 > 2\sigma(F^2)]$, $wR(F^2)$, S	0.029, 0.073, 1.06	0.062, 0.162, 1.08	0.031, 0.112, 1.20
No. of reflections	8442	7691	16616
No. of parameters	517	506	1015
No. of restraints	642	511	0
	$w = 1/[\sigma^2(F_o^2) + (0.0277P)^2 + 10.5019P]$ where $P = (F_o^2 + 2F_c^2)/3$	$w = 1/[\sigma^2(F_o^2) + (0.0734P)^2 + 44.1129P]$ where $P = (F_o^2 + 2F_c^2)/3$	$w = 1/[\sigma^2(F_o^2) + (0.0591P)^2 + 21.696P]$ where $P = (F_o^2 + 2F_c^2)/3$
$\Delta\rho_{max}$, $\Delta\rho_{min}$ (e Å^{-3})	1.34, -1.78	7.89, -3.90	3.07, -1.83

Table 3.3 Summary of crystallographic data of **33d**, **33c and 33e.**

	33d	**33c**	**33e**
CCDC	191339	191340	191341
Crystal data			
Chemical formula	$C_{44}H_{30}F_4IrN_7$	$C_{44}H_{27}F_4IrN_8$	$C_{38}H_{26}F_4IrN_7$
M_r	924.95	935.93	848.86
Crystal system, space group	Triclinic, $P\bar{1}$	Monoclinic, $P2_1/c$	Monoclinic, $C2/c$
a, b, c (Å)	11.8119 (12), 11.9432 (12), 14.7901 (15)	17.897 (5), 8.693 (3), 23.444 (7)	26.377 (4), 24.953 (4), 12.001 (2)
α, β, γ (°)	108.9555 (12), 91.9403 (13), 109.1664 (13)	90, 91.553 (4), 90	90, 114.140 (2), 90
V (Å^3)	1840.7 (3)	3646.1 (18)	7208 (2)
Z	2	4	8
μ (mm^{-1})	3.69	3.73	3.76
Crystal size (mm)	0.40 × 0.26 × 0.16	0.21 × 0.10 × 0.05	0.47 × 0.09 × 0.07
Data collection			
T_{min}, T_{max}	0.602, 0.746	0.562, 0.746	0.491, 0.746
No. of measured, independent and observed [$I > 2\sigma(I)$] reflections	10228, 7383, 7003	22114, 8437, 7123	22704, 8354, 6955
R_{int}	0.014	0.039	0.027
$(\sin\theta/\lambda)_{max}$ (Å^{-1})	0.625	0.652	0.653
Refinement			
$R[F^2 > 2\sigma(F^2)]$, $wR(F^2)$, S	0.026, 0.063, 1.05	0.028, 0.058, 1.01	0.053, 0.139, 1.08
No. of reflections	7383	8437	8354
No. of parameters	526	515	452
No. of restraints	100	0	465
	$w = 1/[\sigma^2(F_o^2) + (0.029P)^2 + 3.7672P]$ where $P = (F_o^2 + 2F_c^2)/3$	$w = 1/[\sigma^2(F_o^2) + (0.0189P)^2]$ where $P = (F_o^2 + 2F_c^2)/3$	$w = 1/[\sigma^2(F_o^2) + (0.0546P)^2 + 83.6126P]$ where $P = (F_o^2 + 2F_c^2)/3$
$\Delta\rho_{max}$, $\Delta\rho_{min}$ (e Å^{-3})	2.07, -0.93	0.95, -0.52	4.42, -3.37

chelating modes of formazanates, however, impact the bond distances within the formazanate core critically. For both cases of **32d′** and **33d′**, which include the "closed" form of the formazanate, full π delocalization within the formazanate is indicated. The two N–N and two N–C distances are nearly equal and intermediate between single and double bonds. In contrast, for "open form" formazanate chelating complexes, in many cases there are alternating short and long bond distances in the formazanate core, which is particularly apparent in the structures of **33c**, **33e, 34a**, and **35a**. In these cases, the N(3)–N(4) distances exterior to the five-member chelate ring shorter than the N(5)–N(6) distances in the chelate ring, and the N(4)–C(1) distance is significantly longer than N(5)–C(1). This pattern of bond distances is consistent with less π delocalization in the "open" form, which in the localized limit consists of alternating single and double bonds, as shown in the structure diagram in Scheme 3.1. Unsurprisingly, the other major structural difference between the "open" and "closed" forms is the chelate angles of formazanates, which for the "open" forms range between 74.10(3) and 74.45(9)° (∠N(4)–Ir–N(6)), except **33d** which has an abnormally small chelate angle (70.50(15)°). The formazanate bite angles are larger for the C_2-symmetric isomers, observed to be 82.45(11)° in **32d′** and 94.5(3)° in **33d′**. There does not appear to be any systematic dependence of the key structural metrics on the presence of electron-withdrawing or electron-donating groups on the formazanate periphery.

The observation of both structure types ("open" and "closed") suggests that the two structures are similar in energy, though overall the "open" isomer seems to be favored. This observation stands in contrast to many previously described platinum(II) formazanates, where only the "closed" binding mode was observed.[54,55] The covalent radii of platinum and iridium

are quite similar,[109] so we don't think the preference for a five-member chelate is because iridium(III) is smaller than platinum(II), nor are there any obvious electronic differences between the two isomers (see description of UV-vis and electrochemistry below). We propose that the "open" binding mode relieves steric pressure in these complexes, avoiding close approaches of the formazanate *N*-aryl substituent with the aryl rings of the cyclometalating ligand. In previously characterized bis-cyclometalated iridium β-diketiminate complexes from our group we noted a close stacking arrangement of the *N*-aryl groups and the cyclometalated aryl groups,[110,111] which is avoided in **32d′** ("closed" isomer) by a buckling of the formazanate backbond. In contrast, in all of the "open" form structures presented here, except in **33d** where the two isomers are disordered, the aryl substituent at the iridium-bound N(6) is safely away from the steric congestion of the cyclometalating ligands, oriented orthogonal to the nearest cyclometalated aryl ring in a cleft between the two C^N ligands. Thus, the crystallographic evidence suggests that it is steric effects that are likely responsible for the "open" chelate conformation most of these complexes adopt.

3.2.3 UV-vis absorption spectroscopy

UV–vis absorption spectra of all cyclometalated iridium formazanate complexes were recorded and Table 3.4 represents the summarized absorption data in tetrahydrofuran (THF) with spectra of the selected complexes **33a**–**33f**, **32b**–**32f** shown in Figure 3.2. None of the complexes are photoluminescent in the visible region at room temperature or 77 K. All of the complexes described here are highly colored, appearing green or bluish green for the triarylformazanate complexes and greenish brown to dark red for the diarylformazanates

complexes. These iridium formazanate compounds display low-energy absorption bands between 525–677 nm with extinction coefficients between 2200–13000 $M^{-1}cm^{-1}$ in the

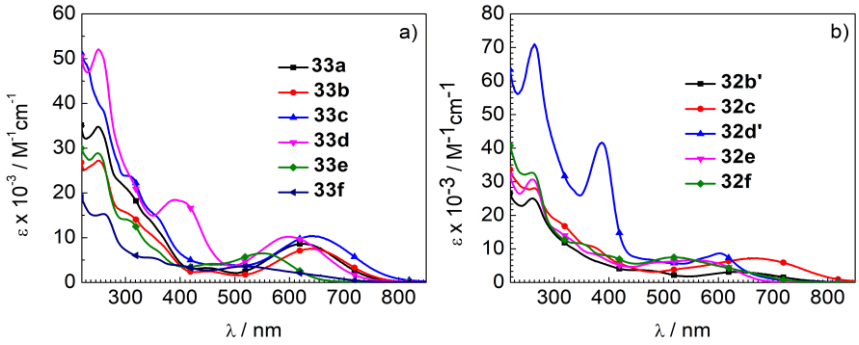

Figure 3.2 Overlaid UV-vis absoption spectra of selected formazanate iridium complexes, recorded in THF solution at room temperature. Data was collected in intervals of 1 nm, and symbols are included on each plot are to help distinguish the overlaid spectra.

visible range of the spectrum, which is assigned as a formazanate ligand-centered $\pi \rightarrow \pi^*$ transition primarily involving HOMO and LUMO orbitals. As shown in Table 3.4 these low-energy absorption maxima are nearly identical for all of the triarylformazanate complexes **32a**/**32b**, **33a**/**33b**, **34a**/**34b** and **35a**, ranging from 628–639 nm for these complexes which have electron-donating substituents at both the R^1/R^5 and R^3 position of the formazanate scaffold. Complex **32a** is isolated as a mixture of "open" and "closed" isomers but no significant spectral differences are observed by comparing this with the other **Fza** complexes that exist exclusively in the "open" configuration. The position of the low-energy absorption band depends strongly on the identity of the substituents at the central R^3 position of the formazanate backbone. Placing the electron-withdrawing 4-cyanophenyl group in the R^3 position (**Fzd**) causes a hypsochromic shift of ~27–38 nm (715–989 cm^{-1}) in the low-energy absorption maximum for complexes **32d'** and **33d** relative to the respective **Fza** and **Fzb**

complexes. In contrast, this low-energy absorption band is red-shifted for complexes **32c** (677 nm) and **33c** (655 nm), when the 4-cyanophenyl groups work as N-aryl substituents.

Table 3.4 Summary of UV-via absorption of formazanate iridium complexes, recorded in THF at room temperature.

	λ / nm (ε × 10^{-3} / $M^{-1}cm^{-1}$)
32a/32a'	265 (53), 480 (6.7), 633 (13)
32b'	261 (25), 463 (3.6), 630 (3.2)
32c	270 (17), 370[a] (6.8), 677 (4.6)
32d'	264 (71), 387 (42), 602 (8.7)
32e	260 (30), 380[a] (8.0), 476 (5.8), 554 (6.6)
32f	258 (33), 342 (10), 401[a] (7.9), 520 (7.5)
33a	250 (34), 347[a] (13), 445 (3.2), 628 (8.6)
33b	252 (27), 454 (2.9), 639 (7.5)
33c	260a (38), 313[a] (23), 360[a] (17), 655 (10)
33d	251 (52), 390 (18), 601 (10)
33e	250 (28), 300 (14), 454[a] (4.2), 551 (6.5)
33f	261 (15), 353[a] (5.4), 532 (3.5)
34a	320 (43), 410[a] (11), 630 (12)
34b	262 (36), 319 (39), 635 (10)
34e	263 (34), 319 (36), 382[a] (18), 443[a] (14), 578 (2.2)
34f	266 (38), 321 (36), 384[a] (13), 443 (12), 596 (6.7)
35a	293 (51), 349[a] (29), 435[a] (9.0), 638 (9.4)
35f	285 (44), 343 (26), 403 (14), 443 (13), 525[a] (10)

[a] shouder peak

As shown in Table 3.4, replacing the aryl group at the R^3 position with a cyano group in diarylformazanate (**Fze** and **Fzf**) complexes results in a significant blue-shift, with the low-energy absorption maximum occurring between 520 nm (**32f**) and 578 nm (**34e**) in this subset

of complexes. This significant blue-shift in the formazanate π→π* transition is likely a result of the decreased conjugation in the diarylformazanate analogues.

Additionally, higher-energy absorption bands are observed in the near-UV and visible regions which are dependent on the identity of the cyclometalated ligands, characteristic of Ir(d)→π* metal-to-ligand charge transfer (MLCT) bands along with a slight dependence on the *N*-aryl substituents of the formazanate ligands. These bands typically overlap with other high-energy absorption features, likely localized π→π* transitions, though in general F_2ppy-ligated complexes **33a**–**33f** display MLCT bands at the shortest wavelengths, with piq complexes having MLCT bands at the longest wavelength, consistent with many other cyclometalated iridium complexes.[112] Complexes of formazanate with 4-cyanophenyl on R^3 position display a distinct absorption at ~400 nm, which is not observed in other members of the series and is likely attributed to a transition localized on the 4-cyanophenyl substituent. In many complexes, particularly in the bt (**34**) and piq series (**35**), the high-energy absorption features overlap with low-energy formazanate-centered bands, giving rise to panchromatic visible absorption, as observed for previously reported piq-ligated platinum formazanate compounds.[55]

UV-vis spectra were also recorded in three solvents of varying polarity (toluene, THF, and MeOH) and only slight solvatochromic shifts of <10 nm were observed for the low-energy absorption bands in all cyclometalated iridium formazanate complexes, further supporting the assignment of this band as a ligand-localized π→π* transition with minimal charge-transfer character. Taken together, these results show the UV-vis absorption features of the iridium formazanate complexes depend on the location and identity of the substituents on the

formazan scaffold as well as the cyclometalating ligand. Changing substituents at the R^1/R^5 and R^3 position of the formazanate ligand allows predictive control over the formazanate-based low energy π→π* transition, which spans a relatively broad range of 520–677 nm in this series of complexes.

3.2.4 Electrochemistry

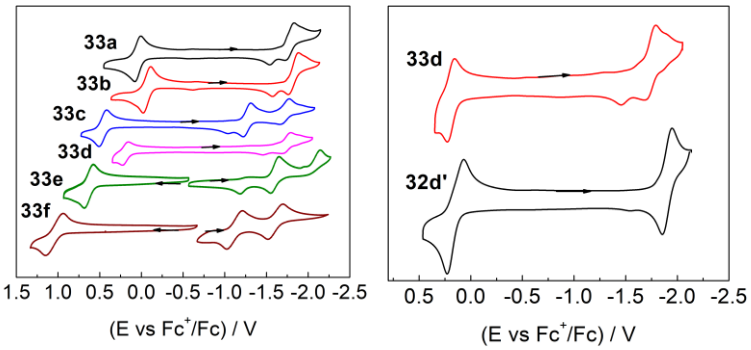

Figure 3.3 Overlaid cyclic voltammograms of selected formazanate iridium complexes **33a**–**33f** (left) and comparison between **32d'** and **33d** (right). CVs were recorded in CH_2Cl_2 with 0.1 M NBu_4PF_6 supporting electrolyte, using a glassy carbon working electrode and a scan rate of 0.1 V/s. The arrows indicate the scan direction.

The electrochemical properties of complexes **32**–**35** were investigated by cyclic voltammetry (CV) experiments, and the results are summarized in Table 3.5 with the voltammograms of selected complexes shown in Figure 3.3. The compounds display both oxidation and reduction features in their cyclic voltammograms. Ligand-centered reductions which occur at mild potentials are generally one of the most important features of coordinated

formazanate complexes, and these features are discussed here along with the Ir^{IV}/Ir^{III} oxidation waves.

The first reduction wave for all complexes is assigned as a formazanate-centered one electron reduction which occurs in the range of −1.22 to −1.98V. The F_2ppy series (**33a**–**33f**) provides the best insight into the effect of the formazanate structure on the redox properties,

Table 3.5 Summary of electrochemical data for all complexes.

	E^{ox} (V)	E^{red} (V)
32a/32a′	−0.02	−1.96[a]
32b′	−0.10	−1.97[a]
32c	+0.37	−1.41
32d′	+0.23	−1.95
32e	+0.55	−1.61, −2.10[a]
32f	+0.86	−1.26, −1.70
33a	+0.08	−1.83[a]
33b	−0.02	−1.89[a]
33c	+0.51	−1.31, −1.78
33d	+0.23	−1.79[a]
33e	+0.70	−1.50, −1.94[a]
33f	+1.15	−1.22, −1.71
34a	+0.01	−1.98[a]
34b	−0.06	−1.95[a]
34e	+0.68[a]	−1.72
34f	+0.97	−1.29, −1.74
35a	+0.01	−1.96[a]
35f	+0.83[a]	−1.27, −1.68

[a] Irreversibe peaks. $E_{p.c}$ or $E_{p.a}$ is reported

since this series includes all six formanazanate ligands studied here and all of them bidentate exclusively in the five-member "open" form in these analogues. As the data in Figure 3.3 and Table 3.5 shows, the redox potentials in **33a**–**33d** follow the trend expected from the electron donating/withdrawing attributes of the substituents, although the effects are modest. Moving from **33a** to **33b**, where CH_3 is replaced by a more electron-donating OCH_3 on the N-aryl

substituents, results in a cathodic (negative) shift of the reduction potential by 60 mV. Similarly, comparing **33a** to **33d**, where the *p*-C_6H_4-OCH_3 R^3 substituent is replaced with the more electron-withdrawing *p*-cyanophenyl, we notice a 40 mV anodic (positive) shift in the reduction potential. A much more dramatic change in potential occurs when electron-withdrawing cyano substituents are added to the R^1/R^5 position, with the potential in **33c** more positive than that of **33a** by over 500 mV. Similarly, large effects are observed in **33e** and **33f**, where the R^3 aryl substituent is replaced with a cyano group only, resulting in comparatively mild formazanate-based reduction potentials, particularly in **33f** (E_{red} = −1.22 V). Similar substituent effects are observed in the other members of the series with different cyclometalating ligands.

Effects of the cyclometalating ligand on the reduction potentials are modest, and in general the observed reduction potential is mainly determined by the substituent pattern on the formazanate. Fluorination of the phenylpyridine ligand does an overall anodic shift (~100 mV on average) for complexes **33a**–**33f** if we compare them with the set **32a**–**32f**, but complexes with C^N = bt or piq have very similar potentials to their ppy analogues, at parity of formazanate structure. In addition, the potentials for the complexes that were isolated as the "closed" isomer (**32b′** and **32d′**) or as a mixture of isomers (**32a**) are all very similar to the other members of the series with the same formazanate structure, suggesting that the formazanate-centered LUMO energy and corresponding redox potential depend little on the chelating modes of the formazanate.

All of the complexes here (except **34e** and **35f**) also display a formal Ir^{IV}/Ir^{III} redox couple which has slight dependence on the identity of the C^N ligand but highly sensitive to the

identity of the formazanate ligands. Electron rich complexes **32a**/**32b'**, **33a**/**33b**, **34a**/**34b** and **35a** oxidize at similar potentials across the series, and again the isomeric form of the complex does not appear to have a large effect on the observed potential (Table 3.5). The oxidation potential of these seven complexes are very near the Fc^+/Fc potential and again have a slight dependence on the formazanate substituents, with the most electron-rich **Fzb** complexes being easiest to oxidize. Addition of cyano substituents in the remaining complexes renders the complexes more difficult to oxidize, with shifts in potential that are qualitatively similar to those discussed above for the reduction potentials. The four **Fzf** complexes, where $R^1 = R^5 = R^3 = CN$, have the most positive oxidiation potentials (≥ 0.83 V), and the complexes where only one of the R^1/R^5 and R^3 positions includes a cyano group (**Fzc**–**e**) have Ir^{IV}/Ir^{III} potentials intermediate between the most electron-rich and electron-poor members of the series. As with the reduction potentials, the C^N ligands exert a modest effect on the formally Ir^{IV}/Ir^{III} couple, with F_2ppy complexes being the most difficult to oxidize for a given formazanate ligand. We note that although this oxidation potential can be formally classified as Ir^{IV}/Ir^{III}, and in typical cyclometalated iridium complexes the HOMO does include significant Ir dπ character,[113] the strong dependence of this potential on the formazanate structure implies that the HOMO in the complexes described here is also primarily formazanate ligand-centered, like the LUMO. Consistent with this supposition, previously reported platinum formazanate complexes from our group,[54] as well as cyclometalated iridium complexes with structurally analogous β-diketiminate ancillary ligands,[111] both have HOMOs that are almost exclusively formazanate or β-diketiminate-centered, with minority contribution from the metal.

One other noteworthy insight to come out of this work is the effect of the metal center and coordination geometry on the formazanate-centered optical transitions and redox properties. Our group has also prepared an extensive series of cyclometalated platinum formazanate complexes,[55,76] using many of the same cyclometalating ligands and formazanates used in this work (except for **Fzc**, and piq, which we did not use to prepare any platinum complexes). In the UV-vis absorption spectra, in every case the low-energy formazanate $\pi \rightarrow \pi^*$ transition is significantly blue-shifted in the iridium complexes, by at least 23 nm (767 cm^{-1}) and as much as 122 nm (3650 cm^{-1}) when comparing **32f** to its platinum congener. In the cyclic voltammograms, the formazanate-centered reduction potentials are substantially different as well, cathodically (negatively) shifted by at least 290 mV and as many as 500 mV in the iridium complexes. We do note that some of the reduction waves in the iridium complexes are irrerversible, which makes these comparisons less quantatively meaningful, but even in cases where both the platinum and iridium analogues have well-behaved, reversible reductions the iridium complex is more difficult to reduce by a substantial margin. Although the electrochemical oxidation of the platinum complexes tends to not be as well-behaved and we have not investigated it thoroughly, we can compare some complexes and we find that the iridium complexes are in general easier to oxidize, although the oxidation potentials are not as sensitive to the identity of the metal as the reduction potentials, in all cases differing by <200 mV. These observations indicate that, compared to cyclometalated platinum formazanate complexes, the iridium analogues have destabilized HOMO and LUMO energies and larger HOMO–LUMO gaps. The significant differences between the formazanate-centered properties in platinum and iridium complexes underscores the importance of d-orbital overlap

with the formazanate in determining frontier orbital energies, an emerging theme in our work on formazanate 5d metal complexes.

3.3 Conclusion

In this chapter, we disclose the first examples of cyclometalated iridium formazanate complexes prepared by a general synthetic strategy and a thorough study of the electronic modification of the formazanate ligand on the electrochemical and photophysical properties is also presented. Structural elucidation of the complexes reveals two chelating modes for the formazanate, with the typical six-membered "closed" form and an unusual five-membered "open" structure both observed. Systematic comparison of different cyclometalated and formazanate ligands reveals that the redox potentials are much more sensitive to the identity of the substituents on the formazanate backbone. The UV-vis absorption features prove some predictable control of photophysical properties by tuning the formazanate and cyclometalated ligands independently. In future works, we plan to continue our exploration of 5d metal formazanate complexes, further underscoring the effects of the metal identity, oxidation state, and coordination geometry on the formazanate-derived redox and optical properties.

3.4 Experimental section

3.4.1 Materials.

Reactions were carried out in a nitrogen atmosphere using standard Schlenk techniques. Solvents, starting materials, and reagents were of commercial origin and used without further purification unless stated otherwise below. Tetrahydrofuran (THF) and toluene for UV-vis spectroscopy, and acetonitrile and dichloromethane (DCM) for electrochemical

measurements were dried by the method of Grubbs[114], passing through dual alumina columns on a commercial solvent purification system (SPS). The acetonitrile was further dried by storage over 3A molecular sieves. Tetrabutylammonium hexafluorophosphate ($TBAPF_6$) was recrystallized from hot ethanol and ferrocene was sublimed at ambient pressure before use in electrochemical experiments. $CDCl_3$ and CD_3CN for NMR spectroscopy were stored over potassium carbonate and molecular sieves to remove acidic impurities and moisture. The ligands 3-*p*-methoxyphenyl-1,5-di-*p*-tolylformazan (**Fza**), 1,3,5-tri-*p*-methoxyphenylformazan (**Fzb**) and 3-*p*-tolyl-1,5-di-*p*-cyanophenylformazan (**Fzc**) and 3-*p*-cyanophenyl-1,5-di-*p*-tolylformazan (**Fzd**) were prepared by the method of Hicks *et al.*[115] The ligands 3-cyano-1,5-di-p-tolylformazan (**Fze**) and 3-cyano-1,5-di-*p*-cyanophenylformazan (**Fzf**) were prepared by following the literature procedures.[116] The iridium precursors $[Ir(ppy)_2(\mu\text{-}Cl)]_2$ (ppy = 2-phenylpyridine), $[Ir(F_2ppy)_2(\mu\text{-}Cl)]_2$ (F_2ppy = 2-(2,4-difluorophenyl)pyridine), $[Ir(bt)_2(\mu\text{-}Cl)]_2$ (bt = 2-phenylbenzothiazole), and $[Ir(piq)_2(\mu\text{-}Cl)]_2$ (piq = 1-phenylisoquinoline) were prepared by a modified version of the well-known Nonoyama procedure.[117,118]

3.4.2 Physical methods.

NMR spectra were recorded at room temperature using a JEOL ECA-600, ECA-500, or ECA-400 NMR spectrometer and are shown in appendix. UV-vis absorption spectra were recorded in THF, toluene, and MeOH solutions in screw-capped 1 cm quartz cuvettes using an Agilent Cary 8454 UV-vis spectrophotometer. Cyclic voltammetry (CV) measurements were performed with a CH Instruments 602E potentiostat interfaced with a nitrogen glovebox via wire feedthroughs. Samples were dissolved in dichloromethane (CH_2Cl_2) with 0.1 M

$TBAPF_6$ as a supporting electrolyte. A 3 mm diameter glassy carbon working electrode, a platinum wire counter electrode, and a silver wire pseudo-reference electrode were used. Potentials were referenced to an internal standard of ferrocene. The bulk purity for all complexes is established by elemental analysis, performed by Atlantic Microlab, Inc.

3.4.3 Synthesis of compounds

Complex 32a/32a′. $[Ir(ppy)_2(\mu\text{-}Cl)]_2$ (101 mg, 0.0942 mmol) and **Fza** (67 mg, 0.19 mmol) were combined in ethanol (15 mL) with excess triethylamine (0.10 mL), and the mixture was deoxygenated under the protection of N_2. The mixture was refluxed for 24 h and the color changed from red to green. The reaction completion was confirmed by TLC, which showed two green products of almost identical polarity, likely the "open" and "closed" isomers. The solvent was removed using rotary evaporation, and the product was re-dissolved in ethyl acetate to filter through neutral alumina in order to remove insoluble impurities. After removing ethyl acetate, column chromatography (hexane / ethyl acetate gradient eluent, neutral alumina) was performed to purify the product but attempts to separate the isomers using chromatography was not successful. Both isomers were eluted together from the column, and the combined products were recrystallized (THF / pentane) later to get dark green solid. NMR analysis suggests a ca. 2:1 ratio of the "open" (**32a**) and "closed" (**32a′**) isomers, which results in very similar integration values for the resonances associated with each isomer. As such, a clear assignment of the peaks was not possible, and integration values for the ^{1}H NMR peaks are not provided. The spectrum is shown in Figure S2 with relative integration values shown. Yield: 83 mg (51%). ^{1}H NMR (400 MHz, $CDCl_3$) δ: 8.70 (d, *J* = 5.6 Hz, ArH), 8.63 (d, *J* = 5.6 Hz, ArH) 8.43 (d, *J* = 6.0 Hz, ArH), 7.93 (d, *J* = 7.8 Hz, ArH),

7.58–7.87 (m, ArH), 7.30 (d, *J* = 7.8 Hz, ArH), 7.20 (dd, *J* = 5.9 Hz, ArH), 6.94–7.11 (m, ArH), 6.86 (d, *J* = 7.8 Hz, ArH), 6.73 (t, *J* = 7.3 Hz, ArH), 6.47–6.69 (m, ArH), 6.12–6.38 (m, ArH), 5.94 (d, *J* = 7.8 Hz, ArH), 5.57 (d, *J* = 7.8 Hz, ArH), 3.80 (s, OCH_3, both isomers coincident), 2.12 (s, CH_3), 2.10 (s, CH_3), 2.04 (s, CH_3). $^{13}C\{^1H\}$ NMR (151 MHz, $CDCl_3$) δ: 169.3, 168.5, 167.5, 158.8, 158.6, 158.2, 156.9, 154.7, 153.7, 152.4, 152.2, 151.8, 150.1, 149.6, 149.0, 143.7, 143.5, 142.8, 136.8, 136.7, 136.5, 134.4, 134.3, 134.2, 133.8, 133.2, 131.1, 130.2, 129.6, 129.0, 128.8, 128.5, 128.3, 127.6, 127.4, 125.6, 123.8, 123.7, 123.4, 122.2, 121.9, 121.5, 121.3, 120.6, 120.1, 119.3, 119.0, 118.9, 118.7, 113.4, 55.47, 55.4, 20.94, 20.85. Anal. Calcd for $C_{44}H_{38}IrN_6O$: C, 61.52; H, 4.46; N, 9.78. Found: C, 61.69; H, 4.47; N, 9.76.

Complex 32b′. The title compound was prepared by the general method described above for complex **32a/32a′**, using $[Ir(ppy)_2(\mu\text{-}Cl)]_2$ (50 mg, 0.047 mmol) and **Fzb** (37 mg, 0.094 mmol). The product was isolated as a mixture of isomers and recrystallized later (CH_2Cl_2/ pentane) to get a dark green solid. Yield: 36 mg (43%). We were unable to obtain satisfactory elemental analysis for this compound, but the NMR spectrum in Figures S4 and S5 provide evidence for bulk purity. The minor impurity peaks in the ^1H NMR spectrum arise from a small amount of the "open" isomer **32b** present in the isolated product. ^1H NMR (400 MHz, $CDCl_3$) δ: 8.70 (d, *J* = 5.5 Hz, 2H, ArH), 7.82 (d, *J* = 8.7 Hz, 2H, ArH), 7.60–7.71 (m, 4H, ArH), 7.21–7.28 (m, 2H, ArH), 6.95–7.03 (m, 2H, ArH), 6.86 (d, *J* = 8.7 Hz, 2H, ArH), 6.65 (t, *J* = 7.3 Hz, 2H, ArH), 6.51–6.61 (m, 6H, ArH), 6.18–6.32 (m, 6H, ArH), 3.80 (s, 3H, OCH_3), 3.62 (s, 6H, OCH_3). $^{13}C\{^1H\}$ NMR (151 MHz, $CDCl_3$) δ: 168.5, 158.3, 156.8, 154.8,

150.0, 149.0, 148.9, 143.7, 136.9, 134.3, 133.8, 130.1, 128.9, 125.6, 124.6, 123.7, 121.5, 120.7, 118.8, 113.4, 113.1, 112.2, 55.47, 55.21.

Complex 32c. $[Ir(ppy)_2(\mu\text{-}Cl)]_2$ (54 mg, 0.05 mmol) and **Fzc** (34 mg, 0.10 mmol) were combined in ethanol (10 mL) with excess triethylamine (0.1 mL), and the mixture was deoxygenated under the protection of N_2. The mixture was refluxed for 36 h, and the color changed from red to green. The reaction completion was confirmed by TLC. Solvent was removed using rotary evaporation, and the product was re-dissolved in a minimum amount of ethyl acetate. After that column chromatography (hexane / ethyl acetate gradient eluent, neutral alumina) was performed to purify the product, which was crystallized by vapor diffusion of pentane into a concentrated CH_2Cl_2 solution. Yield: 62 mg (72%). ^{1}H NMR (500 MHz, $CDCl_3$) δ: 8.46 (d, *J* = 5.7 Hz, 1H, ArH), 8.34 (d, *J* = 5.6 Hz, 1H, ArH), 7.83–7.88 (m, 1H, ArH), 7.82 (d, *J* = 7.2 Hz, 1H, ArH), 7.73 (d, *J* = 8.3 Hz, 2H, ArH), 7.72 (dd, *J* = 7.1, 1.3 Hz, 1H, ArH), 7.68 (d, *J* = 7.2 Hz, 1H, ArH), 7.33 (dd, *J* = 7.9, 1.0 Hz, 1H, ArH), 7.25 (d, *J* = 8.1 Hz, 1H, ArH), 7.20 (s, 2H, ArH), 7.18 (s, 2H, ArH), 7.10 (d, *J* = 8.9 Hz, 4H, ArH), 6.87 (d, *J* = 8.6 Hz, 2H, ArH), 6.79 (td, *J* = 7.6, 1.2 Hz, 1H, ArH), 6.68–6.74 (m, 2H, ArH), 6.40 (td, *J* = 7.5, 1.1 Hz, 1H, ArH), 6.35 (d, *J* = 8.2 Hz, 2H, ArH), 5.91 (dd, *J* = 7.8, 0.9 Hz, 1H, ArH), 5.63–5.67 (m, 1H, ArH), 2.37 (s, 3H, CH_3). ^{13}C{^{1}H} NMR (151 MHz, $CDCl_3$) δ: 168.9, 167.4, 161.3, 160.4, 157.0, 155.9, 155.3, 151.6, 149.1, 148.3, 147.2, 143.4, 142.6, 138.3, 137.6, 137.5, 132.1, 132.0, 130.7, 130.5, 130.2, 129.7, 129.1, 128.9, 124.3, 124.2, 122.6, 122.5, 122.3, 122.2, 121.1, 120.5, 119.8, 119.5, 119.4, 108.3, 105.7, 21.5. Anal. Calcd for $C_{44}H_{31}N_8Ir$: C, 61.17, H, 3.62, N, 12.97. Found: C, 61.03, H, 3.68, N, 12.72.

Complex 32d′. The title compound was prepared by the general method described above for complex **32c**, using $[Ir(ppy)_2(\mu\text{-}Cl)]_2$ (54 mg, 0.050 mmol) and **Fzd** (37 mg, 0.10 mmol).Yield: 43 mg (50%). ^{1}H NMR (500 MHz, $CDCl_3$) δ: 8.68 (d, *J* = 5.5 Hz, 2H, ArH), 7.98 (d, *J* = 8.6 Hz, 2H, ArH), 7.69–7.74 (m, 2H, ArH), 7.65 (d, *J* = 7.9 Hz, 2H, ArH), 7.52 (d, *J* = 8.6 Hz, 2H, ArH), 7.18–7.20 (m, 2H, ArH), 7.05 (ddd, *J* = 7.2, 5.8, 1.2 Hz, 2H, ArH), 6.61–6.65 (m, 2H, ArH), 6.57 (dd, *J* = 7.4, 1.1 Hz, 2H, ArH), 6.53 (d, *J* = 8.1 Hz, 4H, ArH), 6.44 (d, *J* = 8.4 Hz, 4H, ArH), 6.17 (d, *J* = 7.0 Hz, 2H, ArH), 2.11 (s, 6H, CH_3). $^{13}C\{^1H\}$ NMR (151 MHz, $CDCl_3$) δ: 168.5, 153.8, 153.7, 149.7, 146.8, 146.0, 143.5, 137.2, 134.9, 133.7, 131.7, 129.0, 127.6, 124.1, 123.7, 123.1, 121.8, 120.9, 120.4, 119.0, 107.6, 20.9. Anal. Calcd for $C_{44}H_{34}N_7Ir$: C, 61.95, H, 4.02, N, 11.49. Found: C, 62.04, H, 4.00, N, 11.36.

Complex 32e. The title compound was prepared by the general method described above for complex **32c**, using $[Ir(ppy)_2(\mu\text{-}Cl)]_2$ (54 mg, 0.050 mmol) and **Fze** (28 mg, 0.10 mmol). Yield: 47 mg (60%). ^{1}H NMR (500 MHz, $CDCl_3$) δ: 8.37 (d, *J* = 5.5 Hz, 1H, ArH), 8.27 (d, *J* = 5.4 Hz, 1H, ArH), 7.78–7.83 (m, 1H, ArH), 7.76 (d, *J* = 7.7 Hz, 1H, ArH), 7.68–7.72 (m, 1H, ArH), 7.65 (d, *J* = 7.9 Hz, 1H, ArH), 7.27 (s, 1H, ArH), 7.19 (d, *J* = 7.4 Hz, 1H, ArH), 7.12–7.16 (m, 1H, ArH), 7.05–7.09 (m, 1H, ArH), 6.82 (d, *J* = 8.5 Hz, 2H, ArH), 6.74 (td, *J* = 7.5, 0.8 Hz, 1H, ArH), 6.67 (d, *J* = 7.8 Hz, 3H, ArH), 6.59 (t, *J* = 7.8 Hz, 1H, ArH), 6.38 (d, *J* = 8.0 Hz, 2H, ArH), 6.30 (t, *J* = 7.8 Hz, 1H, ArH), 6.22 (d, *J* = 8.1 Hz, 2H, ArH), 5.89 (d, *J* = 7.5 Hz, 1H, ArH), 5.55 (d, *J* = 7.5 Hz, 1H, ArH), 2.13 (s, 3H, CH_3), 2.04 (s, 3H, CH_3). $^{13}C\{^1H\}$NMR (151 MHz, $CDCl_3$) δ: 168.8, 167.2, 167.2, 153.7, 151.2, 150.6, 150.4, 149.7, 148.1, 143.4, 142.6, 137.4, 136.4, 136.3, 135.2, 132.0, 130.9, 129.9, 129.4, 128.5, 128.3,

124.0, 123.9, 122.6, 122.3, 122.1, 121.9, 120.1, 120.1, 119.2, 119.2, 116.2, 21.0, 21.0. Anal. Calcd for $C_{38}H_{30}N_7Ir$: C, 58.75, H, 3.89, N, 12.62. Found: C, 58.90, H, 3.89, N, 12.42.

Complex 32f. The title compound was prepared by the general method described above for complex **32c**, using $[Ir(ppy)_2(\mu\text{-}Cl)]_2$ (54 mg, 0.050 mmol) and **Fzf** (30 mg, 0.10 mmol). Yield: 41 mg (52%). ^{1}H NMR (500 MHz, CD_3CN) δ: 8.40 (d, *J* = 5.6 Hz, 1H, ArH), 8.26 (d, *J* = 5.5 Hz, 1H, ArH), 7.97 (t, *J* = 7.1 Hz, 1H, ArH), 7.91 (d, *J* = 8.0 Hz, 1H, ArH), 7.85 (t, *J* = 7.8 Hz, 1H, ArH), 7.76 (d, *J* = 8.0 Hz, 1H, ArH), 7.32 (d, *J* = 7.7 Hz, 1H, ArH), 7.28 (dd, *J* = 7.6, 4.3 Hz, 2H, ArH), 7.20–7.24 (m, 1H, ArH), 7.17 (d, *J* = 8.7 Hz, 2H, ArH), 7.00 (d, *J* = 8.5 Hz, 2H, ArH), 6.98 (d, *J* = 8.7 Hz, 2H, ArH), 6.75 (t, *J* = 7.0 Hz, 1H, ArH), 6.69 (dd, *J* = 10.7, 4.2 Hz, 1H, ArH), 6.66 (dd, *J* = 11.5, 4.2 Hz, 1H, ArH), 6.49 (d, *J* = 8.4 Hz, 2H, ArH), 6.40 (t, *J* = 6.9 Hz, 1H, ArH), 5.83 (d, *J* = 7.6 Hz, 1H, ArH), 5.60 (d, *J* = 7.5 Hz, 1H, ArH). ^{13}C{^{1}H}NMR (151 MHz, CD_3CN) δ: 167.7, 166.1, 155.3, 154.2, 152.5, 151.5, 150.5, 146.8, 144.0, 143.2, 138.8, 138.8, 137.9, 137.2, 132.2, 132.0, 130.6, 129.9, 129.4, 124.4, 124.1, 123.9, 123.5, 123.0, 122.6, 121.1, 120.6, 120.1, 119.7, 118.7, 118.64, 114.6, 110.1, 108.1. Anal. Calcd for $C_{38}H_{24}N_9Ir$: C, 57.13, H, 3.03, N, 15.78. Found: C, 57.30, H, 3.18, N, 15.56.

Complex 33a. The title compound was prepared by the general method described above for complex **32c**, using $[Ir(F_2ppy)_2(\mu\text{-}Cl)]_2$ (61 mg, 0.050 mmol) and **Fza** (36 mg, 0.10 mmol). Yield: 76 mg (82%). ^{1}H NMR (500 MHz, CD_3CN) δ: 8.57 (d, *J* = 4.3 Hz, 1H, ArH), 8.44 (d, *J* = 4.5 Hz, 1H, ArH), 8.17 (d, *J* = 6.9 Hz, 1H, ArH), 8.03 (d, *J* = 6.9 Hz, 1H, ArH), 7.92 (d, *J* = 8.1 Hz, 2H, ArH), 7.78–7.85 (m, 1H, ArH), 7.71 (td, *J* = 8.0, 1.2 Hz, 1H, ArH), 7.11 (ddd, *J* = 7.3, 5.9, 1.4 Hz, 1H, ArH), 7.08 (ddd, *J* = 7.3, 5.9, 1.4 Hz, 1H, ArH), 6.88 (dd, *J* = 7.0, 3.0 Hz, 4H, ArH), 6.71 (d, *J* = 6.7 Hz, 2H, ArH), 6.51 (d, *J* = 6.5 Hz, 2H, ArH), 6.27 (ddd, *J* =

12.3, 9.1, 2.3 Hz, 1H, ArH), 6.15 (d, *J* = 5.9 Hz, 2H, ArH), 6.06 (ddd, *J* = 12.5, 9.3, 2.3 Hz, 1H, ArH), 5.41 (dd, *J* = 7.0, 1.8 Hz, 1H, ArH), 5.11 (dd, *J* = 7.0, 1.8 Hz, 1H, ArH), 3.81 (s, 3H, OCH_3), 2.15 (s, 3H, CH_3), 2.13 (s, 3H, CH_3). $^{13}C\{^1H\}$NMR (126 MHz, CD_3CN) δ: 165.8 (d, J_{CF} = 5.3 Hz), 164.2 (d, J_{CF} = 5.5 Hz), 163.5 (d, J_{CF} = 10.2 Hz), 163.3, 161.7 (d, J_{CF} = 9.8 Hz), 161.0 (d, J_{CF} = 7.7 Hz), 159.8 (d, J_{CF} = 5.2 Hz), 158.8, 158.4, 154.2, 152.2, 151.8, 151.6, 149.8, 137.9, 137.7, 135.1, 133.9, 130.2, 128.6, 128.2, 127.5, 127.2, 126.9, 123.2 (d, J_{CF} = 15.9 Hz), 122.9 (d, J_{CF} = 16.4 Hz), 122.5, 122.2, 121.7, 120.4, 113.9(d, J_{CF} = 12.5 Hz), 113.5, 113.0 (d, J_{CF} = 13.8 Hz), 97.7 (t, J_{CF} = 26.8 Hz), 95.9 (t, J_{CF} = 27.1 Hz), 55.4, 20.9, 20.6. ^{19}F NMR (470 MHz, $CDCl_3$) δ: −107.6 (dd, *J* = 19.0, 9.2 Hz, 1F), −109.4 (dd, *J* = 18.9, 9.4 Hz, 1F), −110.2 (t, *J* = 12.4 Hz, 1F), −111.1 (t, *J* = 11.4 Hz, 1F). Anal. Calcd for $C_{44}H_{33}N_6F_4OIr$: C, 56.83, H, 3.58, N, 9.04. Found: C, 56.76, H, 3.67, N, 8.90.

Complex 33b. The title compound was prepared by the general method described above for complex **32c**, using $[Ir(F_2ppy)_2(\mu\text{-}Cl)]_2$ (61 mg, 0.050 mmol) and **Fzb** (39 mg, 0.10 mmol). Yield: 53 mg (55%). ^1H NMR (500 MHz, CD_3CN) δ: 8.58–8.62 (m, 1H, ArH), 8.46 (d, *J* = 5.5 Hz, 1H, ArH), 8.13 (d, *J* = 8.6 Hz, 1H, ArH), 7.99 (d, *J* = 8.4 Hz, 1H, ArH), 7.93–7.97 (m, 1H, ArH), 7.83 (dd, *J* = 11.7, 5.1 Hz, 1H, ArH), 7.68 (d, *J* = 9.0 Hz, 2H, ArH), 7.29 (t, *J* = 7.3 Hz, 1H, ArH), 7.24 (t, *J* = 6.6 Hz, 1H, ArH), 6.88 (d, *J* = 9.0 Hz, 2H, ArH), 6.72 (d, *J* = 9.0 Hz, 2H, ArH), 6.41 (d, *J* = 6.9 Hz, 2H, ArH), 6.38–6.42 (m, 1H, ArH), 6.30 (d, *J* = 9.1 Hz, 2H, ArH), 6.21 (d, *J* = 8.1 Hz, 2H, ArH), 6.06–6.12 (m, 1H, ArH), 5.43 (dd, *J* = 7.6, 3.5 Hz, 1H, ArH), 5.21 (dd, *J* = 8.9, 2.4 Hz, 1H, ArH), 3.77 (s, 3H, OCH_3), 3.62 (s, 3H, OCH_3), 3.60 (s, 3H, OCH_3). $^{13}C\ \{^1H\}$ NMR (126 MHz, CD_3CN) δ: 164.9 (d, J_{CF} = 7.1 Hz), 163.2 (d, J_{CF} = 7.4 Hz), 162.4 (d, J_{CF} = 5.2 Hz), 161.7 (d, J_{CF} = 12.1 Hz), 161.6 (d, J_{CF} = 13.8 Hz), 161.5,

159.7 (d, J_{CF} = 4.7 Hz), 159.6 (d, J_{CF} = 3.9 Hz), 158.8, 158.4, 157.5, 156.5, 154.7 (d, J_{CF} = 6.3 Hz), 151.8, 150.8, 148.1, 147.6, 138.7, 138.6, 130.5, 127.7, 127.4, 123.5, 123.3 (d, J_{CF} = 19.9 Hz), 123.1, 123.0, 122.7 (d, J_{CF} = 20.4 Hz), 121.8, 114.1(d, J_{CF} = 16.5 Hz), 113.1, 112.9, 112.8, 112.6, 97.31, 96.16, 55.0, 54.9, 54.8. ^{19}F NMR (470 MHz, CD_3CN) δ: −109.5 (dd, *J* = 18.8, 9.4 Hz, 1F), −111.2 (q, *J* = 9.5 Hz, 1F), −111.7 (t, *J* = 11.8 Hz, 1F), −111.8 (t, *J* = 11.8 Hz, 1F). Anal. Calcd for $C_{44}H_{33}N_6F_4O_3Ir$: C, 54.94, H, 3.46, N, 8.74. Found: C, 54.76, H, 3.51, N, 8.57.

Complex 33c. The title compound was prepared by the general method described above for complex **32c**, using $[Ir(F_2ppy)_2(\mu\text{-}Cl)]_2$ (61 mg, 0.050 mmol) and **Fzc** (37 mg, 0.10 mmol). Yield: 75 mg (80%). ^{1}H NMR (500 MHz, $CDCl_3$) δ: 8.41 (d, *J* = 5.8 Hz, 1H, ArH), 8.37 (d, *J* = 5.7 Hz, 1H, ArH), 8.21 (d, *J* = 8.4 Hz, 1H, ArH), 8.08 (d, *J* = 8.3 Hz, 1H, ArH), 7.93 (t, *J* = 7.9 Hz, 1H, ArH), 7.79 (t, *J* = 7.9 Hz, 1H, ArH), 7.72 (dd, *J* = 8.1, 1.6 Hz, 2H, ArH), 7.14–7.22(m, 6H, ArH), 7.12 (dd, *J* = 8.8, 1.9 Hz, 2H, ArH), 7.03–7.06 (m, 2H, ArH), 6.35 (d, *J* = 8.8 Hz, 3H, ArH), 6.23 (dd, *J* = 12.1, 9.4 Hz, 1H, ArH), 5.35–5.40 (m, 1H, ArH), 5.15–5.19 (m, 1H, ArH), 2.37 (s, 3H, CH_3). ^{13}C{^{1}H}NMR (151 MHz, $CDCl_3$) δ: 165.5 (d, J_{CF} = 7.0 Hz), 164.0, 163.8 (d, J_{CF} = 7.5 Hz), 162.0 (dd, J_{CF} = 17.4, 11.9 Hz), 161.7 (d, J_{CF} = 7.7 Hz), 161.0, 160.1, 160.0, 159.0 (d, J_{CF} = 6.0 Hz), 156.5, 155.6, 152.0 (d, J_{CF} = 6.8 Hz), 151.6, 149.2, 138.7, 138.7, 132.3, 131.5, 129.8, 129.1, 129.0, 127.4, 127.1, 123.7 (d, J_{CF} = 19.8 Hz), 123.4 (d, J_{CF} = 19.8 Hz), 123.0, 122.9, 122.0, 120.7, 119.5, 118.6, 114.2 (d, J_{CF} = 17.8 Hz), 112.9 (d, J_{CF} = 18.0 Hz), 109.0, 106.8, 98.8 (t, J_{CF} = 26.6 Hz), 97.6 (t, J_{CF} = 26.6 Hz), 21.5. ^{19}F NMR (470 MHz, $CDCl_3$) δ: −105.8 (dd, *J* = 8.6, 10 Hz, 1F), −107.0 (dd, *J* = 8.6, 10 Hz, 1F),

−108.7 (t, J = 11 Hz, 1F), −109.2 (t, *J* = 10 Hz, 1F). Anal. Calcd for $C_{44}H_{27}N_8F_4Ir$: C, 56.46, H, 2.91, N, 11.97. Found: C, 56.22, H, 3.13, N, 11.70.

Complex 33d. The title compound was prepared by the general method described above for complex **32c**, using $[Ir(F_2ppy)_2(\mu\text{-}Cl)]_2$ (61 mg, 0.050 mmol) and **Fzd** (34 mg, 0.10 mmol). Yield: 67 mg (73%). ^{1}H NMR (500 MHz, $CDCl_3$) δ: 8.48 (d, *J* = 5.9 Hz, 1H, ArH), 8.40 (d, *J* = 6.5 Hz, 1H, ArH), 8.18 (d, *J* = 8.4 Hz, 3H, ArH), 8.03 (d, *J* = 9.2 Hz, 1H, ArH), 7.85 (t, *J* = 7.8 Hz, 1H, ArH), 7.74 (t, *J* = 7.8 Hz, 1H, ArH), 7.57 (d, *J* = 8.4 Hz, 2H, ArH), 7.14 (t, *J* = 6.6 Hz, 1H, ArH), 7.11 (t, *J* = 6.6 Hz, 1H, ArH), 6.80 (d, *J* = 8.4 Hz, 2H, ArH), 6.73 (d, *J* = 8.4 Hz, 2H, ArH), 6.56 (d, *J* = 8.2 Hz, 2H, ArH), 6.23–6.31 (m, 1H, ArH), 6.18 (d, *J* = 7.8 Hz, 2H, ArH), 6.06–6.12 (m, 1H, ArH), 5.37 (dd, *J* = 8.7, 2.3 Hz, 1H, ArH), 5.11 (dd, *J* = 8.6, 2.3 Hz, 1H, ArH), 2.17 (s, 3H, CH_3), 2.15 (s, 3H, CH_3). ^{13}C{^{1}H}NMR (151 MHz, $CDCl_3$) δ: 165.7 (d, J_{CF} = 5.5 Hz), 164.1 (d, J_{CF} = 4.7 Hz), 163.6 (d, J_{CF} = 2.4 Hz), 160.6, 160.0 (d, J_{CF} = 4.2 Hz), 155.8, 153.0 (d, J_{CF} = 5.8 Hz), 151.5, 151.3, 151.1, 149.6, 138.5, 138.1, 138.0, 136.0, 134.9, 131.9, 128.7, 128.3, 128.3, 127.3, 127.2, 123.4, 123.2, 123.1, 122.7, 122.5, 121.9, 120.3, 119.7, 113.9 (d, J_{CF} = 13.2 Hz), 113.4, 112.9 (d, J_{CF} = 13.9 Hz), 109.3, 97.99 (t, J_{CF} = 26 Hz), 96.41, 96.24, 21.0, 20.7. ^{19}F NMR (470 MHz, $CDCl_3$) δ: −107.2 (dd, *J* = 15.1, 7.4 Hz, 1F), −108.9 (dd, *J* = 15.0, 7.4 Hz, 1F), −110.0 (t, *J* = 9.2 Hz, 1F), −110.6 (t, *J* = 9.1 Hz, 1F). Anal. Calcd for $C_{44}H_{30}N_7F_4Ir$: C, 57.13, H, 3.27, N, 10.60. Found: C, 57.14, H, 3.42, N, 10.46.

Complex 33e. The title compound was prepared by the general method described above for complex **32c**, using $[Ir(F_2ppy)_2(\mu\text{-}Cl)]_2$ (61 mg, 0.050 mmol) and **Fze** (28 mg, 0.10 mmol). Yield: 46 mg (54%). ^{1}H NMR (400 MHz, $CDCl_3$) δ: 8.32 (d, *J* = 5.6 Hz, 1H), 8.27 (d, *J* = 5.7

Hz, 1H, ArH), 8.16 (d, *J* = 8.7 Hz, 1H, ArH), 8.03 (d, *J* = 9.1 Hz, 1H, ArH), 7.89 (t, *J* = 7.9 Hz, 1H, ArH), 7.79 (t, *J* = 7.9 Hz, 1H, ArH), 7.20–7.24 (m, 1H, ArH), 7.13Ą7.19 (m, 1H, ArH), 6.72 (s, 4H, ArH), 6.56 (d, *J* = 8.0 Hz, 2H, ArH), 6.24–6.33 (m, 1H, ArH), 6.20 (d, *J* = 8.0 Hz, 2H, ArH), 6.05–6.15 (m, 1H, ArH), 5.34 (d, *J* = 6.7 Hz, 1H, ArH), 5.06 (d, *J* = 8.6 Hz, 1H, ArH), 2.17 (s, 3H, CH_3), 2.13 (s, 3H, CH_3). $^{13}C\{^1H\}$NMR (151 MHz, $CDCl_3$) δ: 166.3, 163.7 (d, J_{CF} = 6.7 Hz), 161.9 (t, J_{CF} = 11.7 Hz), 161.6 (d, J_{CF} = 12.3 Hz), 159.9, 157.7 (d, J_{CF} = 6.5 Hz), 151.8, 151.7 (d, J_{CF} = 7.2 Hz), 151.2, 150.3, 149.9, 149.8, 138.6, 137.0, 136.1, 128.7, 128.3, 127.8, 127.3, 127.0, 123.4, 123.3 (d, J_{CF} = 20.4 Hz), 123.1, 122.8 (d, J_{CF} = 39.7 Hz), 122.3, 121.9, 120.1, 115.5, 114.2 (d, J_{CF} = 17.0 Hz), 113.0 (d, J_{CF} = 16.8 Hz), 98.4 (t, J_{CF} = 27.0 Hz), 96.7 (t, J_{CF} = 25.5 Hz), 21.0, 20.8. ^{19}F NMR (470 MHz, $CDCl_3$) δ: −106.7 (dd, *J* = 19.1, 9.1 Hz, 1F), −108.4 (dd, *J* = 19.1, 9.4 Hz, 1F), −109.7 (t, *J* = 11.6 Hz, 1F), −110.2 (t, *J* = 11.6 Hz, 1F). Anal. Calcd for $C_{38}H_{26}N_7F_4Ir$: C, 53.77, H, 3.09, N, 11.55. Found: C, 53.75, H, 3.26, N, 11.62.

Complex 33f. The title compound was prepared by the general method described above for complex **32c**, using $[Ir(F_2ppy)_2(\mu\text{-}Cl)]_2$ (61 mg, 0.050 mmol) and **Fzf** (30 mg, 0.10 mmol). Yield: 51 mg (58%). ^1H NMR (500 MHz, CD_3CN) δ: 8.44 (d, *J* = 5.1 Hz, 1H, ArH), 8.31 (d, *J* = 6.5 Hz, 1H, ArH), 8.14 (d, *J* = 8.4 Hz, 1H, ArH), 8.04 (t, *J* = 8.1 Hz, 1H, ArH), 8.00 (d, *J* = 8.4 Hz, 1H, ArH), 7.92 (t, *J* = 8.0 Hz, 1H, ArH), 7.35 (ddd, *J* = 7.4, 5.8, 1.4 Hz, 1H, ArH), 7.29–7.32 (m, 1H, ArH), 7.26–7.29 (m, 2H, ArH), 7.21 (d, *J* = 8.7 Hz, 2H, ArH), 6.92 (d, *J* = 6.8 Hz, 2H, ArH), 6.54 (d, *J* = 8.4 Hz, 2H, ArH), 6.42 (ddd, *J* = 12.6, 9.3, 2.3 Hz, 1H, ArH), 6.29 (ddd, *J* = 12.7, 9.4, 2.3 Hz, 1H, ArH), 5.37 (dd, *J* = 8.7, 2.4 Hz, 1H, ArH), 5.18 (dd, *J* = 8.7, 2.4 Hz, 1H, ArH). $^{13}C\{^1H\}$NMR (151 MHz, CD_3CN) δ: 163.8 (d, J_{CF} = 7.2 Hz), 163.3,

162.3 (d, J_{CF} = 6.6 Hz), 161.6 (d, J_{CF} = 12.5 Hz), 161.1, 159.5 (d, J_{CF} = 3.8 Hz), 156.7 (d, J_{CF} = 6.9 Hz), 154.8, 154.1, 152.1, 151.2, 150.4, 139.8 (d, J_{CF} = 15.9 Hz), 137.7, 132.3, 132.1, 131.7, 127.6, 124.5, 124.2, 123.8 (d, J_{CF} = 19.8 Hz), 123.6, 123.5 (d, J_{CF} = 20.1 Hz), 123.0, 121.0, 118.5, 118.2, 114.4, 114.1, 112.9, 110.6, 108.8, 98.7 (t, J_{CF} = 27.1 Hz), 97.4 (t, J = 27.2 Hz). ^{19}F NMR (470 MHz, CD_3CN) δ: −107.8 (dd, J = 19.1, 9.2 Hz, 1F), −109.4 (dd, J = 19.0, 9.4 Hz, 1F), −110.6 (t, J = 11.4 Hz, 1F), −110.7 (t, J = 11.6 Hz, 1F). Anal. Calcd for $C_{38}H_{20}N_9F_4Ir$: C, 52.41, H, 2.31, N, 14.48. Found: C, 52.34, H, 2.59, N, 14.23.

Complex 34a. The title compound was prepared by the general method described above for complex **32a/32a′**, using $[Ir(bt)_2(\mu\text{-}Cl)]_2$ (51 mg, 0.039 mmol) and **Fza** (37 mg, 0.10 mmol). The dark green solid product was isolated as a mixture of isomers where the major product was the five-member chelate with a trace amount of six-member chelate evident from ^{1}H NMR data (Figure S32). Yield: 35 mg (47%). ^{1}H NMR (500 MHz, $CDCl_3$) δ: 7.97–8.03 (m, 2H, ArH), 7.71–7.91 (m, 4H, ArH), 7.32–7.51 (m, 4H, ArH), 7.22 (d, J = 7.5 Hz, 1H, ArH), 7.02 (d, J = 8.0 Hz, 1H, ArH), 6.78–6.84 (m, 2H, ArH), 6.72 (t, J = 7.4 Hz, 1H, ArH), 6.53–6.67 (m, 2H, ArH), 6.32–6.52 (m, 9H, ArH), 6.19 (d, J = 8.0 Hz, 1H, ArH), 6.12 (d, J = 8.0 Hz, 1H, ArH), 3.76 (s, 3H, CH_3), 2.09 (s 3H, CH_3), 2.08 (s, 3H, CH_3). ^{13}C{^{1}H} NMR (101 MHz, $CDCl_3$) δ: 181.5, 179.8, 161.7, 150.2.150.0, 149.2, 140.0, 139.5, 133.4, 131.5, 131.3, 131.0, 130.9, 130.0, 128.1, 128.0, 127.6, 127.4, 126.1, 125.6, 125.4, 123.6, 122.8, 122.4, 121.7, 121.1, 120.6, 119.7, 113.5, 55.36, 21.05, 20.89. Anal. Calcd for $C_{48}H_{37}IrN_6OS_2$: C, 59.42; H, 3.84; N, 8.66. Found: C, 59.44; H, 3.84; N, 8.58.

Complex 34b. The title compound was prepared by the general method described above for complex **32a/32a′**, using $[Ir(bt)_2(\mu\text{-}Cl)]_2$ (50 mg, 0.039 mmol) and **Fzb** (32 mg, 0.81 mmol).

The product was isolated as a mixture of isomers after column chromatography, and recrystallization of the product from a THF/MeOH mixture afforded pure **34b** as a dark green solid. Yield: 39 mg (50%). ^{1}H NMR (400 MHz, $CDCl_3$) δ: 7.95–8.02 (m, 2H, ArH), 7.78–7.89 (m, 2H, ArH), 7.72 (d, *J* = 8.7 Hz, 2H, ArH), 7.34–7.52 (m, 4H, ArH), 7.22–7.29 (m, 1H, ArH), 7.11 (d, *J* = 7.3 Hz, 1H, ArH), 6.82 (d, *J* = 8.7 Hz, 2H, ArH), 6.72 (t, *J* = 7.3 Hz, 1H, ArH), 6.42–6.67 (m, 7H, ArH), 6.09–6.27 (m, 6H, ArH), 3.78 (s, 3H, OCH_3), 3.62 (s, 3H, OCH_3), 3.61 (s, 3H, OCH_3). ^{13}C{^{1}H} NMR (151 MHz, $CDCl_3$) δ: 181.4, 179.7, 162.6, 158.5, 157.1, 156.2, 150.1, 149.8, 149.7, 149.2, 147.3, 146.5, 140.7, 140.1, 139.6, 134.2, 133.5, 131.6, 131.3, 131.0, 130.9, 130.0, 129.9, 128.2, 127.7, 126.0, 125.7, 125.5, 124.8, 123.7, 122.9, 122.4, 122.3, 121.7, 121.0, 120.5, 120.4, 113.6, 112.8, 112.6, 112.2, 55.55, 55.36, 55.12. Anal. Calcd for $C_{48}H_{37}IrN_6O_3S_2$: C, 57.53; H, 3.72; N, 8.39. Found: C, 57.22; H, 3.57; N, 7.91.

Complex 34e. The title compound was prepared by the general method described above for complex **32c**, using $[Ir(bt)_2(\mu\text{-}Cl)]_2$ (100 mg, 0.0771 mmol) and **Fze** (39 mg, 0.15 mmol). The product was obtained as a reddish green solid. Yield: 45 mg (33%). Elemental analysis returned high percentages for C and H and a low percentage for N, but the NMR spectra in Figures S36 and S37 indicate satisfactory bulk purity. ^{1}H NMR (400 MHz, $CDCl_3$) δ: 8.08 (d, *J* = 7.3 Hz, 2H, ArH), 7.80 (d, *J* = 7.8 Hz, 1H, ArH), 7.74 (d, *J* = 7.8 Hz, 1H, ArH), 7.68 (d, *J* = 8.2 Hz, 1H, ArH), 7.38–7.47 (m, 1H, ArH), 6.98–7.34 (m, 10H, ArH), 6.79–6.93 (m, 3H, ArH), 6.72 (d, *J* = 6.8 Hz, 3H, ArH), 6.49–6.54 (m, 1H, ArH), 6.44 (d, *J* = 7.8 Hz, 1H, ArH), 2.33 (s, 3H, CH_3), 2.24 (s, 3H, CH_3). ^{13}C{^{1}H} NMR (151 MHz, $CDCl_3$) δ: 182.7, 180.0, 178.1, 171.7, 170.8, 150.9, 150.0, 149.9, 141.5, 139.9, 138.7, 138.2, 137.1, 133.0, 132.6,

131.2, 131.1, 130.8, 129.7, 128.5, 127.5, 127.4, 125.8, 125.6, 125.4, 125.3, 124.1, 122.8, 122.2, 121.9, 121.2, 120.8, 119.6, 119.4, 21.34, 21.23. Anal. Calcd for $C_{42}H_{30}IrN_7S_2$: C, 56.74; H, 3.40; N, 11.03. Found: C, 57.70; H, 3.93; N, 10.28.

Complex 34f. The title compound was prepared by the general method described above for complex **32c**, using $[Ir(bt)_2(\mu\text{-}Cl)]_2$ (100 mg, 0.0771 mmol) and **Fzf** (46 mg, 0.15 mmol). The product was isolated as a greenish brown solid. Yield: 51 mg (38%). ^{1}H NMR (500 MHz, $CDCl_3$) δ: 7.92–7.99 (m, 2H, ArH), 7.64–7.71 (m, 1H, ArH), 7.41–7.61 (m, 5H, ArH), 7.23–7.30 (m, 1H, ArH), 7.13 (d, *J* = 7.8 Hz, 2H, ArH), 7.01–7.08 (m, 2H, ArH), 6.95 (d, *J* = 8.2 Hz, 2H, ArH), 6.77–6.86 (m, 2H, ArH), 6.69–6.76 (m, 3H, ArH), 6.58–6.66 (m, 3H, ArH), 6.05 (dd, *J* = 7.8, 22.9 Hz, 2H, ArH). ^{13}C{^{1}H} NMR (126 MHz, $CDCl_3$) δ: 181.6, 180.1, 155.6, 154.8, 152.7, 149.2, 148.4, 146.2, 139.7, 139.4, 139.1, 133.3, 132.0, 131.9, 131.5, 131.3, 131.1, 130.6, 129.1, 128.7, 126.7, 127.7, 126.4, 126.0, 123.7, 123.4, 123.3, 123.2, 122.2, 120.9, 119.2, 119.0, 118.9, 118.6, 114.2, 110.5, 108.7. Anal. Calcd for $C_{42}H_{24}IrN_9S_2 \cdot 0.25C_4H_8O_2$: C, 55.35; H, 2.80; N, 13.51. Found: C, 55.49; H, 2.67; N, 13.52.

Complex 35a. The title compound was prepared by the general method described above for complex **32a/32a′**, using $[Ir(piq)_2(\mu\text{-}Cl)]_2$ (100 mg, 0.0785 mmol) and **Fza** (63 mg, 0.16 mmol). The product was isolated as a mixture of isomer and recrystallized later (CH_2Cl_2/pentane) to get greenish blue solid. Yield: 74 mg (48%). ^{1}H NMR (400 MHz, $CDCl_3$) δ: 8.65–8.74 (m, 1H, ArH), 8.58–8.64 (m, 1H, ArH), 8.46 (d, *J* = 6.4 Hz, 1H, ArH), 8.32 (d, *J* = 6.4 Hz, 1H, ArH), 7.79–7.93 (m, 5H, ArH), 7.58–7.78 (m, 5H, ArH), 7.37 (d, *J* = 6.4 Hz, 1H, ArH), 7.30 (d, *J* = 6.4 Hz, 1H, ArH), 6.78–6.88 (m, 5H, ArH), 6.45–6.64 (m, 5H, ArH), 6.31–6.43 (m, 3H, ArH), 6.21–6.28 (m, 2H, ArH), 6.14 (d, *J* = 6.4 Hz, 1H, ArH), 5.79

(d, *J* = 8.0 Hz, 1H, ArH), 3.78 (s, 3H, OCH_3), 2.06 (s, 3H, CH_3), 2.02 (s, 3H, CH_3). $^{13}C\{^1H\}$ NMR (151 MHz, $CDCl_3$) δ: 169.8, 169.4, 168.7, 160.6, 158.7, 158.6, 153.5, 153.3, 152.4, 152.0, 144.8, 144.6, 143.4, 142.7, 136.8, 136.6, 134.5, 134.2, 133.1, 133.0, 131.5, 130.9, 130.2, 129.8, 129.4, 129.3, 128.5, 128.4, 128.2, 127.7, 127.4, 127.2, 127.1, 126.2, 123.6, 122.0, 121.0, 120.6, 120.2, 119.6, 119.1, 113.4, 55.37, 20.87, 20.82. Anal. Calcd for $C_{52}H_{41}IrN_6O$: C, 65.18; H, 4.31; N, 8.77. Found: C, 65.15; H, 4.46; N, 8.50.

Complex 35f. The title compound was prepared by the general method described above for complex **32c**, using $[Ir(piq)_2(\mu\text{-}Cl)]_2$ (75 mg, 0.0589 mmol) and **Fzf** (46 mg, 0.12 mmol). The product was isolated as a greenish brown solid. Yield: 60 mg (56%). ^1H NMR (600 MHz, $CDCl_3$) δ: 8.63 (dd, *J* = 8.3, 16.2 Hz, 2H, ArH), 8.10 (d, *J* = 6.2 Hz, 1H, ArH), 8.03 (d, *J* = 6.2 Hz, 1H, ArH), 7.93–8.00 (m, 2H, ArH), 7.77–7.91 (m, 5H, ArH), 7.71 (t, *J* = 7.9 Hz, 1H, ArH), 7.52 (d, *J* = 6.9 Hz, 1H, ArH), 7.44 (d, *J* = 6.2 Hz, 1H, ArH), 7.01–7.10 (m, 2H, ArH), 6.86–6.98 (m, 5H, ArH), 6.75–6.83 (m, 1H, ArH), 6.68 (t, *J* = 6.9 Hz, 1H, ArH), 6.42–6.52 (m, 3H, ArH), 6.04–6.10 (m, 1H, ArH), 5.82 (d, *J* = 8.3 Hz, 1H, ArH). $^{13}C\{^1H\}$ NMR (151 MHz, $CDCl_3$) δ: 169.1, 168.1, 156.0, 155.2, 153.9, 149.6, 144.7, 144.3, 142.3, 141.6, 138.4, 137.0, 136.9, 133.1, 132.1, 131.9, 131.7, 131.5, 131.2, 130.3, 130.0, 129.8, 129.0, 128.9, 127.8, 127.5, 126.9, 126.8, 126.2, 126.1, 122.9, 122.6, 121.7, 121.5, 121.2, 119.1, 118.7, 114.6, 110.2, 108.5. Anal. Calcd for $C_{46}H_{28}N_9Ir$: C, 61.46; H, 3.14; N, 14.02. Found: C, 60.99; H, 3.18; N, 14.04.

3.4.4 X-ray crystallography details.

Single crystals of **32c, 32d′, 33a, 33c, 33d, 33e, 34a,** and **35a** were grown by layering concentrated CH_2Cl_2 solutions with pentane or diffusing pentane into concentrated ethyl

acetate solution. Crystals were mounted on a Bruker Apex II three-circle diffractometer using MoKα radiation (λ = 0.71073 Å), conducted by Prof.Teets. The data were collected at 123(2) K and was processed and refined within the APEXII software. Structures were solved by direct methods in SHELXS and refined by standard difference Fourier techniques in the program SHELXL.[78] Hydrogen atoms were placed in calculated positions using the standard riding model and refined isotropically. All non-hydrogen atoms were refined anisotropically.

4 Chapter Four Azo-triazolide Bis-cyclometalated Ir(III) Complexes via Cyclization of 3-Cyanodiarylformazanate Ligands

Reproduced from Ref. 58 with permission from the Royal Society of Chemistry.

4.1 Introduction

1,2,3-triazoles, a class of five-membered heterocyclic aromatic molecules containing three consecutive nitrogen atoms, have been attractive units over the past few decades, and continue to be developed further today.[119–121] The synthetic chemistry of these organic molecules has been explored in considerable detail, with the well-known copper-catalyzed azide-alkyne Huisgen cycloaddition,[122] the most popular of all "click" reactions, being the most widespread and enabling method for the construction of 1,2,3-triazole substructures. These compounds have been applied in energetic materials[121,123–125] and also work as the core structures in a large variety of compounds with pharmaceutical applications,[126–130] because of their high resistance to metabolic degradation and ability to hydrogen bond with biomolecules.

The ease of synthesis of a wide range of 1,2,3-triazole-based compounds, as well as the ability to include a variety of functional groups into the triazole core[131–135] have led to a rich metal coordination chemistry for triazoles.[136–139] The nitrogen-rich heterocycle can coordinate to metals in a variety of ways, and chelating ligands can be accessed by appending another donor group as a substituent. Deprotonation or C–H activation at the 5-position may allow access to anionic triazolides,[140,141] while alkylation at the N–3 position, followed by deprotonation of this relatively acidic C–H bond, leads to the formation of abnormal

mesoionic carbenes.[142–144] As representative examples of 1,2,3-triazolide metal complexes, Straub and co-workers have isolated a copper triazolide complex which has been crystallographically characterized,[145] Swager and co-workers have reported a method for the one-pot synthesis of tris-cyclometalated iridium triazolide complexes,[146] and Gray's group has reported extensively on gold triazolides formed under similar conditions as the typical Huisgen cycloaddition route.[147–149]

Despite the rich organic and coordination chemistry of 1,2,3-triazoles summarized above, some challenges remain in further diversifying this class of ligands. Nitrogen substituents in most click-derived 1,2,3-triazole ligands are limited to the N1 or N3 position,[131,142,150–152] and while there are successful synthetic routes for preparing 2-substituted 1,2,3-triazoles,[128,134,153–156] these structures remain rare in coordination compounds.[128,157] In addition, although arylazo moieties are ubiquitous in many chelating redox-active ligands,[158] the azo-triazole ligand class has not been disclosed, presumably due to the incompatibility of copper-catalyzed Huisgen cycloadditions with azo functionalities and the observation that the azo-substituted triazoles that have been prepared are energetic materials.[121,123,150]

These observations motivate continued pursuit of alternative methods for preparing N2-substituted azo-1,2,3-triazole complexes, to access chelating ligands that are not available by the typical click chemistry routes. Such an effort would require investigating alternative precursors for these ligands and exploring new reaction conditions that could allow their formation on a wider range of platforms. In this chapter, we show that 2-aryl-4-arylazo-1,2,3-triazolide bis-cyclometalated Ir(III) complexes, which were not accessible using Cu(I)-catalyzed "click" reactions, can instead be prepared from 3-cyanodiarylformazan precursors.

Formazanates, the monoanionic form of formazans, feature a NNCNN backbone and the two more nitrogen atoms provide formazanates with more accessible redox properties and strong absorption due to the more stabilized LUMOs compared with β-diketiminates. The coordination chemistry of formazanates with many main group metals[34,37,40,72,95,159] and first- and second-row transition metals[25,49,89,91] have been established, and we have expanded the coordination chemistry of formazanates to third-row transition metals with a series of heteroleptic platinum complexes and bis-cyclometalated iridium complexes.[54,55,57] Recent work has also been progressed to characterize the chemical reactivity of formazans, where reduction of formazanate complexes is sometimes accompanied by structural rearrangements and we reported recently a suite of rare derivatives, homoleptic platinum azo-iminate complexes via hydrogenative cleavage of formazans.[56] The new mode of reactivity described here, which involves templated, cyclization of 3-cyanodiarylformazanate to form 2-aryl-4-arylazo-1,2,3-triazolide, an unprecedented isomer of formazanate, further highlights the redox and chemical reactivity of formazanates and gives access to a new class of compounds. This reaction is not general for diarylformazanates and the products in most cases are still cyclometalated Ir(III) "open" form formazanate complexes, which is accord with the work we reported in chapter three. However, with enhancement of steric effect from both cyclometalated(C^N) ligands and N-aryl substituents of formazanates, 2-aryl-4-arylazo-1,2,3-triazolide Ir(III) complexes are prepared. We prepared two 2-aryl-4-arylazo-1,2,3-triazolide Ir(III) complexes and five relevant cyclometalated Ir(III) "open" form formazanate complexes in this study. Both 2-aryl-4-arylazo-1,2,3-triazolide complexes and one formazanate compound are structurally characterized by single-crystal X-ray diffraction and the rest are

determined by Infrared spectroscopy. All the compounds are interrogated by cyclic voltammetry and UV-vis absorption spectroscopy for their different molecular and electronic structures. The cyclization of formazanates and the different coordination mode exhibits similar ligand-centered reduction behaviors with formazanate complexes, which is influenced mainly by substitution on formazanates/4-azo-1,2,3-triazolide and C^N ligands, but a strong anodic shift on oxidation potentials and display a much larger ligand-center HOMO–LUMO gap, which, in part, accounts for a significant blue shift of major peaks in absorption and offers an insight into the inevitable electronic structure difference.

4.2 Results and discussion

4.2.1 Synthesis

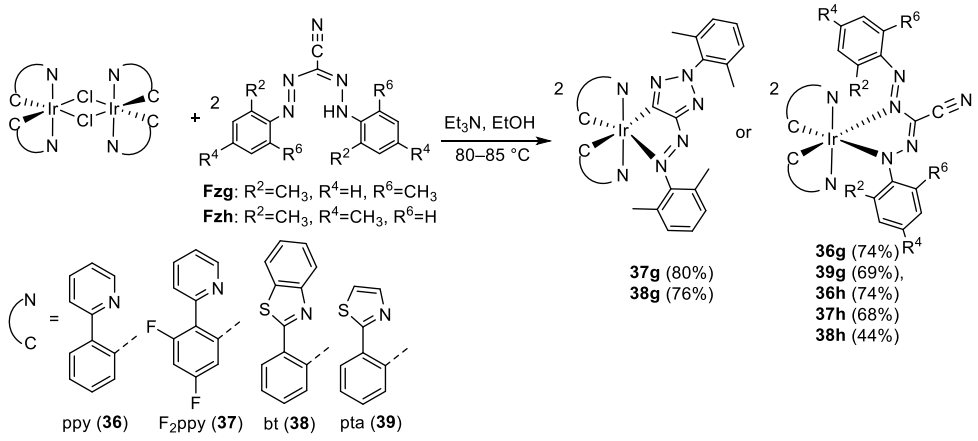

Scheme 4.1 General synthesis of complexes **37g**–**39g** and **36h**–**38h**.

Scheme 4.1 depicts the reaction conditions used to prepare the compounds described in this work. Compounds are numbered based on the identity of the cyclometalating ligand, with letters representing the two different formazan structures. Our previous work on cyclometalated iridium formazanate complexes[57] revealed two formazanate chelating modes

on these complexes, one the typical six-member chelate involving the 1- and 5-positions of the formazan core, the other a five-member chelate involving the 1- and 4-positions. With an effort to further understand the structural preferences, we began investigating the more sterically encumbered formazan **Fzg**, which has 2,6-dimethylphenyl groups as the *N*-aryl substituents. Our hypothesis was that the increased steric bulk would result in exclusive formation of the five-member chelate isomer, since that binding mode relieves steric crowding between the *N*-aryl ring and the cyclometalated aryl.

We initially treated the chloro-bridged dimers $[Ir(C\text{^}N)_2(\mu\text{-}Cl)]_2$, where C^N is the cyclometalating ligand 2-phenylpyridine (ppy) or 2-(2,4-difluorophenyl)pyridine (F_2ppy), with stoichiometric amounts of **Fzg** in refluxing ethanol with excess triethylamine. Both of these reactions gave high yields of products with ^{1}H and $^{13}\{C\}$ NMR spectra consistent with C_1-symmetric complexes, but close inspection of the NMR spectra show some key differences. Unlike product **36g** (Figure S53 and S54), product **37g** only has 3 CH_3 resonances in its ^{1}H and $^{13}C\{^1H\}$ NMR spectra (Figure S55 and S57), consistent with free rotation of one of the 2,6-dimethylphenyl rings. In addition, the $^{13}C\{^1H\}$ NMR spectrum of **37g** includes a downfield resonance at 179.0 ppm not present in **36g**, and the characteristic C≡N stretching frequency in the IR spectrum, which occurs at 2206 cm^{-1} in complex **36g**, is completely absent in complex **37g**. As unequivocally established by X-ray crystallography (see below), complex **36g** is the usual five-member chelate iridium formazanate complex, whereas **37g** is a cyclized arylazo-triazolide complex. Cyclization in **37g** (C^N = F_2ppy) but not in **36g** (C^N = ppy) suggests electronic effects may be important. To investigate steric effects in the cyclization reaction, we explored modifications to both the cyclometalating and

formazanate ligands. First, the formazan **Fzg** was paired with two different cyclometalating ligands, 2-phenylbenzothiazole (bt) and 2-phenylthiazole (pta), which on the basis of electrochemistry are very similar, but sterically are quite different on account of the fused benzo in bt, which "hangs over" the cleft where the formazanate ancillary ligand binds. Spectroscopic and crystallographic analysis clearly indicate that cyclization of the formazanate to the triazolide occurs in the more sterically encumbered complex **38g**, but in **39g** the formazanate does not cyclize, suggesting that cyclization is preferred in a more crowded steric environment. Finally, the isomeric formazan **Fzh**, with 2,4-dimethylphenyl substituents, was also subjected to the same reaction conditions. **Fzh** was partnered with the three C^N ligands ppy, F_2ppy, and bt, and in all cases only the formazanate products were obtained, **36h–38h**. All three of these products give a characteristic C≡N stretching band in their IR spectra (Table 4.1), and the downfield $^{13}C\{^1H\}$ NMR signal attributed to the triazolide is absent in each case. Thus, by relieving steric pressure in the formazan ligand, only the uncyclized formazanate products were obtained. The related NMR data are shown in Figure S51–S68 in appendix.

Table 4.1 IR spectra data of complexes.

Compound	ν(CN)/ cm^{-1}	ν(NH)/ cm^{-1}	Other transitions, ν cm^{-1}
36g	2206	N.A.	1608(m), 1479, 1214
37g	N.A.	N.A.	1597(m), 1474(m), 1289(m)
38g	N.A.	N.A.	1582(m), 1434(m), 1295(m)
39g	2207	N.A.	1582, 1438, 1216
36h	2202	N.A.	1607(m), 1476, 1224(m)
37h	2213	N.A.	1738, 1601(m), 1402, 1228(m)
38h	2205	N.A.	1581(m), 1406(m), 1223(m)
Fzg	2219(m)	3313	1525, 1281(m)
Fzh	2222	3332	1527, 1277(m)

4.2.2 X-ray crystallography

The structures of complexes **36g**, **37g** and **38g** were confirmed by single-crystal X-ray diffraction, and are shown in Figure 4.1. Bond lengths and bond angles of both azo-triazolide complexes summarized in Table 4.2, with refinement data is summarized in Table 4.3. As is usually the case for bis-cyclometalated iridium complexes, the nitrogen atoms of the two C^N ligands are trans to one another, and all three complexes have very similar bond metrics associated with the C^N ligands, namely the Ir–C_{C^N} and Ir–N_{C^N} bond distances (2.012(5)–2.086(2) Å) as well as the C^N chelate angles, which span from 78.19(8)° to 80.01(13)°.

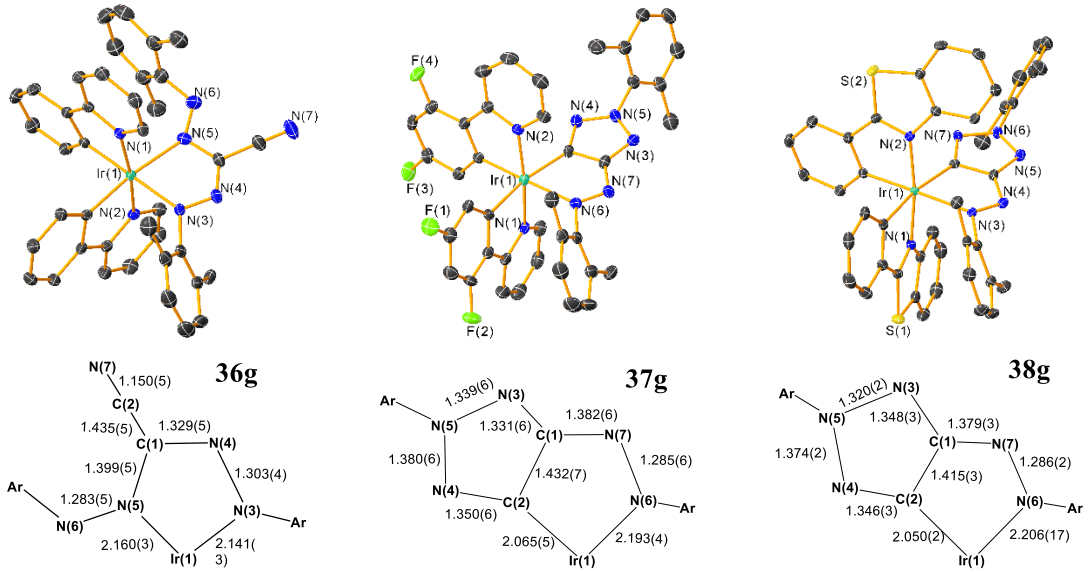

Figure 4.1 X-ray crystal structure of complexes **36g**, **37g** and **38g**, with ellipsoids shown at the 50% probability level and hydrogen atoms omitted. The bottom stick diagrams show bond lengths in Å, with esd values in parentheses.

Formazanate complex **36g** has a structure reminiscent of several other "open" form cyclometalated iridium complexes recently reported by our group.[57] Like these previous examples, for complex **36g** the π electrons on the formazanate backbone are primarily localized on the C1–N4 and N5–N6 bonds, significantly shorter than the C1–N5 and N3–N4

bonds. Similarly, in complexes **37g** and **38g**, the N6–N7 azo bond distances (1.285(6) Å and 1.286(2) Å, respectively), suggest a non-radical azo group. In the 1,2,3-triazolide ring, the C1–N3 (1.331(6) Å and 1.348(3) Å) and C2–N4 (1.350(6) Å and 1.346(3) Å) distances are consistent with imine-like C=N double-bond character, whereas the N4–N5 distances are closer to N–N single-bond distances, suggesting the π electrons are not fully delocalized over the five-membered aromatic ring.

Table 4.2 Summary of crystallographic bond lengths (Å) and angles (deg) for complex **37g** and **38g**.

	37g	**38g**
d (Ir–N6)	2.193(4)	2.206(17)
d (Ir–C2)	2.065(5)	2.050(2)
d (N6–N7)	1.285(6)	1.286(2)
d (N7–C1)	1.382(6)	1.379(3)
d (C1–C2)	1.432(7)	1.415(3)
d (C1–N3)	1.331(6)	1.348(3)
d (C2–N4)	1.350(6)	1.346(3)
d (N3–N5)	1.339(6)	1.320(2)
d (N4–N5)	1.380(6)	1.374(2)
∠C2–Ir–N6	75.53(17)	74.91(7)

Table 4.3 Crystallographic summary of complexes **36g**, **37g** and **38g**.

	36g·2$CHCl_3$	**37g**	**38g**
Crystal data			
Chemical formula	$C_{42}H_{36}Cl_6IrN_7$	$C_{40}H_{30}F_4IrN_7$	$C_{44}H_{34}IrN_7S_2$
M_r	1043.68	876.91	917.10
Crystal system, space group	Monoclinic, $P2_1/c$	Triclinic, $P\bar{1}$	Monoclinic, $P2_1/n$
a, b, c (Å)	16.837 (3), 17.611 (3), 14.610 (3)	9.724 (4), 12.386 (5), 15.409 (6)	15.0406 (11), 13.7393 (10), 18.9988 (14)
α, β, γ (°)	90, 108.390 (2), 90	83.506 (4), 86.618 (4), 67.247 (3)	90, 105.613 (1), 90
V (Å^3)	4110.9 (14)	1700.2 (11)	3781.2 (5)
Z	4	2	4
μ (mm^{-1})	3.68	3.99	3.68
Crystal size (mm)	0.40 × 0.28 × 0.10	0.23 × 0.16 × 0.07	0.37 × 0.29 × 0.15
Data collection			
T_{min}, T_{max}	0.521, 0.746	0.416, 0.746	0.553, 0.746
No. of measured, independent and observed [$I > 2\sigma(I)$] reflections	25545, 9473, 8663	22822, 7662, 6820	23405, 8759, 7783
R_{int}	0.026	0.050	0.027
$(\sin\theta/\lambda)_{max}$ (Å^{-1})	0.651	0.648	0.652
Refinement			
$R[F^2 > 2\sigma(F^2)]$, $wR(F^2)$, S	0.031, 0.088, 1.05	0.039, 0.089, 1.05	0.021, 0.047, 1.05
No. of reflections	9473	7662	8759
No. of parameters	528	473	491
No. of restraints	78	0	0
	$w = 1/[\sigma^2(F_o^2) + (0.0481P)^2 + 10.8851P]$ where $P = (F_o^2 + 2F_c^2)/3$	$w = 1/[\sigma^2(F_o^2) + 11.079P]$ where $P = (F_o^2 + 2F_c^2)/3$	$w = 1/[\sigma^2(F_o^2) + (0.0202P)^2]$ where $P = (F_o^2 + 2F_c^2)/3$
$\Delta\rho_{max}$, $\Delta\rho_{min}$ (e Å^{-3})	2.07, -1.44	3.27, -2.97	0.67, -0.83

4.2.3 UV-vis absorption spectroscopy

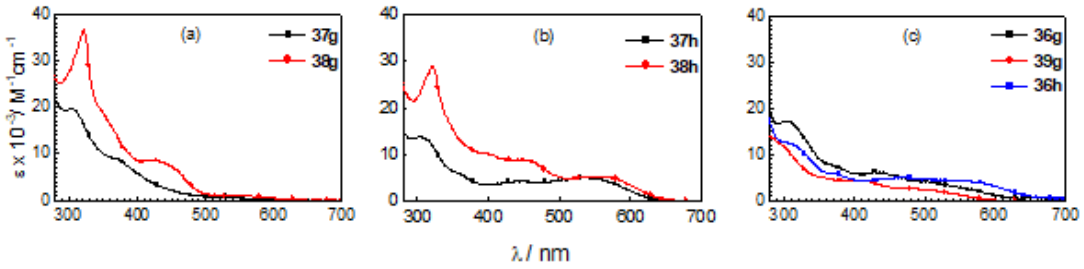

Figure 4.2 Overlaid electronic absorption spectra of (a) triazolide complexes **37g** and **38g**, (b) analogous **Fzh** complexes **37h** and **38h**, and (c) the remaining formazanate complexes **36g**, **39g**, and **36h**. Spectra were recorded in tetrahydrofuran (THF) solution at room temperature. Data was collected in intervals of 1 nm, and symbols are included on each plot are to help distinguish the overlaid spectra.

The colors of the triazolide and formazanate complexes are visually distinguishable, with triazolides **37g** & **38g** exhibiting a dark orange color in solution while the other formazanate complexes are dark red or purple in solution, similar to the free formazans. UV-vis spectra for the complexes are shown in Figure 4.2, with a summary of the data in Table 4.4. The plots in Figure 4.2 are arranged to easily discern differences between the triazolide complexes and the related formazanate complexes. Figure 4.2a shows the two triazolide complexes **37g** and **38g**, and the analogous **Fzh** complexes **37h** and **38h**, which have the same C^N ligands, are shown directly in the middle in Figure 4.2b. The spectra of the remaining three formazanate complexes are overlaid in Figure 4.2c.

In addition to intense peaks in the UV ($\lambda < 350$ nm) attributed to localized $\pi \rightarrow \pi^*$ transitions of the aryl substituents from both C^N and formazanate/4-azo-1,2,3-triazolide ligands, a notable absorption between 480 nm and 600 nm stands out among the 3-cyanodiarylformazanate complexes, which is assigned as a $\pi \rightarrow \pi^*$ within formazanate

framework with minimal Ir(d)→π* metal-to-ligand-charge transfer (MLCT), in accord with the diarylformazanate Ir(III) complexes we reported recently.[57] All formazanate complexes

Table 4.4 Summary of UV-vis absorption data recoeded in THF at room temperature.

	λ/ nm (ε × 10^{-3} / $M^{-1}cm^{-1}$)
36g	305 (18), 434 (6.2)
37g	306 (20), 369 (sh) (8.9)
38g	321 (37), 430 (8.4)
39g	413 (4.4), 509 (sh) (2.3)
36h	309 (sh) (12), 469 (5.0), 542 (sh) (4.2)
37h	306 (14), 439 (4.3), 536 (5.0)
38h	321 (29), 402 (sh) (10), 453 (8.9), 557 (5.4)

show significant visible absorption, and two overlapping visible absorption bands. That said, in **Fzh** complexes the low-energy band (between 536 and 557 nm) is more pronounced and has a discernible maximum, compared to **Fzg** complexes where the low-energy band is an ill-defined shoulder. The differences in visible absorption profile between **Fzg** and **Fzh** complexes may be due to the lager steric profile of **Fzg**, which hinders the rotation of the aryl substituents and decreases the conjugation between the formazanate backbone and the aryl rings. That said, while the absorption profiles are only subtly different for **Fzg** and **Fzh** complexes, there are large differences observed for triazolide complexes **37g** and **38g**. In these complexes there is comparatively little visible absorption, with multiple overlapping bands blue and near-UV regions, 380–430 nm. The absorption profile of F_2ppy complex **37g** does tail to longer wavelengths than is often observed for other neutral bis-cyclometalated iridium complexes with the same cyclometalating ligand,[160,161] suggesting some visible

absorption of the azo-triazolide ancillary ligand, but it is clear that the formazanates are much stronger visible chromophores than their triazolide isomers. UV-vis spectra were also recorded in three solvents of varying polarity (toluene, THF, and MeOH), and only small spectral differences (<10 nm) are observed in the different solvents, which indicates very minimal charge-transfer character in the UV-vis absorption bands.

4.2.4 Electrochemistry

The redox properties of all the complexes were evaluated by cyclic voltammetry, with overlaid votammograms shown in Figure 4.3 and redox potentials summarized in Table 4.5. Each complex shows one oxidation and one reduction feature within the accessible electrochemical window. In all cases the reduction peaks are electrochemically reversible and oxidation waves are mostly reversible, although in some cases the ratio of the cathodic return current to the anodic current ($i_{p,c}/i_{p,a}$) is less than 1, indicating the features are not completely reversible. This is most clearly apparent in **38g**, where an additional cathodic wave is observed on the return sweep after oxidation, and in **36g** and **39g** where the oxidation is clearly not fully reversible. The potentials of all redox events are responsive to the substitution pattern of C^N and formazanate/azo-triazolide ligands, such that complexes with electron withdrawing groups are easier to reduce but harder to oxidize than the congeners with electron donating groups. For example, replacing the ppy C^N ligand in **36h** with a F_2ppy ligand in **37h** results in a 180 mV anodic shift of the reduction wave and a 220 mV shift of the oxidation wave, owing to the electron-withdrawing effect of the fluorine atoms in F_2ppy.

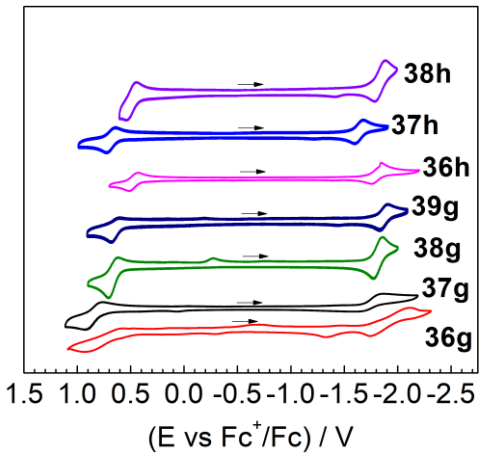

Figure 4.3 Overlaid cyclic voltammograms of complexes **36g**–**39g**, **36h**–**38h**. CVs were recorded in CH_2Cl_2 with 0.1 M NBu_4PF_6 supporting electrolyte, using a glassy carbon working electrode and a scan rate of 0.1 V/s. The arrows indicate the scan direction.

The separation between the reduction and oxidation potentials for the formazanate complexes, i.e., the electrochemical HOMO–LUMO gap, does seem to depend on the structure of the formazanate. Complexes of **Fzg** exhibit separations of 2.51 V (**36g**) and 2.49 V (**39g**), whereas those for **Fzh** complexes are significantly smaller and span a narrow range of 2.28–2.33 V. Consistent with this observation, as noted above **Fzh** complexes have low-energy absorption bands, likely HOMO→LUMO in nature, which are red-shifted compared to the **Fzg** complexes. For triazolide complexes **37g** and **38g** the electrochemical features are not drastically different than the formazanate complexes. The reduction potentials are quite similar, whereas the oxidation potentials are slightly more positive than the potentials for the respective **Fzh** complexes that have the same C^N ligands (**37h** and **38h**). The electrochemical HOMO–LUMO gaps in the triazolide complexes all fall in the range spanned by the formazanate complexes, suggesting that the frontier orbital energies of the azo-triazolide complexes are not substantially different from their formazanate relatives, even though the UV-vis absorption spectra are markedly different (Figure 4.2).

Table 4.5 Summary of electrochemical data of complexes **36g**–**39g**, **36h**–**38h**.

	E^{ox} (V)	E^{red} (V)
36g	+0.66	−1.85
37g	+0.84	−1.76
38g	+0.66	−1.82
39g	+0.61	−1.88
36h	+0.46	−1.82
37h	+0.68	−1.64
38h	+0.49	−1.84

Although the redox potentials of the complexes described here fall into a relatively narrow range, owing to the rather similar substituent patterns of the formazanate and azo-triazolide ligands, we can make tentative electrochemical assignments based on analogies with other cyclometalated iridium complexes, with and without formazanate ancillary ligands. The complexes described here have similar reduction potentials to cyclometalated iridium formazanate complexes[57] and are all significantly easier to reduce than bis-cyclometalated iridium complexes where the LUMO resides on the C^N ligand,[162,163] suggesting that the first reduction occurs on the formazanate or azo-triazolide ancillary ligand. This observation indicates that, like formazanates, the isomeric azo-triazolides introduced here are also redox-active. Assignment of the oxidation waves is less clear from the data available here, and likely involves a HOMO that is delocalized with mixed contribution from Ir, the C^N ligand, and the formazanate/azo-triazolide ancillary ligand. We do note that in more electronically diverse iridium formazanate complexes we prepared previously, the oxidation potential was quite sensitive to the formazanate substitution, suggesting the HOMO has significant contribution from the formazanate. That said, the potentials of the complexes described here are not atypical for neutral bis-cyclometalated iridium complexes and are quite responsive to

fluorination of the C^N ligand (see **37g** and **37h** in Table 4.5), so it is likely that the HOMO in these compounds also includes significant Ir-aryl character, as is normal for cyclometalated iridium complexes.[113] We also characterized the redox behaviors of all the complexes in an extended scan window. For all the complexes, additional irreversible oxidation peaks were observed, and in most cases oxidation by >1 electron results in the first oxidation also becoming irreversible. Additional reduction peaks were observed only in complexes **36h** and **37h**. For other complexes, no additional reduction peak was detected within the dichloromethane solvent window.

4.2.5 DFT calculations

Molecular geometries for four compounds related to this study were optimized in the gas phase, using the B3LYP-D3 functional with 6-311G(d,p) basis set for non-metal atoms and SDD basis set for Ir. Chart 4.1 shows the structures of these four compounds. The computed compounds are $Ir(ppy)_2$(**Fzg**) (**36g**) and its unobserved triazolide analogue **36g′**, and triazolide compound **37g** and the unobserved formazate analogue $Ir(F_2ppy)_2$(**Fzg**) (**37g′**). For **36g** and **37g**, the optimized geometries are a good match for the crystal structures, with very similar bond lengths, bond angles, and ligand conformations observed. For unobserved products **36g′** and **37g′**, the structural metrics are in line with the other characterized triazolide and formazanate complexes. In the gas phase, DFT predicts that in both cases the uncyclized formazanate isomer is the more stable species, by ~13 kcal/mol in each case. This result is consistent with the outcome when C^N = ppy, where formazanate complex **36g** is observed as the exclusive product but is at odds with the outcome when C^N = F_2ppy. Since DFT optimizations were run in the gas phase we also did a single-point calculation with implicit

EtOH solvation, the solvent used during synthesis, and the energy landscape was not significantly altered. It is unclear why the identity of the cyclometalating ligand, in particular when changing from ppy to F_2ppy, has such a dramatic effect on the selectivity for formazanate versus triazolide forms.

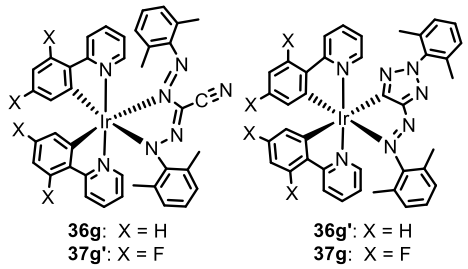

Chart 4.1 Structures of compounds evaluated by DFT method

In spite of the lack of clarity with regards to product selectivity, DFT results give a clear picture of the electronic structure and are consistent with the CV and UV-vis spectroscopic measurements described above. Figure 4.4 summarizes some of the key DFT results, showing frontier orbital energies for both **36g** and **37g**. In addition, TD-DFT, calculated using the TD-M06-2X functional with the same atomic basis sets, was used to compute the lowest-energy UV-vis transition. TD-DFT results, showing the computed transition wavelengths and the orbitals that constitute the major one-electron transition for each excited state, are also summarized in Figure 4.4. CV results described above predicted rather similar frontier orbital energies and HOMO–LUMO gaps for **36g** and **37g**, trends that are reproduced well by DFT. The experimentally determined HOMO–LUMO gaps for **37g** is <0.1 eV larger than **36g**, and DFT calculations predict that the HOMO–LUMO gap for **27g** is slightly smaller, by 0.02 eV. The frontier orbitals for both **36g** and **37g** are primarily ligand-centered π and π^* orbitals residing on the formazanate or triazolide ligand.

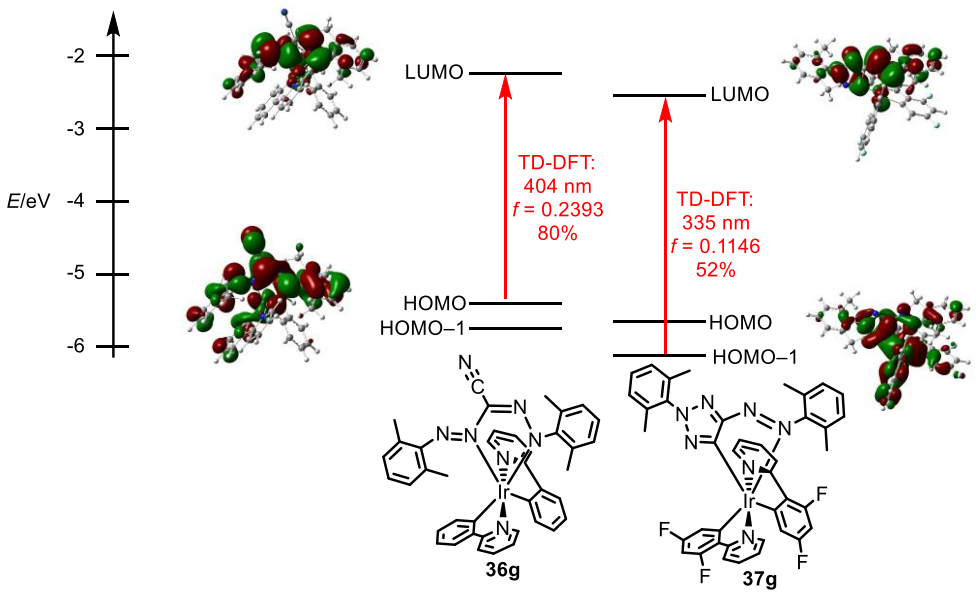

Figure 4.4 Summary of DFT results for complexes **36g** and **37g**. The chemical structures show the orientation of the molecules in the orbital contour plots, with a "front-facing" orientation of the formazanate or triazolide ligand. Frontier orbital energies are indicated, and the red arrow shows the transition that is the major contributor to the lowest-energy singlet state, with the computed wavelength and oscillator strength shown. The percent contribution of that one-electron transition to the excited state is also shown, and contour plots (0.3 au) depict the orbitals that are principally involved, HOMO and LUMO for **36g**, HOMO−1 and LUMO for **37g**.

Both experiment and theory are consistent with the idea that **36g** and **37g** have very similar HOMO–LUMO gaps, but in spite of this similarity the UV-vis spectra (Figure 4.2) are quite different, with **36g** having strong visible absorption and **37g** absorbing primarily UV and blue regions. This disparity is clearly explained by the TD-DFT results. In both compounds, the lowest-energy electronic transition involves substantial configuration interaction, but for **36g** the transition occurs in the visible region (λ = 404 nm) that has 80% HOMO→LUMO character, and thus is primarily an intraligand π→π* transition. In contrast, for **37g** the lowest-energy transition occurs at much shorter wavelength (λ = 335 nm) and has majority (HOMO−1)→LUMO character, and only 5% contribution from the HOMO→LUMO

transition. The (HOMO−1) orbital in **37g** involves contributions from both the triazolide and F_2ppy ligands, so the (HOMO−1)→LUMO transition can be described as having mixed intraligand and ligand-to-ligand charge transfer character. Thus, the frontier orbital energies are very similar for **36g** and **37g**, but the UV-vis transitions for these two isomers involve different frontier orbitals and thus occur in different parts of the spectrum.

4.3 Conclusion

In this work, we disclosed examples of 2-aryl-4-arylazo-2*H*-1,2,3-triazolide bis-cyclometalated iridium complexes, formed by cyclization of 3-cyano-1,5,-diarylformazanates. In most cases the typical reaction conditions left the formazanate ligand in its uncyclized form, but steric effects on both the formazanate ligand and the cyclometalating ligand appear to be important for driving the cyclization to the azo-triazolide. The two distinct ligand structures are discernible spectroscopically and unequivocally established by single-crystal X-ray diffraction. A systematic comparison of different C^N and formazanate/4-azo-1,2,3-triazolide ligands reveals that the redox potentials are rather similar within the series of compounds, although the UV-vis absorption profiles are distinct and the triazolide complexes have much less pronounced visible absorption, due to the predominance of (HOMO−1)→LUMO transitions in these complexes versus HOMO→LUMO transitions in the formazanate isomer. In future work we aim to develop a more general route for this new 4-azo-1,2,3-triazolide ligand class and expand the coordination chemistry to other late transition metals, like Ru and Re.

4.4 Experimental section

4.4.1 Materials

Reactions were carried out in a nitrogen atmosphere using standard Schlenk techniques. Solvents, starting materials, and reagents were of commercial origin and used without further purification unless stated otherwise below. Tetrahydrofuran (THF), methanol (MeOH), and toluene for UV-vis spectroscopy, and dichloromethane (DCM) for electrochemical measurements were dried by the method of Grubbs, passing through dual alumina columns on a commercial solvent purification system (SPS). Tetrabutylammonium hexafluorophosphate ($TBAPF_6$) was recrystallized from hot ethanol and ferrocene was sublimed at ambient pressure before use in electrochemical experiments. $CDCl_3$ and CD_3CN for NMR spectroscopy were stored over potassium carbonate and molecular sieves to remove acidic impurities and moisture. The ligand 3-cyano-1,5-bis(2,6-dimethylphenyl)formazan (**Fzg**) was prepared by following the literature procedures[19] and 3-cyano-1,5-bis(2,4-dimethylphenyl)formazan (**Fzh**) was prepared by a modified version described below. The iridium precursors $[Ir(ppy)_2(\mu\text{-}Cl)]_2$ (ppy = 2-phenylpyridine), $[Ir(F_2ppy)_2(\mu\text{-}Cl)]_2$ (F_2ppy = 2-(2,4-difluorophenyl)pyridine), $[Ir(bt)_2(\mu\text{-}Cl)]_2$ (bt = 2-phenylbenzothiazole), and $[Ir(pta)_2(\mu\text{-}Cl)]_2$ (pta = 2-phenylthiazole) were prepared by a modified version of the well-known Nonoyama procedure.[117,118]

4.4.2 Physical methods

NMR spectra were recorded at room temperature using a JEOL ECA-600, ECA-500, or ECA-400 NMR spectrometer and are shown in appendix. Infrared (IR) spectra were measured

using a Thermo Nicolet Avatar FT-IR spectrometer with diamond ATR. UV-vis absorption spectra were recorded in THF, toluene, and MeOH solutions in screw-capped 1 cm quartz cuvettes using an Agilent Cary 8454 UV-vis spectrophotometer. Cyclic voltammetry (CV) measurements were performed with a CH Instruments 602E potentiostat interfaced with a nitrogen glovebox via wire feedthroughs. Samples were dissolved in dichloromethane (CH_2Cl_2) with 0.1 M $TBAPF_6$ as a supporting electrolyte. A 3 mm diameter glassy carbon working electrode, a platinum wire counter electrode, and a silver wire pseudo-reference electrode were used. Potentials were referenced to an internal standard of ferrocene. The bulk purity for all complexes is established by elemental analysis, performed by Atlantic Microlab, Inc.

4.4.3 Synthesis of compounds

Ligand Fzh. The title compound was prepared by a modified version of the literature procedures used for related formazanate ligands.[19] Sodium nitrite (3.0 g, 0.043 mol) was added to a solution of 2,4-dimethylaniline (4.9 mL, 0.040 mmol), 12 M concentrated hydrochloric acid (10 mL) and water (10 mL) at −5 °C in small portions over a 10 min period. After 15 min of stirring, the mixture was added to a second solution containing cyanoacetic acid (1.7 g, 0.020 mmol), sodium hydroxide (8.0 g, 0.20 mmol), and water (100 mL) at 0 °C over a 30 min period. The reaction completion was confirmed by TLC. The resulting dark red organic layer obtained after biphasic extraction from dichloromethane/water was dehydrEd by $MgSO_4$ and concentrated to dryness. The crude product was purified via column chromatography (neutral alumina stationary phase and dichloromethane eluent), and the eluate was concentrated in vacuo to afford **Fzh** as dark red solid. Yield: 1.3 g (21%). ^{1}H NMR

(400 MHz, $CDCl_3$): δ 12.22 (s, 1H, NH), 7.58 (d, J = 8.1 Hz, 2H, ArH), 7.10 (d, J = 8.8 Hz, 4H, ArH), 2.50 (s, 6H, CH_3), 2.35 (s, 6H, CH_3). ^{13}C NMR (151 MHz, $CDCl_3$): δ 143.0, 139.4, 132.0, 131.7, 128.1, 126.5, 115.9, 114.6, 21.3, 17.7. FT-IR: 3332 (ν_{NH}), 2222 (ν_{CN}), 1527, 1277(m) cm^{-1}. Anal. Calcd for $C_{18}H_{19}N_5$: C, 70.80, H, 6.27, N, 22.93. Found: C, 70.85, H, 6.13, N, 23.02.

Complex 36g. $[Ir(ppy)_2(\mu\text{-}Cl)]_2$ (54 mg, 0.050 mmol) and **Fzg** (30 mg, 0.10 mmol) were combined in ethanol (10 mL) with excess triethylamine (0.1 mL), and the mixture was deoxygenated under the protection of N_2. The mixture was refluxed for 36 h. A red precipitate was observed at the bottom of the flask after the reaction was completed. Solvent was removed by filtration, and the solid was re-crystalized from CH_2Cl_2 and pentane to purify the product, which was crystallized again by vapor diffusion of pentane into a concentrated $CHCl_3$ solution. Yield: 65 mg (74%). ^{1}H NMR (500 MHz, $CDCl_3$): δ 8.53 (d, J = 4.7 Hz, 1H, ArH), 8.39 (d, J = 4.7 Hz, 1H, ArH), 7.81 (t, J = 7.6 Hz, 1H, ArH), 7.75 (t, J = 7.5 Hz, 1H, ArH), 7.68 (d, J = 8.1 Hz, 1H, ArH), 7.54 (d, J = 8.1 Hz, 1H, ArH), 7.13 (d, J = 6.6 Hz, 3H, ArH), 6.96 (d, J = 7.4 Hz, 1H, ArH), 6.67 (t, J = 7.2 Hz, 1H, ArH), 6.61–6.52 (m, 2H, ArH), 6.52–6.43 (m, 2H, ArH), 6.43–6.34 (m, 3H, ArH), 6.29 (d, J = 7.2 Hz, 1H, ArH), 6.21 (d, J = 7.1 Hz, 1H, ArH), 5.85 (d, J = 7.5 Hz, 1H, ArH), 5.76 (d, J = 7.4 Hz, 1H, ArH), 2.14 (s, 3H, CH_3), 1.99 (s, 3H, CH_3), 1.36 (s, 3H, CH_3), 1.11 (s, 3H, CH_3). ^{13}C NMR (151 MHz, $CDCl_3$): δ 169.8, 167.8, 152.7, 152.6, 152.3, 149.6, 149.4, 146.7, 142.8, 142.4, 137.9, 137.7, 134.6, 132.8, 131.7, 131.3, 130.4, 129.1, 128.6, 128.5, 128.4, 128.2, 127.6, 126.9, 126.3, 126.2, 125.7, 124.3, 122.7, 122.1, 121.8, 121.5, 120.8, 119.3, 119.2, 116.2, 22.6, 20.0, 18.2, 16.9.

FT-IR: 2206 (ν_{CN}), 1608(m), 1479, 1214 cm^{-1}. Anal. Calcd for $C_{40}H_{34}N_7Ir$: C, 59.68, H, 4.26, N, 12.18. Found: C, 59.50, H, 4.37, N, 12.09.

Complex 37g. The title compound was prepared by the general method described above for complex **36g**, using $[Ir(F_2ppy)_2(\mu\text{-}Cl)]_2$ (61 mg, 0.050 mmol) and **Fzg** (30 mg, 0.10 mmol), being crystallized by vapor diffusion of pentane into concentrated ethyl acetate solution. Yield: 70 mg (80%). ^1H NMR (500 MHz, $CDCl_3$): δ 8.44 (d, J = 5.5 Hz, 1H, ArH), 8.25 (d, J = 8.4 Hz, 1H, ArH), 7.98 (d, J = 8.3 Hz, 1H, ArH), 7.86 (d, J = 5.6 Hz, 1H, ArH), 7.71 (dd, J = 16.6, 8.3 Hz, 2H, ArH), 7.22 (t, J = 7.5 Hz, 1H, ArH), 7.09 (d, J = 7.5 Hz, 2H, ArH), 6.95–6.87 (m, 2H, ArH), 6.85 (t, J = 6.5 Hz, 1H, ArH), 6.74 (d, J = 7.4 Hz, 1H, ArH), 6.65 (d, J = 7.2 Hz, 1H, ArH), 6.32 (t, J = 10.9 Hz, 1H, ArH), 6.19 (t, J = 10.7 Hz, 1H, ArH), 6.03 (d, J = 7.4 Hz, 1H, ArH), 5.57 (d, J = 9.3 Hz, 1H, ArH), 2.12 (s, 3H, CH_3), 1.92 (s, 6H, CH_3), 1.13 (s, 3H, CH_3). ^{19}F NMR (470 MHz, $CDCl_3$): δ −108.6 (s, 1F), −109.5 (s, 1F), −110.6 (s, 1F), −110.9 (s, 1F). ^{13}C NMR (151 MHz, $CDCl_3$): δ 179.0, 173.6, 172.7,170.0, 167.1, 164.3, 163.7, 162.1, 162.0, 155.1, 153.8, 150.6, 150.3, 140.3, 138.0, 136.7, 135.5, 130.8, 130.1, 129.6, 128.4, 128.2, 128.2, 128.1, 127.8, 126.3, 123.2, 122.9, 122.7, 120.5, 115.1, 111.7, 97.8, 96.9, 21.3, 17.5, 16.9. FT-IR 1597(m), 1474(m), 1289(m) cm^{-1}. Anal. Calcd for $C_{40}H_{30}N_7F_4Ir$: C, 54.79, H, 3.45, N, 11.18. Found: C, 54.98, H, 3.61, N, 10.94.

Complex 38g. The title compound was prepared by the general method described above for complex **36g**, using $[Ir(bt)_2(\mu\text{-}Cl)]_2$ (65 mg, 0.050 mmol) and **Fzg** (30 mg, 0.10 mmol), being crystallized by vapor diffusion of pentane into concentrated ethyl acetate solution. Yield: 70 mg (76%). ^1H NMR (600 MHz, $CDCl_3$): δ 7.78 (d, J = 7.9 Hz, 3H, ArH), 7.64 (d, J = 7.6 Hz, 1H, ArH), 7.34 (t, J = 7.5 Hz, 1H, ArH), 7.25 (t, J = 7.5 Hz, 1H, ArH), 7.20–7.10 (m, 4H,

ArH), 7.02 (d, J = 7.7 Hz, 3H, ArH), 6.87 (t, J = 7.3 Hz, 1H, ArH), 6.82–6.71 (m, 5H, ArH), 6.52 (t, J = 7.5 Hz, 1H, ArH), 6.44 (d, J = 7.2 Hz, 1H, ArH), 6.13 (d, J = 7.8 Hz, 1H, ArH), 2.02 (s, 3H, CH_3), 1.78 (s, 6H, CH_3), 0.98 (s, 3H, CH_3). ^{13}C NMR (151 MHz, $CDCl_3$): δ 183.2, 180.1, 178.4, 170.2, 169.7, 151.1, 150.5, 150.2, 149.9, 141.4, 140.4, 139.5, 138.4, 135.5, 134.3, 133.2, 131.5, 131.4, 131.0, 130.8, 130.5, 129.7, 129.4, 128.4, 128.2, 128.0, 127.8, 127.2, 126.22, 126.18, 125.6, 124.9, 124.1, 122.5, 122.2, 121.9, 120.7, 120.5, 23.2, 17.2, 17.0. FT-IR: 1582(m), 1434(m), 1295(m) cm^{-1}. Anal. Calcd for $C_{44}H_{34}N_7S_2Ir$: C, 57.62, H, 3.74, N, 10.69. Found: C, 57.72, H, 3.87, N, 10.44.

Complex 39g. The title compound was prepared by the general method described above for complex **36g**, using $[Ir(pta)_2(\mu\text{-}Cl)]_2$ (55 mg, 0.050 mmol) and **Fzg** (30 mg, 0.10 mmol). Yield: 56 mg (69%). ^{1}H NMR (500 MHz, $CDCl_3$): δ 7.74 (d, J = 3.3 Hz, 1H, ArH), 7.63 (d, J = 3.4 Hz, 1H, ArH), 7.38 (dd, J = 10.0, 3.3 Hz, 2H, ArH), 7.01 (d, J = 7.3 Hz, 1H, ArH), 6.97 (d, J = 7.6 Hz, 1H, ArH), 6.72 (t, J = 7.4 Hz, 1H, ArH), 6.67 (d, J = 7.4 Hz, 1H, ArH), 6.57 (t, J = 7.3 Hz, 1H, ArH), 6.54–6.42 (m, 5H, ArH), 6.39 (t, J = 7.5 Hz, 1H, ArH), 6.17 (d, J = 7.4 Hz, 1H, ArH), 5.91 (d, J = 7.6 Hz, 1H, ArH), 5.81 (d, J = 7.0 Hz, 1H, ArH), 2.10 (s, 3H, CH_3), 2.09 (s, 3H, CH_3), 1.45 (s, 3H, CH_3), 1.39 (s, 3H, CH_3). ^{13}C NMR (126 MHz, $CDCl_3$): δ 181.5, 179.4, 151.0, 149.4, 149.3, 145.7, 142.3, 142.2, 138.9, 138.7, 135.1, 132.6, 131.7, 131.5, 130.8, 129.3, 129.2, 128.5, 128.3, 128.1, 127.5, 126.9, 126.7, 126.5, 125.8, 124.7, 123.3, 122.1, 121.1, 117.3, 116.8, 115.9, 22.0, 19.8, 17.9, 17.2. FT-IR: 2207 (ν_{CN}), 1582, 1438, 1216. Anal. Calcd for $C_{36}H_{30}N_7S_2Ir$: C, 52.92, H, 3.70, N, 12.00. Found: C, 52.87, H, 3.91, N, 11.93.

Complex 36h. $[Ir(ppy)_2(\mu\text{-}Cl)]_2$ (54 mg, 0.050 mmol) and **Fzh** (30 mg, 0.10 mmol) were combined in ethanol (10 mL) with excess triethylamine (0.1 mL), and the mixture was deoxygenated under the protection of N_2. The mixture was refluxed for 36 h and the color changed from dark red to purple. The reaction completion was confirmed by TLC. Solvent was removed using rotary evaporation, and the product was re-dissolved in a minimum amount of ethyl acetate. After that column chromatography (hexane / ethyl acetate gradient eluent, neutral alumina) was performed to purify the product. Yield: 65 mg (74%). ^{1}H NMR (500 MHz, $CDCl_3$): δ 8.50 (d, J = 5.6 Hz, 1H, ArH), 8.41 (d, J = 5.6 Hz, 1H, ArH), 7.79 (t, J = 7.7 Hz, 1H, ArH), 7.73 (dd, J = 14.4, 7.8 Hz, 2H, ArH), 7.58 (d, J = 8.1 Hz, 1H, ArH), 7.13 (td, J = 13.2, 6.5 Hz, 3H, ArH), 7.06 (d, J = 7.3 Hz, 1H, ArH), 6.58 (dt, J = 14.8, 7.6 Hz, 4H, ArH), 6.43–6.35 (m, 3H, ArH), 6.32 (d, J = 8.1 Hz, 1H, ArH), 6.02 (d, J = 7.7 Hz, 1H, ArH), 5.91 (d, J = 7.8 Hz, 1H, ArH), 5.88 (d, J = 7.2 Hz, 1H, ArH), 5.81 (d, J = 7.6 Hz, 1H, ArH), 2.06 (s, 3H, CH_3), 1.99 (s, 3H, CH_3), 1.74 (s, 3H, CH_3), 1.60 (s, 3H, CH_3). ^{13}C NMR (151 MHz, $CDCl_3$) δ 169.1, 167.6, 155.4, 151.09, 151.06, 150.5, 148.9, 148.3, 148.0, 143.0, 142.2, 137.5, 137.3, 136.6, 134.8, 132.2, 131.2, 130.9, 130.8, 130.5, 129.5, 129.4, 129.2, 126.2, 125.3, 124.5, 124.1, 123.5, 122.5, 122.2, 121.6, 119.9, 119.2, 119.1, 118.5, 116.5, 29.8, 18.2, 17.3, 17.3. FT-IR: 2202 (ν_{CN}), 1607(m), 1476, 1224(m) cm^{-1}. Anal. Calcd for $C_{40}H_{34}N_7Ir$: C, 59.68, H, 4.26, N, 12.18. Found: C, 59.64, H, 4.27, N, 11.99.

Complex 37h. The title compound was prepared by the general method described above for complex **36h**, using $[Ir(F_2ppy)_2(\mu\text{-}Cl)]_2$ (61 mg, 0.050 mmol) and **Fzh** (30 mg, 0.10 mmol). Yield: 60 mg (68%). ^{1}H NMR (500 MHz, $CDCl_3$): δ 8.47 (d, J = 5.3 Hz, 1H, ArH), 8.39 (d, J = 5.4 Hz, 1H, ArH), 8.12 (d, J = 8.3 Hz, 1H, ArH), 7.99 (d, J = 8.3 Hz, 1H, ArH), 7.88 (t, J =

7.9 Hz, 1H, ArH), 7.82 (t, J = 7.9 Hz, 1H, ArH), 7.2 (dt, J = 23.0, 6.3 Hz, 2H, ArH), 6.64 (s, 1H, ArH), 6.55 (s, 1H, ArH), 6.41 (d, J = 8.0 Hz, 1H, ArH), 6.38 (d, J = 8.1 Hz, 1H, ArH), 6.21 (d, J = 7.7 Hz, 1H, ArH), 6.18–6.06 (m, 2H, ArH), 5.89 (d, J = 7.7 Hz, 1H, ArH), 5.30 (d, J = 8.5 Hz, 1H, ArH), 5.25 (d, J = 8.5 Hz, 1H, ArH), 2.11 (s, 3H, CH_3), 2.08 (s, 3H, CH_3), 1.67 (s, 3H, CH_3), 1.53 (s, 3H, CH_3). ^{19}F NMR (470 MHz, $CDCl_3$): δ −107.2 (q, J = 9.3 Hz, 1F), −108.7 (q, J = 9.3 Hz, 1F), −109.9 (t, J = 11.5 Hz, 1F), −110.2 (t, J = 11.4 Hz, 1F). ^{13}C NMR (151 MHz, $CDCl_3$): δ 165.5, .1, 163.6, 163.4, 161.9, 161.7, 161.3, 160.1, 159.6, 159.1, 152.1, 151.1, 150.5, 149.0, 147.4, 138.7, 138.5, 137.3, 135.6, 134.5, 131.5, 130.8, 129.6, 126.9, 125.8, 125.4, 124.0, 123.4, 123.3, 123.0, 122.7, 118.5, 115.7, 114.2, 113.1, 98.1, 96.4, 20.9, 20.7, 17.9, 17.2. FT-IR: 2213 (ν_{CN}), 1738, 1601(m), 1402, 1228(m) cm^{-1}. Anal. Calcd for $C_{40}H_{30}N_7F_4Ir$: C, 54.79, H, 3.45, N, 11.18. Found: C, 54.93, H, 3.40, N, 11.02.

Complex 38h. The title compound was prepared by the general method described above for complex **36h**, using $[Ir(bt)_2(\mu\text{-}Cl)]_2$ (65 mg, 0.050 mmol) and **Fzh** (30 mg, 0.10 mmol). Yield: 40 mg (44%). ^1H NMR (500 MHz, $CDCl_3$): δ 7.92 (d, J = 8.0 Hz, 1H, ArH), 7.88 (t, J = 8.2 Hz, 2H, ArH), 7.73 (d, J = 8.1 Hz, 1H, ArH), 7.63 (t, J = 7.7 Hz, 1H, ArH), 7.54 (t, J = 7.6 Hz, 1H, ArH), 7.49–7.41 (m, 2H, ArH), 7.12 (d, J = 7.6 Hz, 1H, ArH), 7.05 (d, J = 7.6 Hz, 1H, ArH), 6.64 (q, J = 7.0 Hz, 2H, ArH), 6.56 (dd, J = 14.0, 6.0 Hz, 2H, ArH), 6.54–6.49 (m, 2H, ArH), 6.44 (d, J = 7.9 Hz, 1H, ArH), 6.37 (d, J = 8.1 Hz, 1H, ArH), 6.19 (d, J = 8.1 Hz, 1H, ArH), 6.09 (d, J = 7.7 Hz, 1H, ArH), 6.03 (d, J = 7.7 Hz, 1H, ArH), 5.86 (d, J = 7.9 Hz, 1H, ArH), 2.06 (s, 3H, CH_3), 2.03 (s, 3H, CH_3), 1.43 (s, 3H, CH_3), 1.33 (s, 3H, CH_3). ^{13}C NMR (151 MHz, $CDCl_3$): δ 181.8, 180.3, 158.2, 149.5, 149.5, 148.8, 147.3, 147.0, 139.2, 138.9, 136.8, 136.1, 134.7, 133.1, 131.7, 131.6, 131.3, 131.2, 131.1, 131.0, 130.8, 130.6,

129.1, 128.6, 128.4, 126.2, 126.1, 126.0, 125.6, 125.5, 125.24, 125.20, 123.1, 122.6, 122.2, 120.4, 120.3, 119.9, 118.4, 116.2, 21.0, 20.9, 17.7, 17.0. FT-IR: 2205 (ν_{CN}), 1581(m), 1406(m), 1223(m) cm^{-1}. Anal. Calcd for $C_{44}H_{34}N_7S_2Ir$: C, 57.62, H, 3.74, N, 10.69. Found: C, 57.78, H, 3.72, N, 10.60.

4.4.4 X-ray Crystallography Details.

Single crystals of **36g**, **37g**, and **38g** were grown by diffusing pentane into concentrated chloroform, dichloromethane, or ethyl acetate (EA) solutions. Crystals were mounted on a Bruker Apex II three-circle diffractometer using MoKα radiation (λ = 0.71073 Å), conducted by Prof.Teets. The data were collected at 123(2) K and was processed and refined within the APEXII software. Structures were solved by direct methods in SHELXS and refined by standard difference Fourier techniques in the program SHELXL.[78] Hydrogen atoms were placed in calculated positions using the standard riding model and refined isotropically. All non-hydrogen atoms were refined anisotropically. In the structure of **36g**, one of the two chloroform solvate molecules was modeled as a two-part disorder. Distance restraints were used to affix the 1,2 and 1,3, distances in the disordered parts, and rigid bond restraints (SIMU and DELU) were used for the thermal ellipsoid parameters.

5 Chapter Five Dinuclear Complexes of Flexidentate Pyridine-Substituted Formazanate Ligands

5.1 Introduction

Formazanates, the monoanionic form of formazans with a 1,2,4,5-tetraazapentadienyl (NNCNN) core, have become a well-known N-chelating ligand class in recent years. They are structurally related to β-diketiminates, but the two additional nitrogen atoms in the backbone provide formazanates with more accessible redox properties and stronger visible absorption, due to their more stabilized LUMOs.[20] Formazanates have garnered considerable attention in coordination chemistry due to their ligand-based redox processes, which may facilitate multielectron redox transformations,[7] bond activations,[8] and excited-state charge separation.[9] A variety of formazanate complexes of many main group metals[34,37,38,40,94,95,159,164] and first- and second-row transition metals[25,46,89–91,107] have been described, highlighting the versatile coordination chemistry of formazanate ligands and providing many examples of and much insight into the intense visible absorption and accessible redox states of formazanates. Some copper complexes can also mediate oxygen activation,[48,49] certain cobalt and iron complexes exhibit unique magnetic characteristics,[25,108] and boron complexes in many cases feature not only the tunable redox properties but also visible to near-infrared photoluminescence,[34,37,94,95] finding applications as cell-imaging agents[36,41] and electrochemiluminescence emitters.[94]

Compared to the numerous formazanate complexes where a single metal atom is chelated within the NNCNN framework, polynuclear compounds involving formazanates remain rare. Access to complex polynuclear formazanate complexes is desirable for a number of reasons; in addition to greatly expanding the fundamental coordination chemistry of formazanates, there is the possibility of designing compounds with enhanced or unusual redox, magnetic, or photophysical properties, enabled by electronic communication between the building blocks mediated by the redox-active formazanate. In addition, compared to the rigid polypyridyl-based bridging ligands that are ubiquitous in coordination chemistry, formazanates offer the advantage of greater coordination flexibility and redox potentials that can be more easily tuned over a wide range. There are a few existing categories of polynuclear complexes involving formazanates, with representative examples shown in Chart 5.1. In some cases, the formazanate binds in a normal chelating mode, with other bridging moieties, either covalently attached to the formazanate periphery or added in as exogenous ligands, templating the polynuclear structure. This type of assembly was reported in two different works by the Gilroy group, one where boron difluoride formazanates are conjugated to platinum acetylide complexes, via aryl acetylene groups on the formazanate periphery,[38] and another involving a cyclic trimeric boroxine compound, with the three boron atoms are linked by oxo bridges.[165] In other cases, the formazanate itself is the polynucleating ligand and binds multiple metals at once. The Holland group isolated dimeric iron formazanate complexes which formed following alkali metal reduction of a mononuclear iron formazanate precursor; the alkali metal cation templates the formation of the dimer, and the formazanate coordinates via a hybrid binding mode, chelating the iron through N1 and N4, with N5 bridging to the adjacent

iron center.[46] In another recent effort from the Gilroy group, formazanates substituted with a 2-pyridyl group were shown to be able to simultaneously bind BF_2^+ and divalent nickel.[37] With these few recent precedents in mind, we reasoned that the flexidentate pyridyl-substituted ligands introduced by Gilroy's group, and other related derivatives, could serve as versatile polynucleating ligands for a wide range of structures.

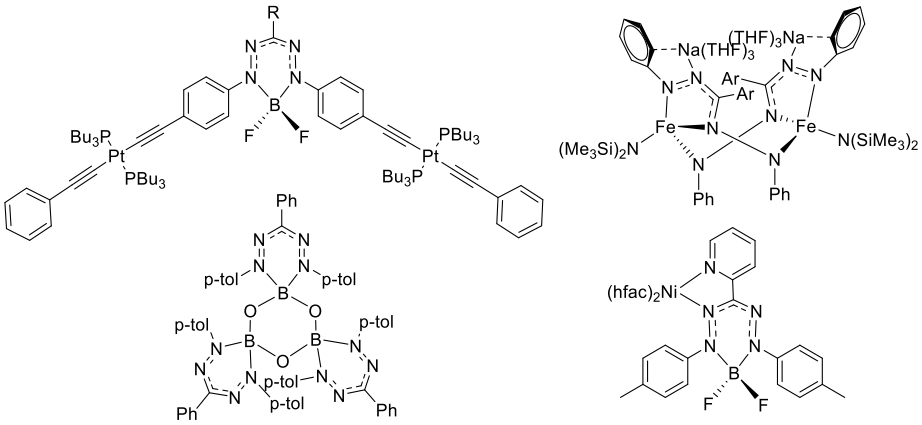

Chart 5.1 Some previously reported polynuclear formazanate complexes

Having extensively studied the coordination chemistry of formazanates with Ir(III)[57,58] and Pt(II),[54,55] our initial effort presented herein includes a series of complexes containing different combinations of these two metals bridged by pyridyl-substituted formazanates. We elaborate the coordination chemistry of formazans with either 4- and 2-pyridyl substituents as the central aryl ring. The pyridyl substituents offer one additional coordination site, and we show in this work the diversity of coordination modes possible with these ligands. The dinuclear complexes that are presented in this study are generally assembled in a stepwise fashion, adding one metal at a time to structure, which allows for the rational and modular preparation of the complexes. A total of nine new formazanate complexes are introduced, with four mononuclear and four dinuclear complexes structurally characterized by single-

crystal X-ray diffraction. All the compounds are interrogated by cyclic voltammetry and UV-vis absorption spectroscopy, revealing the effects of the coordination modes and complex structures on the formazanate-centered frontier orbitals and visible absorption transitions.

5.2 Results and discussion

5.2.1 Synthesis and related structural characterization

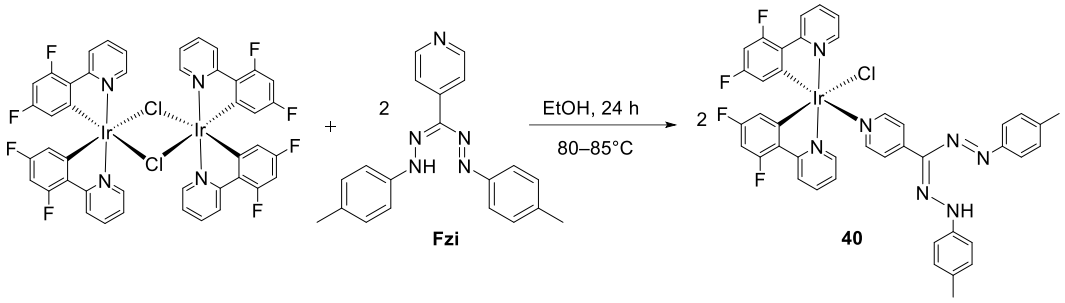

Scheme 5.1 Synthesis of Complex **40**

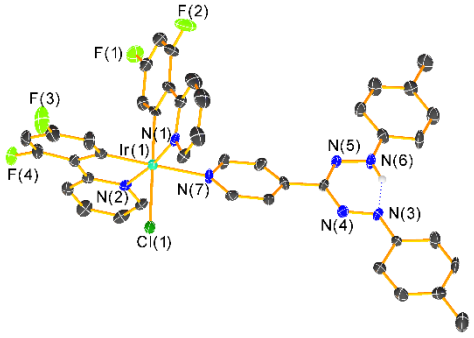

Figure 5.1 Molecular structure of complex **40**, determined by single-crystal X-ray diffraction. Ellipsoids are shown at 50% probability level with solvent molecules and carbon-bound hydrogen atoms omitted.

In this work, we prepared 9 Ir(III)/Pt(II) pyridylformazanate complexes in total, which include mononuclear building blocks and dinuclear assemblies. We began our efforts with the new formazan 1,5-bis(*p*-tolyl)-3-(4-pyridyl)formazan (**Fzi**); closely related derivatives with 1,5-diphenyl substitution have been described,[166] but their coordination chemistry has only

been described in one isolated report on homoleptic nickel bis-formazanate complexes.[167] Scheme 5.1 depicts the synthetic route of a mononuclear cyclometalated Ir(III) complex of **Fzi**. Initially we used reaction conditions identical to those outlined in our previous report on cyclometalated iridium formazanate complexes,[57] so our hypothesis was that **Fzi** would chelate the iridium center through the formazanate backbone. We treated the chloro-bridged dimer $[Ir(F_2ppy)_2(\mu\text{-}Cl)]_2$ (F_2ppy is 2-(2,4-difluorophenyl)pyridine) with a stoichiometric amount of **Fzi** in refluxing ethanol with excess triethylamine present. NMR spectroscopy confirmed isolation of a single product, but the ^1H NMR spectrum shows a downfield resonance at 15.79 ppm, consistent with the N–H proton of the formazanate (Figure S71). We thus concluded that **Fzi** binds to the Ir(III) center in a monodentate fashion through the nitrogen of the pyridyl substituent, with the chloride ligand still attached and an empty formazan backbone. The structure was unambiguously assigned by the crystal structure shown in Figure 5.1, which clearly shows the κ^1 coordination through pyridine. In addition, the N–H hydrogen atom was located in the difference map, further confirming that the formazan core is intact during this reaction. Recognizing that no deprotonation occurs during the formation of **40**, as shown in Scheme 5.1, we removed triethylamine and performed the reaction without any base present, and the product was still formed in nearly identical isolated yield.

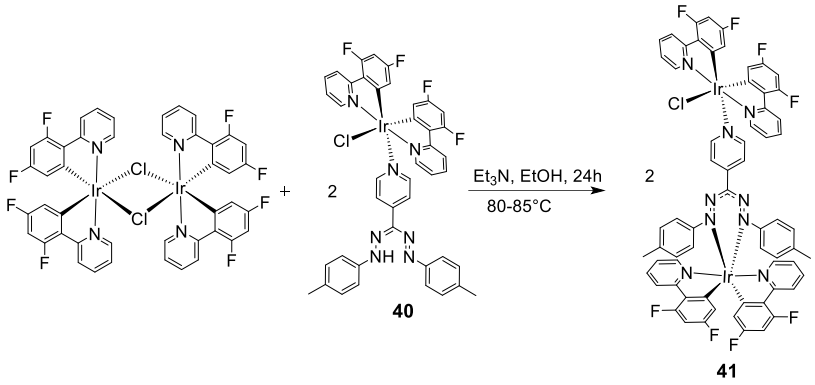

Scheme 5.2 Synthesis of complex **41**

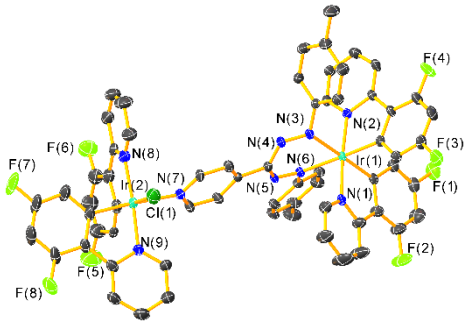

Figure 5.2 Molecular structure of complex **41**, determined by single-crystal X-ray diffraction. Ellipsoids are shown at 50% probability level with solvent molecules and carbon-bound hydrogen atoms omitted.

We then investigated complex **40** as a precursor for subsequent reactions targeting polynuclear complexes. Scheme 5.2 displays the synthetic route of the bimetallic cyclometalated Ir(III) complex **41**, bridged by **Fzi**. To install the second bis-cyclometalated iridium fragment, complex **40** was treated with a stoichiometric amount of $[Ir(F_2ppy)_2(\mu\text{-}Cl)]_2$ in refluxing ethanol with excess triethylamine. Following column chromatography, bimetallic complex **41** was isolated in moderate yield, 32%. Formation of the bimetallic structure was evident from NMR spectroscopy (Figure S74–S76). The characteristic downfield N–H resonance, observed at 15.79 ppm in **40**, is no longer present. In addition, the ^{1}H and ^{19}F NMR spectra of **41** display two sets of resonances for the F_2ppy ligands; in one set there are

two chemically equivalent F_2ppy ligands, and in the other the two F_2ppy ligands are chemically inequivalent. This observation suggests that one of the bis-cyclometalated iridium centers has local C_1 symmetry, as is the case in precursor complex **40**, whereas the other has local C_2 symmetry. The structure of complex **41** thus includes the second $[Ir(F_2ppy)_2]^+$ fragment being chelated by N1 and N5 of the formazanate core, which is often typical "closed" form of the formazanate.[57] This binding mode was confirmed by X-ray crystallography, with the structure shown in Figure 5.2. The flexidentate ligand **Fzi** exhibits a dual coordination mode in the structure of **41**, with the formazanate core chelating one metal center and the 4-pyridyl ring bound to the other. This confirms that the overall outcome of the reaction shown in Scheme 5.2 is to use complex **40** as a "metalloligand" to chelate a second iridium fragment.

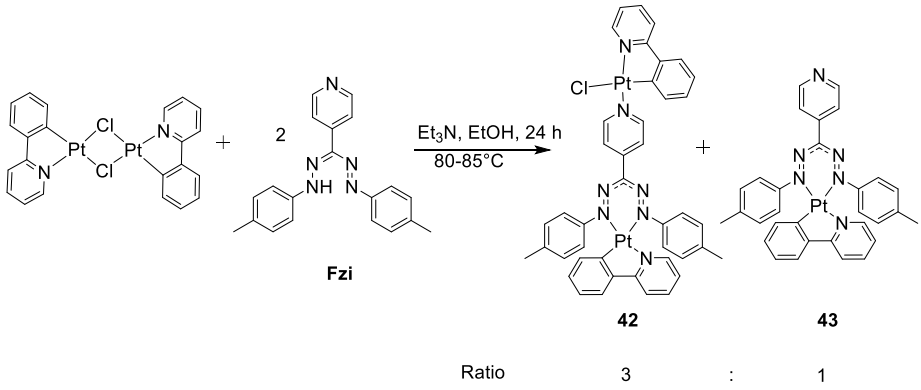

Scheme 5.3 Synthesis of complex **42** and **43**.

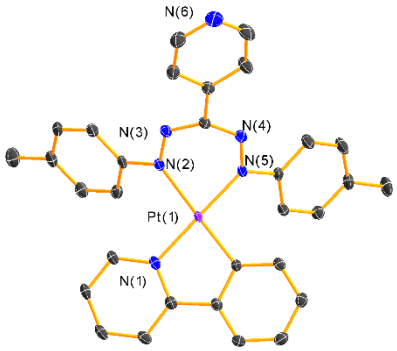

Figure 5.3 Molecular structure of complex **43**, determined by single-crystal X-ray diffraction. Ellipsoids are shown at 50% probability level with solvent molecules and carbon-bound hydrogen atoms omitted.

The same binding mode of **Fzi** observed in complex **41** was also observed with cyclometalated platinum. Whereas no reaction is observed between **Fzi** and Pt(N^N)Cl_2 precursors ((N^N is 2,2′-bipyridine (bpy) or 4,4′-di-tert-butyl-2,2′-bipyridine (tbbpy)) in the presence of base, **Fzi** does react with the chloro-bridged dimer [Pt(ppy)(μ-Cl)]$_2$, as shown in Scheme 5.3. A 1:2 reaction between [Pt(ppy)(μ-Cl)]$_2$ and **Fzi** in refluxing ethanol with excess triethylamine produces two products, a bimetallic complex **42** (major product) and chelated monoplatinum complex **43** (minor product). Crude NMR spectra indicate a ca. 3:1 ratio of the two products, and upon chromatographic separation complex **42** is obtained in 64% yield (based on the platinum precursor), whereas **43** is obtained in 12% yield. The formation of both products during the same reaction suggests that monoplatinum complex **43** may be an intermediate in the formation of diplatinum complex **42**. In addition, comparing the reaction with cyclometalated platinum shown in Scheme 5.3 to the reaction with iridium in Scheme 5.2 shows that **Fzi** backbone more readily chelates Pt(II) than Ir(III) and does not form products with platinum that are exclusively bound through the pyridine. The structure of complex **43** was verified by X-ray crystallography (Figure 5.3), and is very similar to several

other structurally characterized Pt(C^N)(formazanate) complexes from our group.[54,55] We were unable to obtain single crystals of diplatinum complex **42**, but NMR spectroscopy and mass spectrometry are all consistent with the proposed structure (Figure S77 & S78). In particular, the ^{1}H NMR spectrum of **42** shows two sets of resonances for the ppy ligands, indicating two chemically inequivalent [Pt(ppy)]$^{+}$ fragments, and one set of resonances attributed to **Fzi**. All of these observations are consistent with the same binding mode for **Fzi** in diplatinum complex **42** as is observed in diiridium complex **41** (Scheme 5.2 and Figure 5.2).

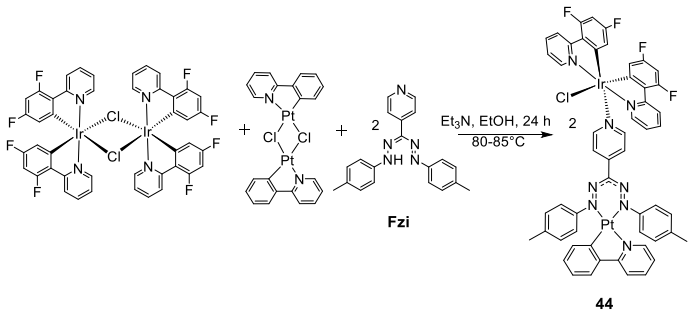

Scheme 5.4 Synthesis of complex **44**

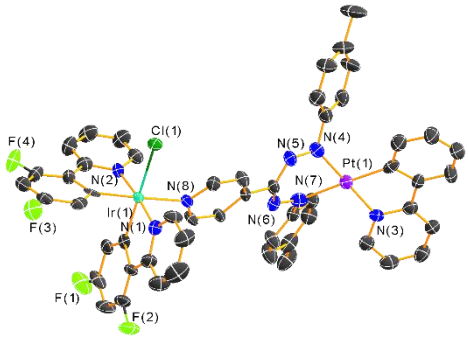

Figure 5.4 Molecular structure of complex 44, determined by single-crystal X-ray diffraction. Ellipsoids are shown at 50% probability level with solvent molecules and carbon-bound hydrogen atoms omitted.

We also found that 4-pyridyl-substituted **Fzi** can support a heterobimetallic complex, in this case prepared by a one-pot self-assembly. Recognizing that **Fzi** has two different preferred binding modes with iridium and platinum (Schemes 5.1 and 5.3) we treated equimolar amounts of $[Ir(F_2ppy)_2(\mu\text{-}Cl)]_2$ and $[Pt(ppy)(\mu\text{-}Cl)]_2$ with two equivalents of **Fzi**, in the presence of triethylamine in refluxing ethanol (Scheme 5.4). Clean self-assembly of the heterobimetallic complex **44** was observed, and following recrystallization the product was isolated in good yield (72%). ^{19}F NMR spectroscopy evinces local C_1 symmetry at the iridium center, with four distinct resonances for the F_2ppy fluorine atoms, and the ^{1}H NMR spectrum, while complex in the aromatic region, shows the expected number of peaks and integration values for the proposed structure (Figure S81 & S82). Single crystals of complex **44** were obtained, with the structure determined by X-ray diffraction depicted in Figure 5.4. The binding mode of **Fzi** is clearly confirmed in the structure, with chelation to the cyclometalated platinum fragment and κ^1 binding through pyridine at the iridium site. As observed in complex **43** and many other platinum formazanate complexes from our group,[54,55] the formazanate in complex **44** binds to the platinum in a "dragonfly" conformation, where the backbone carbon and 4-pyridyl substituent in the formazanate are splayed out of the platinum coordination plane. Looking at select bond distances, we note that the Ir–N(pyridyl) bond distance in **44**, 2.165(8) Å, is very similar to, but slightly shorter than, the analogous distance in complex **40**, which averages 2.184(11) Å for two crystallographically independent molecules. This observation suggests that the electronic nature of the pyridine is minimally altered when **Fzi** coordinates to a metal. Similarly, the formazanate Pt–N distances, 2.037(2)

Å and 2.088(2) Å in monoplatinum complex **43**, are only slightly shifted in bimetallic complex **44**, where the same distances are 2.000(9) Å and 2.107(10) Å.

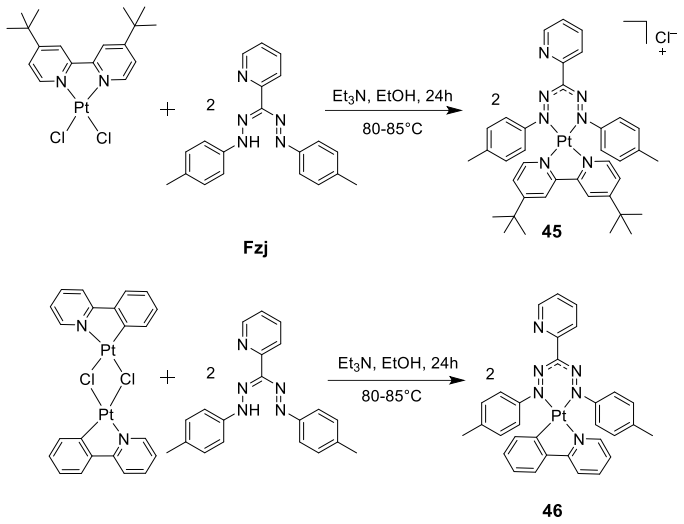

Scheme 5.5 Synthesis of complexes **45** and **46**.

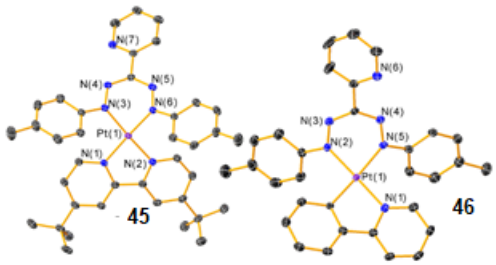

Figure 5.5 Molecular structure of complex 45 and 46, determined by single-crystal X-ray diffraction. Ellipsoids are shown at 50% probability level with solvent molecules and carbon-bound hydrogen atoms omitted.

The 2-pyridyl isomer **Fzj** does not react cleanly with cyclometalated iridium precursors, but we were able to construct diplatinum complexes with this ligand, exhibiting two distinct binding modes. Two monoplatinum precursor compounds **45** and **46** with a chelated **Fzj** were prepared as described in Scheme 5.5, and their structures were confirmed by NMR spectroscopy (Figure S84–S87) and single-crystal X-ray diffraction (Figure 5.5). Of note,

complex **45** represents a new structure type in platinum formazanate chemistry, with the neutral tbbpy and monoanionic **Fzj** supporting a cationic Pt(II) complex with an outer-sphere chloride anion.

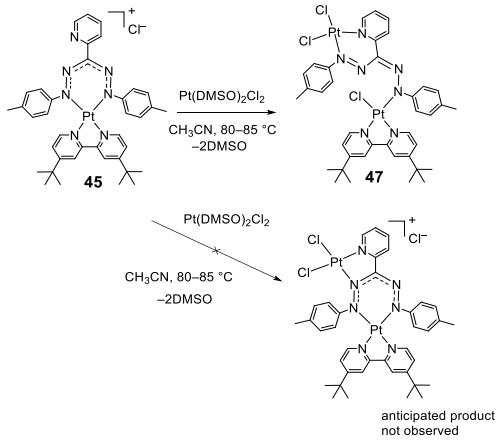

Scheme 5.6 Synthesis of complex **47**

We reasoned that complexes **45** and **46** could serve as chelating metalloligands, using the 2-pyridyl and an adjacent nitrogen atom in the formazanate core to chelate the second metal, in the same manner observed by Gilroy's group previously (see Chart 5.1).[37] We first introduced the labile platinum precursor $Pt(DMSO)_2Cl_2$ to complex **45**, anticipating the formation of a complex with $PtCl_2$ chelated by the 2-pyridyl and an adjacent formazanate

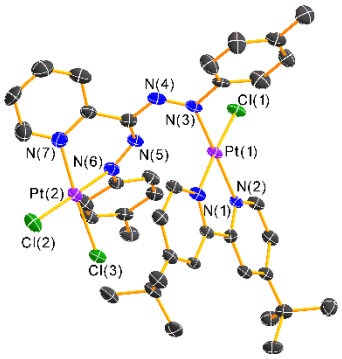

Figure 5.6 Molecular structure of complex **47**, determined by single-crystal X-ray diffraction. Ellipsoids are shown at 50% probability level with solvent molecules and hydrogen atoms omitted.

nitrogen, as shown in Scheme 5.6. The ^{1}H NMR spectrum of the resulting product was consistent with the formation of a more rigid product with the pyridine locked into a single conformation by virtue of coordination (Figure S88). Specifically, the formazanate C*H*$_3$ resonances, which are chemically equivalent in **45** by virtue of free rotation of the 2-pyridyl ring, split substantially in the product, separated by 0.2 ppm. In addition, the *tert*-butyl ^{1}H resonances likewise occur at different chemical shifts, albeit minimally split. However, the crystal structure of complex **47**, displayed in Figure 5.6, reveals that a rearrangement occurs during the reaction, whereby the chloride counterion opens up the chelated formazanate at the [Pt(bpy)]$^{+}$ site, and the formazanate splays open to bind the $PtCl_2$ through the 2-pyridyl moiety and N1 of the formazanate core, forming a 6-membered chelate ring. The structure of **47** represents a new and unexpected binding mode for the flexidentate formazan **Fzj**, but nonetheless does show that this ligand can template dinuclear transition metal complexes.

Applying the same reaction conditions with neutral cyclometalated complex **46**, we presumed that binding of $PtCl_2$ would also occur, possibly via the same binding mode as in complex **47**, but likely avoiding opening of the platinum-formazanate since there is not an

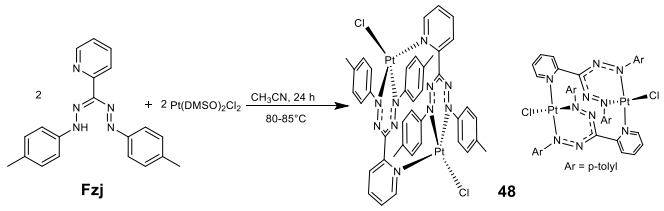

Scheme 5.7 Synthesis of complex **48**.

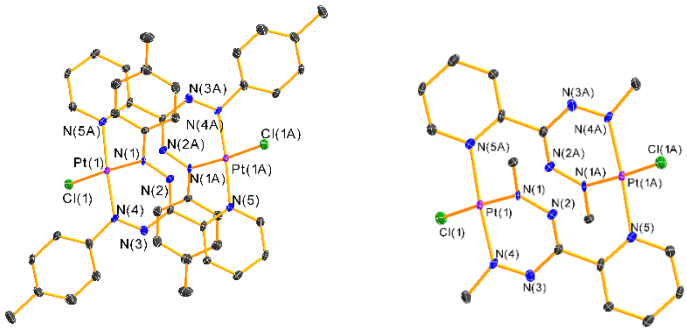

Figure 5.7 Molecular structure of complex **48**, determined by single-crystal X-ray diffraction. Ellipsoids are shown at 50% probability level with solvent molecules and hydrogen atoms omitted. The right structure more clearly shows the coordination environment and bimetallic core, eliminating the p-toyl substituents except for the carbon atoms bound to the formazanate nitrogen atoms.

additional equivalent of Cl^- present in the reaction. Treating complex **46** with $Pt(DMSO)_2Cl_2$ resulted in the formation of a new product, but the ^1H NMR spectrum did not match the expected product that would form from binding $PtCl_2$ (Figure S90). In particular, the ^1H NMR spectrum of the product has fewer aromatic resonances than the starting material (**46**), and one resonance occurs very far downfield, at 13.70 ppm. We determined by single-crystal X-ray diffraction that the product that formed (Figure 5.7) is a C_2-symmetric neutral diplatinum formazanate complex of the formula Pt_2(**Fzb**)$_2Cl_2$ (**48**), where each **Fzj** ligand chelates one platinum center and bridges to the other with the 2-pyridyl group. Thus the coordination geometry of each platinum includes the two nitrogen atoms from a chelating formazanate, a pyridyl nitrogen from the neighboring formazanate, and a terminal chloride. The fate of the

Table 5.1 Summary of crystallographic bond lengths (Å) and angles (deg) for dinuclear compounds **41**, **44**, **47** and **48**.

	41	**44**	**47**	**48**
			Bond Distances (Å)	
M–N (Formazanate)	2.133(7)	1.990(8)	2.023(7)	2.009(4)
	2.170(7)	2.104(8)	1.995(7)	2.003(4)
M–N (pyridyl)	2.182(8)	2.173(7)	2.015(8)	2.056(5)
N–N (Formazanate)	1.287(10)	1.300(10)	1.305(11)	1.299(6)
	1.293(10)	1.291(10)	1.288(9)	1.286(6)
N–C (Formazanate)	1.351(11)	1.349(11)	1.322(11)	1.350(7)
	1.351(12)	1.346(11)	1.372(10)	1.353(7)
M–Cl	2.527(3)	2.463(2)	2.3083(19) 2.303(2) 2.294(2)	2.307(14)
			Formazanate Bond Angles (°)	
N–M–N	82.8(3)	81.2(3)	N/A	85.23(18)
M–N–N	127.2(6)	124.6(6)	126.8(5)	121.6(3)
	122.5(6)	122.7(6)	122.5(5)	121.8(4)
N–N–C	120.9(7)	121.0(8)	119.8(7)	120.4(4)
	120.9(7)	120.8(8)	119.2(7)	120.9(5)
N–C–N	129.4(8)	126.2(8)	120.8(8)	127.5(5)

$[Pt(ppy)]^+$ fragment that is lost during this reaction is not known, but we did find, as depicted in Scheme 5.7, that product **48** could be prepared rationally and much more efficiently by simply treating $Pt(DMSO)_2Cl_2$ with equimolar **Fzj** in refluxing acetonitrile, allowing the diplatinum complex to be isolated in 64% yield. Examining the structure in Figure 5.7, we note that the platinum centers are separated by a large distance, 4.78 Å, indicating they are non-interacting, and we presume that the very downfield chemical shift in the ^{1}H NMR spectrum (13.70 ppm) is attributed to the protons at the 6-position of the 2-pyridyl rings, which are in a locked position that result in close approach (2.53 Å) to N(3) and N(3A). Bond distances and angles of dinuclear compounds are listed in Table 5.1 with refinement details collected in Tables 5.2 and 5.3. Related NMR data are shown in Figure S69–S91 in appendix.

Table 5.2 Summary of crystallographic data for mononuclear complexes **40**, **43**, **45**, and **46**.

	40·1.5EtOAc ·0.5MeOAc	**43**	**45**·1.25CH_2Cl_2	**46**
CCDC	1985158	1985160	1985162	1985163
Crystal data				
Chemical formula	$C_{49.50}H_{46}ClF_4IrN_7O_4$	$C_{31}H_{26}N_6Pt$	$C_{39.25}H_{44.50}Cl_{3.50}N_7Pt$	$C_{31}H_{26}N_6Pt$
M_r	1106.58	677.67	933.48	677.67
Crystal system, space group	Monoclinic, $P2_1$	Monoclinic, $C2/c$	Monoclinic, $C2/c$	Monoclinic, $P2_1/c$
a, b, c (Å)	8.4851 (6), 29.971 (2), 18.2966 (13)	25.091 (4), 14.391 (2), 14.736 (2)	43.514 (2), 16.9264 (8), 31.006 (3)	9.5091 (14), 24.500 (4), 11.1488 (16)
α, β, γ (°)	90, 91.335 (1), 90	90, 104.506 (2), 90	90, 134.348 (1), 90	90, 96.017 (3), 90
V (Å^3)	4651.7 (6)	5151.3 (13)	16330.9 (18)	2583.0 (7)
Z	4	8	16	4
μ (mm^{-1})	3.00	5.48	3.70	5.47
Crystal size (mm)	0.44 × 0.13 × 0.01	0.55 × 0.50 × 0.50	0.41 × 0.19 × 0.18	0.29 × 0.21 × 0.11
Data collection				
T_{min}, T_{max}	0.548, 0.745	0.509, 0.746	0.540, 0.746	0.417, 0.746
No. of measured, independent and observed [$I > 2\sigma(I)$] reflections	47166, 19483, 17827	15772, 5912, 5609	50780, 18787, 16270	32009, 5985, 5568
R_{int}	0.047	0.022	0.027	0.038
$(\sin\theta/\lambda)_{max}$ (Å^{-1})	0.631	0.650	0.651	0.653
Refinement				
$R[F^2 > 2\sigma(F^2)]$, $wR(F^2)$, S	0.051, 0.114, 1.16	0.019, 0.048, 1.06	0.029, 0.088, 1.08	0.035, 0.077, 1.49
No. of reflections	19483	5912	18787	5985
No. of parameters	1193	373	969	339
No. of restraints	1171	154	100	0
	$w = 1/[\sigma^2(F_o^2) + (0.0474P)^2 + 10.3822P]$ where $P = (F_o^2 + 2F_c^2)/3$	$w = 1/[\sigma^2(F_o^2) + (0.0224P)^2 + 10.7064P]$ where $P = (F_o^2 + 2F_c^2)/3$	$w = 1/[\sigma^2(F_o^2) + (0.0461P)^2 + 46.8527P]$ where $P = (F_o^2 + 2F_c^2)/3$	$w = 1/[\sigma^2(F_o^2) + (0.0016P)^2 + 10.9925P]$ where $P = (F_o^2 + 2F_c^2)/3$
$\Delta\rho_{max}$, $\Delta\rho_{min}$ (e Å^{-3})	3.06, -3.44	0.93, -1.76	1.94, -0.95	1.89, -1.33

Table 5.3 Summary of crystallographic data for dinuclear complexes **41**, **44**, **47**, and **48**.

	41·C_5H_{12}	**44**·C_5H_{12}	**47**·1.5C_5H_{12}	**48**·CH_2Cl_2
CCDC	1985159	1985161	1985164	1985165
Crystal data				
Chemical formula	$C_{69}H_{54}ClF_8Ir_2N_9$	$C_{58}H_{50}ClF_4IrN_8Pt$	$C_{45.50}H_{60}Cl_3N_7Pt_2$	$C_{20.50}H_{19}Cl_2N_5Pt$
M_r	1581.06	1357.80	1201.53	601.40
Crystal system, space group	Triclinic, $P\bar{1}$	Triclinic, $P\bar{1}$	Tetragonal, $I4_1/a$	Triclinic, $P\bar{1}$
a, b, c (Å)	12.009 (2), 16.242 (3), 17.642 (3)	12.049 (6), 14.088 (7), 18.227 (9)	30.570 (5), 30.570 (5), 20.173 (4)	7.511 (2), 11.577 (4), 12.304 (4)
α, β, γ (°)	92.054 (2), 109.382 (2), 99.074 (2)	89.082 (6), 70.887 (6), 74.845 (6)	90, 90, 90	96.758 (4), 103.618 (4), 97.405 (4)
V (Å^3)	3190.9 (10)	2813 (2)	18853 (7)	1019.0 (6)
Z	2	2	16	2
μ (mm^{-1})	4.28	4.95	6.14	7.17
Crystal size (mm)	0.53 × 0.17 × 0.05	0.17 × 0.09 × 0.04	0.47 × 0.43 × 0.20	0.34 × 0.28 × 0.05
Data collection				
T_{min}, T_{max}	0.377, 0.746	0.601, 0.746	0.512, 0.746	0.376, 0.746
No. of measured, independent and observed [$I > 2\sigma(I)$] reflections	64985, 14077, 11225	32409, 9906, 6779	52362, 10399, 7897	6020, 4252, 4054
R_{int}	0.057	0.075	0.051	0.027
$(\sin\theta/\lambda)_{max}$ (Å^{-1})	0.641	0.595	0.641	0.633
Refinement				
$R[F^2 > 2\sigma(F^2)]$, $wR(F^2)$, S	0.069, 0.180, 1.06	0.048, 0.127, 1.02	0.048, 0.149, 1.09	0.036, 0.095, 1.04
No. of reflections	14077	9906	10399	4252
No. of parameters	804	661	527	264
No. of restraints	834	40	77	13
	$w = 1/[\sigma^2(F_o^2) + (0.0561P)^2 + 91.9469P]$ where $P = (F_o^2 + 2F_c^2)/3$	$w = 1/[\sigma^2(F_o^2) + (0.0579P)^2 + 5.7177P]$ where $P = (F_o^2 + 2F_c^2)/3$	$w = 1/[\sigma^2(F_o^2) + (0.0722P)^2 + 411.9535P]$ where $P = (F_o^2 + 2F_c^2)/3$	$w = 1/[\sigma^2(F_o^2) + (0.0635P)^2 + 1.9936P]$ where $P = (F_o^2 + 2F_c^2)/3$
$\Delta\rho_{max}$, $\Delta\rho_{min}$ (e Å^{-3})	14.41, -7.56	2.15, -1.72	4.40, -1.38	2.64, -2.82

5.2.2 UV-vis absorption spectroscopy

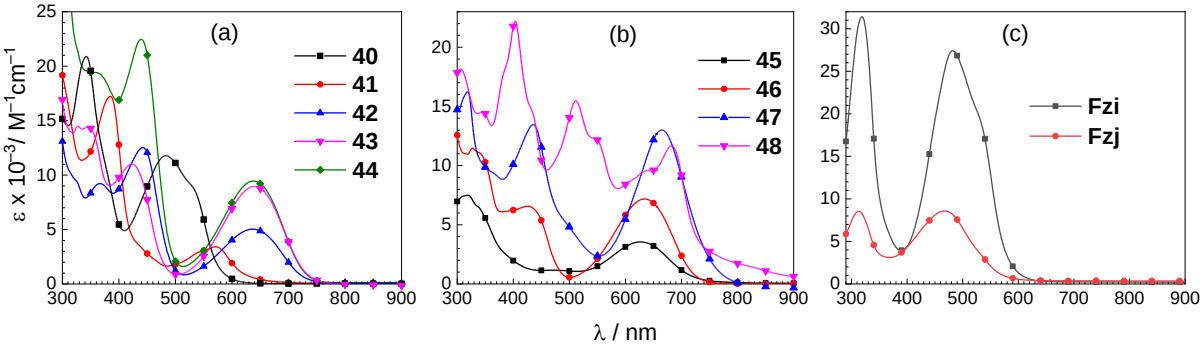

Figure 5.8 Overlaid electronic absorption spectra of (a) **Fzi** complexes, (b) **Fzj** complexes, and (c) free formazans **Fzi** and **Fzj**. Spectra were recorded in tetrahydrofuran (THF) solution at room temperature. Data was collected in intervals of 1 nm, and symbols are included on each plot are to help distinguish the overlaid spectra.

Recognizing that formazanates are well-known for their redox and optical properties, this study provides an opportunity to assess how the binding mode of flexidentate formazanates influences the frontier orbitals and excited states. The absorption spectra and the corresponding visual color of the complexes depend strongly on the binding mode. UV-vis spectra for the complexes are shown in Figure 5.8, with a summary of the data in Table 5.4. The plots in Figure 5.8 are arranged by the nuclearity of the respective complex. Figure 5.8a shows the five complexes involving **Fzi** (**40**, **41**, **42**, **43**, and **44**) with rest with **Fzj** (**45**, **46**, **47**, and **48**) shown directly in the middle in Figure 5.8b, and the spectra of the free formazans are included in Figure 5.8c.

Apart from intense peaks in the UV ($\lambda < 350$ nm) attributed to localized $\pi \rightarrow \pi^*$ transitions of the aryl substituents from both C^N and formazanate, a notable absorption between 460 nm and 700 nm stands out among all compounds, which is assigned as a $\pi \rightarrow \pi^*$ within the formazanate framework. The free formazans have similar UV-vis absorption wavelengths,

with the low-energy transition occurring 482 nm in **Fzi** and 466 nm in **Fzj**. Coordination through the 4-pyridyl substituent of **Fzi**, as observed in complex **40**, has a minimal effect on the absorption wavelength, which occurs at nearly identical wavelength (483 nm) in this complex. When the formazanate chelates the metal center, as observed in most other complexes, we observe a sizeable red-shift of the π→π* transition, as we have previously noted in studying many other Pt and Ir formazanates.[54,55,57] The magnitude of this shift depends on the metal that is chelated; in dinuclear complex **41**, the only member of the series where the formazanate chelates to iridium, the low-energy absorption shifts to 571 nm. In the **Fzi** complexes where Pt is chelated (**42**–**44**), the corresponding absorption maxima span 635–640 nm. Comparison of the mononuclear complex Pt(ppy)(**Fzi**) (**43**) (λ_{max} = 640 nm) to dincuclear complexes **42** and **44**, where the 4-pyridyl is coordinated to a secondary metal center, again shows minimal impact of 4-pyridyl coordination on the absorption wavelength.

Table 5.4 Summary of UV-vis absorption spectra of complexes **40**–**48**.

	λ / nm (ε x 10^{-3}/$M^{-1}cm^{-3}$)
Fzi	319 (31), 482 (27), 535(sh) (19)
Fzj	313 (8.5), 466 (8.6)
40	343 (21), 483 (12), 530(sh) (8.9)
41	384 (17), 571 (3.4)
42	325(sh)(9.4), 367(9.2), 442(13), 635(5.0)
43	328 (14), 346 (14), 424 (11), 640 (9.0)
44	364(sh) (19), 440 (22), 636 (9.5)
45	320 (7.5), 336(sh) (6.6), 626 (3.6)
46	328 (11), 341(sh) (11), 428 (6.6), 634 (7.2)
47	319 (16), 436 (13), 664 (13)
48	306 (18), 349(sh) (14), 384(sh) (18), 404 (22), 430(sh) (15), 511 (15), 548(sh) (12), 649(sh) (9.6), 682 (12)

In the **Fzj** series, mononuclear precursors **45** and **46** behave similarly to the other Pt chelates. The π→π* transition in **Fzj** occurs at 466 nm, and shifts to 626 nm in [Pt(tbbpy)(**Fzj**)](Cl) (**45**) and 634 nm in Pt(ppy)(**Fzj**) (**46**), indicating a small effect of the secondary ligand on the absorption energy. When complex **45** binds an equivalent of $PtCl_2$ to form complex **47**, which involves a rearrangement of the formazanate binding mode (Scheme 5.6), the low-energy absorption band shifts significantly from 626 nm to 664 nm, indicating that the π→π* gap is sensitive to the ligand conformation and/or to the coordination of a second metal ion to the formazanate. Finally, diplatinum complex **48** has the most distinct UV-vis absorption spectrum in the series. The lowest-energy maximum in **48** occurs at the longest wavelength in the series, 682 nm, and involves a high-energy shoulder at 649 nm. Moreover, complex **48** has a second set of overlapped, intense visible bands, at 511 and 548 nm, in a region of the spectrum where the other complexes are transparent. The origin of this second visible band is not immediately obvious from the available data, but we propose the most likely explanation for the appearance of the absorption spectrum in **48** is that each formazanate has a π→π* excited state, and the two states mix through configuration interaction to produce two state that give rise to the two intense visible absorption bands. UV-vis spectra were also recorded in three solvents of varying polarity (toluene, THF, and MeOH) and the low-energy absorption bands of most complexes exhibit small but measureable solvatochromism, indicating some amount of charge-transfer character in the excited state. For complexes with a chelated formazanate the solvatochromism is typically larger for Pt complexes vs. Ir, in line with what we have previously reported.[55–57]

5.2.3 Electrochemistry

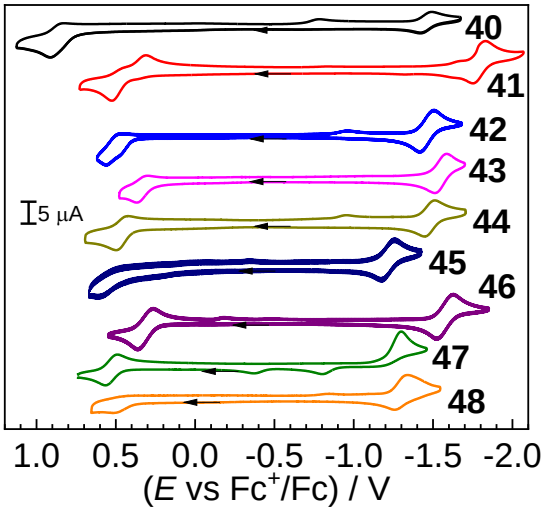

Figure 5.9 Overlaid cyclic voltammograms of complexes **40**–**48**. CVs were recorded in CH_2Cl_2 with 0.1 M NBu_4PF_6 supporting electrolyte, using a glassy carbon working electrode and a scan rate of 0.1 V/s. The arrows indicate the scan direction.

Table 5.5 Summary of electrochemical data of complexes **40**–**48.**

	E^{ox}(V)	E^{red}(V)
40	0.88	−1.45
41	0.52[a]	−1.79
42	0.56[a]	−1.46
43	0.34	−1.55
44	0.47	−1.48
45	0.59[a]	−1.22
46	0.31	−1.58
47	0.53	−1.30[a]
48	0.49[a]	−1.33[a]

[a] irreversible waves. $E_{p.a}$ or $E_{p.c}$ is reported.

The redox properties of all complexes were evaluated by cyclic voltammetry, to determine the effect of formazanate binding mode on the redox potentials and frontier orbitals. Overlaid voltammograms shown in Figure 5.9 and redox potentials are summarized in Table 5.5. Each complex shows one oxidation and one reduction feature within the accessible electrochemical window. We notice that complex **40**, which contains a neutral formazan coordinated to

iridium through the pyridine, is the most difficult to oxidize in the series, whereas in the rest of the compounds, with formally monoanionic metal-bound formazanate cores the oxidation waves are cathodically shifted. In most cases other than complexes **47** and **48**, the reduction waves are electrochemically reversible ranging from −1.22 to −1.79 V. This reduction is assigned to a formazanate-centered reduction, and some trends emerge from examining this series. First, we note that complex **41**, which has a chelated Ir(III) center, is significantly more difficult to reduce than any of the Pt(II) chelates, a trend we previously observed in many mononuclear formazanate complexes.[55,57] Other insights come from comparing mononuclear Pt(II) complex **43** to the two dinuclear complexes which contain this building block, **42** and **44**. The reduction potential in **43** is −1.55 V, which shift anodically to −1.46 V when the pyridine is capped with another Pt(II) unit in **42**, and similarly to −1.48 V when Ir(III) binds to the pyridine in **44**. Likewise, the one-electron oxidation couples are influenced to a small extent, with **42** and **44** more difficult to oxidize by ~0.1–0.2 V. This observation suggests that when the pyridine coordinates to another Lewis-acidic metal center, the formazanate-centered frontier orbitals are stabilized by a small amount, indicating that dincuclear assembly can influence formazanate-based orbital energies. In the **Fzj** series, we see that the mononuclear precursors **45** and **46** differ significantly in their reduction potentials. In cationic complex **45** the reduction is anodically shifted to −1.22 V, compared to −1.58 V in neutral cyclometalated complex **46**, indicating that the secondary ligand, tbbpy or ppy, couples electronically with the formazanate π system. Relatedly, cationic complex **45** has a formal oxidation couple that is ~0.3 V more positive than neutral complex **46**. When complex **45** binds $PtCl_2$ and rearranges to complex **47**, the reduction becomes irreversible and undergoes a slight cathodic

shift, whereas the oxidation is minimally perturbed. In the other dinuclear **Fzj** complex, **48**, the reduction is also irreversible, and we propose that it is a concerted two-electron reduction of both formazanates, given the larger observed current compared to the oxidation wave. All that said, in the compounds that have the formazanate core chelated to platinum (**42**–**46** and **48**) or bridging two platinum centers (**47**), the oxidation and reduction potentials are separated by a similar amount, ~1.8 V in most cases and no larger than 2.0 V (**42**), indicating HOMO–LUMO gaps that are all quite similar. Consistent with this, in the UV-vis spectra described above, all of these Pt(II) complexes have very similar low-energy absorption maxima, ascribed to the formazanate-centered HOMO→LUMO ($\pi \rightarrow \pi^*$) transition.

5.3 Conclusion

In this chapter, we show that flexidentate, redox-active pyridine-substituted formazanates can template the assembly of a variety of dinuclear assemblies. The formazanates exhibit three distinct binding modes in the five dinuclear complexes, which include diiridium, diplatinum, and mixed platinum-iridium constructs. The redox and optical properties are dominated by the formazanate dinucleating ligand, and they do depend on the nuclearity of the complex, the binding mode of the formazanate, as well as the metals that are coordinated. This work shows that these types of formazanates are versatile ligands for the facile assembly of complex structures, where the frontier orbitals of the formazanate can play a large role in determining the electronic structure, redox potentials, and excited-state chemistry of the resulting assemblies. We believe that the two flexidentate formazanates described here, as well as related derivatives, will emerge as ideal scaffolds for the assembly of polynuclear coordination complexes with desirable properties.

5.4 Experimental section

5.4.1 Materials

Reactions were carried out in a nitrogen atmosphere using standard Schlenk techniques. Solvents, starting materials, and reagents were of commercial origin and used without further purification unless stated otherwise below. Tetrahydrofuran (THF), methanol (MeOH), and toluene for UV-vis spectroscopy, and dichloromethane (DCM) for electrochemical measurements were dried by the method of Grubbs, passing through dual alumina columns on a commercial solvent purification system (SPS). Tetrabutylammonium hexafluorophosphate ($TBAPF_6$) was recrystallized from hot ethanol and ferrocene was sublimed at ambient pressure before use in electrochemical experiments. CD_2Cl_2, $CDCl_3$, and CD_3CN for NMR spectroscopy were stored over potassium carbonate and molecular sieves to remove acidic impurities and moisture. The ligand 3-(2-pyridyl)-1,5-bis(4-methylphenyl)formazan (**Fzj**) was prepared by following the literature procedure[37] and 3-(4-pyridyl)-1,5-bis(4-methylphenyl)formazan (**Fzi**) was prepared by a modified version described below. The iridium precursor $[Ir(F_2ppy)_2(\mu\text{-}Cl)]_2$ (F_2ppy = 2-(2,4-difluorophenyl)pyridine), and platinum precursors $[Pt(ppy)(\mu\text{-}Cl)]_2$ (ppy = 2-phenylpyridine) and $Pt(tbbpy)Cl_2$(tbbpy =4,4'-di-tert-butyl-2,2'-dipyridine), were prepared by a modified version of well-known procedures.[117,118,168–170]

5.4.2 Physical methods.

NMR spectra were recorded at room temperature using a JEOL ECA-600 or ECA-500 NMR spectrometer and ar shown in appendix. UV–vis absorption spectra were recorded in

THF, toluene, and MeOH solutions in screw-capped 1 cm quartz cuvettes using an Agilent Cary 8454 UV–vis spectrophotometer. Cyclic voltammetry (CV) measurements were performed with a CH Instruments 602E potentiostat interfaced with a nitrogen glovebox via wire feedthroughs. Samples were dissolved in dichloromethane (CH_2Cl_2) with 0.1 M $TBAPF_6$ as a supporting electrolyte. A 3 mm diameter glassy carbon working electrode, a platinum wire counter electrode, and a silver wire pseudo-reference electrode were used. Potentials were referenced to an internal standard of ferrocene. The static nanoESI-MS experiments were carried out using a Thermo Exactive mass spectrometer and operated in positive ionization mode, with a spray voltage of 1.5 kV.

5.4.3 Synthesis of compounds

Ligand Fzi. The title compound was prepared by a modified version of the literature procedure used for Fzb. 4-pyridinecarboxaldehyde (1.76g, 16.4 mmol) was dissolved in ethanol (50 mL) with p-tolylhydrazine hydrochloride (2.62 g, 16.5 mmol). After stirring for 2 h, a dark red precipitate had formed. The mixture was treated with Na_2CO_3 (8.25g, 77.8 mmol), tetrabutylammonium bromide (0.630 g, 1.95 mmol), water (50 mL), and dichloromethane (100 mL) before being stirred at 0 °C for 1 h and the color turned yellow. In a separate flask, p-toluidine (2.03g, 18.9 mmol) and 12 M concentrated hydrochloric acid (10.0 mL) were mixed in deionized H_2O (10 mL) and cooled in an ice bath. A cooled solution of sodium nitrite (1.60 g, 23.2 mmol) was added slowly to the amine solution over a 5 min period and this mixture was stirred at 0°C for 30 min, after which time it was added dropwise to the biphasic reaction mixture described above over a 10 min period. The resulting solution was stirred for overnight, gradually turning dark red over this time. The reaction completion

was confirmed by TLC. The resulting dark red organic layer obtained after biphasic extraction from dichloromethane/water was dehydrated by MgSO4 and concentrated to dryness. The crude product was purified via column chromatography (neutral alumina stationary phase and hexane / ethyl acetate gradient eluent), and the eluate was concentrated in vacuo to afford **Fzi** as dark red solid. Yield: 4.80 g (89%). ^{1}H NMR (500 MHz, $CDCl_3$): δ 15.71 (s, 1H, NH), 8.59 (d, J = 4.9 Hz, 2H, ArH), 7.92 (d, J = 5.0 Hz, 2H, ArH), 7.49 (d, J = 7.9 Hz , 4H, ArH), 7.22 (d, J = 7.9 Hz, 4H, ArH), 2.36 (s, 6H, CH_3). ^{13}C{^{1}H} NMR (126 MHz, $CDCl_3$): δ 149.9, 145.4, 145.3, 138.5, 138.3, 130.3, 119.7, 119.0, 21.4 (*C*H_3). HRMS-ESI (m/z): $[M+H]^+$ calcd for $C_{20}H_{19}N_5$: 330.16405; found: 330.17062. Anal. Calcd for $C_{20}H_{19}N_5$: C, 72.92, H, 5.81, N, 21.26. Found: C, 73.10, H, 5.68, N, 21.38.

Complex 40. $[Ir(F_2ppy)_2(\mu\text{-}Cl)]_2$ (61 mg, 0.050 mmol) and **Fzi** (33 mg, 0.10 mmol) were combined in ethanol (10 mL), and the mixture was deoxygenated under the protection of N_2 and refluxed for 24 h. A red precipitate was observed at the bottom of the flask after the reaction was completed. The solvent was removed by filtration, and the solid was re-crystalized from ethyl acetate by vapour diffusion of pentane. Yield: 50 mg (53%). ^{1}H NMR (600 MHz, CD_2Cl_2): δ 15.79 (s, 1H, NH), 9.89 (d, *J* = 5.5 Hz, 1H, ArH), 8.29 (d, *J* = 8.4 Hz, 1H, ArH), 8.17 (d, *J* = 5.7 Hz, 1H, ArH), 8.12 (d, *J* = 8.3 Hz, 1H, ArH), 7.93 (s, 2H, ArH), 7.81 (t, *J* = 7.8 Hz, 1H, ArH), 7.75 (t, *J* = 7.8 Hz, 1H, ArH), 7.54 (d, *J* = 8.2 Hz, 5H, ArH), 7.29–7.24 (m, 6H, ArH), 7.11 (t, *J* = 6.5 Hz, 1H, ArH), 6.42 (t, *J* = 11.5 Hz, 1H, ArH), 6.35 (t, *J* = 11.7 Hz, 1H, ArH), 5.84 (dd, *J* = 8.6, 2.0 Hz, 1H, ArH), 5.63 (dd, *J* = 8.7, 1.9 Hz, 1H, ArH), 2.37 (s, 6H, CH_3). ^{19}F NMR (470 MHz, $CDCl_3$) δ −107.2 (dd, *J* = 18.8, 9.3 Hz, 1F), −108.3 (dd, *J* = 18.7, 9.3 Hz, 1F), −109.7 (t, *J* = 11.3 Hz, 1F), −110.7 (t, *J* = 11.4 Hz, 1F).

$^{13}C\{^{1}H\}$ NMR (151 MHz, $CDCl_3$): δ 166.4 (d, J_{CF} = 6.9 Hz), 164.7 (d, J_{CF} = 6.8 Hz), 164.5 (d, J_{CF} = 12.3 Hz), 163.7 (d, J_{CF} = 12.2 Hz), 162.9 (d, J_{CF} = 12.8 Hz), 162.0 (t, J_{CF} = 13.3 Hz), 161.7 (d, J_{CF} = 13.1 Hz), 160.2 (d, J_{CF} = 12.9 Hz), 160.0 (d, J_{CF} = 12.9 Hz), 154.8 (d, J_{CF} = 6.2 Hz), 152.5, 151.1, 149.2, 146.5, 145.0, 139.1, 138.0, 137.7, 137.3, 130.3, 128.0 (d, J_{CF} = 11.2 Hz), 123.5 (d, J_{CF} = 19.7 Hz), 122.5, 122.4, 122.1, 121.1, 119.1, 114.2 (d, J_{CF} = 17.9 Hz), 113.6 (d, J_{CF} = 16.6 Hz), 97.8 (td, J_{CF} = 26.9, 8.1 Hz), 21.4 (CH_3). HRMS-ESI (m/z): $[M-Cl]^+$ calcd for $C_{42}H_{31}N_7ClF_4Ir$: 902.22063; found: 902.21997. Anal. Calcd for $C_{42}H_{31}N_7ClF_4Ir$: C, 53.81, H, 3.33, N, 10.46. Found: C, 53.58, H, 3.56, N, 10.22.

Complex 41. $[Ir(F_2ppy)_2(\mu\text{-}Cl)]_2$ (61 mg, 0.050 mmol) and complex **40** (94 mg, 0.10 mmol) were combined in ethanol (10 mL) with excess triethylamine (0.1 mL), and the mixture was deoxygenated under the protection of N_2 and refluxed for 24 h. During the reaction the color changed from dark red to purple. The reaction completion was confirmed by TLC. Solvent was removed using rotary evaporation, and the product was re-dissolved in a minimum amount of ethyl acetate. After that column chromatography (hexane / ethyl acetate gradient eluent, neutral alumina) was performed to purify the product, which was crystallized by vapor diffusion of pentane into concentrated ethyl acetate solution. Yield: 48 mg (32%). ^{1}H NMR (600 MHz, $CDCl_3$): δ 9.98–9.82 (m, 2H, ArH), 8.61 (d, *J* = 5.6 Hz, 2H, ArH), 8.29 (d, *J* = 8.5 Hz, 1H, ArH), 8.18 (d, *J* = 5.3 Hz, 1H, ArH), 8.16–8.07 (m, 2H, ArH), 8.04 (d, *J* = 8.2 Hz, 2H, ArH), 7.81 (t, *J* = 7.9 Hz, 2H, ArH), 7.78–7.67 (m, 2H, ArH), 7.62 (s, 2H, ArH), 7.19 (t, *J* = 6.3 Hz, 1H, ArH), 7.13 (t, *J* = 6.4 Hz, 2H, ArH), 7.07–6.98 (m, 1H, ArH), 6.60 (d, *J* = 8.0 Hz, 4H, ArH), 6.39–6.27 (m, 2H, ArH), 6.25 (d, *J* = 8.1 Hz, 4H, ArH), 6.14 (t, *J* = 10.7 Hz, 2H, ArH), 5.72 (t, *J* = 7.8 Hz, 1H, ArH), 5.66–5.53 (m, 3H, ArH), 2.15 (s, 6H, CH_3). ^{19}F

NMR (470 MHz, $CDCl_3$) δ −107.5 (dt, *J* = 37.8, 18.0 Hz, 1F), −108.5 (q, *J* = 19.8 Hz, 1F), −108.6 (dd, *J* = 37.8, 19.8 Hz, 2F), −110.0 (dd, *J* = 76.5, 20.7 Hz, 1F), −110.2 (d, *J* = 45.0 Hz, 2F), −110.8 (dd, *J* = 45.9, 24.3 Hz, 1F). $^{13}C\{^1H\}$ NMR (151 MHz, $CDCl_3$): δ 165.5 (d, J_{CF} = 7.7 Hz), 165.0, 164.7 (d, J_{CF} = 6.6 Hz), 163.5 (d, J_{CF} = 10.8 Hz), 161.8, 161.7, 160.1, 157.6, 155.1, 153.1, 151.2, 151.1, 150.2, 149.8, 149.5, 149.2, 144.5, 138.4, 137.7, 137.5, 136.1, 128.7, 128.4, 128.0, 127.8, 127.5, 123.4, 123.3, 122.6, 122.4, 122.3, 121.9, 119.6, 115.5 (d, J_{CF} = 16.1 Hz), 114.3 (d, J_{CF} = 15.6 Hz), 113.5 (d, J_{CF} = 16.1 Hz), 97.7, 97.6, 97.5, 97.4, 97.2, 20.9 (CH_3). HRMS-ESI (m/z): $[M+H]^+$ calcd for $C_{64}H_{42}N_9ClF_8Ir_2$: 1510.24607; found: 1510.24463. Anal. Calcd for $C_{64}H_{42}N_9ClF_8Ir_2$: C, 50.94, H, 2.81, N, 8.35. Found: C, 50.67, H, 2.75, N, 8.26.

Complexes 42 and 43. $[Pt(ppy)(\mu\text{-}Cl)]_2$ (38 mg, 0.050 mmol) and **Fzi** (33 mg, 0.10 mmol) were added to ethanol (10 mL) with excess triethylamine (0.1 mL), and the mixture was deoxygenated under the protection of N_2 and refluxed for 24 h during which the color changed from red to dark green. The reaction completion was confirmed by TLC. Solvent was removed using rotary evaporation, and the product was re-dissolved in a minimum amount of dichloromethane. After that column chromatography (hexane/ethyl acetate gradient eluent, neutral alumina) was performed to separate and purify both green products.

42. Yield: 34 mg (64%). ^1H NMR (600 MHz, $CDCl_3$): δ 9.75 (d, *J* = 5.5 Hz, 1H, ArH), 8.88 (d, *J* = 6.1 Hz, 2H, ArH), 8.16 (d, *J* = 8.0 Hz, 2H, ArH), 8.11 (d, *J* = 8.1 Hz, 2H, ArH), 7.99 (d, *J* = 6.2 Hz, 2H, ArH), 7.96 (d, *J* = 5.6 Hz, 1H, ArH), 7.81 (t, *J* = 7.7 Hz, 1H, ArH), 7.67 (dd, *J* = 16.8, 8.1 Hz, 2H, ArH), 7.62 (d, *J* = 8.1 Hz, 1H, ArH), 7.47 (d, *J* = 7.6 Hz, 1H, ArH), 7.41 (d, *J* = 7.6 Hz, 1H, ArH), 7.22 (d, *J* = 8.0 Hz, 2H, ArH), 7.15 (d, *J* = 7.8 Hz, 3H, ArH),

7.09 (t, *J* = 7.4 Hz, 1H, ArH), 6.98 (dt, *J* = 14.6, 7.5 Hz, 2H, ArH), 6.78 (t, *J* = 7.4 Hz, 1H, ArH), 6.66 (t, *J* = 6.5 Hz, 1H, ArH), 6.59 (d, *J* = 7.7 Hz, 1H, ArH), 6.52 (d, *J* = 7.7 Hz, 1H, ArH), 2.41 (s, 6H, CH_3). $^{13}C\{^1H\}$ NMR (151 MHz, $CDCl_3$): δ 152.8, 151.5, 151.4, 150.8, 150.7, 150.0, 149.9, 146.8, 146.2, 145.9, 142.2, 142.1, 138.8, 138.7, 138.4, 138.3, 136.7, 131.3, 130.3, 130.1, 129.3, 126.0, 125.92, 125.87, 124.8, 124.1, 123.6, 123.5, 123.0, 121.9, 121.1, 120.4, 118.6, 118.2, 21.31 (*C*H_3), 21.26 (*C*H_3). HRMS-ESI (m/z): $[M-Cl]^+$ calcd for $C_{42}H_{34}N_7ClPt_2$: 1026.21712; found: 1026.21606. Anal. Calcd for $C_{42}H_{34}N_7ClPt_2$: C, 47.48, H, 3.23, N, 9.23. Found: C, 47.37, H, 3.44, N, 9.25.

43. Yield: 8 mg (12%). ^1H NMR (600 MHz, $CDCl_3$): δ 8.62 (d, *J* = 5.4 Hz, 2H, ArH), 8.18 (d, *J* = 8.2 Hz, 2H, ArH), 8.13 (d, *J* = 8.2 Hz, 2H, ArH), 8.02 (d, *J* = 5.8 Hz, 1H, ArH), 7.92 (d, *J* = 5.6 Hz, 2H, ArH), 7.65 (t, *J* = 7.4 Hz, 1H, ArH), 7.60 (d, *J* = 7.9 Hz, 1H, ArH), 7.42 (d, *J* = 7.6 Hz, 1H, ArH), 7.19 (d, *J* = 8.1 Hz, 2H, ArH), 7.14 (d, *J* = 8.2 Hz, 2H, ArH), 6.95 (t, *J* = 7.4 Hz, 1H, ArH), 6.78 (t, *J* = 7.5 Hz, 1H, ArH), 6.66 (t, *J* = 6.7 Hz, 1H, ArH), 6.63 (d, *J* = 7.7 Hz, 1H, ArH), 2.40 (s, 6H, CH_3). $^{13}C\{^1H\}$ NMR (151 MHz, $CDCl_3$): δ 168.3, 151.1, 150.7, 150.6, 150.0, 149.3, 147.1, 146.7, 145.6, 144.8, 138.4, 137.5, 137.3, 136.5, 129.7, 128.9, 125.7, 124.5, 123.7, 122.7, 120.8, 118.8, 118.3, 21.03 (*C*H_3), 20.99 (*C*H_3). HRMS-ESI (m/z): $[M+H]^+$ calcd for $C_{31}H_{26}N_6Pt$: 678.19449; found: 678.19379. Anal. Calcd for $C_{31}H_{26}N_6Pt$: C, 54.94, H, 3.87, N, 12.40. Found: C, 54.85, H, 3.98, N, 12.16.

Complex 44. $[Ir(F_2ppy)_2(\mu\text{-}Cl)]_2$ (61 mg, 0.050 mmol), $[Pt(ppy)(\mu\text{-}Cl)]_2$ (38 mg, 0.050 mmol) and **Fzi** (33 mg, 0.10 mmol) were added to ethanol (10 mL) with excess triethylamine (0.1 mL), and the mixture was deoxygenated under the protection of N_2 and refluxed for 24 h. A

green precipitate was observed at the bottom of the flask after the reaction was completed. Solvent was removed by filtration, and the solid was re-crystalized from ethyl acetate and pentane to purify the product, which was crystallized again by vapor diffusion of pentane into concentrated ethyl acetate solution. Yield: 92 mg (72%). ^{1}H NMR (600 MHz, $CDCl_3$): δ 9.93 (d, *J* = 5.4 Hz, 1H, ArH), 8.30 (d, *J* = 8.4 Hz, 1H, ArH), 8.16 (d, *J* = 5.5 Hz, 1H, ArH), 8.11 (d, *J* = 8.3 Hz, 1H, ArH), 8.08 (d, *J* = 8.1 Hz, 2H, ArH), 8.03 (d, *J* = 8.1 Hz, 2H, ArH), 7.90 (d, *J* = 5.5 Hz, 1H, ArH), 7.82 (s, 2H, ArH), 7.75 (t, *J* = 7.7 Hz, 1H, ArH), 7.70 (t, *J* = 7.7 Hz, 1H, ArH), 7.64 (t, *J* = 7.7 Hz, 1H, ArH), 7.58 (d, *J* = 7.9 Hz, 2H, ArH), 7.38 (d, *J* = 7.6 Hz, 2H, ArH), 7.22 (t, *J* = 6.6 Hz, 1H, ArH), 7.17 (d, *J* = 8.0 Hz, 2H, ArH), 7.11 (d, *J* = 8.1 Hz, 2H, ArH), 7.05 (t, *J* = 6.5 Hz, 1H, ArH), 6.93 (t, *J* = 7.4 Hz, 1H, ArH), 6.74 (t, *J* = 7.4 Hz, 1H, ArH), 6.63 (t, *J* = 6.4 Hz, 1H, ArH), 6.52 (d, *J* = 7.6 Hz, 1H, ArH), 6.41 (t, *J* = 10.1 Hz, 1H, ArH), 6.32 (t, *J* = 10.8 Hz, 1H, ArH), 5.79 (d, *J* = 8.3 Hz, 1H, ArH), 5.65 (d, *J* = 10.2 Hz, 1H, ArH), 2.38 (s, 6H, CH_3). ^{19}F NMR (470 MHz, $CDCl_3$) δ −107.3 (dd, *J* = 17.8, 8.8 Hz, 1F), −108.5 (dd, *J* = 17.4, 8.5 Hz, 1F), −109.8 (t, *J* = 10.8 Hz, 1F), −110.8 (t, *J* = 10.7 Hz, 1F). ^{13}C{^{1}H} NMR (151 MHz, $CDCl_3$): δ 168.5, 165.4(d, J_{CF} = 6.4 Hz), 164.65, 164.55, 163.8(d, J_{CF} = 12.3 Hz), 162.8 (d, J_{CF} = 12.8 Hz), 162.0 (t, J_{CF} = 14.2 Hz), 161.7 (d, J_{CF} = 12.8 Hz), 160.7, 160.3, 160.1, 154.8 (d, J_{CF} = 6.4 Hz), 152.8 (d, J_{CF} = 6.9 Hz), 151.1, 150.7, 150.2, 149.9, 149.3, 146.3, 146.2, 145.8, 138.8, 138.3, 138.2, 137.9, 137.6, 136.6, 130.1, 129.2, 128.0, 125.8, 124.7, 124.1, 123.4, 123.3(d, J_{CF} = 19.7 Hz), 123.0, 122.50, 122.46, 122.4, 122.1, 121.1, 120.2, 118.7, 114.2 (d, J_{CF} = 17.5 Hz), 113.5 (d, J_{CF} = 16.5 Hz), 97.73 (t, J_{CF} = 26.8 Hz), 97.66 (t, J_{CF} = 26.8 Hz), 21.3 (CH_3), 21.2 (CH_3). HRMS-ESI (m/z): $[M-Cl]^+$

calcd for $C_{53}H_{38}N_8F_4ClIrPt$:1250.24325; found: 1250.23779. Anal. Calcd for $C_{53}H_{38}N_8F_4ClIrPt$: C, 49.51, H, 2.98, N, 8.72. Found: C, 49.27, H, 2.88, N, 8.69.

Complex 45. The title compound was prepared by the general method described above for complex **43**, using $Pt(tbbpy)Cl_2$ (53 mg, 0.10 mmol) and **Fzj** (33 mg, 0.10 mmol). Yield: 58 mg (70%). ^1H NMR (600 MHz, CD_3CN): δ 8.62 (d, *J* = 4.5 Hz, 1H, ArH), 8.26 (s, 2H, ArH), 8.14 (d, *J* = 8.1 Hz, 4H, ArH), 8.08 (d, *J* = 8.0 Hz, 1H, ArH), 7.86 (t, *J* = 7.7 Hz, 1H, ArH), 7.59 (d, *J* = 6.2 Hz, 2H, ArH), 7.39 (dd, *J* = 7.2, 4.9 Hz, 1H, ArH), 7.25 (d, *J* = 8.1 Hz, 4H, ArH), 7.13 (d, *J* = 6.1 Hz, 2H, ArH), 2.40 (s, 6H, CH_3), 1.33 (s, 18H, CH_3). $^{13}C\{^1H\}$ NMR (151 MHz, $CDCl_3$): δ 168.2, 157.1, 155.1, 153.0, 149.7, 149.4, 147.4, 139.8, 136.6, 134.1, 130.4, 125.3, 124.9, 123.8, 122.9, 121.3, 36.8 ($C(CH_3)_3$), 30.5 ($C(CH_3)_3$), 21.4 (CH_3). HRMS-ESI (m/z): $[M-Cl]^+$ calcd for $C_{38}H_{41}N_7ClPt$: 791.31494; found: 791.31396. Anal. Calcd for $C_{38}H_{41}N_7ClPt$: C, 55.23, H, 5.00, N, 11.87. Found: C, 55.26, H, 5.18, N, 11.93.

Complex 46. The title compound was prepared by the general method described above for complex **43**, using $[Pt(ppy)(\mu\text{-}Cl)]_2$ (38 mg, 0.050 mmol) and **Fzj** (33 mg, 0.10 mmol). Yield: 46 mg (68%). ^1H NMR (600 MHz, $CDCl_3$): δ 8.71 (d, *J* = 4.4 Hz, 1H, ArH), 8.26 (d, *J* = 8.0 Hz, 2H, ArH), 8.17 (d, *J* = 8.0 Hz, 2H, ArH), 8.10 (d, *J* = 8.3 Hz, 2H, ArH), 7.74 (t, *J* = 7.6 Hz, 1H, ArH), 7.63 (t, *J* = 7.6 Hz, 1H, ArH), 7.57 (d, *J* = 8.0 Hz, 1H, ArH), 7.40 (d, *J* = 7.6 Hz, 1H, ArH), 7.23 – 7.18 (m, 1H, ArH), 7.16 (d, *J* = 8.0 Hz, 2H, ArH), 7.13 (d, *J* = 8.0 Hz, 2H, ArH), 6.94 (t, *J* = 7.4 Hz, 1H, ArH), 6.77 (t, *J* = 7.4 Hz, 1H, ArH), 6.68 (d, *J* = 7.7 Hz, 1H, ArH), 6.63 (t, *J* = 6.5 Hz, 1H, ArH), 2.38 (s, 3H, CH_3), 2.37 (s, 3H, CH_3). $^{13}C\{^1H\}$ NMR (151 MHz, $CDCl_3$): δ 168.4, 155.0, 153.8, 151.0, 150.8, 150.1, 149.4, 147.5, 145.9, 138.5, 137.4, 137.2, 136.9, 136.1, 129.8, 129.13, 129.09, 125.9, 124.9, 123.7, 122.9, 122.5, 121.0,

120.8, 118.5, 21.3 (CH_3), 21.2 (CH_3). HRMS-ESI (m/z): $[M+H]^+$ calcd for $C_{31}H_{26}N_6Pt$: 678.19449; found: 678.19391. Anal. Calcd for $C_{31}H_{26}N_6Pt$: C, 54.94, H, 3.87, N, 12.40. Found: C, 54.99, H, 3.79, N, 12.62.

Complex 47. Complex **45** (40 mg, 0.048 mmol) was treated with $Pt(DMSO)_2Cl_2$ (21 mg, 0.050 mmol) in a degassed solution of acetonitrile (10 mL). The mixture was deoxygenated under the protection of N_2 and refluxed for 24 h and then it was cooled down to 0 °C. The color changed from blue to green. The reaction completion was confirmed by TLC. Solvent was removed using rotary evaporation, and the product was re-dissolved in a minimum amount of ethyl acetate. After that column chromatography (hexane/ethyl acetate gradient eluent, neutral alumina) was performed to purify the product. Yield: 32 mg (59%). ^{1}H NMR (600 MHz, CD_3CN): δ 9.52 (d, *J* = 6.2 Hz, 1H, ArH), 8.81 (s, 1H, ArH), 8.36 (d, *J* = 8.4 Hz, 2H, ArH), 8.32 (d, *J* = 6.3 Hz, 1H, ArH), 8.29 (d, *J* = 8.4 Hz, 2H, ArH), 8.26 (d, *J* = 8.2 Hz, 1H, ArH), 8.04 (d, *J* = 1.8 Hz, 1H, ArH), 7.97 (d, *J* = 1.8 Hz, 1H, ArH), 7.88 (s, 1H, ArH), 7.68 (dd, *J* = 6.2, 2.0 Hz, 1H, ArH), 7.45 (dd, *J* = 6.2, 1.9 Hz, 1H, ArH), 7.22 (d, *J* = 8.3 Hz, 2H, ArH), 7.18 – 7.12 (m, 1H, ArH), 6.85 (d, *J* = 8.4 Hz, 2H, ArH), 2.34 (s, 3H, CH_3), 2.16 (s, 3H, CH_3), 1.32 (s, 9H, CH_3), 1.31 (s, 9H, CH_3). $^{13}C\{^1H\}$ NMR (151 MHz, CD_3CN): δ 165.4, 165.3, 157.2, 155.6, 152.4, 150.8, 149.7, 149.6, 149.5, 148.4, 145.7, 138.8, 138.2, 137.2, 129.3, 127.9, 125.9, 125.4, 124.0, 123.5, 123.3, 122.5, 121.4, 120.7, 35.8 ($C(CH_3)_3$), 35.7 ($C(CH_3)_3$), 29.34 ($C(CH_3)_3$), 29.30 ($C(CH_3)_3$), 20.2 (CH_3), 20.1 (CH_3). HRMS-ESI (m/z): $[M+H]^+$ calcd for $C_{38}H_{42}N_7Cl_3Pt_2$: 1094.19410; found: 1094.19067. Anal. Calcd for $C_{38}H_{42}N_7Cl_3Pt_2$: C, 41.75, H, 3.87, N, 8.97. Found: C, 41.58, H, 3.91, N, 9.25.

Complex 48. Fzj (33 mg, 0.10 mmol) was treated with $Pt(DMSO)_2Cl_2$ (42 mg, 0.10 mmol) in a degassed solution of acetonitrile (10 mL). The mixture was deoxygenated under the protection of N_2 and refluxed for 24 h and then it was cooled down to 0 °C. The color changed from red to purple. The reaction completion was confirmed by TLC. Solvent was removed using rotary evaporation, and the product was re-dissolved in a minimum amount of ethyl acetate. After that column chromatography (hexane/ethyl acetate gradient eluent, neutral alumina) was performed to purify the product. Yield: 36 mg (64%). ^{1}H NMR (600 MHz, $CDCl_3$): δ 13.70 (s, 2H, ArH), 8.89 (s, 2H, ArH), 8.00 (dt, *J* = 15.4, 7.8 Hz, 4H, ArH), 7.62 (d, *J* = 7.2 Hz, 2H, ArH), 7.54 (s, 2H, ArH), 7.43 (s, 2H, ArH), 7.33 (d, *J* = 7.6 Hz, 4H, ArH), 7.22 (d, *J* = 7.7 Hz, 4H, ArH), 6.93 (d, *J* = 7.7 Hz, 2H, ArH), 2.35 (s, 6H, CH_3), 2.31 (s, 6H, CH_3). $^{13}C\{^1H\}$ NMR (151 MHz, $CDCl_3$): δ 164.1, 156.9, 147.1, 146.6, 145.4, 139.6, 139.4, 137.8, 135.1, 134.9, 130.5, 127.9, 126.2, 124.5, 121.8, 115.5, 22.9 (*C*H_3), 21.2 (*C*H_3). HRMS-ESI (m/z): $[M-Cl]^+$ calcd for $C_{40}H_{36}N_{10}Cl_2Pt_2$: 1082.21084; found: 1082.21008. Anal. Calcd for $C_{40}H_{36}N_{10}Cl_2Pt_2$: C, 42.98, H, 3.25, N, 12.53. Found: C, 42.97 , H, 3.14, N, 12.40.

5.4.4 X-ray Crystallography Details.

Single crystals of **40**, **41**, **43**, **44**, **45**, **46**, **47,** and **48** were grown by diffusing pentane into concentrated chloroform, dichloromethane, or ethyl acetate (EA) solutions. Crystals were mounted on a Bruker Apex II three-circle diffractometer using MoKα radiation (λ = 0.71073 Å), conducted by Prof.Teets. The data were collected at 123(2) K and processed and refined within the APEXII software. Structures were solved by intrinsic phasing methods in SHELXT and refined by standard difference Fourier techniques in the program SHELXL.[78] The most

disagreeable reflections, identified from the .lst file, were omitted from refinement. Carbon-bound hydrogen atoms were placed in calculated positions using the standard riding model and refined isotropically. The N–*H* hydrogen atoms in **40** were located in the difference map, constrained to a distance of 0.88 Å, and refined isotropically. For one of the two crystallographically independent molecules, an additional restraint (FLAT) was used to ensure the N-bound hydrogen atom remained coplanar with the formazanate core. All non-hydrogen atoms were refined anisotropically. In the structure of **43**, the 4-pyridyl ring was modelled as a 2-part rotational disorder, and the structures of **45** and **48** each included a disordered dichloromethane solvate. The 1,2 and 1,3 distances were restrained (SADI), and rigid bond restraints (SIMU and DELU) were used on ellipsoid parameters. The structures of **41** and **44** included electron density attributed to heavily disordered solvent that could not be modelled, necessitating the use of the SQUEEZE function in PLATON.[171] Complexes **40**, **41**, and **44** crystallized as thin plates, which led to some minor issues with absorption correction that resulted in level A checkCIF errors for residual electron density near the metal centers. We don't believe these checkCIF errors indicate any significant problems with the model.

6 Bibliography

(1) Escuer, A.; Comas, T.; Vicente, R.; Ribas, J. Complexes with Diimine Ligands. Syntheses and Magnetic Behaviour of Dinuclear Complexes of Copper(II), Nickel(II) and Cobalt(II) with 2,5-Bis(2-Pyridyl)Pyrazine. *Transit. Met. Chem.* **1993**, *18* (1), 42–44.

(2) Kaim, W. The Coordination Chemistry of 1,2,4,5-Tetrazines. *Coord. Chem. Rev.* **2002**, *230* (1), 127–139.

(3) Kaim, W. Manifestations of Noninnocent Ligand Behavior. *Inorg. Chem.* **2011**, *50* (20), 9752–9765.

(4) Kaim, W.; Schwederski, B. Non-Innocent Ligands in Bioinorganic Chemistry—An Overview. *Coord. Chem. Rev.* **2010**, *254* (13), 1580–1588.

(5) Lyaskovskyy, V.; de Bruin, B. Redox Non-Innocent Ligands: Versatile New Tools to Control Catalytic Reactions. *ACS Catal.* **2012**, *2* (2), 270–279.

(6) Luca, O. R.; Crabtree, R. H. Redox-Active Ligands in Catalysis. *Chem. Soc. Rev.* **2013**, *42* (4), 1440–1459.

(7) Zarkesh, R. A.; Ichimura, A. S.; Monson, T. C.; Tomson, N. C.; Anstey, M. R. Voltage Clustering in Redox-Active Ligand Complexes: Mitigating Electronic Communication through Choice of Metal Ion. *Dalton Trans.* **2016**, *45* (24), 9962–9969.

(8) Ketterer, N. A.; Fan, H.; Blackmore, K. J.; Yang, X.; Ziller, J. W.; Baik, M.-H.; Heyduk, A. F. Π•−π• Bonding Interactions Generated by Halogen Oxidation of Zirconium(IV) Redox-Active Ligand Complexes. *J. Am. Chem. Soc.* **2008**, *130* (13), 4364–4374.

(9) Cameron, L. A.; Ziller, J. W.; Heyduk, A. F. Near-IR Absorbing Donor–Acceptor Ligand-to-Ligand Charge-Transfer Complexes of Nickel(Ii). *Chem. Sci.* **2016**, *7* (3), 1807–1814.

(10) Nineham, A. W. The Chemistry of Formazans and Tetrazolium Salts. *Chem. Rev.* **1955**, *55* (2), 355–483.

(11) Shawali, A. S.; Samy, N. A. Functionalized Formazans: A Review on Recent Progress in Their Pharmacological Activities. *J. Adv. Res.* **2015**, *6* (3), 241–254..

(12) Bernas, T.; Dobrucki, J. Mitochondrial and Nonmitochondrial Reduction of MTT: Interaction of MTT with TMRE, JC-1, and NAO Mitochondrial Fluorescent Probes. *Cytometry* **2002**, *47* (4), 236–242.

(13) Berridge, M. V.; Herst, P. M.; Tan, A. S. Tetrazolium Dyes as Tools in Cell Biology: New Insights into Their Cellular Reduction. In *Biotechnology Annual Review*; Elsevier, 2005; Vol. 11, pp 127–152.

(14) Gilroy, J. B.; McKinnon, S. D. J.; Koivisto, B. D.; Hicks, R. G. Electrochemical Studies of Verdazyl Radicals. *Org. Lett.* **2007**, *9* (23), 4837–4840.

(15) Koivisto, B. D.; Hicks, R. G. The Magnetochemistry of Verdazyl Radical-Based Materials. *Coord. Chem. Rev.* **2005**, *249* (23), 2612–2630.

(16) Neugebauer, F. A. Hydrazidinyl Radicals: 1 2,4,5-Tetraazapentenyls, Verdazyls, and Tetrazolinyls. *Angew. Chem. Int. Ed. Engl.* **1973**, *12* (6), 455–464.

(17) Katritzky, A. A.; Belyakov, S. A.; Cheng, D.; Durst, H. D. Syntheses of Formazans Under Phase-Transfer Conditions. *Synthesis* **1995**, *1995* (5), 577–581.
(18) Hubbard, D. M.; Scott, E. W. Synthesis of Di-Beta-Naphthylthiocarbazone and Some of Its Analogs *. *J. Am. Chem. Soc.* **1943**, *65* (12), 2390–2393.
(19) Gilroy, J. B.; Otieno, P. O.; Ferguson, M. J.; McDonald, R.; Hicks, R. G. Synthesis and Characterization of 3-Cyano- and 3-Nitroformazans, Nitrogen-Rich Analogues of β-Diketimine Ligands. *Inorg. Chem.* **2008**, *47* (4), 1279–1286.
(20) Gilroy, J. B.; Otten, E. Formazanate Coordination Compounds: Synthesis, Reactivity, and Applications. *Chem. Soc. Rev.* **2020**, *49* (1), 85–113.
(21) Sarish, S. P.; Nembenna, S.; Nagendran, S.; Roesky, H. W. Chemistry of Soluble β-Diketiminatoalkaline-Earth Metal Complexes with M−X Bonds (M = Mg, Ca, Sr; X = OH, Halides, H). *Acc. Chem. Res.* **2011**, *44* (3), 157–170.
(22) Tsai, Y.-C. The Chemistry of Univalent Metal β-Diketiminates. *Coord. Chem. Rev.* **2012**, *256* (5), 722–758.
(23) Bourget-Merle, L.; Lappert, M. F.; Severn, J. R. The Chemistry of β-Diketiminatometal Complexes. *Chem. Rev.* **2002**, *102* (9), 3031–3066.
(24) Travieso-Puente, R.; Chang, M.-C.; Otten, E. Alkali Metal Salts of Formazanate Ligands: Diverse Coordination Modes as a Result of the Nitrogen-Rich [NNCNN] Ligand Backbone. *Dalton Trans.* **2014**, *43* (48), 18035–18041.
(25) Travieso-Puente, R.; Broekman, J. O. P.; Chang, M.-C.; Demeshko, S.; Meyer, F.; Otten, E. Spin-Crossover in a Pseudo-Tetrahedral Bis(Formazanate) Iron Complex. *J. Am. Chem. Soc.* **2016**, *138* (17), 5503–5506.
(26) Chang, M.-C.; Dann, T.; Day, D. P.; Lutz, M.; Wildgoose, G. G.; Otten, E. The Formazanate Ligand as an Electron Reservoir: Bis(Formazanate) Zinc Complexes Isolated in Three Redox States. *Angew. Chem. Int. Ed.* **2014**, *53* (16), 4118–4122.
(27) Travieso-Puente, R.; Budzak, S.; Chen, J.; Stacko, P.; Jastrzebski, J. T. B. H.; Jacquemin, D.; Otten, E. Arylazoindazole Photoswitches: Facile Synthesis and Functionalization via SNAr Substitution. *J. Am. Chem. Soc.* **2017**, *139* (9), 3328–3331.
(28) Gilroy, J. B.; Ferguson, M. J.; McDonald, R.; Patrick, B. O.; Hicks, R. G. Formazans as β-Diketiminate Analogues. Structural Characterization of Boratatetrazines and Their Reduction to Borataverdazyl Radical Anions. *Chem. Commun.* **2006**, No. 2, 126–128.
(29) Chang, M.-C.; Otten, E. Synthesis and Ligand-Based Reduction Chemistry of Boron Difluoride Complexes with Redox-Active Formazanate Ligands. *Chem. Commun.* **2014**, *50* (56), 7431–7433.
(30) Barbon, S. M.; Reinkeluers, P. A.; Price, J. T.; Staroverov, V. N.; Gilroy, J. B. Structurally Tunable 3-Cyanoformazanate Boron Difluoride Dyes. *Chem. – Eur. J.* **2014**, *20* (36), 11340–11344.
(31) Barbon, S. M.; Price, J. T.; Reinkeluers, P. A.; Gilroy, J. B. Substituent-Dependent Optical and Electrochemical Properties of Triarylformazanate Boron Difluoride Complexes. *Inorg. Chem.* **2014**, *53* (19), 10585–10593.

(32) Barbon, S. M.; Staroverov, V. N.; Gilroy, J. B. Effect of Extended π Conjugation on the Spectroscopic and Electrochemical Properties of Boron Difluoride Formazanate Complexes. *J. Org. Chem.* **2015**, *80* (10), 5226–5235.
(33) Chang, M.-C.; Chantzis, A.; Jacquemin, D.; Otten, E. Boron Difluorides with Formazanate Ligands: Redox-Switchable Fluorescent Dyes with Large Stokes Shifts. *Dalton Trans.* **2016**, *45* (23), 9477–9484.
(34) Maar, R. R.; Zhang, R.; Stephens, D. G.; Ding, Z.; Gilroy, J. B. Near-Infrared Photoluminescence and Electrochemiluminescence from a Remarkably Simple Boron Difluoride Formazanate Dye. *Angew. Chem. Int. Ed.* **2019**, *58* (4), 1052–1056.
(35) Maar, R. R.; Gilroy, J. B. Aggregation-Induced Emission Enhancement in Boron Difluoride Complexes of 3-Cyanoformazanates. *J. Mater. Chem. C* **2016**, *4* (27), 6478–6482.
(36) Maar, R. R.; Barbon, S. M.; Sharma, N.; Groom, H.; Luyt, L. G.; Gilroy, J. B. Evaluation of Anisole-Substituted Boron Difluoride Formazanate Complexes for Fluorescence Cell Imaging. *Chem. – Eur. J.* **2015**, *21* (44), 15589–15599.
(37) Barbon, S. M.; Buddingh, J. V.; Maar, R. R.; Gilroy, J. B. Boron Difluoride Adducts of a Flexidentate Pyridine-Substituted Formazanate Ligand: Property Modulation via Protonation and Coordination Chemistry. *Inorg. Chem.* **2017**, *56* (19), 12003–12011.
(38) Dhindsa, J. S.; Melenbacher, A.; Barbon, S. M.; Stillman, M. J.; Gilroy, J. B. Altering the Optoelectronic Properties of Boron Difluoride Formazanate Dyes via Conjugation with Platinum(II)-Acetylides. *Dalton Trans.* **2019**.
(39) Schorn, W.; Grosse-Hagenbrock, D.; Oelkers, B.; Sundermeyer, J. Formazanido Complexes of Heavier Group 13 Elements Aluminium, Gallium, and Indium. *Dalton Trans.* **2016**, *45* (3), 1201–1207.
(40) Maar, R. R.; Rabiee Kenaree, A.; Zhang, R.; Tao, Y.; Katzman, B. D.; Staroverov, V. N.; Ding, Z.; Gilroy, J. B. Aluminum Complexes of $N_2O_2^{3-}$ Formazanate Ligands Supported by Phosphine Oxide Donors. *Inorg. Chem.* **2017**, *56* (20), 12436–12447.
(41) Barbon, S. M.; Novoa, S.; Bender, D.; Groom, H.; Luyt, L. G.; Gilroy, J. B. Copper-Assisted Azide–Alkyne Cycloaddition Chemistry as a Tool for the Production of Emissive Boron Difluoride 3-Cyanoformazanates. *Org. Chem. Front.* **2017**, *4* (2), 178–190.
(42) Novoa, S.; Gilroy, J. B. (Co)Polymers Containing Boron Difluoride 3-Cyanoformazanate Complexes: Emission Enhancement via Random Copolymerization. *Polym. Chem.* **2017**, *8* (35), 5388–5395.
(43) Gorbatenko, Yu. A.; Rezinskikh, Z. G.; Lipunova, G. N.; Pervova, I. G.; Maslakova, T. I.; Slepukhin, P. A.; Lipunov, I. N. Synthesis and Spectroscopic Features of Iron(II) 1-Aryl-5-Benzothiazol-2-Ylformazanates. *Russ. J. Appl. Chem.* **2008**, *81* (12), 2127–2131.
(44) Brown, D. A.; Bögge, H.; Lipunova, G. N.; Müller, A.; Plass, W.; Walsh, K. G. Iron and Manganese Complexes of Benzothiazolyformazans. *Inorganica Chim. Acta* **1998**, *280* (1), 30–38.
(45) Gilroy, J. B.; Patrick, B. O.; McDonald, R.; Hicks, R. G. Transition Metal Complexes of 3-Cyano- and 3-Nitroformazans. *Inorg. Chem.* **2008**, *47* (4), 1287–1294.

(46) Broere, D. L. J.; Mercado, B. Q.; Bill, E.; Lancaster, K. M.; Sproules, S.; Holland, P. L. Alkali Cation Effects on Redox-Active Formazanate Ligands in Iron Chemistry. *Inorg. Chem.* **2018**, *57* (16), 9580–9591.
(47) Frolova, N. A.; Vatsadze, S. Z.; Zavodnik, V. E.; Rakhimov, R. D.; Zyk, N. V. Pyridine-Containing Nickel(II) Bis-Formazanates: Synthesis, Structure, and Electrochemical Study. *Russ. Chem. Bull.* **2006**, *55* (10), 1810–1818.
(48) Hong, S.; Hill, L. M. R.; Gupta, A. K.; Naab, B. D.; Gilroy, J. B.; Hicks, R. G.; Cramer, C. J.; Tolman, W. B. Effects of Electron-Deficient β-Diketiminate and Formazan Supporting Ligands on Copper(I)-Mediated Dioxygen Activation. *Inorg. Chem.* **2009**, *48* (10), 4514–4523.
(49) Hong, S.; Gupta, A. K.; Tolman, W. B. Intermediates in Reactions of Copper(I) Complexes with N-Oxides: From the Formation of Stable Adducts to Oxo Transfer. *Inorg. Chem.* **2009**, *48* (14), 6323–6325.
(50) Rush, R. M.; Yoe, J. H. Colorimetric Determination of Zinc and Copper with 2-Carboxy-2´-Hydroxy-5´-Sulfoformazylbenzene. *Anal. Chem.* **1954**, *26* (8), 1345–1347.
(51) Mandal, A.; Schwederski, B.; Fiedler, J.; Kaim, W.; Lahiri, G. K. Evidence for Bidirectional Noninnocent Behavior of a Formazanate Ligand in Ruthenium Complexes. *Inorg. Chem.* **2015**, *54* (16), 8126–8135.
(52) Gilroy, J. B.; Ferguson, M. J.; McDonald, R.; Hicks, R. G. Synthesis and Characterization of Palladium Complexes of 3-Nitroformazans. *Inorganica Chim. Acta* **2008**, *361* (12), 3388–3393.
(53) Lipunova, G. N.; Rezinskikh, Z. G.; Maslakova, T. I.; Slepukhin, P. A.; Pervova, I. G.; Lipunov, I. N.; Sigeikin, G. I. Palladium(II) Benzazolylformazanates: Synthesis, Structure and Optical Properties. *Russ. J. Coord. Chem.* **2009**, *35* (3), 215–221.
(54) Kabir, E.; Wu, C.-H.; Wu, J. I.-C.; Teets, T. S. Heteroleptic Complexes of Cyclometalated Platinum with Triarylformazanate Ligands. *Inorg. Chem.* **2016**, *55* (2), 956–963.
(55) Kabir, E.; Patel, D.; Clark, K.; Teets, T. S. Spectroscopic and Electrochemical Properties of Electronically Modified Cycloplatinated Formazanate Complexes. *Inorg. Chem.* **2018**, *57* (17), 10906–10917.
(56) Mu, G.; Cong, L.; Wen, Z.; Wu, J. I.-C.; Kadish, K. M.; Teets, T. S. Homoleptic Platinum Azo-Iminate Complexes via Hydrogenative Cleavage of Formazans. *Inorg. Chem.* **2018**, *57* (15), 9468–9477.
(57) Kabir, E.; Mu, G.; Momtaz, D. A.; Bryce, N. A.; Teets, T. S. Formazanate Complexes of Bis-Cyclometalated Iridium. *Inorg. Chem.* **2019**, *58* (17), 11672–11683.
(58) Mu, G.; Wen, Z.; Wu, J. I.-C.; Teets, T. S. Azo-Triazolide Bis-Cyclometalated Ir(III) Complexes via Cyclization of 3-Cyanodiarylformazanate Ligands. *Dalton Trans.* **2020**, *49*, 3775–3785.
(59) Mu, G.; Jiang, C.; Teets, T. S. Dinuclear Complexes of Flexidentate Pyridine-Substituted Formazanate Ligands. *Chem. – Eur. J.* **2020**, *n/a* (n/a).
(60) Kalia, K. C.; Chakravorty, A. Complexes of Arylazo Oximes. II. Rhodium(III) and Palladium(II) Chelates. *Inorg. Chem.* **1969**, *8* (12), 2586–2590.

(61) Kalia, K. C.; Chakravorty, A. Complexes of Arylazooximes. I. Structure of Ligands and Cobalt(III) Chelates. *Inorg. Chem.* **1968**, *7* (10), 2016–2020.
(62) Mascharak, P. K.; Chakravorty, A. Selective Cleavage of the Two Types of Pd–N Bonds in Di-μ-Halogeno-Bis[Arylazo-Oximatopalladium(II)]. *J. Chem. Soc. Dalton Trans.* **1980**, No. 9, 1698–1702.
(63) Pal, S.; Melton, T.; Mukherjee, R.; Chakravarty, A. R.; Tomas, M.; Falvello, L. R.; Chakravorty, A. Trinucleation of Arylazo Oxime Ensembles: Structure and Reactions of Novel Linear $Fe^{II}Fe^{III}Fe^{II}$ Species. *Inorg. Chem.* **1985**, *24* (8), 1250–1257.
(64) Basu, P.; Pal, S.; Chakravorty, A. New Binuclear Iron–Vanadium Complexes of Arylazo Oximates. Crystal Structure of $[Fe(PhN{=}NCPh{=}NO)_3VO(Bipy)]PF_6$ (Bipy = 2,2′-Bipyridine). *J. Chem. Soc. Dalton Trans.* **1991**, 3217–3221.
(65) Manivannan, V.; Dutta, S.; Basu, P.; Chakravorty, A. Binding of Copper(I) and Copper(II) to the Pendent O_3-Face of Iron Arylazo Oximates: Synthesis and Structure of $Cu^{I}Fe^{II}$ and $Cu^{II}Fe^{II}_2$ Families. *Inorg. Chem.* **1993**, *32* (22), 4807–4811.
(66) Bhattacharyya, I.; Ganguly, S.; Panda, B. K.; Chakravorty, A. Oximato Bridged $Rh^{III}_2M^{II}$ and $Rh^{III}M^{I}$ Species (M^{II} = Mn, Co, Ni; M^{I} = Cu, Ag). *J. Chem. Sci.* **2008**, *120* (1), 87–93.
(67) Pal, C. K.; Chattopadhyay, S.; Sinha, C.; Chakravorty, A. A Bis(Azo−imine)Palladium(II) System with 10 Ligand π Electrons. Synthesis, Structure, Serial Redox, and Relationship to Bis(Azooximates) and Other Species. *Inorg. Chem.* **1996**, *35* (9), 2442–2447.
(68) Pramanik, S.; Roy, S.; Ghorui, T.; Ganguly, S.; Pramanik, K. Iridium(III) Mediated Reductive Transformation of Closed-Shell Azo-Oxime to Open-Shell Azo-Imine Radical Anion: Molecular and Electronic Structure, Electron Transfer, and Optoelectronic Properties. *Inorg. Chem.* **2016**, *55* (4), 1461–1468.
(69) Chakraborty, I.; Panda, B. K.; Gangopadhyay, J.; Chakravorty, A. Rhenium Chemistry of Azooximes: Oxygen Atom Transfer, Azoimine Chelation, and Imine−Oxime Contrast. *Inorg. Chem.* **2005**, *44* (4), 1054–1060.
(70) Pal, C. K.; Chattopadhyay, S.; Sinha, C.; Chakravorty, A. Synthesis, Structure, and Solution Equilibria of Diamagnetic and Paramagnetic Azooximates of Bivalent Platinum. Geometrical Change Associated with Ligand-Based Electroprotic Reactions. *Inorg. Chem.* **1994**, *33* (26), 6140–6147.
(71) Chang, M.-C.; Otten, E. Intramolecular Hydride Transfer Reactions in (Formazanate)Boron Dihydride Complexes. *Organometallics* **2016**, *35* (4), 534–542.
(72) Chang, M.-C.; Otten, E. Reduction of (Formazanate)Boron Difluoride Provides Evidence for an N-Heterocyclic B(I) Carbenoid Intermediate. *Inorg. Chem.* **2015**, *54* (17), 8656–8664.
(73) Compounds of General Interest. In *Inorganic Syntheses*; Coucouvanis, D., Ed.; John Wiley & Sons, Inc.: New York, USA, 2002; Vol. 33, pp 171–245.
(74) Samanta, S.; Ghosh, P.; Goswami, S. Recent Advances on the Chemistry of Transition Metal Complexes of 2-(Arylazo)Pyridines and Its Arylamino Derivatives. *Dalton Trans.* **2012**, *41* (8), 2213–2226.

(75) *CRC Handbook of Chemistry and Physics: A Ready-Reference Book of Chemical and Physical Data*, 84th ed.; Chemical Rubber Company, Lide, D. R., Eds.; CRC Press: Boca Raton, 2003.
(76) Kabir, E.; Wu, C.-H.; Wu, J. I.-C.; Teets, T. S. Heteroleptic Complexes of Cyclometalated Platinum with Triarylformazanate Ligands. *Inorg. Chem.* **2016**, *55*, 956–963.
(77) Gilroy, J. B.; McKinnon, S. D. J.; Koivisto, B. D.; Hicks, R. G. Electrochemical Studies of Verdazyl Radicals. *Org. Lett.* **2007**, *9*, 4837–4840.
(78) Sheldrick, G. M. A Short History of SHELX. *Acta Crystallogr. A* **2008**, *64* (1), 112–122.
(79) Pavlova, I. S.; Pervova, I. G.; Belov, G. P.; Khasbiullin, I. I.; Slepukhin, P. A. Ethylene Oligomerization Mediated by Iron Formazanates and Organoaluminum Compounds. *Pet. Chem.* **2013**, *53* (2), 127–133.
(80) Szymczyk, M.; El-Shafei, A.; Freeman, H. S. Design, Synthesis, and Characterization of New Iron-Complexed Azo Dyes. *Dyes Pigments* **2007**, *72* (1), 8–15.
(81) Gruden, C. L.; Fevig, S.; Abu-Dalo, M.; Hernandez, M. 5-Cyano-2,3-Ditolyl Tetrazolium Chloride (CTC) Reduction in a Mesophilic Anaerobic Digester: Measuring Redox Behavior, Differentiating Abiotic Reduction, and Comparing FISH Response as an Activity Indicator. *J. Microbiol. Methods* **2003**, *52* (1), 59–68.
(82) Frederiks, W. M.; Marle, J. van; Oven, C. van; Comin-Anduix, B.; Cascante, M. Improved Localization of Glucose-6-Phosphate Dehydrogenase Activity in Cells with 5-Cyano-2, 3-Ditolyl-Tetrazolium Chloride as Fluorescent Redox Dye Reveals Its Cell Cycle-Dependent Regulation. *J. Histochem. Cytochem.* **2006**, *54* (1), 47–52.
(83) Hunter, L.; Roberts, C. B. 145. The Associating Effect of the Hydrogen Atom. Part IX. The N–H–N Bond. Virtual Tautomerism of the Formazyl Compounds. *J. Chem. Soc. Resumed* **1941**, 820–823.
(84) Irving, H.; Gill, J. B.; Cross, W. R. 423. The Structure of Some Di-(3-Methyl-1,5-Diarylformazyl)-Nickel(II) Complexes. *J. Chem. Soc. Resumed* **1960**, 2087–2095.
(85) Budesinsky, B.; Svecova, J. Hydrogen and Metal Complexes of Some 3-Cyanoformazans. *Inorg. Chem.* **1971**, *10* (2), 313–317.
(86) Siedle, A. R.; Pignolet, L. H. Formazanylpalladium Compounds. Synthesis and Structure of Bis(1,3,5-Tri-p-Tolylformazanyl)Palladium. *Inorg. Chem.* **1980**, *19* (7), 2052–2056.
(87) Singha Hazari, A.; Mandal, A.; Beyer, K.; Paretzki, A.; Kaim, W.; Lahiri, G. K. Metal–Metal Bridging Using the DPPP Dye System: Electronic Configurations within Multiple Redox Series. *Inorg. Chem.* **2017**, *56* (5), 2992–3004.
(88) Milocco, F.; Demeshko, S.; Meyer, F.; Otten, E. Ferrate(II) Complexes with Redox-Active Formazanate Ligands. *Dalton Trans.* **2018**, *47* (26), 8817–8823.
(89) Broere, D. L. J.; Mercado, B. Q.; Lukens, J. T.; Vilbert, A. C.; Banerjee, G.; Lant, H. M. C.; Lee, S. H.; Bill, E.; Sproules, S.; Lancaster, K. M.; Holland, P. L. Reversible Ligand-Centered Reduction in Low-Coordinate Iron Formazanate Complexes. *Chem. – Eur. J.* **2018**, *24* (37), 9417–9425.

(90) Chang, M.-C.; Roewen, P.; Travieso-Puente, R.; Lutz, M.; Otten, E. Formazanate Ligands as Structurally Versatile, Redox-Active Analogues of β-Diketiminates in Zinc Chemistry. *Inorg. Chem.* **2015**, *54* (1), 379–388.
(91) Chang, M.-C.; Dann, T.; Day, D. P.; Lutz, M.; Wildgoose, G. G.; Otten, E. The Formazanate Ligand as an Electron Reservoir: Bis(Formazanate) Zinc Complexes Isolated in Three Redox States. *Angew. Chem. Int. Ed.* **2014**, *53* (16), 4118–4122.
(92) Protasenko, N. A.; Poddel'sky, A. I.; Bogomyakov, A. S.; Starikov, A. G.; Smolyaninov, I. V.; Berberova, N. T.; Fukin, G. K.; Cherkasov, V. K. The Chemical and Electrochemical Reduction of Heteroligand O-Semiquinonato-Formazanato Cobalt Complexes. *Inorganica Chim. Acta* **2019**, *489*, 1–7.
(93) Maar, R. R.; Catingan, S. D.; Staroverov, V. N.; Gilroy, J. B. Formazanate Complexes of Hypervalent Group 14 Elements as Precursors to Electronically Stabilized Radicals. *Angew. Chem. Int. Ed.* **2018**, *57* (31), 9870–9874.
(94) Hesari, M.; Barbon, S. M.; Staroverov, V. N.; Ding, Z.; Gilroy, J. B. Efficient Electrochemiluminescence of a Readily Accessible Boron Difluoride Formazanate Dye. *Chem. Commun.* **2015**, *51* (18), 3766–3769.
(95) Barbon, S. M.; Staroverov, V. N.; Gilroy, J. B. Structurally Diverse Boron–Nitrogen Heterocycles from an $N_2O_2^{3-}$ Formazanate Ligand. *Angew. Chem. Int. Ed.* **2017**, *56* (28), 8173–8177.
(96) Meriwether, L. S.; Breitner, E. C.; Sloan, C. L. The Photochromism of Metal Dithizonates. *J. Am. Chem. Soc.* **1965**, *87* (20), 4441–4448.
(97) Petersen, R. L.; McFarland, J. T.; Watters, K. L. Resonance Raman Study of Metal-Formazans: A Model for Complexes of Metalloenzymes with Chelate Inhibitors. *Bioinorg. Chem.* **1978**, *9* (4), 355–367.
(98) Zhang, H.-Y.; Sun, W.-X.; Wu, Q.-A.; Zhangb, H.-Q.; Chen, Y.-Y. Study on 1,5-Bis(2-Carboxyphenyl)-3-Phenylformazan and Its Complexes. *Synth. React. Inorg. Met.-Org. Chem.* **2000**, *30* (4), 571–582.
(99) Bait, S.; Meuldijk, J.; Renkema, W. E. Square Planar Complexes of Nickel(II), Palladium(II) and Platinum(II) with 1-(2-Hydroxyphenyl)-3,5-Diphenylformazan. *Transit. Met. Chem.* **1980**, *5* (1), 357–361.
(100) Balt, S.; Meuldijk, J. Solvent Effects in Square Planar Complexes: Kinetics of Substitution at 1-(2-Hydroxyphenyl)-3,5-(Diphenylformazanato)-Platinum(II) Complexes. *Inorganica Chim. Acta* **1981**, *47*, 217–223.
(101) Tsuboyama, A.; Iwawaki, H.; Furugori, M.; Mukaide, T.; Kamatani, J.; Igawa, S.; Moriyama, T.; Miura, S.; Takiguchi, T.; Okada, S.; Hoshino, M.; Ueno, K. Homoleptic Cyclometalated Iridium Complexes with Highly Efficient Red Phosphorescence and Application to Organic Light-Emitting Diode. *J. Am. Chem. Soc.* **2003**, *125* (42), 12971–12979.
(102) Longhi, E.; Cola, L. D. Iridium(III) Complexes for OLED Application. In *Iridium(III) in Optoelectronic and Photonics Applications*; John Wiley & Sons, Ltd, 2017; pp 205–274.
(103) Tamayo, A. B.; Garon, S.; Sajoto, T.; Djurovich, P. I.; Tsyba, I. M.; Bau, R.; Thompson, M. E. Cationic Bis-Cyclometalated Iridium(III) Diimine Complexes and

Their Use in Efficient Blue, Green, and Red Electroluminescent Devices. *Inorg. Chem.* **2005**, *44* (24), 8723–8732.
(104) Lowry, M. S.; Goldsmith, J. I.; Slinker, J. D.; Rohl, R.; Pascal, R. A.; Malliaras, G. G.; Bernhard, S. Single-Layer Electroluminescent Devices and Photoinduced Hydrogen Production from an Ionic Iridium(III) Complex. *Chem. Mater.* **2005**, *17* (23), 5712–5719.
(105) Lo, K. K.-W.; Ng, D. C.-M.; Chung, C.-K. First Examples of Luminescent Cyclometalated Iridium(III) Complexes as Labeling Reagents for Biological Substrates. *Organometallics* **2001**, *20* (24), 4999–5001.
(106) Lo, K. K.-W.; Chung, C.-K.; Lee, T. K.-M.; Lui, L.-H.; Tsang, K. H.-K.; Zhu, N. New Luminescent Cyclometalated Iridium(III) Diimine Complexes as Biological Labeling Reagents. *Inorg. Chem.* **2003**, *42* (21), 6886–6897.
(107) Milocco, F.; Vries, F. de; Dall'Anese, A.; Rosar, V.; Zangrando, E.; Otten, E.; Milani, B. Palladium Alkyl Complexes with a Formazanate Ligand: Synthesis, Structure and Reactivity. *Dalton Trans.* **2018**, *47* (41), 14445–14451.
(108) Protasenko, N. A.; Poddel'sky, A. I.; Bogomyakov, A. S.; Fukin, G. K.; Cherkasov, V. K. Heteroligand O-Semiquinonato-Formazanato Cobalt Complexes. *Inorg. Chem.* **2015**, *54* (13), 6078–6080.
(109) Cordero, B.; Gómez, V.; Platero-Prats, A. E.; Revés, M.; Echeverría, J.; Cremades, E.; Barragán, F.; Alvarez, S. Covalent Radii Revisited. *Dalton Trans.* **2008**, No. 21, 2832–2838.
(110) Radwan, Y. K.; Maity, A.; Teets, T. S. Manipulating the Excited States of Cyclometalated Iridium Complexes with β-Ketoiminate and β-Diketiminate Ligands. *Inorg. Chem.* **2015**, *54* (14), 7122–7131.
(111) Lai, P.-N.; Brysacz, C. H.; Alam, M. K.; Ayoub, N. A.; Gray, T. G.; Bao, J.; Teets, T. S. Highly Efficient Red-Emitting Bis-Cyclometalated Iridium Complexes. *J. Am. Chem. Soc.* **2018**, *140* (32), 10198–10207.
(112) Lamansky, S.; Djurovich, P.; Murphy, D.; Abdel-Razzaq, F.; Kwong, R.; Tsyba, I.; Bortz, M.; Mui, B.; Bau, R.; Thompson, M. E. Synthesis and Characterization of Phosphorescent Cyclometalated Iridium Complexes. *Inorg. Chem.* **2001**, *40*, 1704–1711.
(113) Li, J.; Djurovich, P. I.; Alleyne, B. D.; Yousufuddin, M.; Ho, N. N.; Thomas, J. C.; Peters, J. C.; Bau, R.; Thompson, M. E. Synthetic Control of Excited-State Properties in Cyclometalated Ir(III) Complexes Using Ancillary Ligands. *Inorg. Chem.* **2005**, *44* (6), 1713–1727.
(114) Pangborn, A. B.; Giardello, M. A.; Grubbs, R. H.; Rosen, R. K.; Timmers, F. J. Safe and Convenient Procedure for Solvent Purification. *Organometallics* **1996**, *15* (5), 1518–1520.
(115) Gilroy, J. B.; McKinnon, S. D. J.; Koivisto, B. D.; Hicks, R. G. Electrochemical Studies of Verdazyl Radicals. *Org. Lett.* **2007**, *9* (23), 4837–4840.
(116) Barbon, S. M.; Reinkeluers, P. A.; Price, J. T.; Staroverov, V. N.; Gilroy, J. B. Structurally Tunable 3-Cyanoformazanate Boron Difluoride Dyes. *Chem. – Eur. J.* **2014**, *20* (36), 11340–11344.

(117) Nonoyama, M. Benzo[h]Quinolin-10-Yl-N Iridium(III) Complexes. *Bull. Chem. Soc. Jpn.* **1974**, *47* (3), 767–768.
(118) Peng, T.; Yang, Y.; Liu, Y.; Ma, D.; Hou, Z.; Wang, Y. A Phosphorescent Material with High and Balanced Carrier Mobility for Efficient OLEDs. *Chem. Commun.* **2011**, *47* (11), 3150–3152.
(119) Bourne, Y.; Sharpless, K. B.; Taylor, P.; Marchot, P. Steric and Dynamic Parameters Influencing In Situ Cycloadditions to Form Triazole Inhibitors with Crystalline Acetylcholinesterase. *J. Am. Chem. Soc.* **2016**, *138* (5), 1611–1621.
(120) Zhai, W.; Chapin, B. M.; Yoshizawa, A.; Wang, H.-C.; Hodge, S. A.; James, T. D.; Anslyn, E. V.; Fossey, J. S. "Click-Fluors": Triazole-Linked Saccharide Sensors. *Org. Chem. Front.* **2016**, *3* (8), 918–928.
(121) Türker, L. Azo-Bridged Triazoles: Green Energetic Materials. *Def. Technol.* **2016**, *12* (1), 1–15.
(122) Rostovtsev, V. V.; Green, L. G.; Fokin, V. V.; Sharpless, K. B. A Stepwise Huisgen Cycloaddition Process: Copper(I)-Catalyzed Regioselective "Ligation" of Azides and Terminal Alkynes. *Angew. Chem. Int. Ed.* **2002**, *41* (14), 2596–2599.
(123) Qu, Y.; Babailov, S. P. Azo-Linked High-Nitrogen Energetic Materials. *J. Mater. Chem. A* **2018**, *6* (5), 1915–1940.
(124) Lin, Q.-H.; Li, Y.-C.; Li, Y.-Y.; Wang, Z.; Liu, W.; Qi, C.; Pang, S.-P. Energetic Salts Based on 1-Amino-1,2,3-Triazole and 3-Methyl-1-Amino-1,2,3-Triazole. *J. Mater. Chem.* **2011**, *22* (2), 666–674.
(125) Kumar, A. S.; Ghule, V. D.; Subrahmanyam, S.; Sahoo, A. K. Synthesis of Thermally Stable Energetic 1,2,3-Triazole Derivatives. *Chem. – Eur. J.* **2013**, *19* (2), 509–518.
(126) Brik, A.; Alexandratos, J.; Lin, Y.-C.; Elder, J. H.; Olson, A. J.; Wlodawer, A.; Goodsell, D. S.; Wong, C.-H. 1,2,3-Triazole as a Peptide Surrogate in the Rapid Synthesis of HIV-1 Protease Inhibitors. *ChemBioChem* **2005**, *6* (7), 1167–1169.
(127) Weide, T.; Saldanha, S. A.; Minond, D.; Spicer, T. P.; Fotsing, J. R.; Spaargaren, M.; Frère, J.-M.; Bebrone, C.; Sharpless, K. B.; Hodder, P. S.; Fokin, V. V. NH-1,2,3-Triazole Inhibitors of the VIM-2 Metallo-β-Lactamase. *ACS Med. Chem. Lett.* **2010**, *1* (4), 150–154.
(128) Gup, R.; Erer, O.; Dilek, N. A Rapid Synthesis of 2-Substituted 1,2,3- Triazole-1-Oxide Derivative Starting from 4-(Methyl)Isonitrosoacetophenone and Its Ni(II) Complex: Characterization, DNA Binding and Cleavage Properties. *J. Mol. Struct.* **2017**, *1129*, 142–151.
(129) Minetti, P.; Tinti, M. O.; Carminati, P.; Castorina, M.; Di Cesare, M. A.; Di Serio, S.; Gallo, G.; Ghirardi, O.; Giorgi, F.; Giorgi, L.; Piersanti, G.; Bartoccini, F.; Tarzia, G. 2- *n* -Butyl-9-Methyl-8-[1,2,3]Triazol-2-Yl-9 *H* -Purin-6-Ylamine and Analogues as A $_{2A}$ Adenosine Receptor Antagonists. Design, Synthesis, and Pharmacological Characterization. *J. Med. Chem.* **2005**, *48* (22), 6887–6896.
(130) Harit, T.; Bellaouchi, R.; Rokni, Y.; Riahi, A.; Malek, F.; Asehraou, A. Synthesis, Characterization, Antimicrobial Activity, and Docking Studies of New Triazolic Tripodal Ligands. *Chem. Biodivers.* **2017**, *14* (12), e1700351.

(131) Proulx, C.; Lubell, W. D. Aza-1,2,3-Triazole-3-Alanine Synthesis via Copper-Catalyzed 1,3-Dipolar Cycloaddition on Aza-Progargylglycine. *J. Org. Chem.* **2010**, *75* (15), 5385–5387.
(132) Das Adhikary, N.; Chattopadhyay, P. Design and Synthesis of 1,2,3-Triazole-Fused Chiral Medium-Ring Benzo-Heterocycles, Scaffolds Mimicking Benzolactams. *J. Org. Chem.* **2012**, *77* (12), 5399–5405.
(133) Donald, J. R.; Martin, S. F. Synthesis and Diversification of 1,2,3-Triazole-Fused 1,4-Benzodiazepine Scaffolds. *Org. Lett.* **2011**, *13* (5), 852–855.
(134) Zhang, J.; Chang, C.-W. T. One-Pot Synthesis of 1- and 2-Substituted Naphtho[2,3-d][1,2,3]Triazole-4,9-Diones. *J. Org. Chem.* **2009**, *74* (11), 4414–4417.
(135) Beghdadi, S.; Abdelhedi Miladi, I.; Ben Romdhane, H.; Bernard, J.; Drockenmuller, E. RAFT Polymerization of Bio-Based 1-Vinyl-4-Dianhydrohexitol-1,2,3-Triazole Stereoisomers Obtained via Click Chemistry. *Biomacromolecules* **2012**, *13* (12), 4138–4145.
(136) Leonardi, M. J.; Topka, M. R.; Dinolfo, P. H. Efficient Förster Resonance Energy Transfer in 1,2,3-Triazole Linked BODIPY-Zn(II) Meso-Tetraphenylporphyrin Donor–Acceptor Arrays. *Inorg. Chem.* **2012**, *51* (24), 13114–13122.
(137) Huff, G. S.; Lo, W. K. C.; Horvath, R.; Turner, J. O.; Sun, X.-Z.; Weal, G. R.; Davidson, H. J.; Kennedy, A. D. W.; McAdam, C. J.; Crowley, J. D.; George, M. W.; Gordon, K. C. Excited States of Triphenylamine-Substituted 2-Pyridyl-1,2,3-Triazole Complexes. *Inorg. Chem.* **2016**, *55* (23), 12238–12253.
(138) Connell, T. U.; White, J. M.; Smith, T. A.; Donnelly, P. S. Luminescent Iridium(III) Cyclometalated Complexes with 1,2,3-Triazole "Click" Ligands. *Inorg. Chem.* **2016**, *55* (6), 2776–2790.
(139) Lo, W. K. C.; Huff, G. S.; Cubanski, J. R.; Kennedy, A. D. W.; McAdam, C. J.; McMorran, D. A.; Gordon, K. C.; Crowley, J. D. Comparison of Inverse and Regular 2-Pyridyl-1,2,3-Triazole "Click" Complexes: Structures, Stability, Electrochemical, and Photophysical Properties. *Inorg. Chem.* **2015**, *54* (4), 1572–1587.
(140) Winn, J.; Pinczewska, A.; Goldup, S. M. Synthesis of a Rotaxane CuI Triazolide under Aqueous Conditions. *J. Am. Chem. Soc.* **2013**, *135* (36), 13318–13321.
(141) Schuster, E. M.; Nisnevich, G.; Botoshansky, M.; Gandelman, M. Synthesis of Novel Bulky, Electron-Rich Propargyl and Azidomethyl Dialkyl Phosphines and Their Use in the Preparation of Pincer Click Ligands. *Organometallics* **2009**, *28* (17), 5025–5031.
(142) Crowley, J. D.; McMorran, D. A. "Click-Triazole" Coordination Chemistry: Exploiting 1,4-Disubstituted-1,2,3-Triazoles as Ligands. In *Click Triazoles*; Košmrlj, J., Ed.; Topics in Heterocyclic Chemistry; Springer Berlin Heidelberg: Berlin, Heidelberg, 2012; pp 31–83.
(143) Elliott, P. I. P. Chapter 1. Organometallic Complexes with 1,2,3-Triazole-Derived Ligands. In *Organometallic Chemistry*; Fairlamb, I. J. S., Lynam, J. M., Eds.; Royal Society of Chemistry: Cambridge, 2014; Vol. 39, pp 1–25.
(144) Álvarez, C. M.; García-Escudero, L. A.; García-Rodríguez, R.; Miguel, D. Beyond Click Chemistry: Spontaneous C-Triazolyl Transfer from Copper to Rhenium and

Transformation into Mesoionic C-Triazolylidene Carbene. *Chem. Commun.* **2012**, *48* (57), 7209–7211.
(145) Nolte, C.; Mayer, P.; Straub, B. F. Isolation of a Copper(I) Triazolide: A "Click" Intermediate. *Angew. Chem. Int. Ed.* **2007**, *46* (12), 2101–2103.
(146) Liu, S.; Müller, P.; Takase, M. K.; Swager, T. M. "Click" Synthesis of Heteroleptic Tris-Cyclometalated Iridium(III) Complexes: Cu(I) Triazolide Intermediates as Transmetalating Reagents. *Inorg. Chem.* **2011**, *50* (16), 7598–7609.
(147) Partyka, D. V.; Updegraff, J. B.; Zeller, M.; Hunter, A. D.; Gray, T. G. Carbon−Gold Bond Formation through [3 + 2] Cycloaddition Reactions of Gold(I) Azides and Terminal Alkynes. *Organometallics* **2007**, *26* (1), 183–186.
(148) Partyka, D. V.; Gao, L.; Teets, T. S.; Updegraff, J. B.; Deligonul, N.; Gray, T. G. Copper-Catalyzed Huisgen [3 + 2] Cycloaddition of Gold(I) Alkynyls with Benzyl Azide. Syntheses, Structures, and Optical Properties. *Organometallics* **2009**, *28* (21), 6171–6182.
(149) Heckler, J. E.; Anderson, B. L.; Gray, T. G. A Tri-Gold Triazolide with Long-Lived Luminescence. *J. Organomet. Chem.* **2016**, *818*, 68–71.
(150) Li, Y.-C.; Qi, C.; Li, S.-H.; Zhang, H.-J.; Sun, C.-H.; Yu, Y.-Z.; Pang, S.-P. 1,1′-Azobis-1,2,3-Triazole: A High-Nitrogen Compound with Stable N_8 Structure and Photochromism. *J. Am. Chem. Soc.* **2010**, *132* (35), 12172–12173.
(151) Huo, J.; Hu, H.; Zhang, M.; Hu, X.; Chen, M.; Chen, D.; Liu, J.; Xiao, G.; Wang, Y.; Wen, Z. A Mini Review of the Synthesis of Poly-1,2,3-Triazole-Based Functional Materials. *RSC Adv.* **2017**, *7* (4), 2281–2287.
(152) Engel-Andreasen, J.; Wellhöfer, I.; Wich, K.; Olsen, C. A. Backbone-Fluorinated 1,2,3-Triazole-Containing Dipeptide Surrogates. *J. Org. Chem.* **2017**, *82* (21), 11613–11619.
(153) Aziz, S. I.; Anwar, H. F.; Elnagdi, M. H.; Fleita, D. H. Studies with 2-Arylhydrazononitriles: A Novel Simple, Efficient Route to 5-Acyl-2-Substituted-1,2,3-Triazol-4-Amines. *J. Heterocycl. Chem.* **2007**, *44* (3), 725–729.
(154) Kalisiak, J.; Sharpless, K. B.; Fokin, V. V. Efficient Synthesis of 2-Substituted-1,2,3-Triazoles. *Org. Lett.* **2008**, *10* (15), 3171–3174.
(155) Liu, Y.; Yan, W.; Chen, Y.; Petersen, J. L.; Shi, X. Efficient Synthesis of *N* -2-Aryl-1,2,3-Triazole Fluorophores via Post-Triazole Arylation. *Org. Lett.* **2008**, *10* (23), 5389–5392.
(156) Wang, X.; Zhang, L.; Krishnamurthy, D.; Senanayake, C. H.; Wipf, P. General Solution to the Synthesis of *N* -2-Substituted 1,2,3-Triazoles. *Org. Lett.* **2010**, *12* (20), 4632–4635.
(157) Cai, R.; Yan, W.; Bologna, M. G.; de Silva, K.; Ma, Z.; Finklea, H. O.; Petersen, J. L.; Li, M.; Shi, X. Synthesis and Characterization of N-2-Aryl-1,2,3-Triazole Based Iridium Complexes as Photocatalysts with Tunable Photoredox Potential. *Org. Chem. Front.* **2015**, *2* (2), 141–144.
(158) Samanta, S.; Ghosh, P.; Goswami, S. Recent Advances on the Chemistry of Transition Metal Complexes of 2-(Arylazo)Pyridines and Its Arylamino Derivatives. *Dalton Trans.* **2012**, *41* (8), 2213–2226.

(159) Mondol, R.; Otten, E. Aluminum Complexes with Redox-Active Formazanate Ligand: Synthesis, Characterization, and Reduction Chemistry. *Inorg. Chem.* **2019**, *58* (9), 6344–6355.
(160) Na, H.; Teets, T. S. Highly Luminescent Cyclometalated Iridium Complexes Generated by Nucleophilic Addition to Coordinated Isocyanides. *J. Am. Chem. Soc.* **2018**, *140* (20), 6353–6360.
(161) Na, H.; Maity, A.; Morshed, R.; Teets, T. S. Bis-Cyclometalated Iridium Complexes with Chelating Dicarbene Ancillary Ligands. *Organometallics* **2017**, *36* (15), 2965–2972.
(162) Shon, J.-H.; Teets, T. S. Potent Bis-Cyclometalated Iridium Photoreductants with β-Diketiminate Ancillary Ligands. *Inorg. Chem.* **2017**, *56* (24), 15295–15303.
(163) Lai, P.-N.; Teets, T. S. Ancillary Ligand Effects on Red-Emitting Cyclometalated Iridium Complexes. *Chem. – Eur. J.* **2019**, *25* (23), 6026–6037.
(164) Mondol, R.; Snoeken, D. A.; Chang, M.-C.; Otten, E. Stable, Crystalline Boron Complexes with Mono-, Di- and Trianionic Formazanate Ligands. *Chem. Commun.* **2017**, *53* (3), 513–516.
(165) Maar, R. R.; Hoffman, N. A.; Staroverov, V. N.; Gilroy, J. B. Oxoborane Formation Turns on Formazanate-Based Photoluminescence. *Chem. – Eur. J.* **2019**, *25* (47), 11015–11019.
(166) Frolova, N. A.; Vatsadze, S. Z.; Stash, A. I.; Rakhimov, R. D.; Zyk, N. V. Oxidation of 3-(3-or 4-Pyridyl)-1,5-Diphenylformazans in Tetrazolium Trichlorometallates: Structural and Electrochemical Investigation. *Chem. Heterocycl. Compd.* **2006**, *42* (11), 1444–1456.
(167) Frolova, N. A.; Vatsadze, S. Z.; Zavodnik, V. E.; Rakhimov, R. D.; Zyk, N. V. Pyridine-Containing Nickel(II) Bis-Formazanates: Synthesis, Structure, and Electrochemical Study. *Russ. Chem. Bull.* **2006**, *55* (10), 1810–1818.
(168) Mitchell, K. A.; Jensen, C. M. Synthesis, Characterization, and Reactivity of Platinum Cysteinato and Related Thiolato Complexes: Molecular Structure of Pt2(.Mu.-N-Acetyl-L-Cysteine-S)2(Bpy)2. *Inorg. Chem.* **1995**, *34* (17), 4441–4446.
(169) Rendina, L. M.; Vittal, J. J.; Puddephatt, R. J. Cationic Carbene Complexes of Platinum(IV): Structure of a Secondary Carbene Complex. *Organometallics* **1995**, *14* (2), 1030–1038.
(170) Godbert, N.; Pugliese, T.; Aiello, I.; Bellusci, A.; Crispini, A.; Ghedini, M. Efficient, Ultrafast, Microwave-Assisted Syntheses of Cycloplatinated Complexes. *Eur. J. Inorg. Chem.* **2007**, *2007* (32), 5105–5111.
(171) Spek, A. L. Structure Validation in Chemical Crystallography. *Acta Crystallogr. D Biol. Crystallogr.* **2009**, *65* (2), 148–155.

7 Appendice

A. NMR data

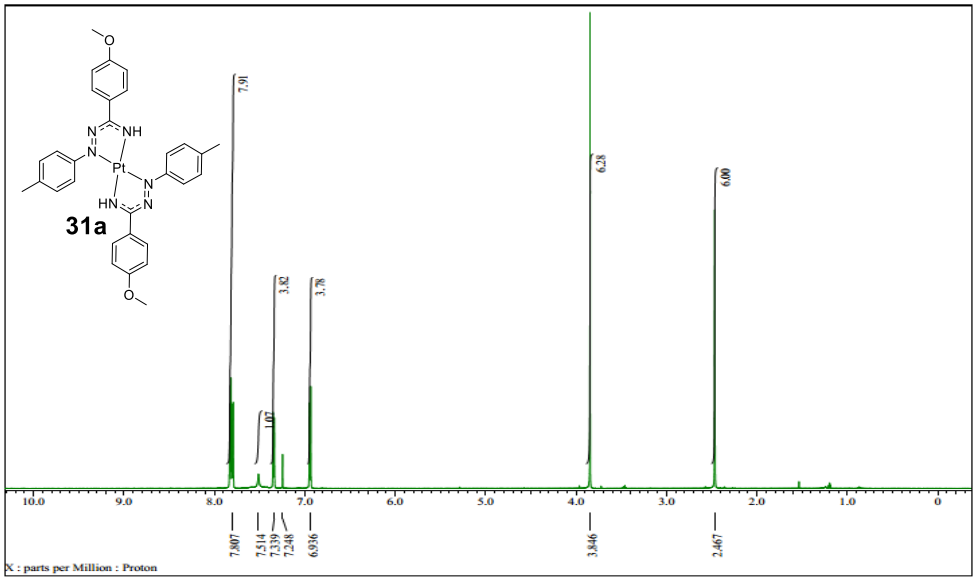

Figure S1. Room-temperature ^{1}H NMR spectrum of complex **31a**, recorded in $CDCl_3$ at 600 MHz.

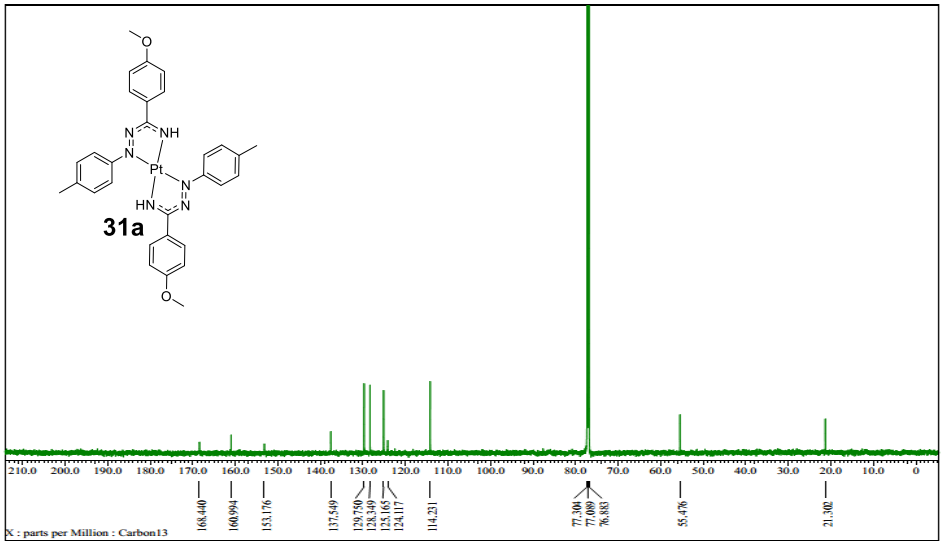

Figure S2. Room-temperature $^{13}C\{^{1}H\}$ NMR spectrum of complex **31a**, recorded in $CDCl_3$ at 151 MHz.

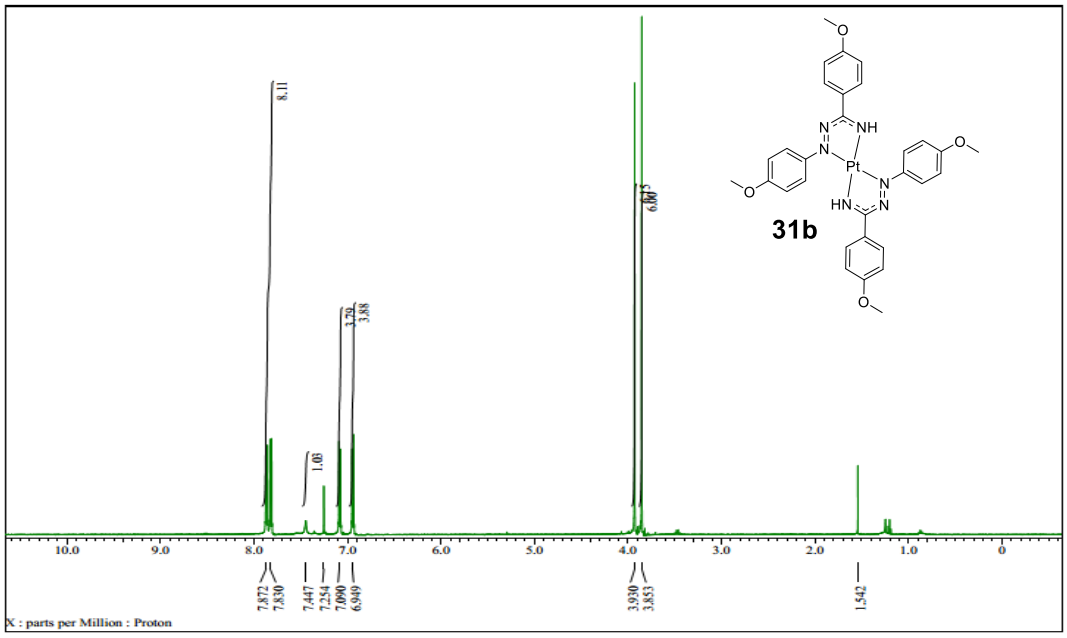

Figure S3. Room-temperature ^{1}H NMR spectrum of complex **31b**, recorded in $CDCl_3$ at 500 MHz.

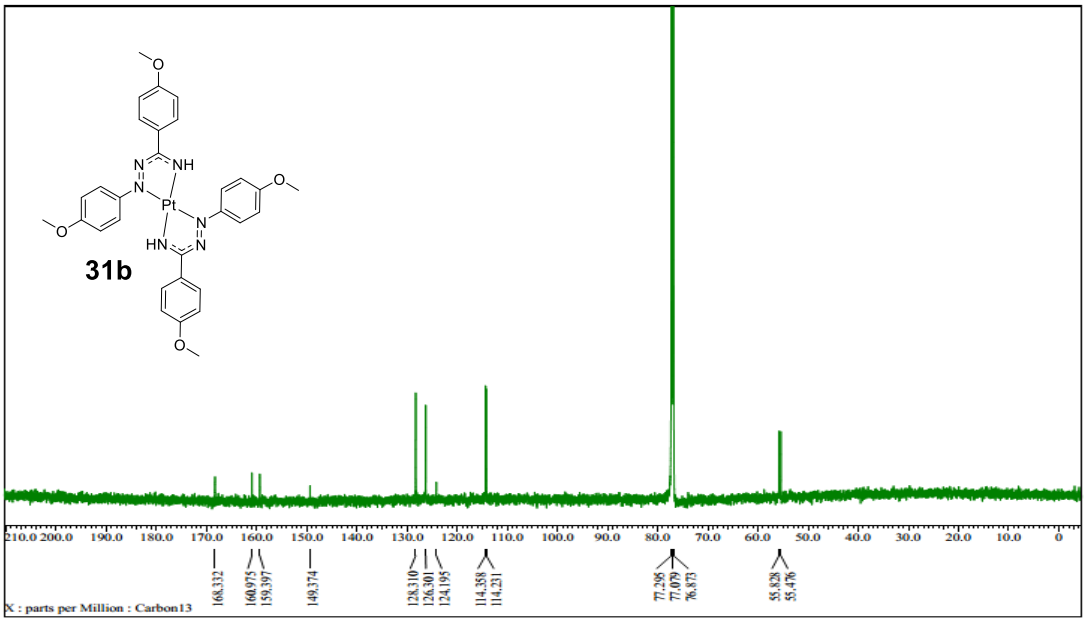

Figure S4. Room-temperature $^{13}C\{^{1}H\}$ NMR spectrum of complex **31b** , recorded in $CDCl_3$ at 151 MHz.

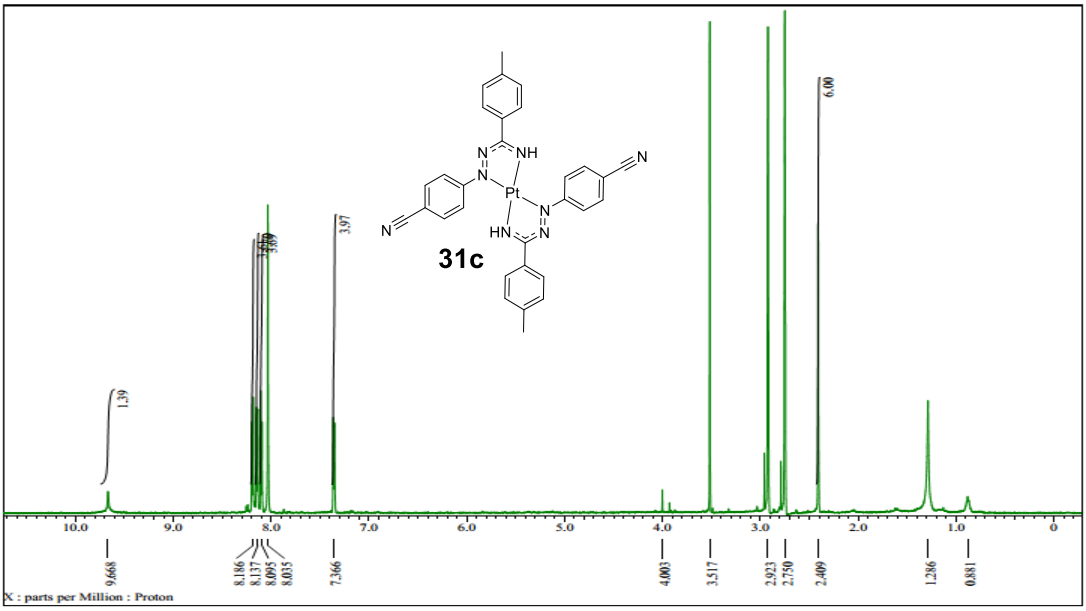

Figure S5. Room-temperature ^{1}H NMR spectrum of complex **31c**, recorded in DMF-d_7 at 600 MHz.

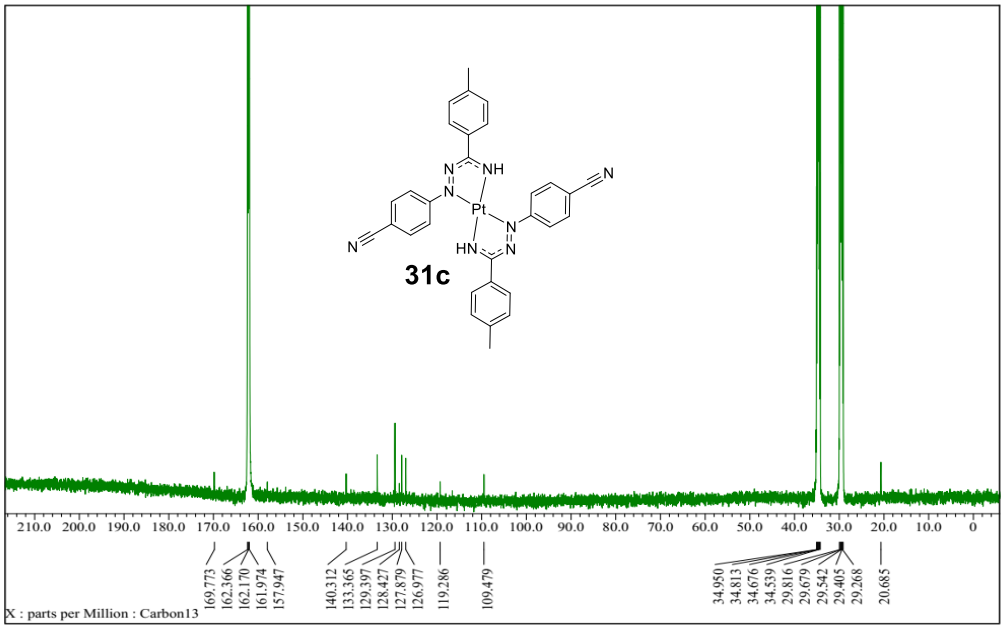

Figure S6. Room-temperature $^{13}C\{^{1}H\}$ NMR spectrum of complex **31c** , recorded in DMF-d_7 at 151 MHz.

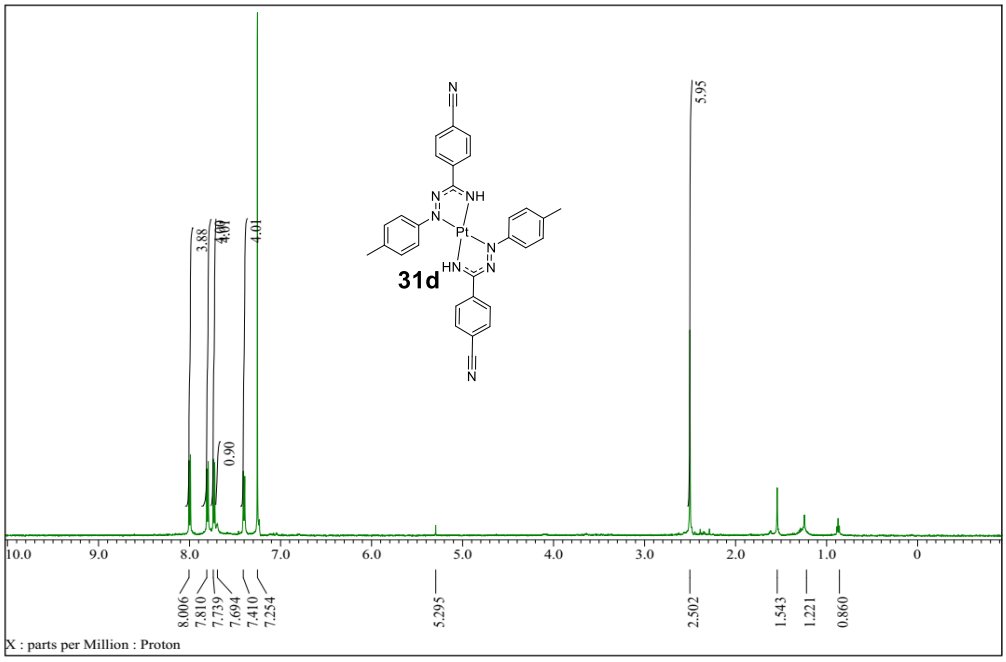

Figure S7. Room-temperature ^{1}H NMR spectrum of complex **31d**, recorded in $CDCl_3$ at 500 MHz.

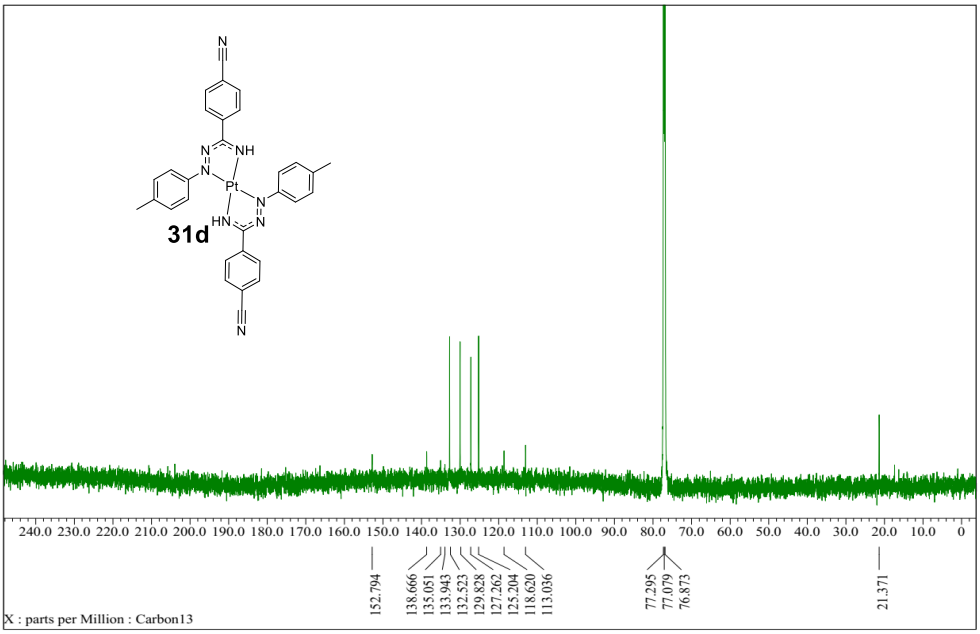

Figure S8. Room-temperature $^{13}C\{^{1}H\}$ NMR spectrum of complex **31d**, recorded in $CDCl_3$ at 151 MHz.

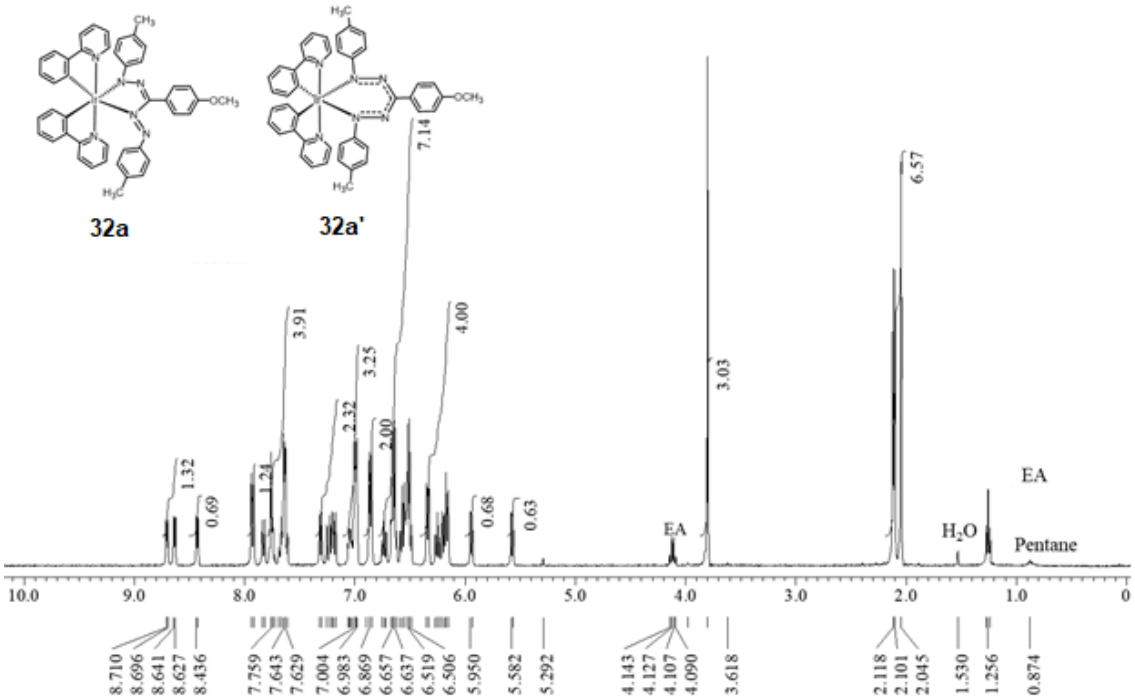

Figure S9 ^{1}H NMR spectrum of Ir(ppy)$_2$(**Fza**) (**32a** and **32a'**), recorded at 400 MHz in $CDCl_3$.

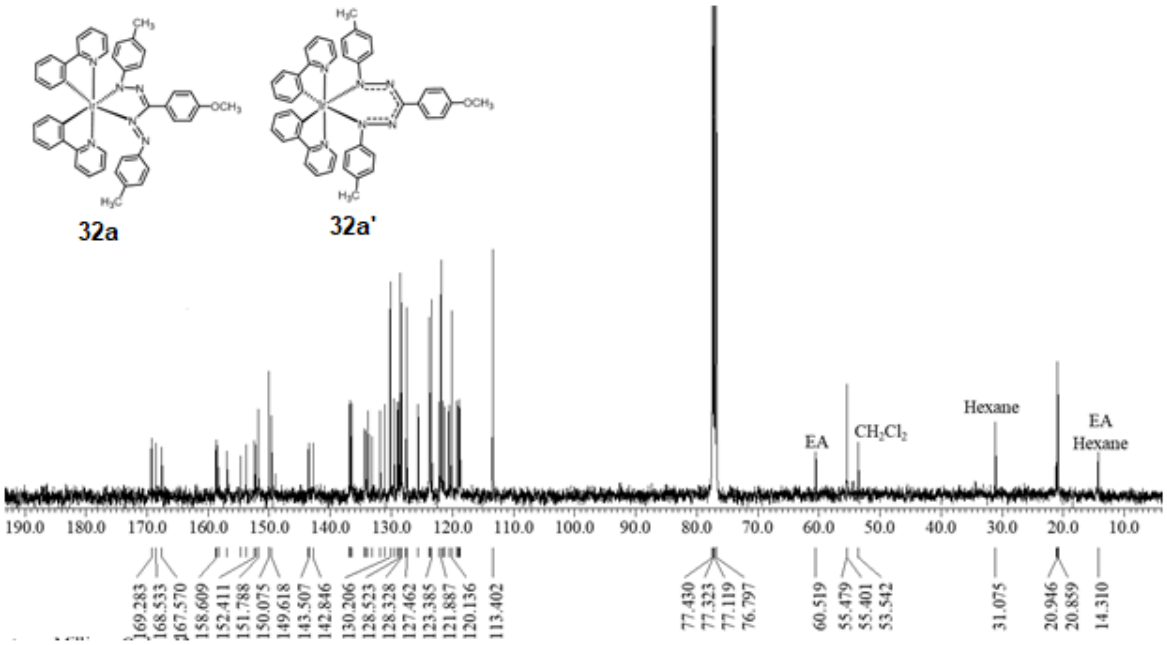

Figure S10. ^{13}C{^{1}H} NMR spectrum of Ir(ppy)$_2$(**Fza**) (**32a** and **32a'**), recorded at 100 MHz in $CDCl_3$.

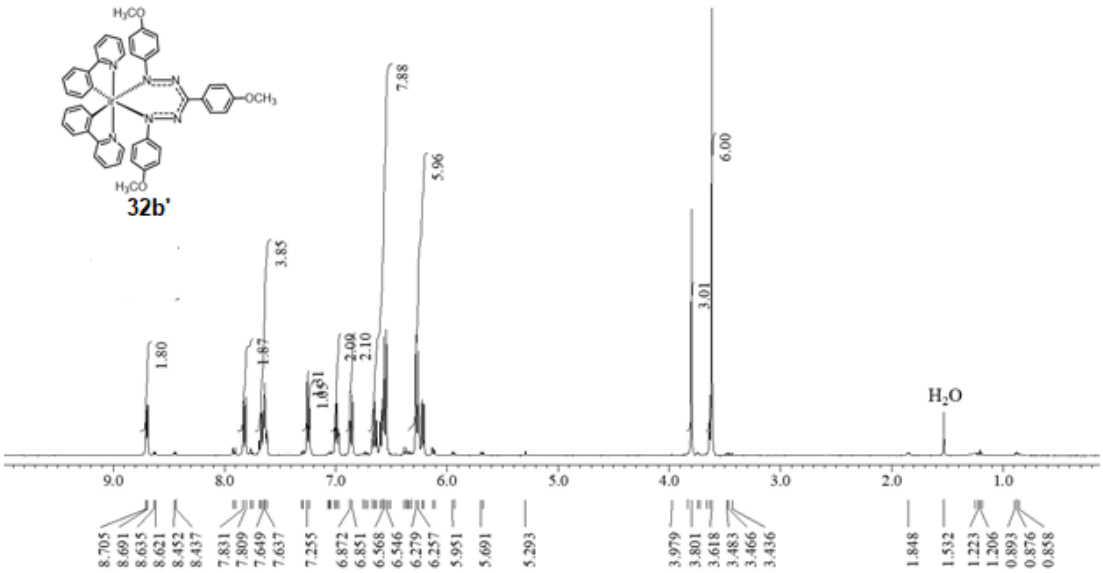

Figure S11. ^{1}H NMR spectrum of Ir(ppy)$_2$(**Fzb**) (**32b'**), recorded at 400 MHz in $CDCl_3$.

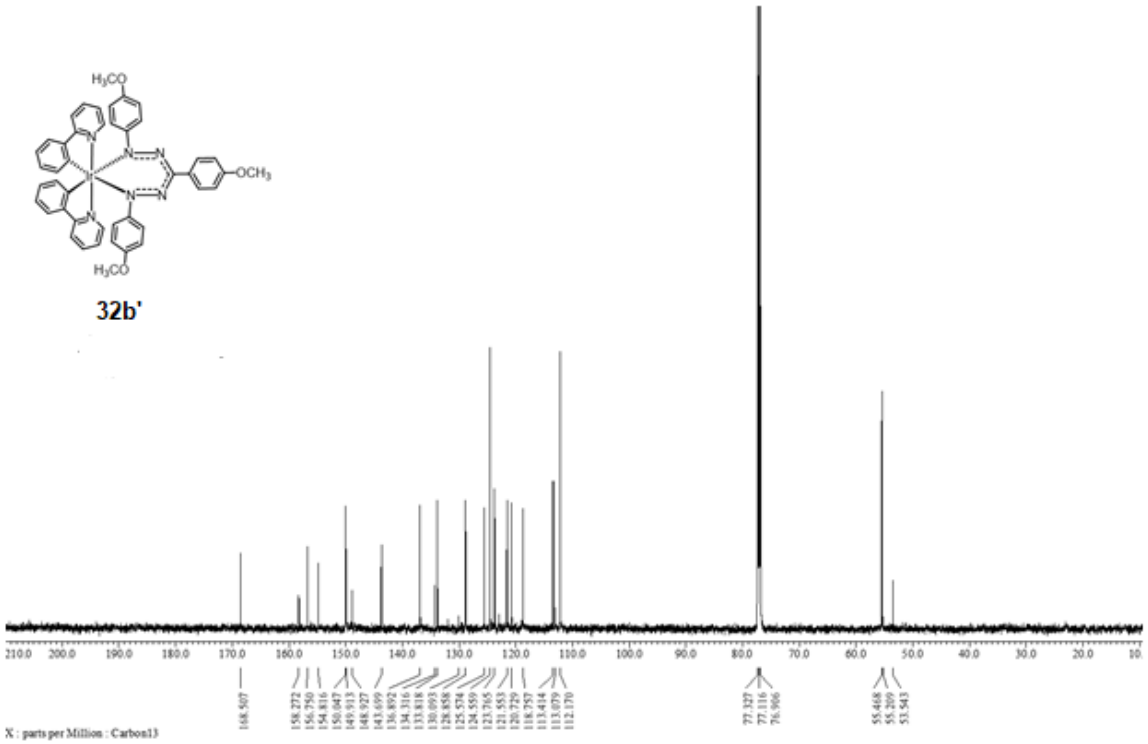

Figure S12. ^{13}C{^{1}H} NMR spectrum of Ir(ppy)$_2$(**Fzb**) (**32b'**), recorded at 151 MHz in $CDCl_3$.

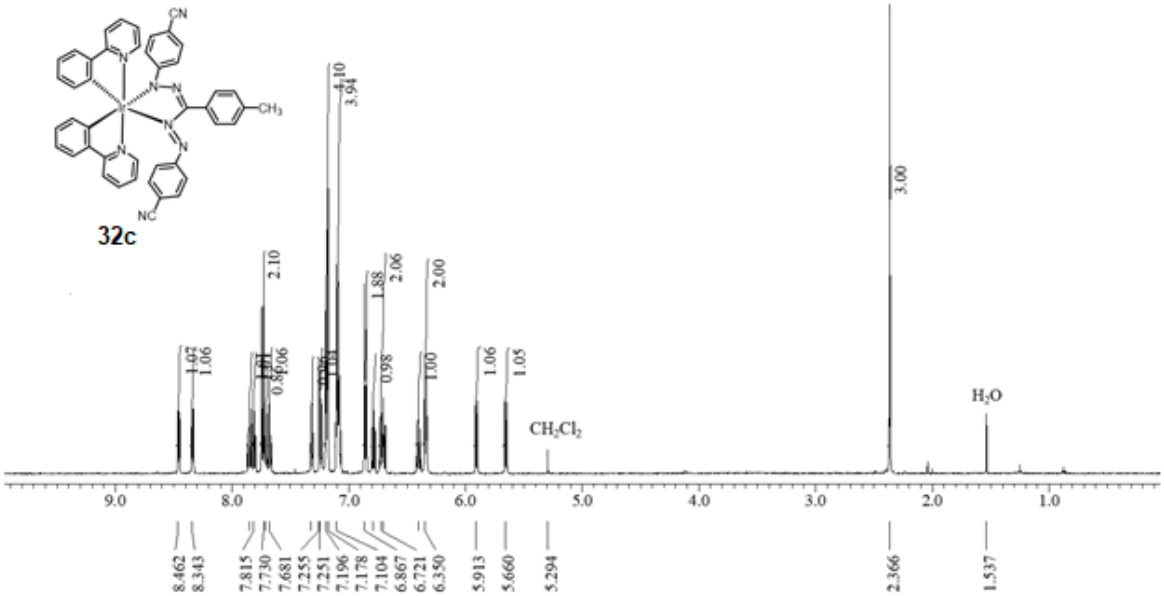

Figure S13. ^{1}H NMR spectrum of Ir(ppy)$_2$(**Fzc**) (**32c**), recorded at 500 MHz in $CDCl_3$.

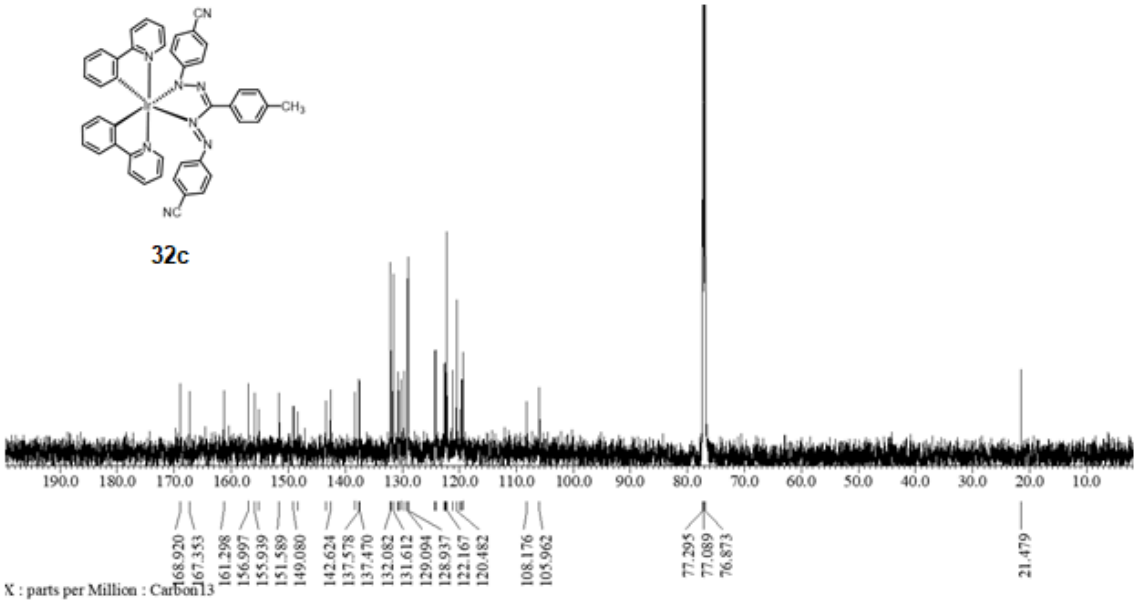

Figure S14. ^{13}C{^{1}H} NMR spectrum of Ir(ppy)$_2$(**Fzc**) (**32c**), recorded at 151 MHz in $CDCl_3$.

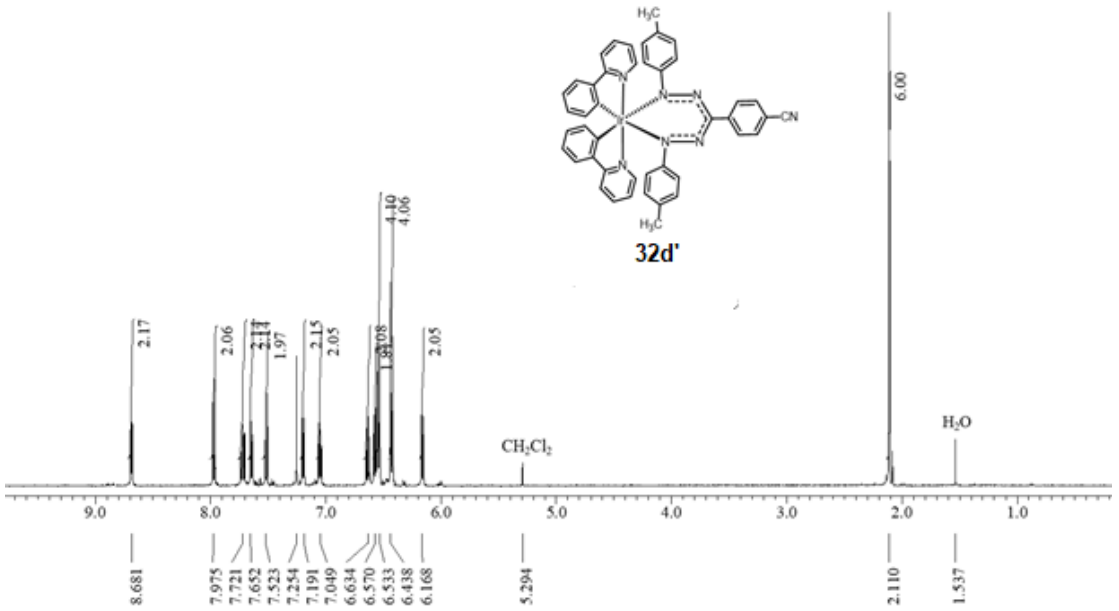

Figure S15. ^{1}H NMR spectrum of Ir(ppy)$_2$(**Fzd**) (**32d'**), recorded at 500 MHz in $CDCl_3$

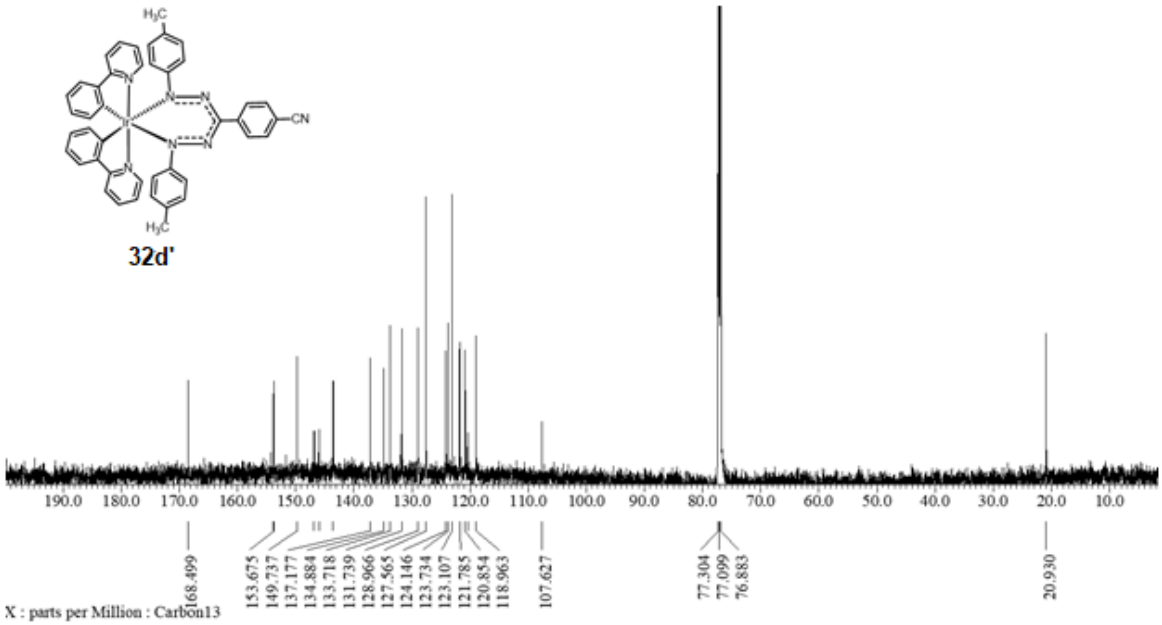

Figure S16. ^{13}C{^{1}H} NMR spectrum of Ir(ppy)$_2$(**Fzd**) (**32d'**), recorded at 151 MHz in $CDCl_3$.

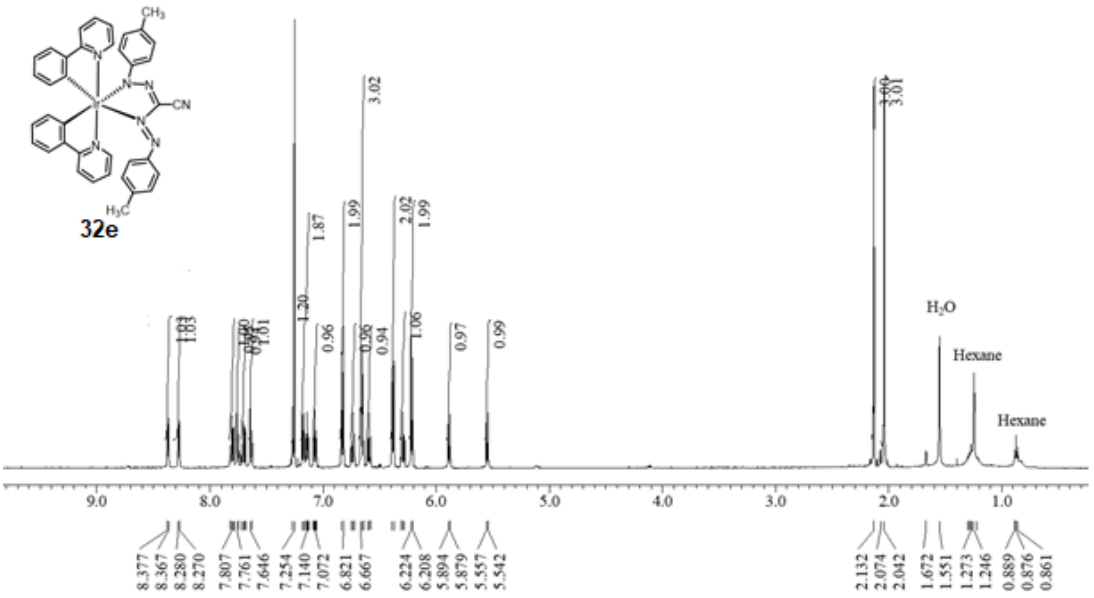

Figure S17. ^{1}H NMR spectrum of $Ir(ppy)_2$(**Fze**) (**32e**), recorded at 500 MHz in $CDCl_3$

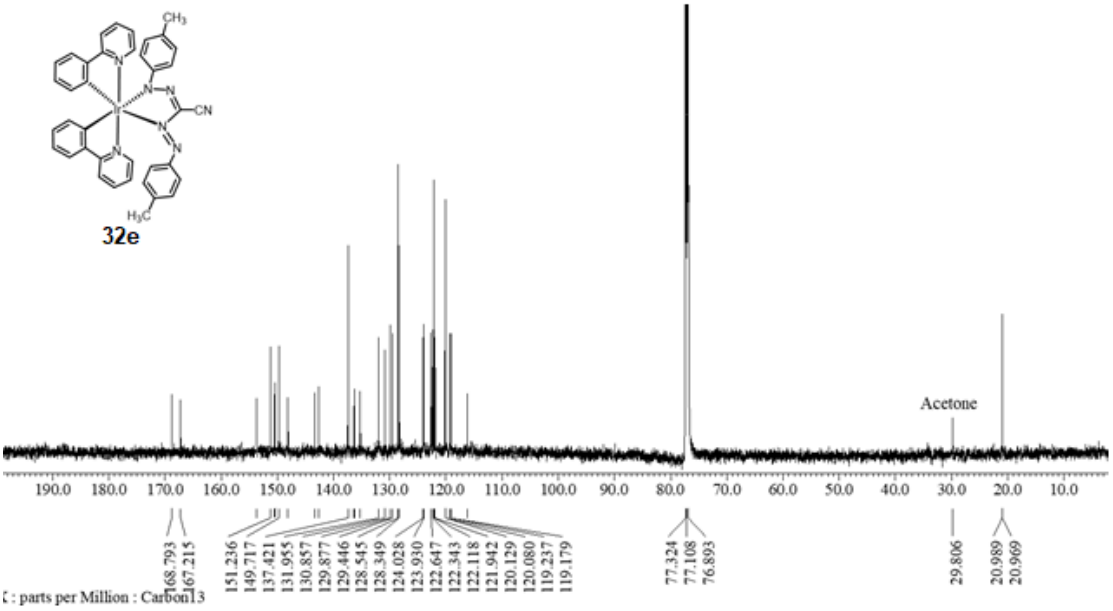

Figure S18. $^{13}C\{^{1}H\}$ NMR spectrum of $Ir(ppy)_2$(**Fze**) (**32e**), recorded at 151 MHz in $CDCl_3$.

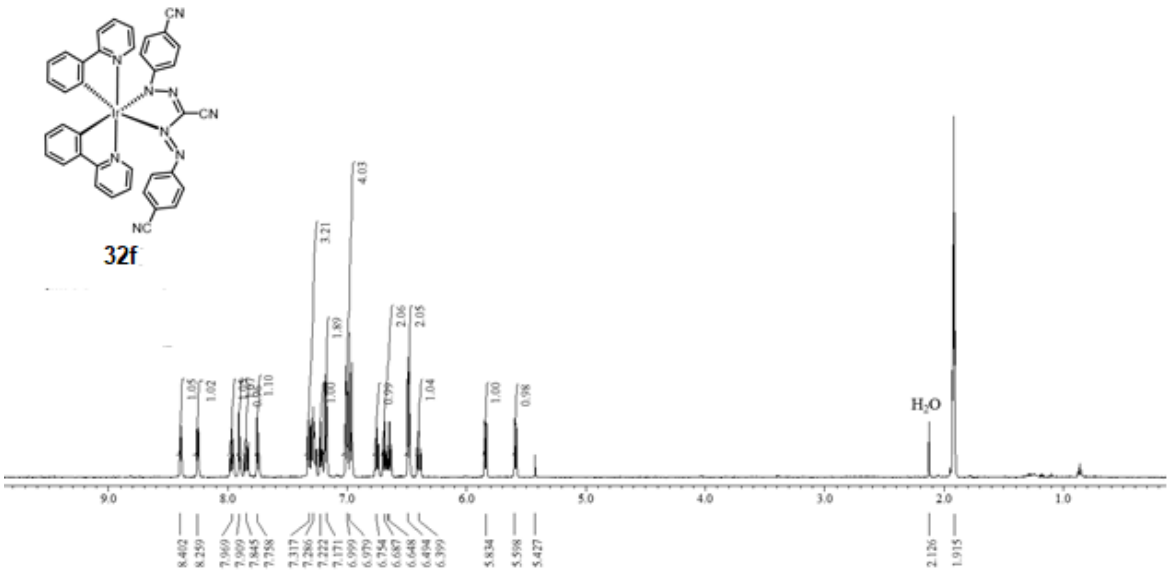

Figure S19. ^{1}H NMR spectrum of Ir(ppy)$_2$(**Fzf**) (**32f**), recorded at 500 MHz in CD_3CN.

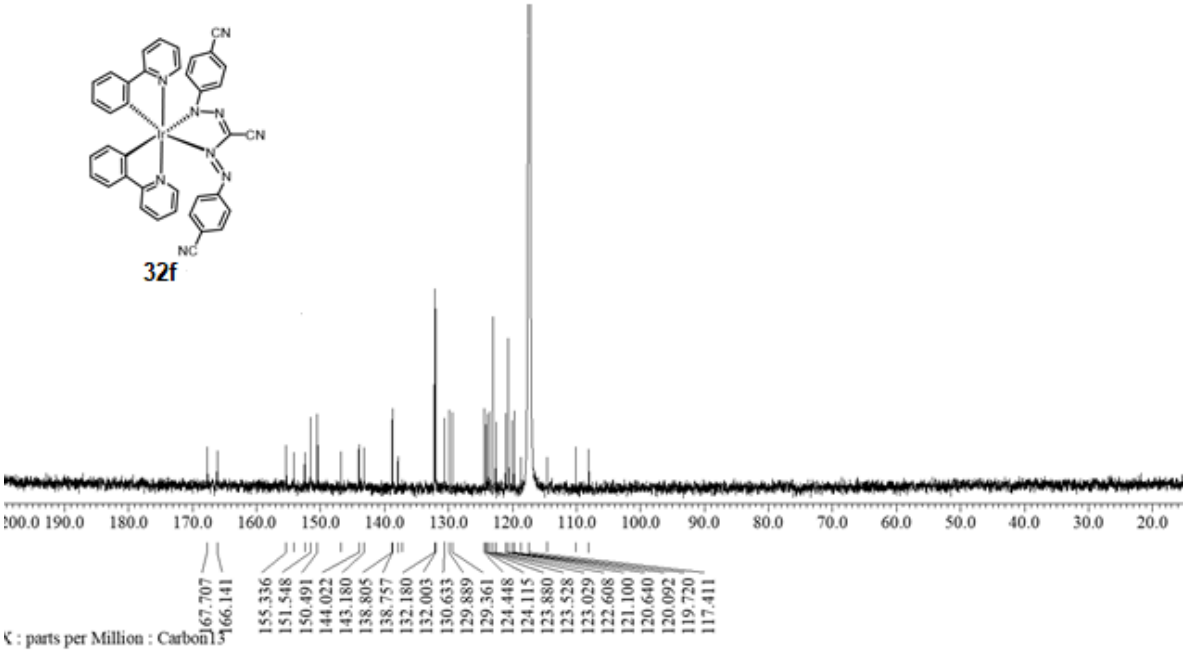

Figure S20. $^{13}C\{^{1}H\}$ NMR spectrum of Ir(ppy)$_2$(**Fzf**) (**32f**), recorded at 151 MHz in CD_3CN.

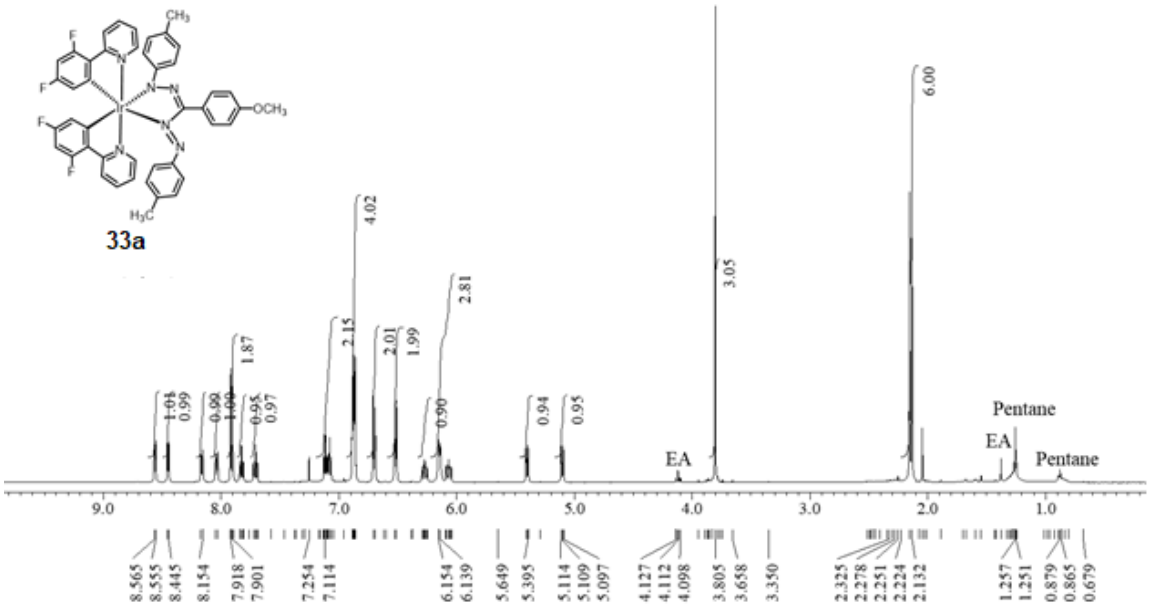

Figure S21. ^{1}H NMR spectrum of Ir(F_2ppy)$_2$(**Fza**) (**33a**), recorded at 500 MHz in $CDCl_3$.

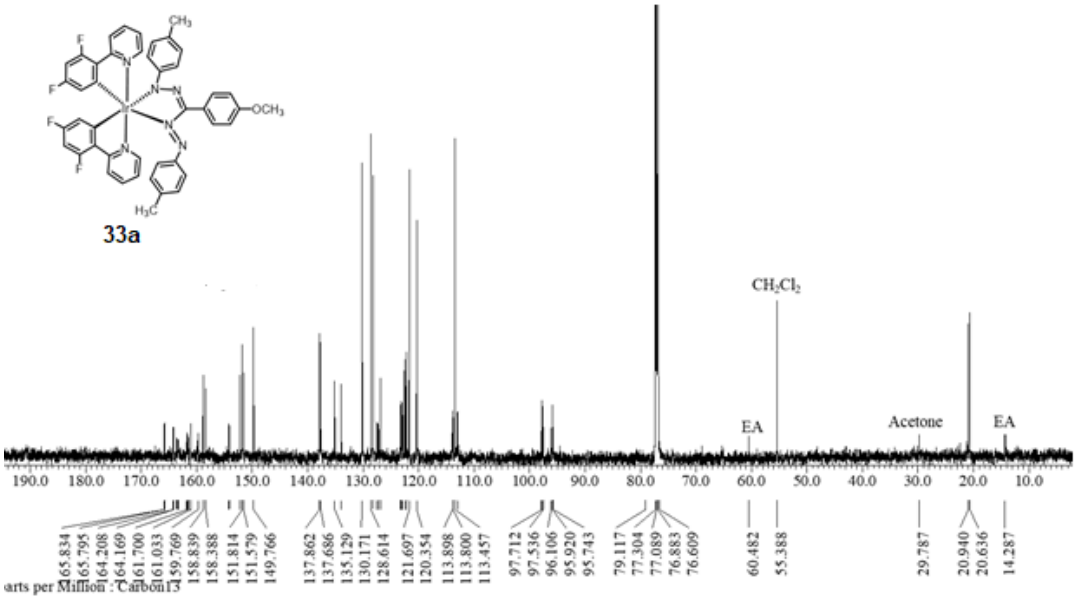

Figure S22. ^{13}C{^{1}H} NMR spectrum of Ir(F_2ppy)$_2$(**Fza**) (**33a**), recorded at 126 MHz in $CDCl_3$.

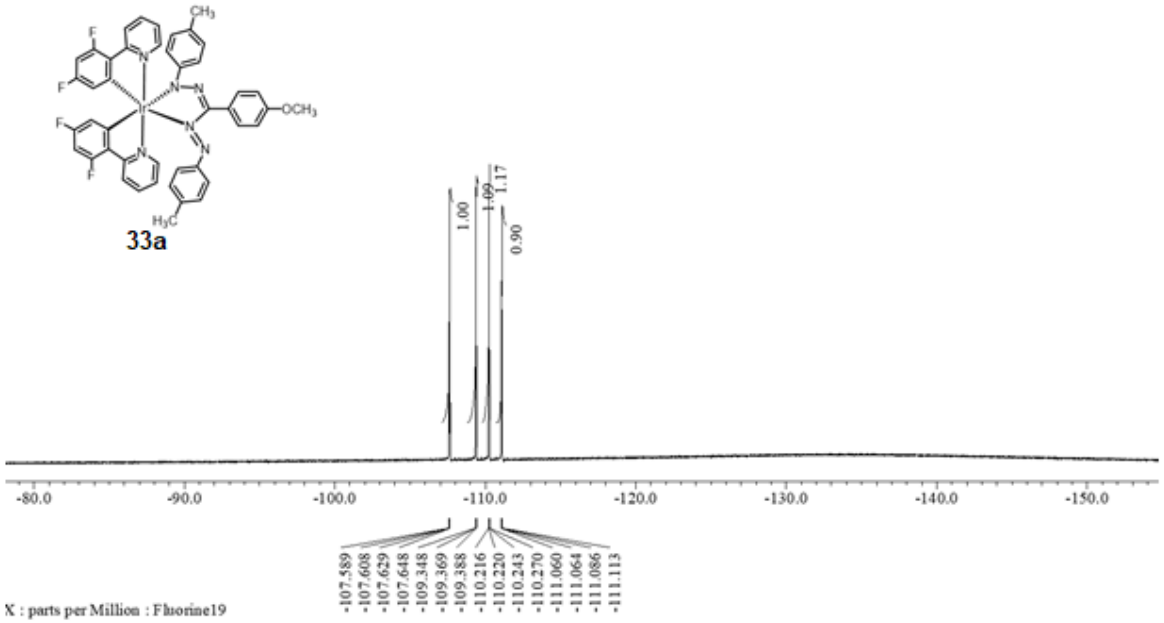

Figure S23. ^{19}F NMR spectrum of $Ir(F_2ppy)_2$(**Fza**) (**33a**), recorded at 470 MHz in $CDCl_3$.

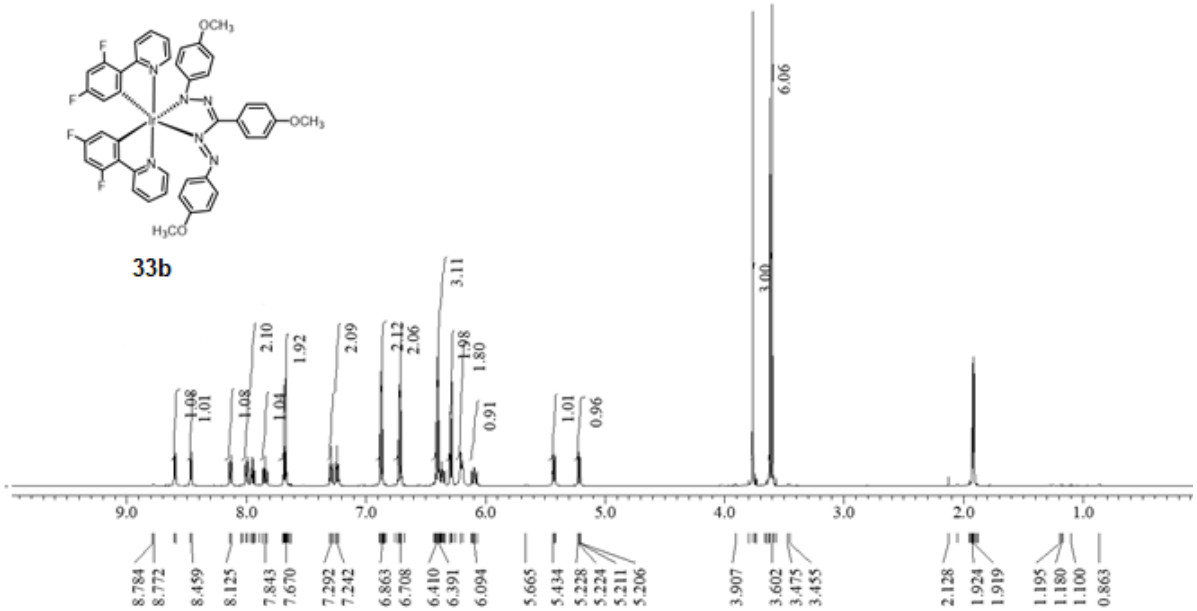

Figure S24. ^1H NMR spectrum of $Ir(F_2ppy)_2$(**Fzb**) (**33b**), recorded at 500 MHz in CD_3CN.

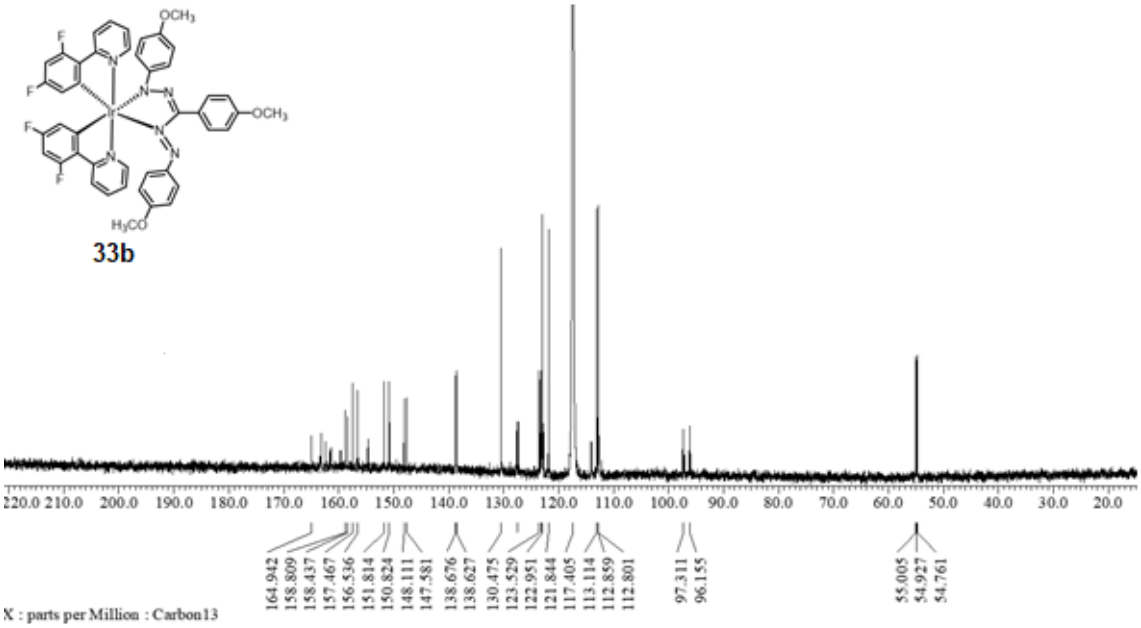

Figure S25. $^{13}C\{^{1}H\}$ NMR spectrum of Ir(F_2ppy)$_2$(**Fzb**) (**33b**), recorded at 126 MHz in CD_3CN.

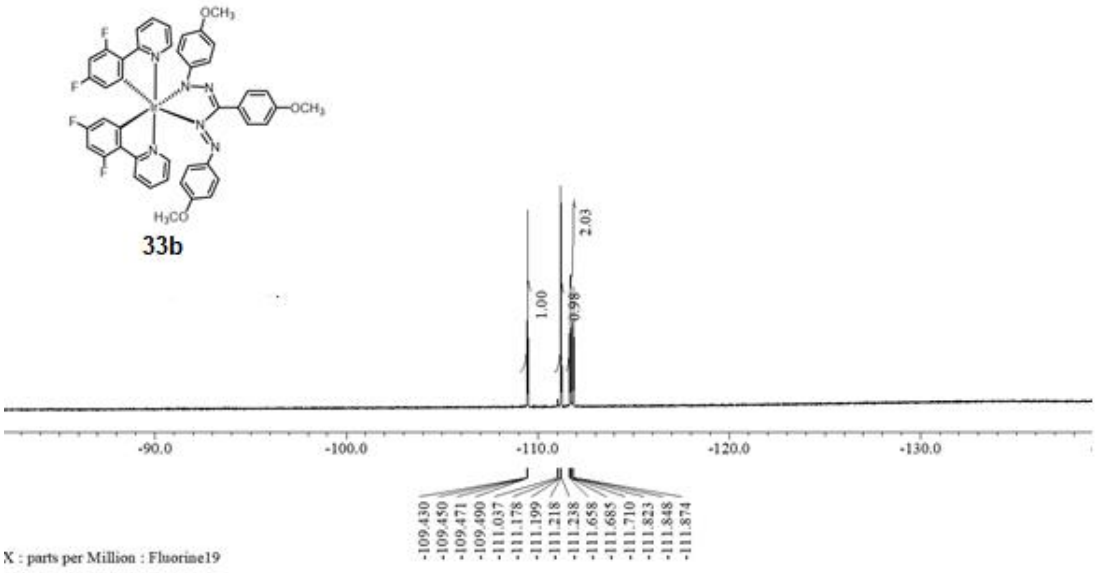

Figure S26. ^{19}F NMR spectrum of Ir(F_2ppy)$_2$(**Fzb**) (**33b**), recorded at 470 MHz in CD_3CN.

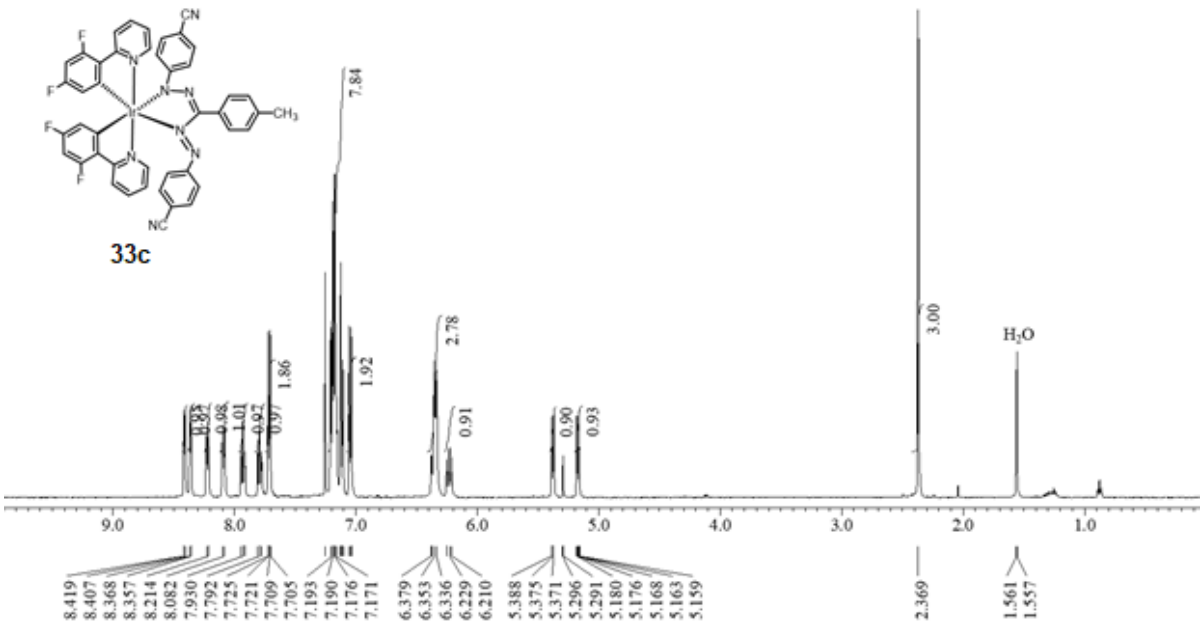

Figure S27. ^{1}H NMR spectrum of Ir(F_2ppy)$_2$(**Fzc**) (**33c**), recorded at 500 MHz in $CDCl_3$.

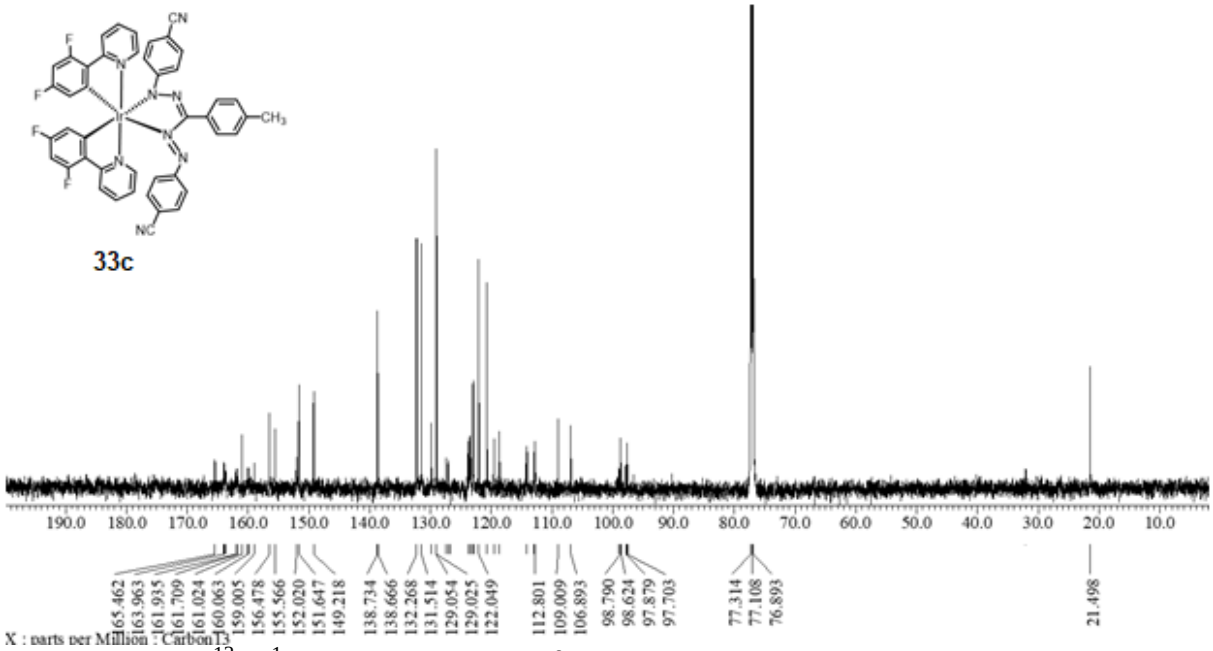

Figure S28. ^{13}C{^{1}H} NMR spectrum of Ir(F_2ppy)$_2$(**Fzc**) (**33c**), recorded at 151 MHz in $CDCl_3$

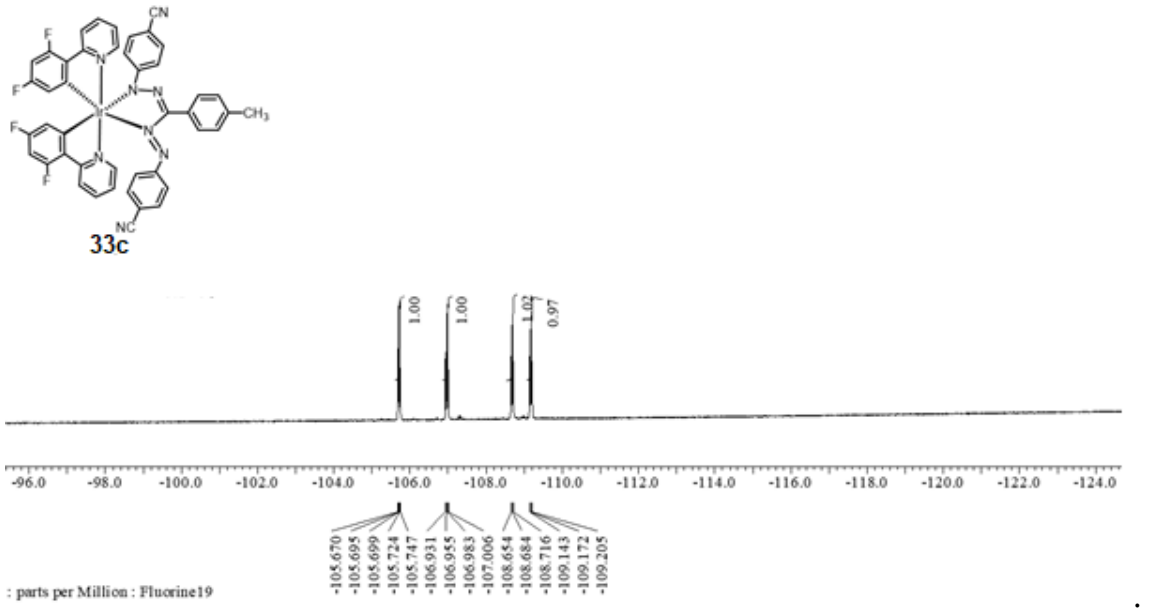

Figure S29. ^{19}F NMR spectrum of $Ir(F_2ppy)_2$(**Fzc**) (**33c**), recorded at 470 MHz in $CDCl_3$.

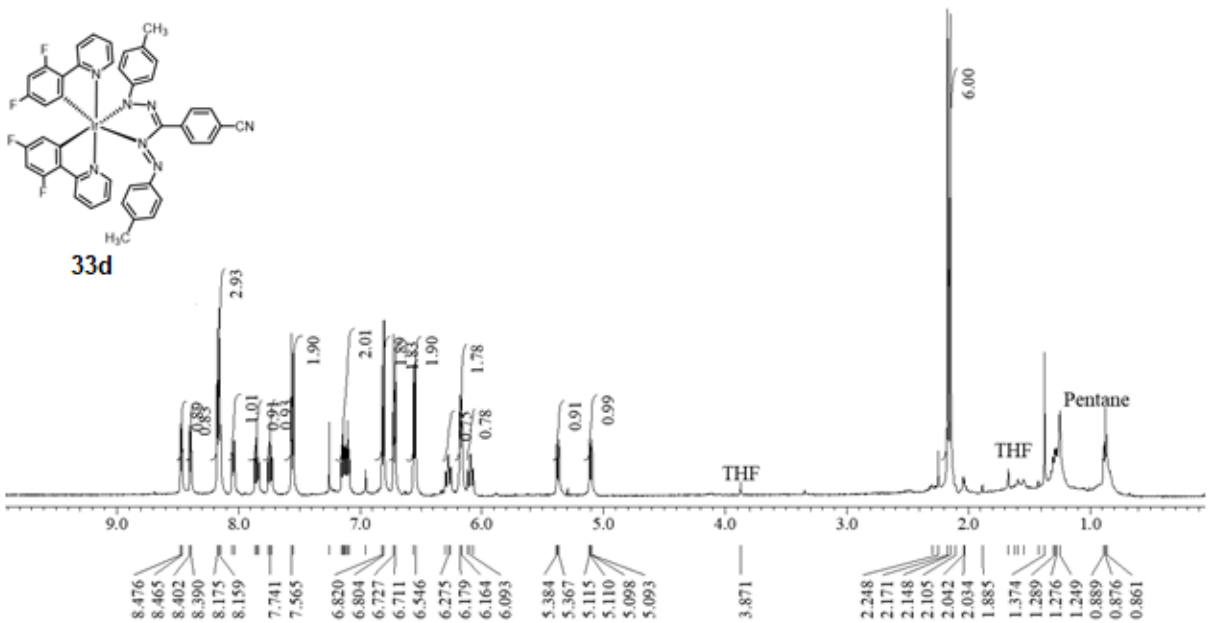

Figure S30. ^{1}H NMR spectrum of $Ir(F_2ppy)_2$(**Fzd**) (**33d**), recorded at 500 MHz in $CDCl_3$.

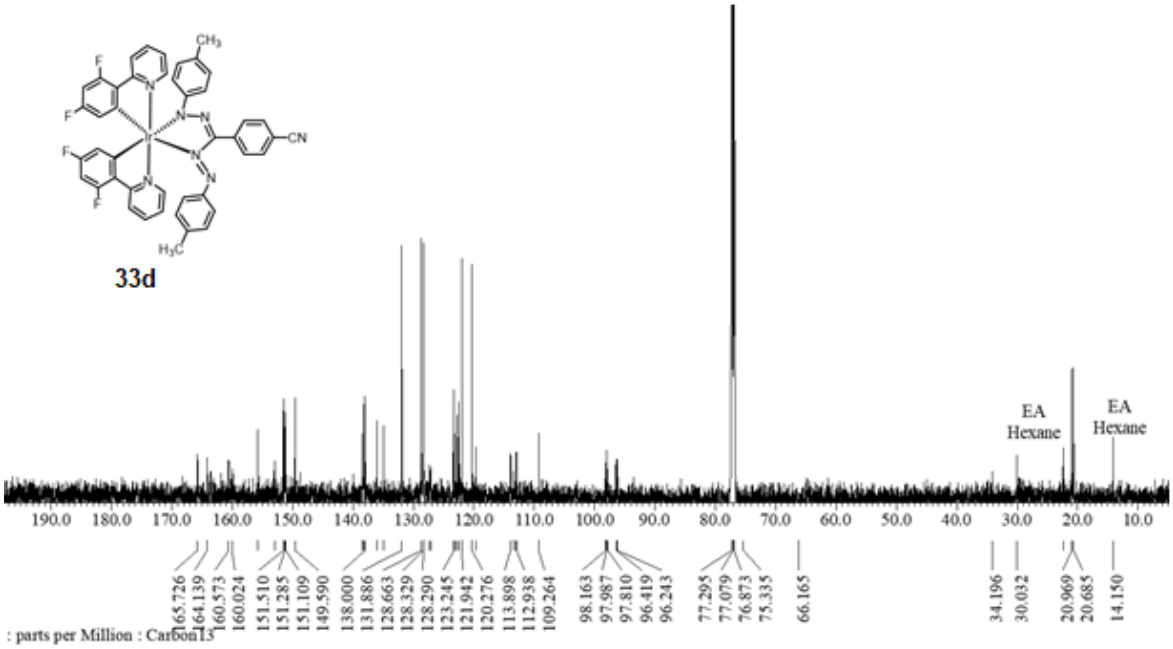

Figure S31. $^{13}C\{^{1}H\}$ NMR spectrum of $Ir(F_2ppy)_2$(**Fzd**) (**33d**), recorded at 151 MHz in $CDCl_3$.

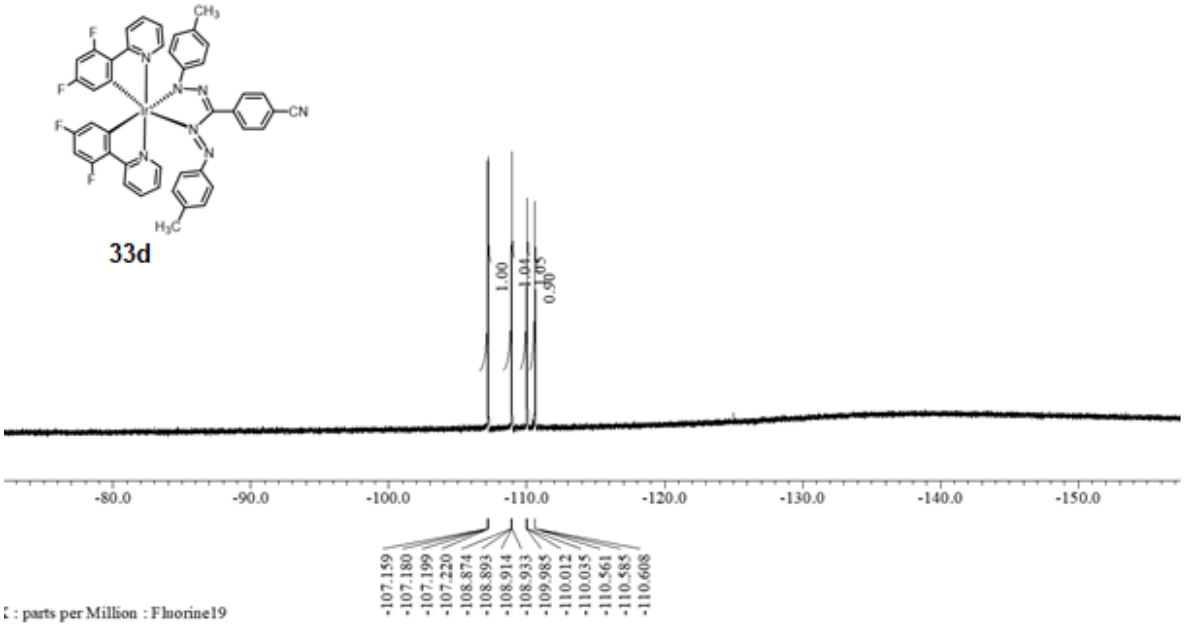

Figure S32. ^{19}F NMR spectrum of Ir(F_2ppy)$_2$(**Fzd**) (**33d**), recorded at 470 MHz in $CDCl_3$.

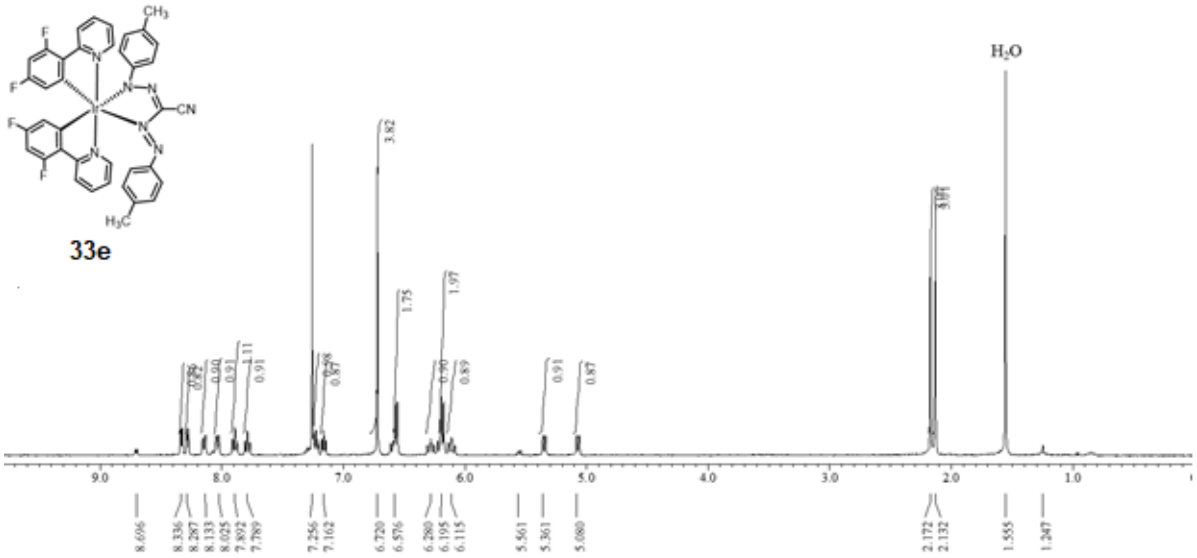

Figure S33. ^{1}H NMR spectrum of Ir(F_2ppy)$_2$(**Fze**) (**33e**), recorded at 400 MHz in $CDCl_3$.

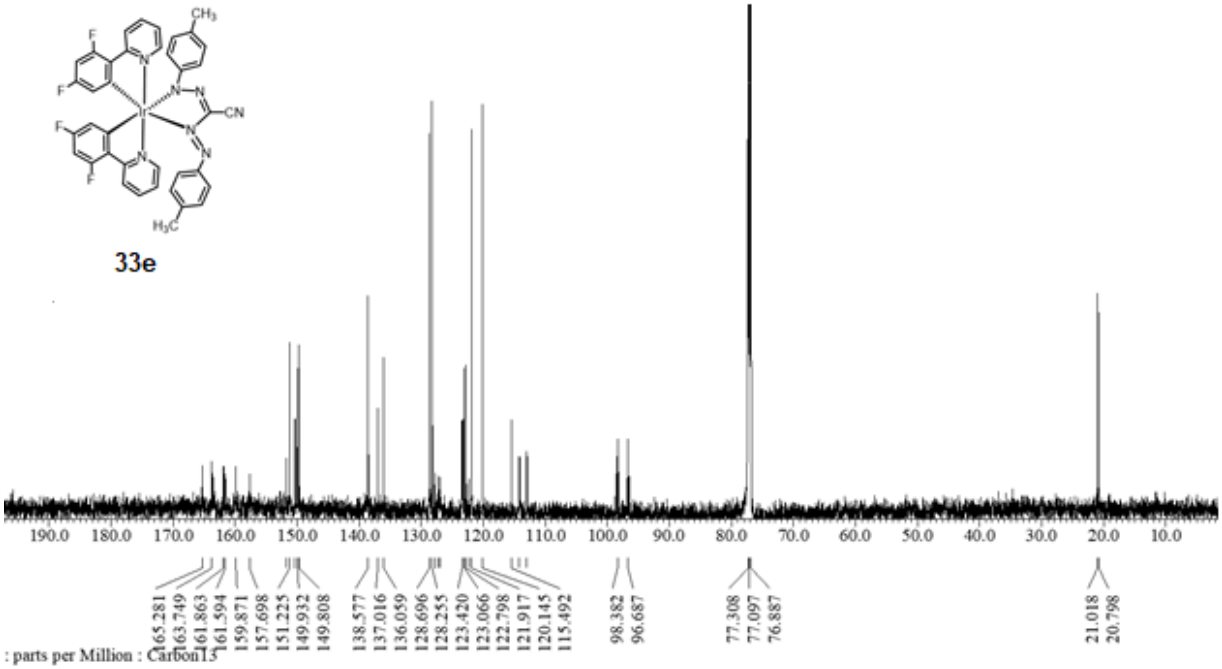

Figure S34. $^{13}C\{^{1}H\}$ NMR spectrum of Ir(F_2ppy)$_2$(**Fze**) (**33e**), recorded at 151 MHz in $CDCl_3$.

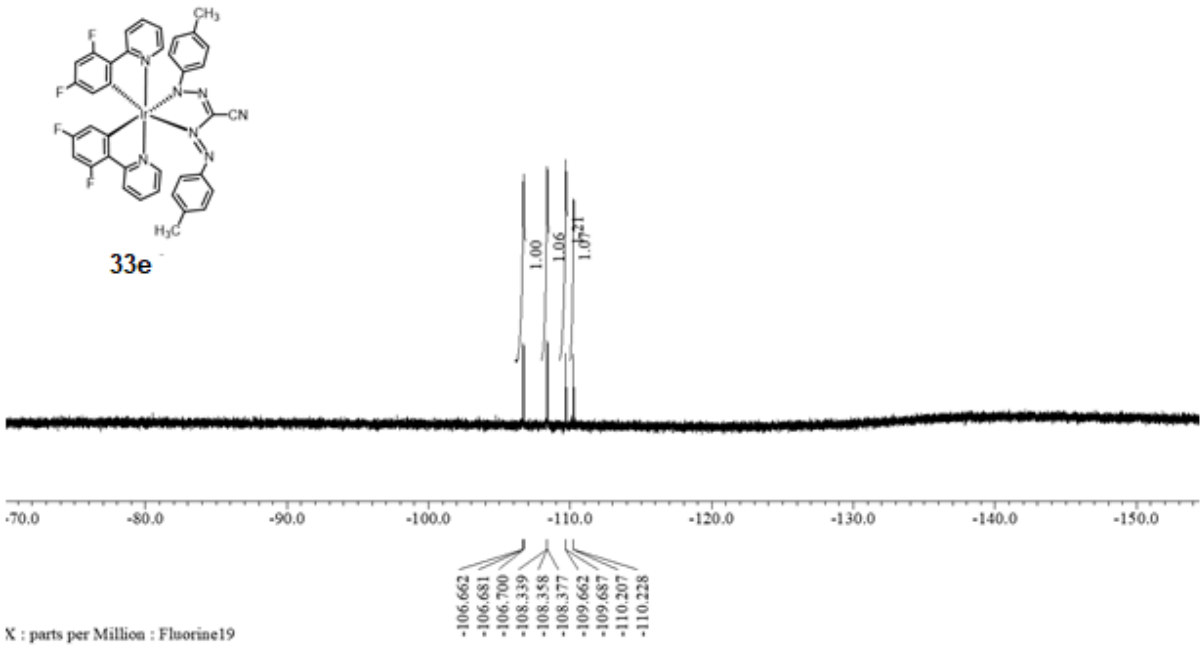

Figure S35. ^{19}F NMR spectrum of Ir(F_2ppy)$_2$(**Fze**) (**33e**), recorded at 470 MHz in $CDCl_3$.

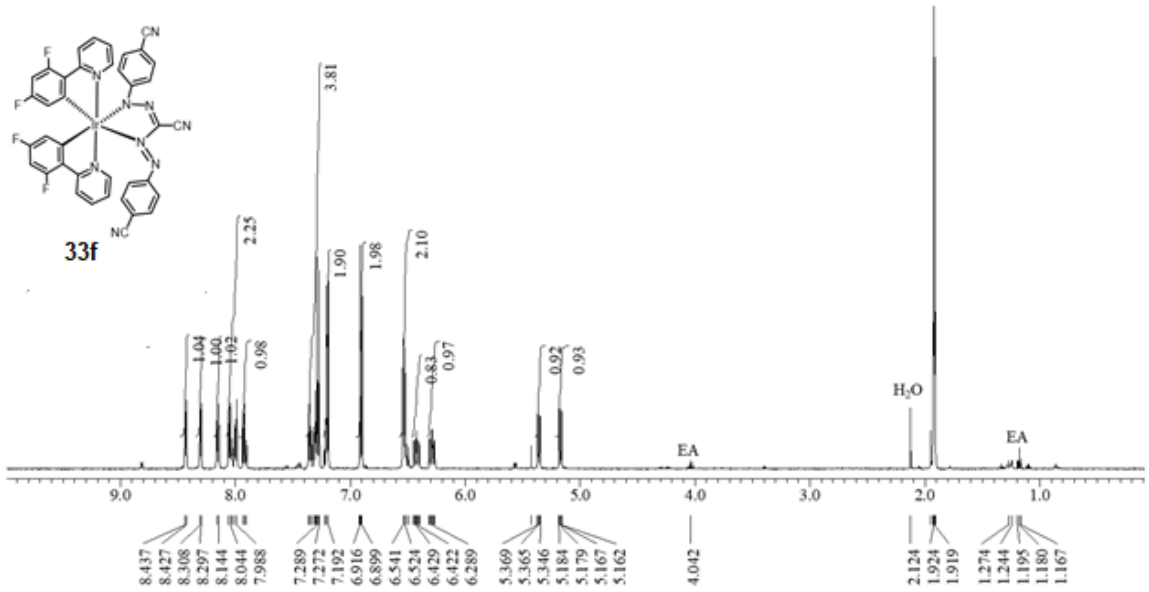

Figure S36. ^{1}H NMR spectrum of Ir(F_2ppy)$_2$(**Fzf**) (**33f**), recorded at 400 MHz in CD_3CN.

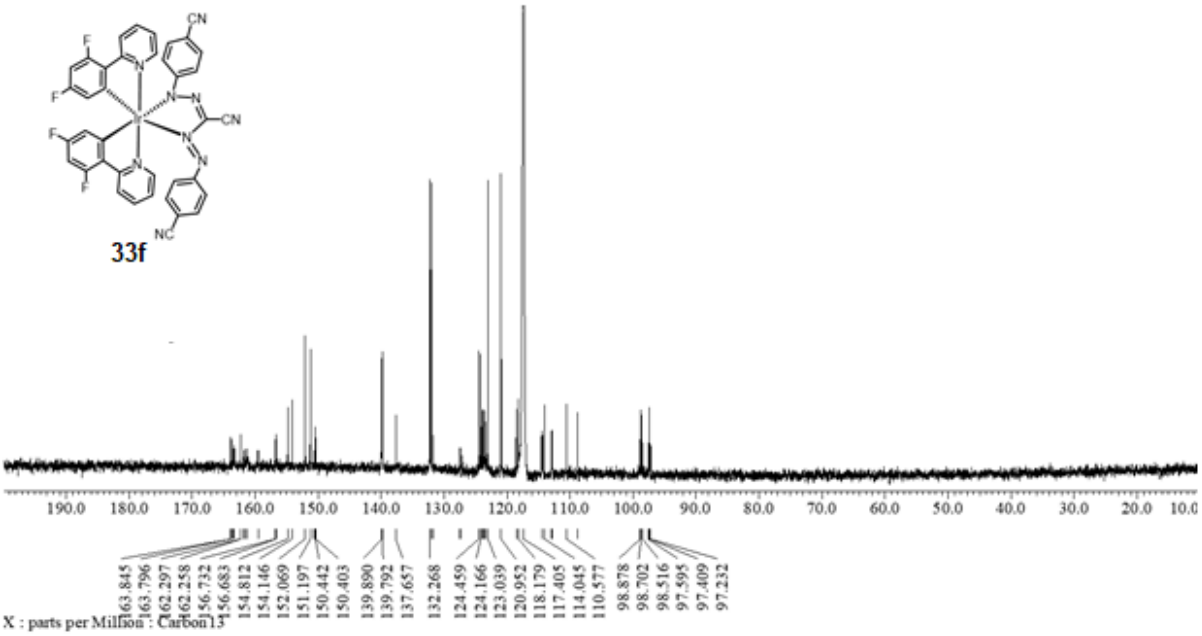

Figure S37. $^{13}C\{^{1}H\}$ NMR spectrum of Ir(F_2ppy)$_2$(**Fzf**) (**33f**), recorded at 151 MHz in CD_3CN.

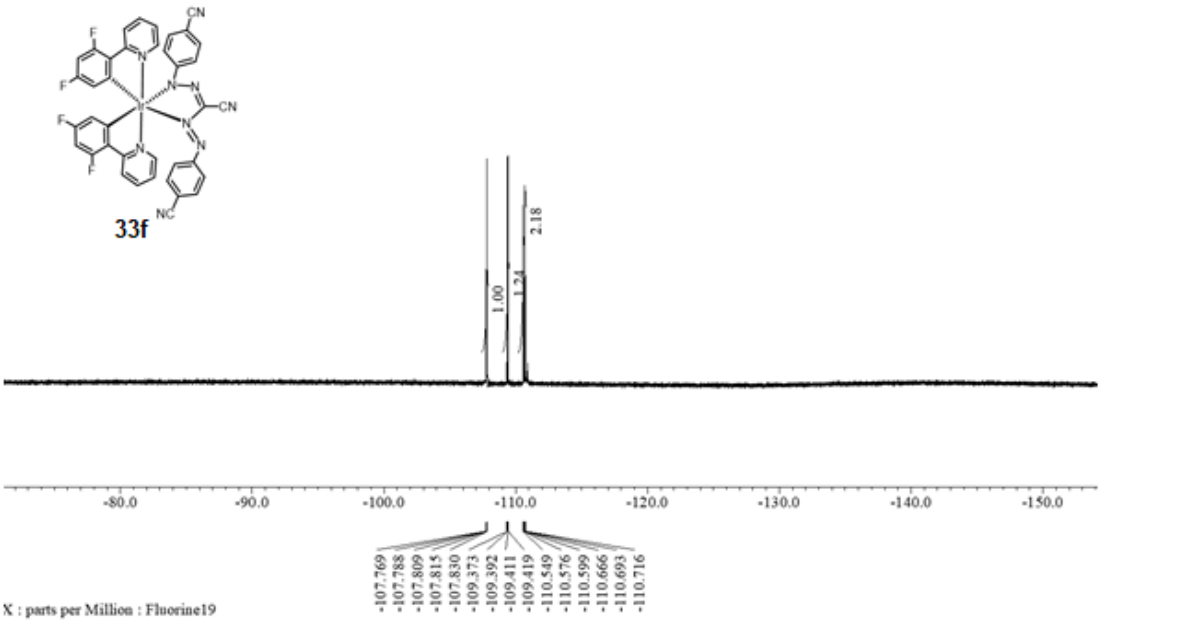

Figure S38. ^{19}F NMR spectrum of Ir(F_2ppy)$_2$(**Fzf**) (**33f**), recorded at 470 MHz in CD_3CN.

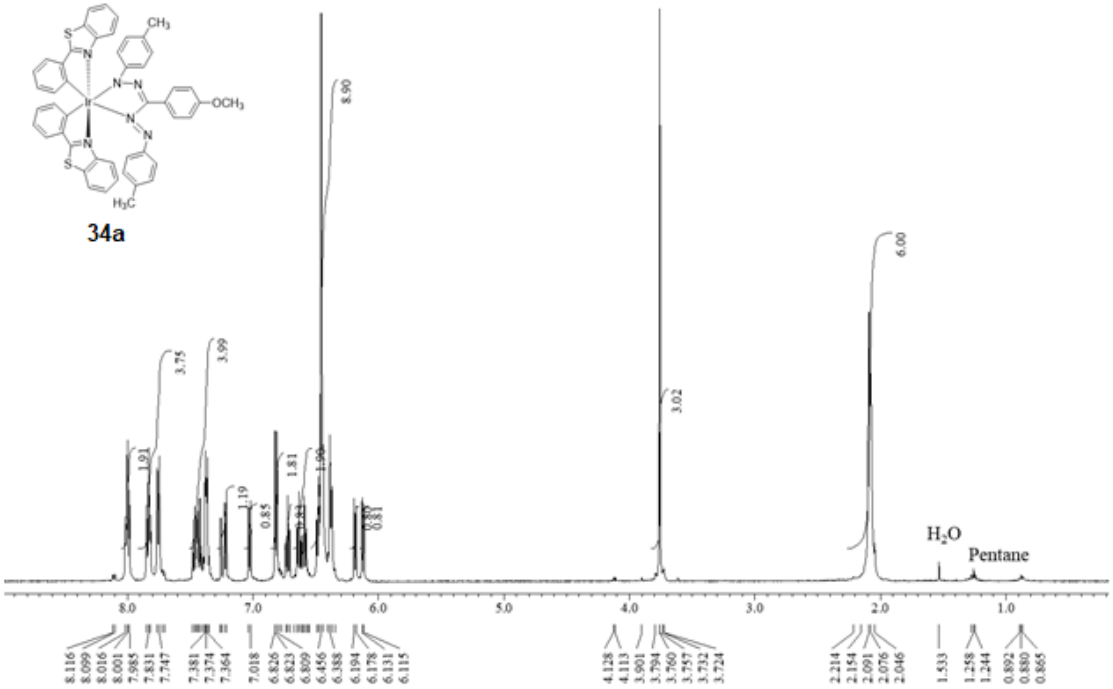

Figure S39. ^{1}H NMR spectrum of Ir(bt)$_2$(**Fza**) (**34a**), recorded at 500 MHz in $CDCl_3$.

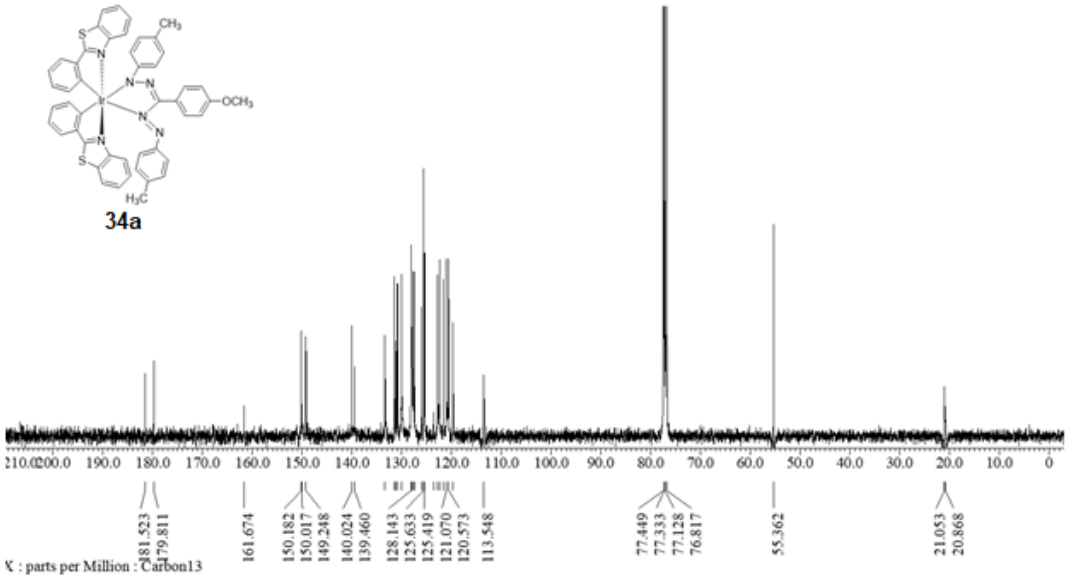

Figure S40. ^{13}C{^{1}H} NMR spectrum of Ir(bt)$_2$(**Fza**) (**34a**), recorded at 151 MHz in $CDCl_3$.

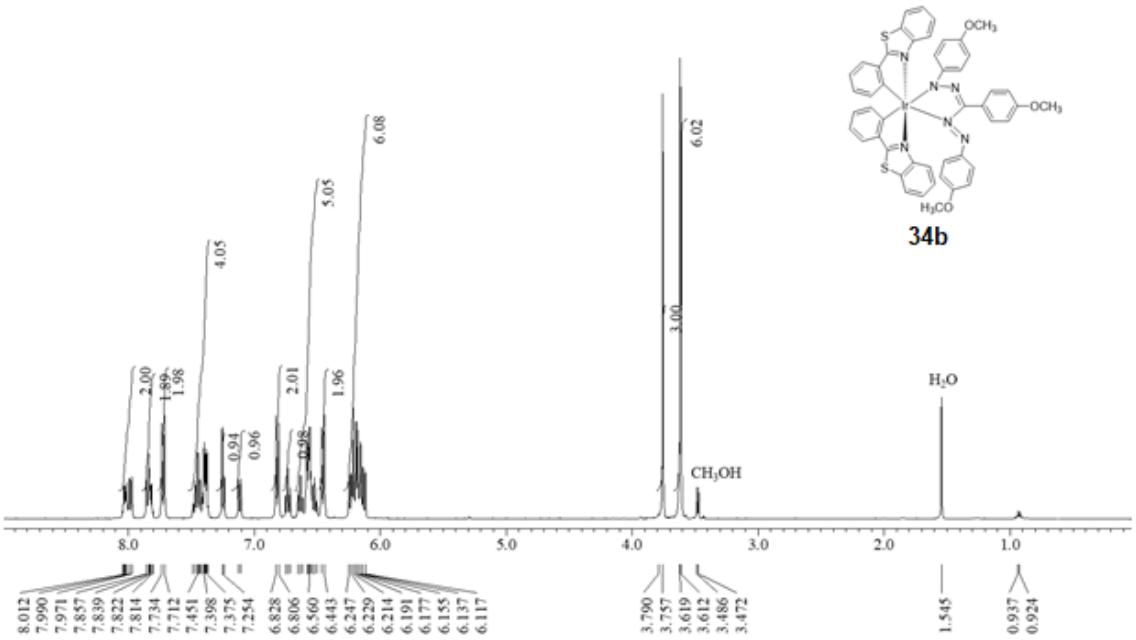

Figure S41. ^{1}H NMR spectrum of Ir(bt)$_2$(**Fzb**) (**34b**), recorded at 500 MHz in $CDCl_3$.

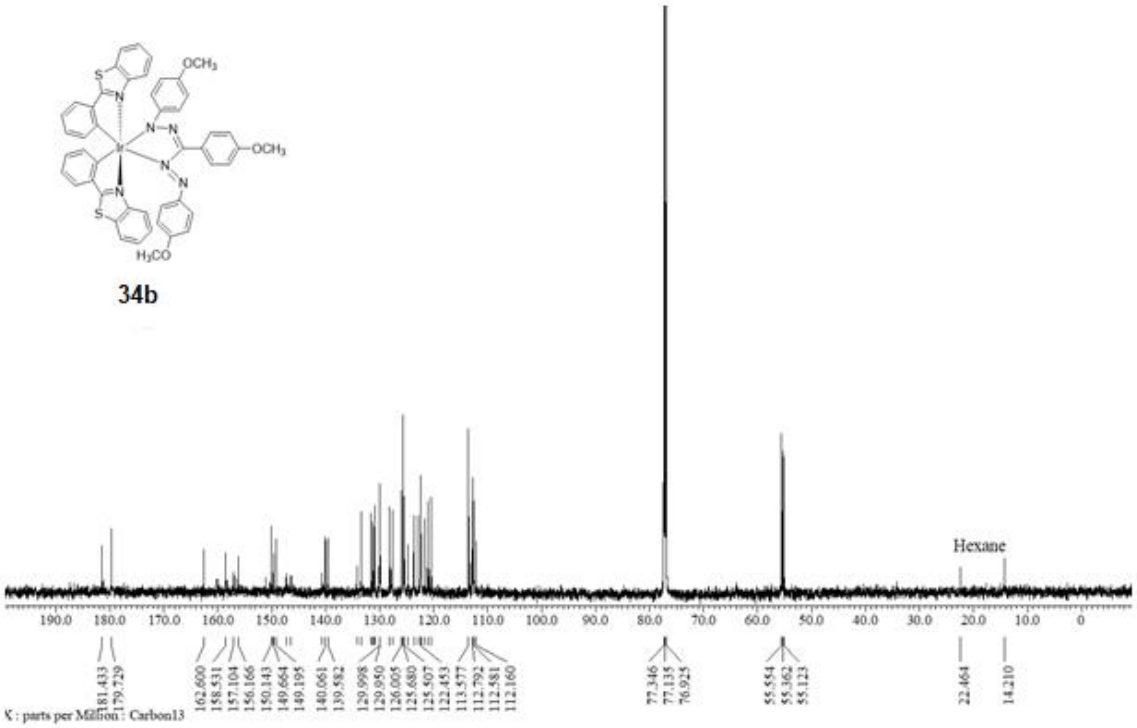

Figure S42. $^{13}C\{^{1}H\}$ NMR spectrum of Ir(bt)$_2$(**Fzb**) (**34b**), recorded at 151 MHz in $CDCl_3$.

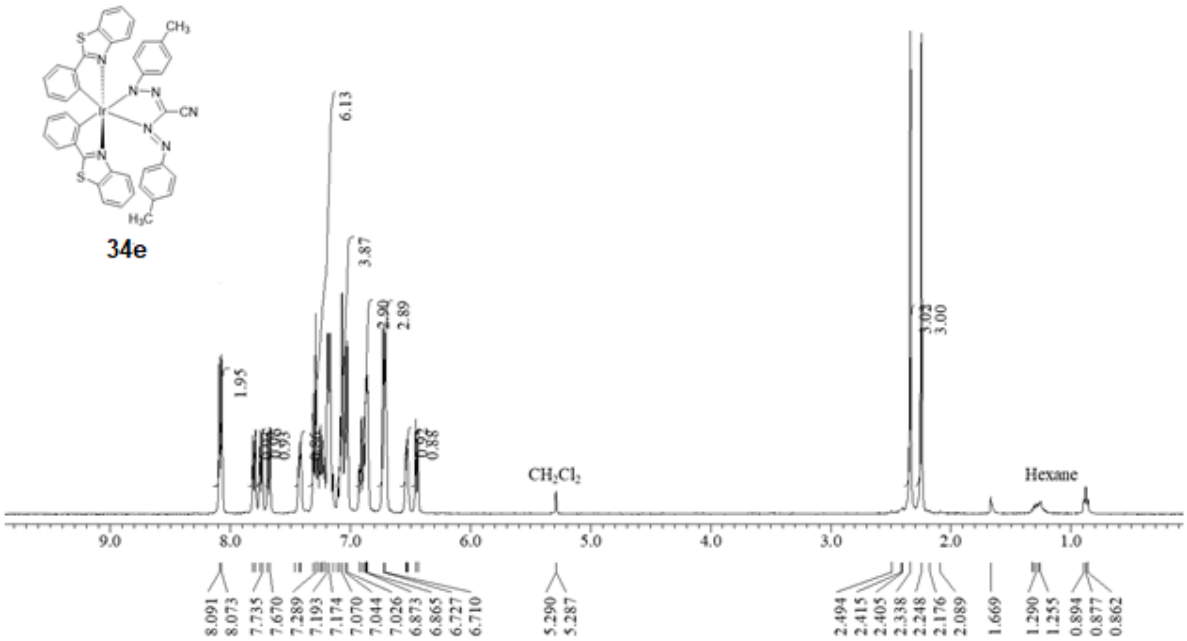

Figure S43. ^{1}H NMR spectrum of Ir(bt)$_2$(**Fze**) (**34e**), recorded at 400 MHz in $CDCl_3$.

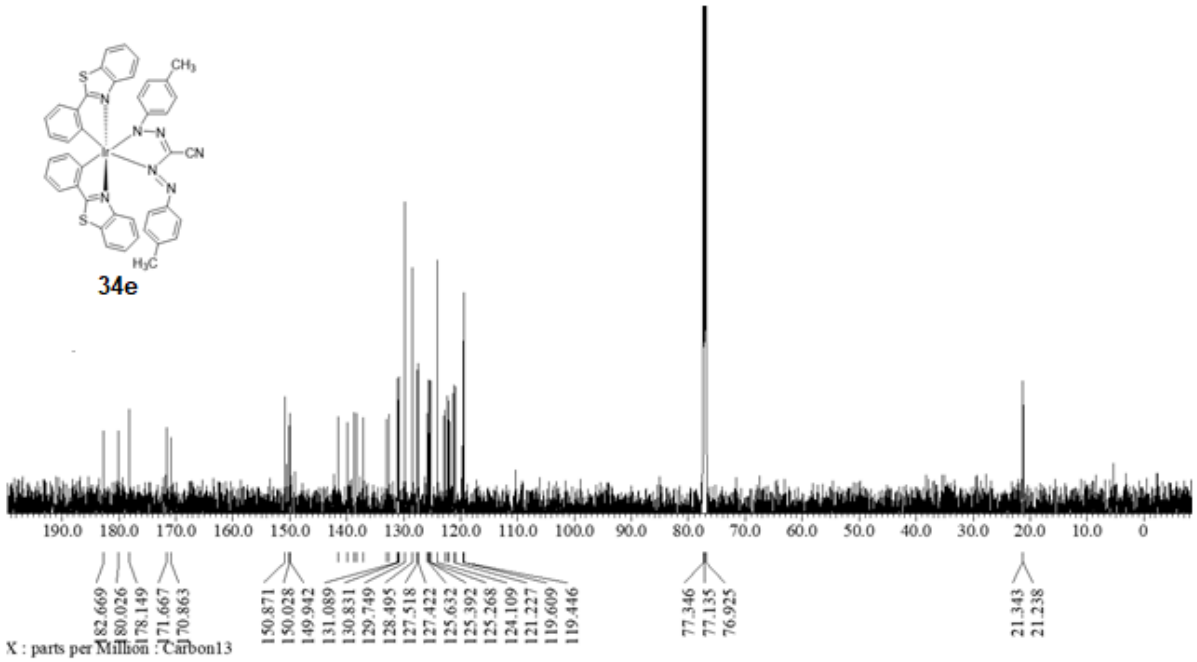

Figure S44. ^{13}C{^{1}H} NMR spectrum of Ir(bt)$_2$(**Fze**) (**34e**), recorded at 151 MHz in $CDCl_3$.

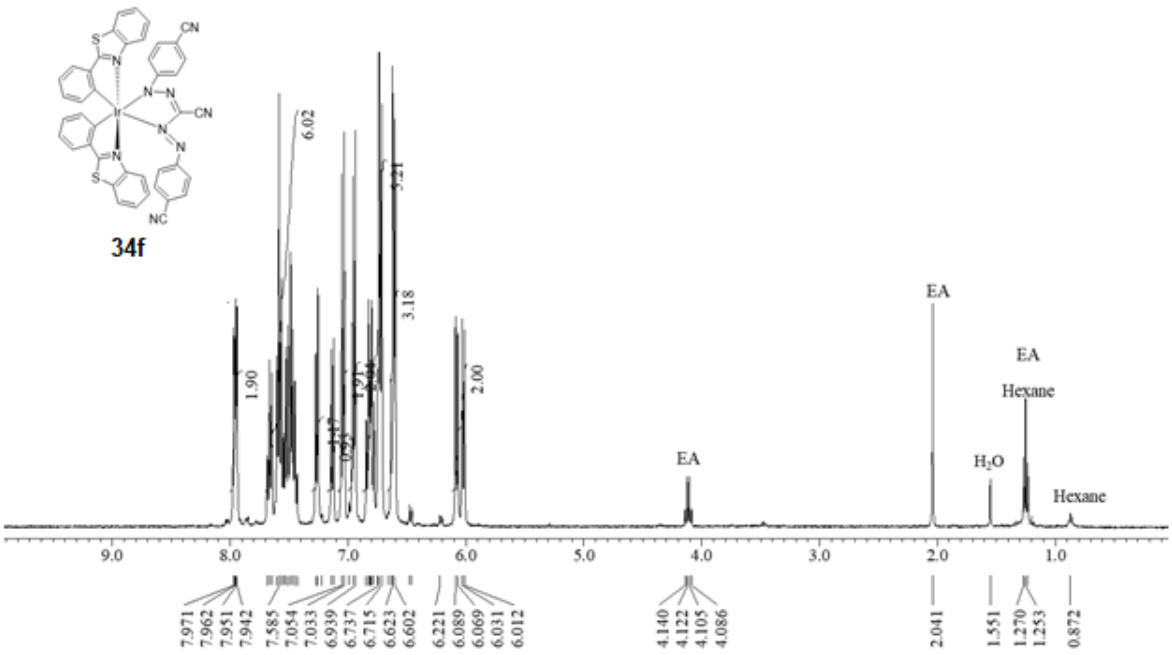

Figure S45. ^{1}H NMR spectrum of Ir(bt)$_2$(**Fzf**) (**34f**), recorded at 500 MHz in $CDCl_3$.

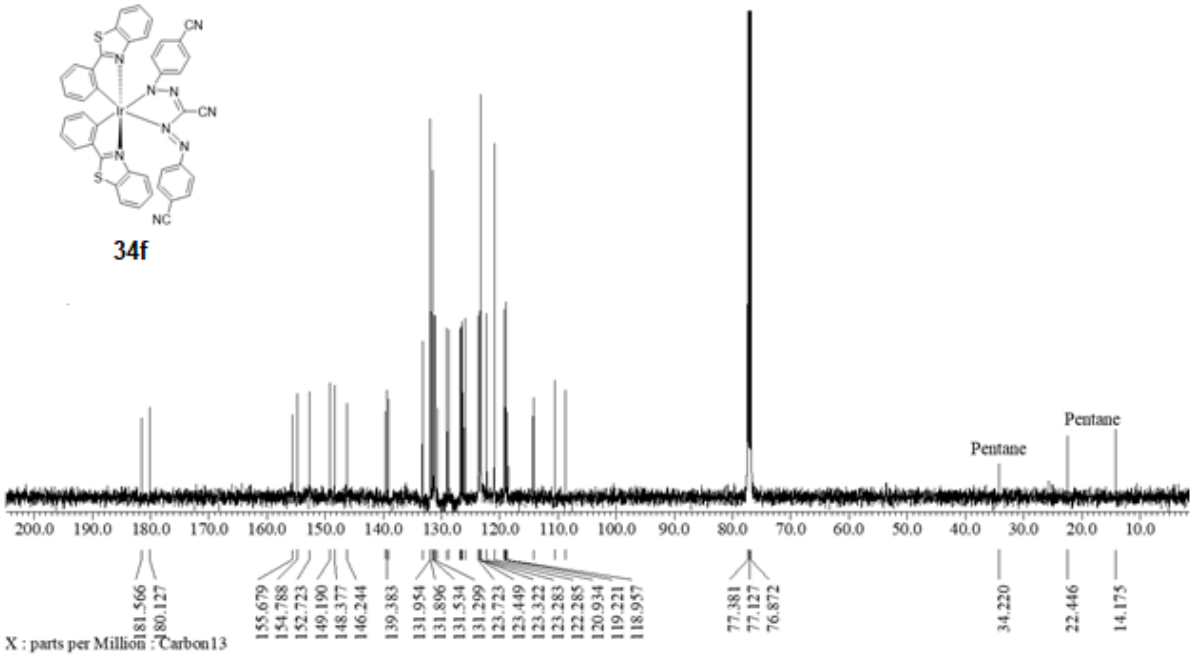

Figure S46. $^{13}C\{^{1}H\}$ NMR spectrum of Ir(bt)$_2$(**Fzf**) (**34f**), recorded at 151 MHz in $CDCl_3$.

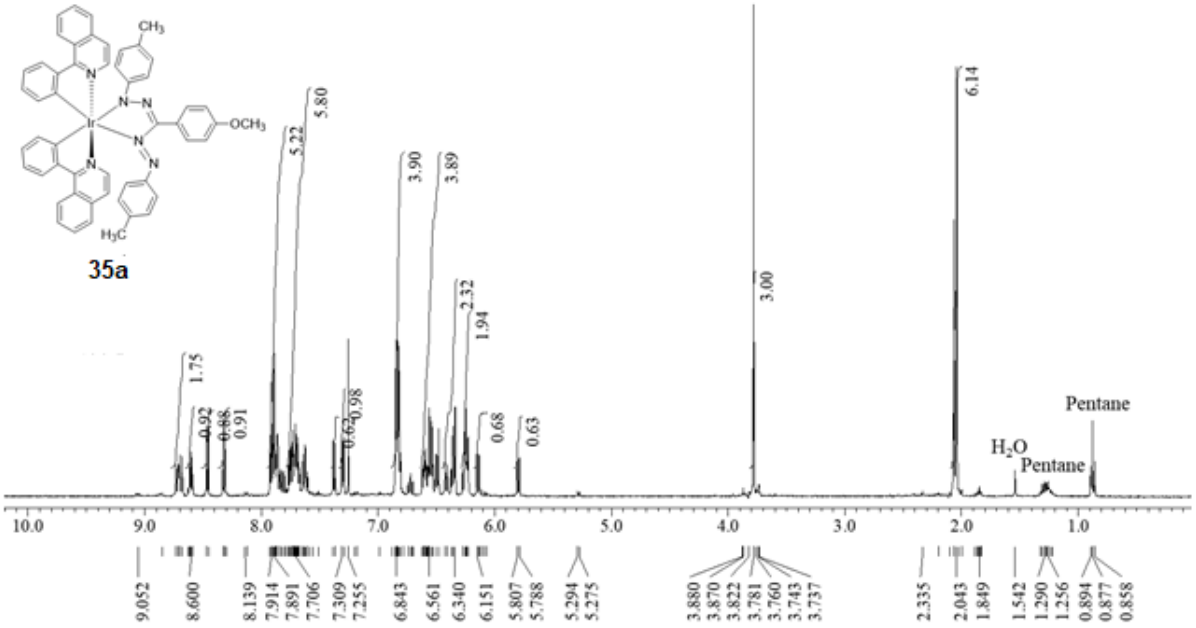

Figure S47. ^{1}H NMR spectrum of Ir(piq)$_2$(**Fza**) (**35a**), recorded at 400 MHz in $CDCl_3$.

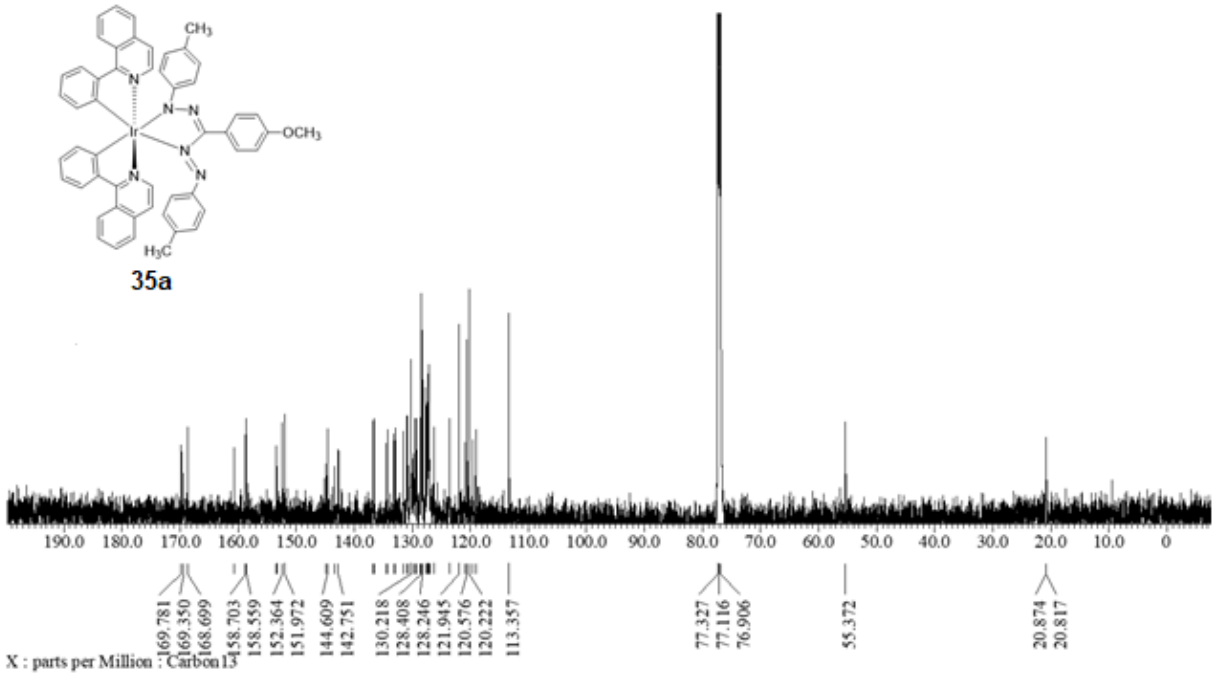

Figure S48. ^{13}C{^{1}H} NMR spectrum of Ir(piq)$_2$(**Fza**) (**35a**), recorded at 151 MHz in $CDCl_3$.

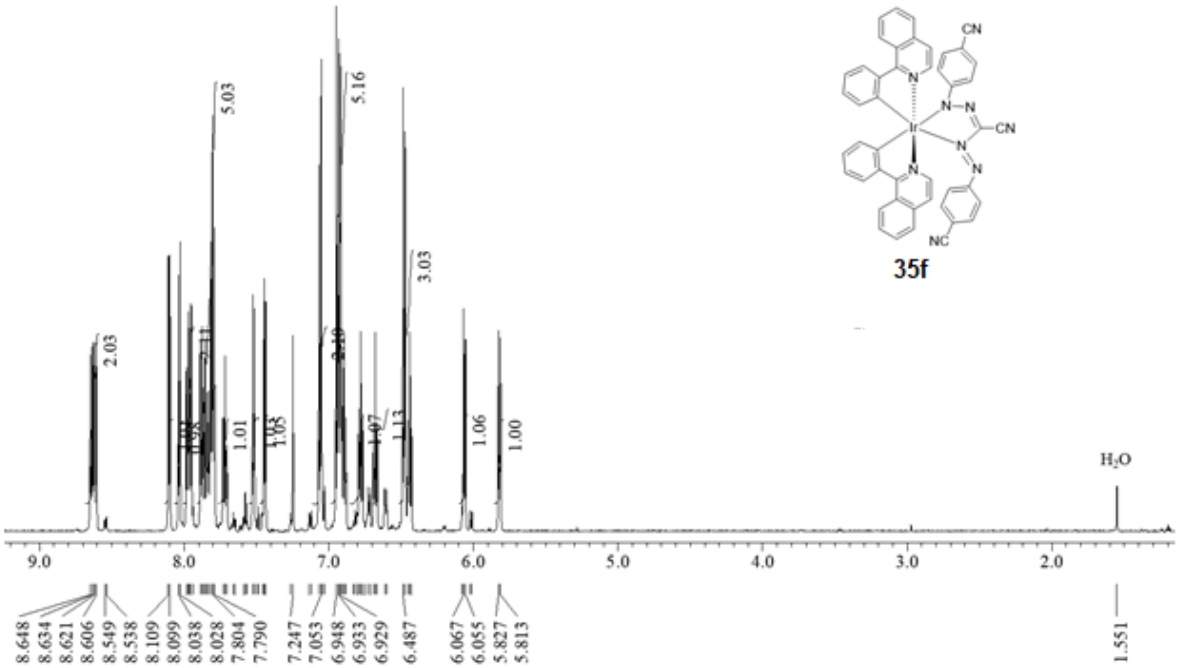

Figure S49. ^{1}H NMR spectrum of Ir(piq)$_2$(**Fzf**) (**35f**), recorded at 500 MHz in $CDCl_3$.

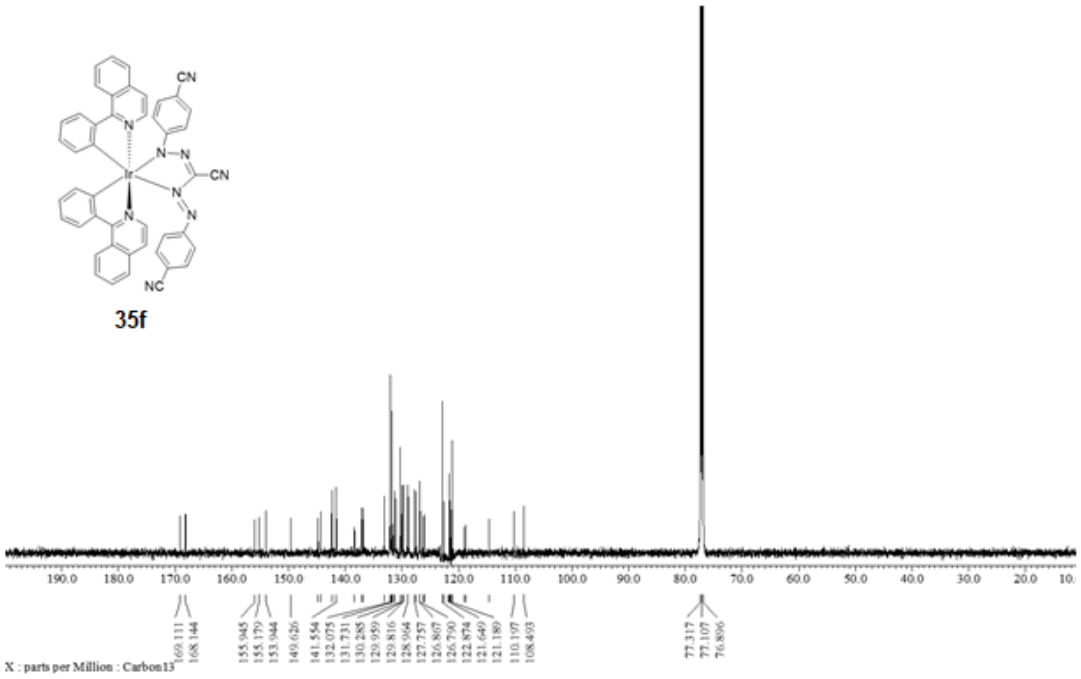

Figure S50. ^{13}C{^{1}H} NMR spectrum of Ir(piq)$_2$(**Fzf**) (**35f**), recorded at 151 MHz in $CDCl_3$.

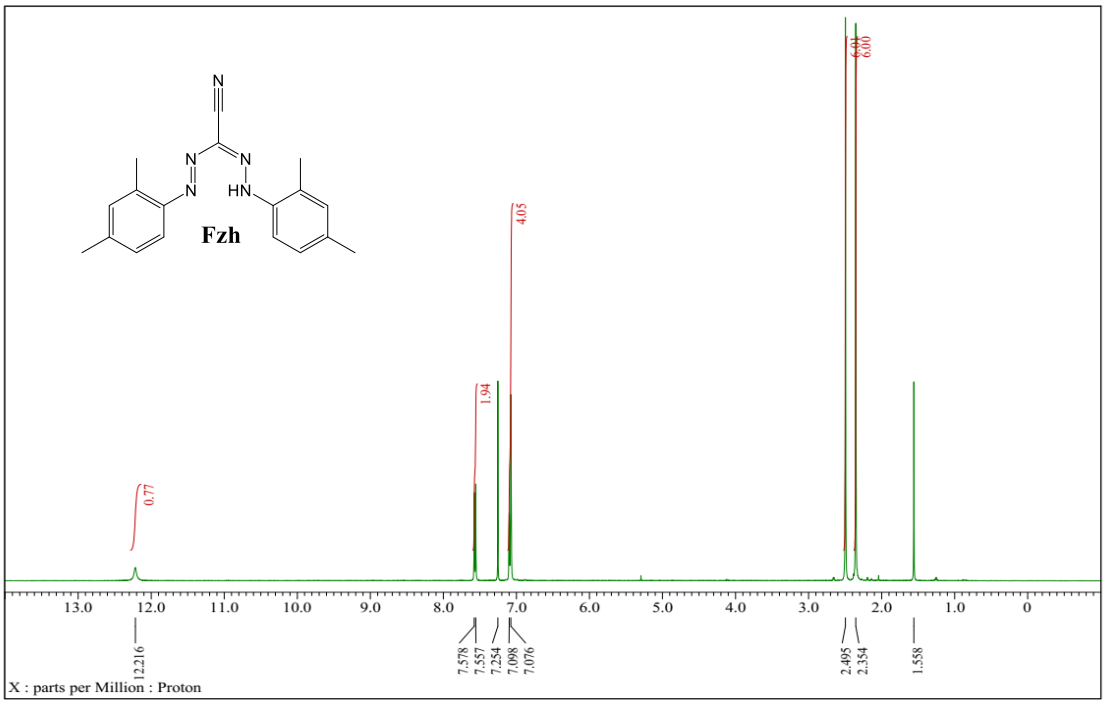

Figure S51. ^{1}H NMR spectrum of **Fzh**, recorded at 400 MHz in $CDCl_3$.

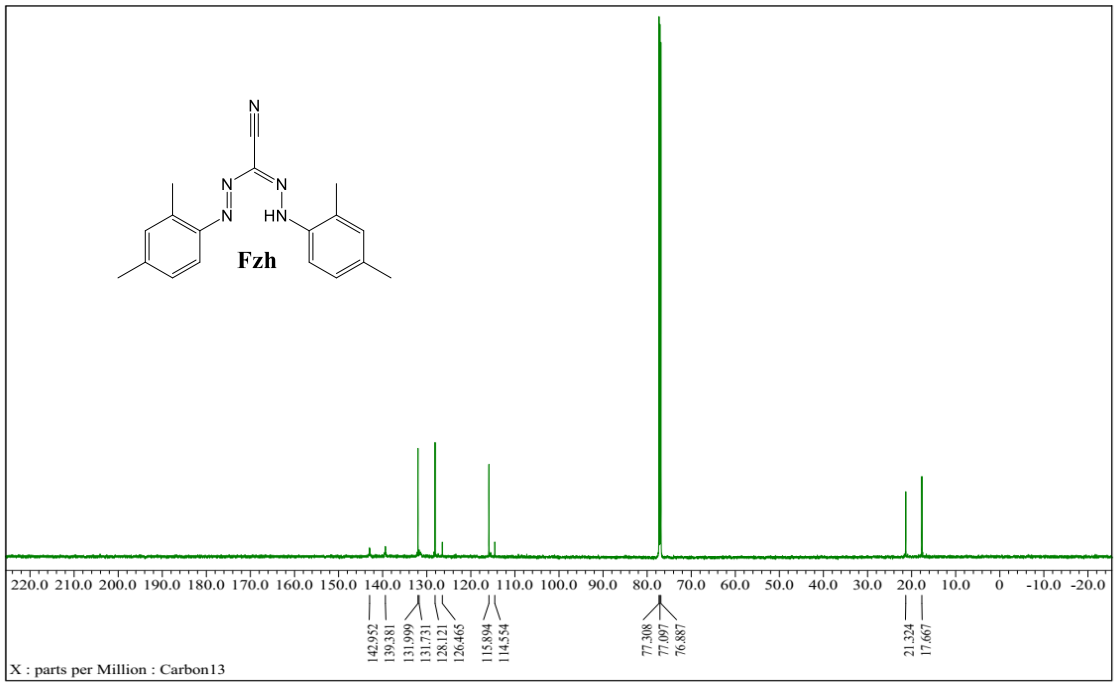

Figure S52. $^{13}C\{^{1}H\}$ NMR spectrum of **Fzh**, recorded at 151 MHz in $CDCl_3$.

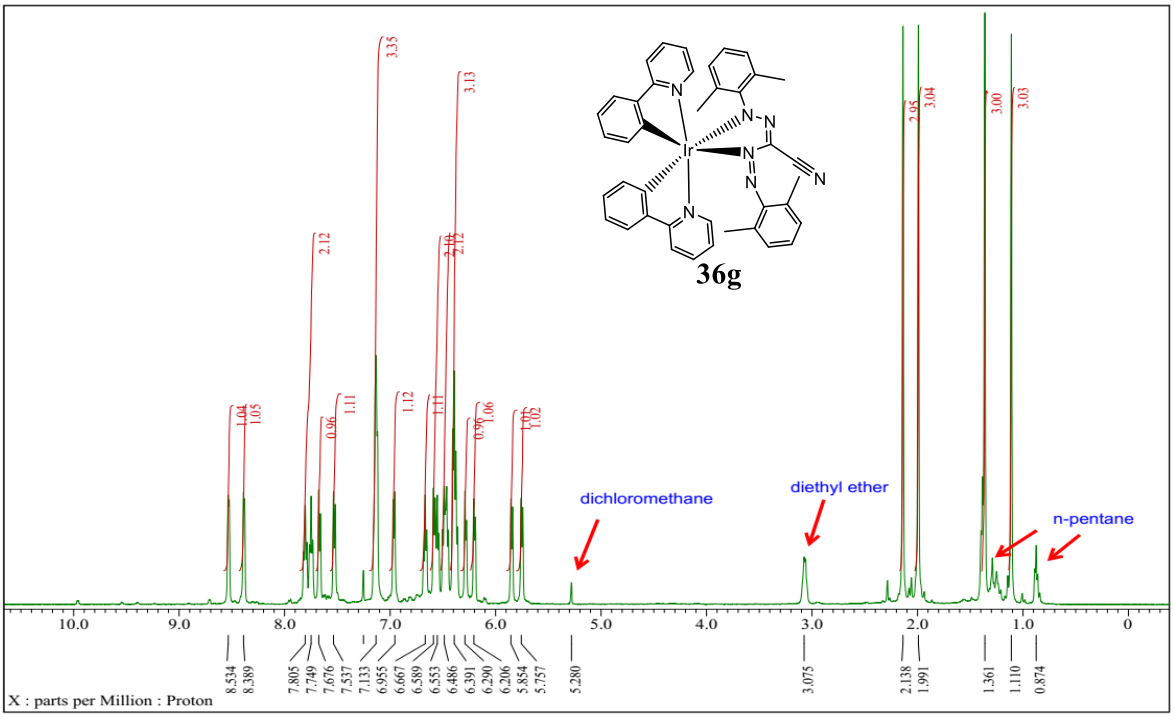

Figure S53. ^{1}H NMR spectrum of **36g**, recorded at 500 MHz in $CDCl_3$.

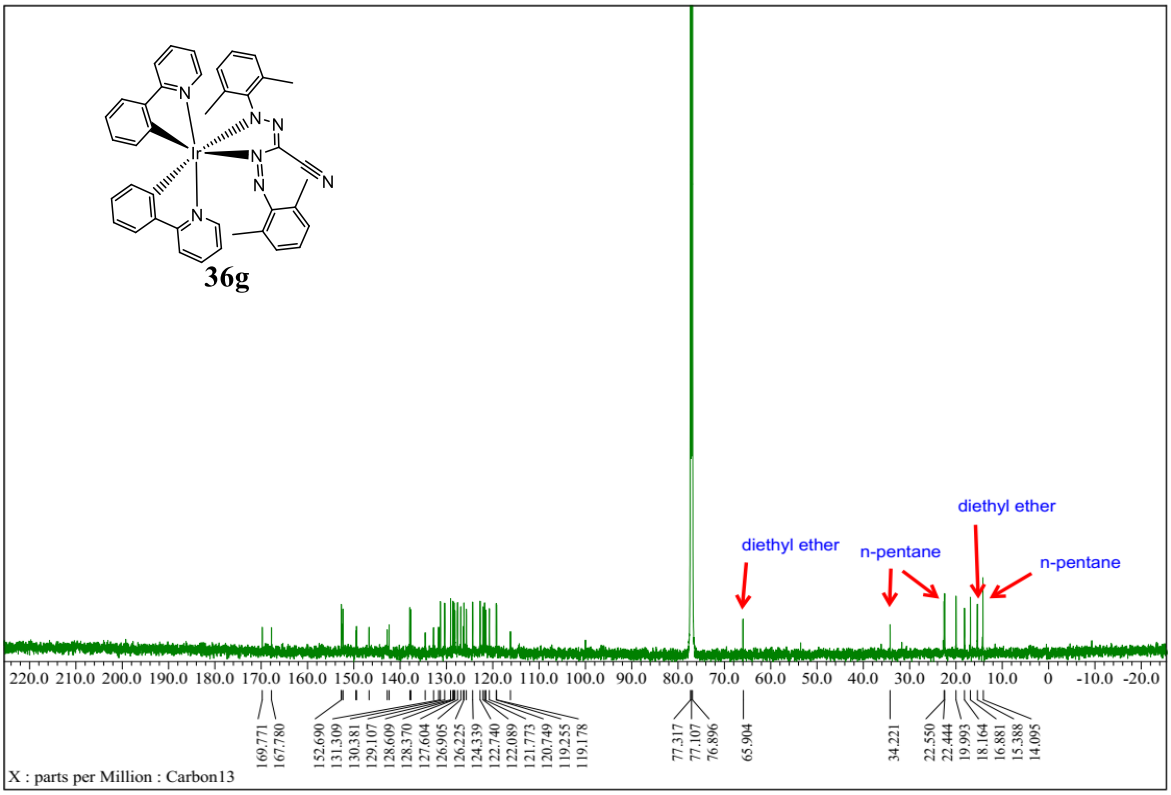

Figure S54. Room-temperature $^{13}C\{^{1}H\}$ NMR spectrum of **36g**, recorded at 151 MHz in $CDCl_3$.

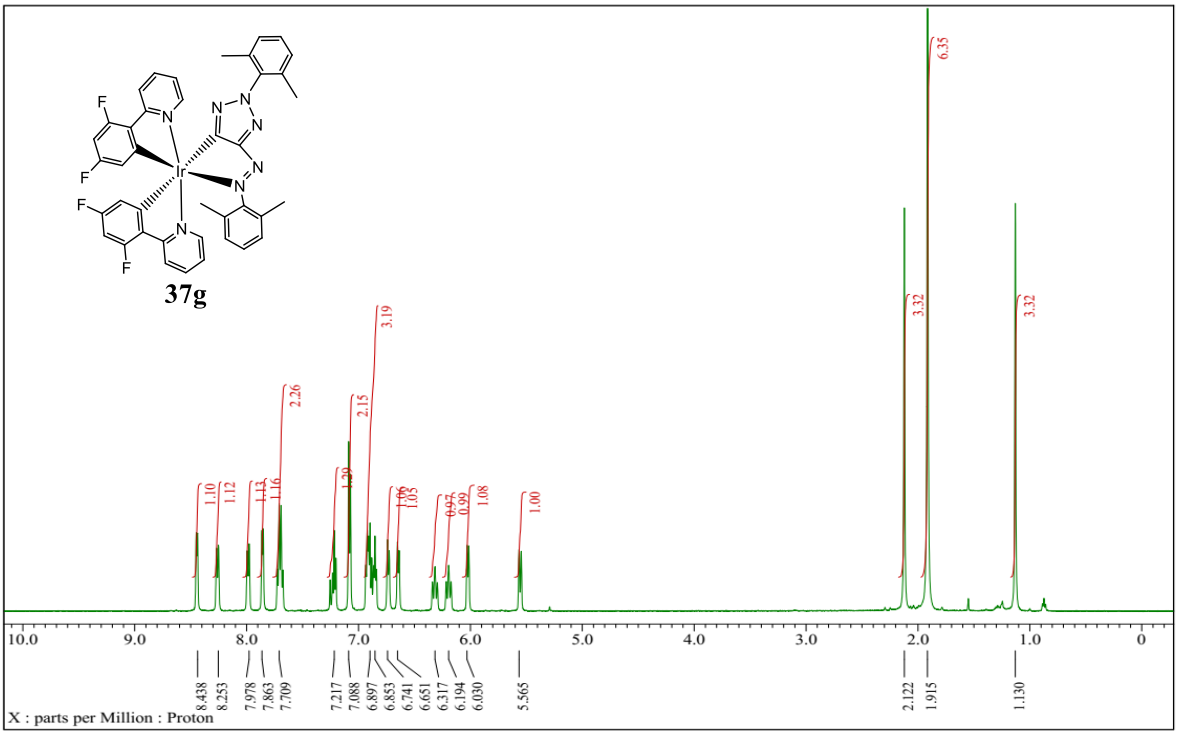

Figure S55. ^{1}H NMR spectrum of **37g**, recorded at 500 MHz in $CDCl_3$.

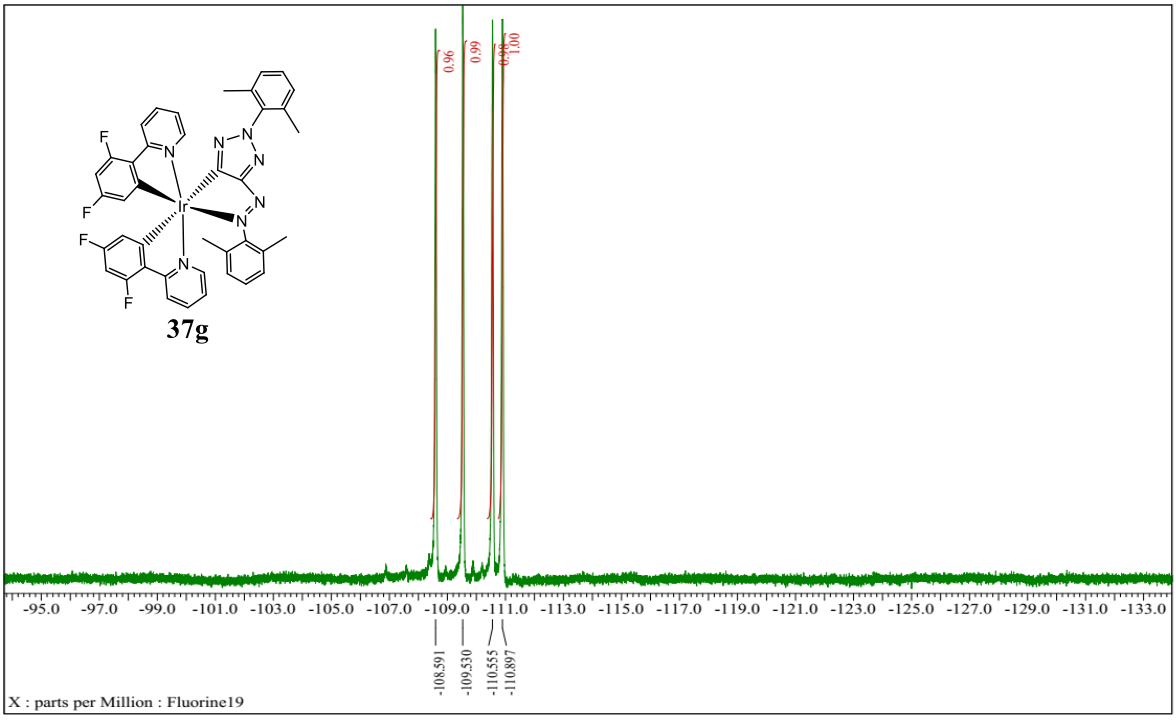

Figure S56. ^{19}F NMR spectrum of **37g**, recorded at 470 MHz in $CDCl_3$.

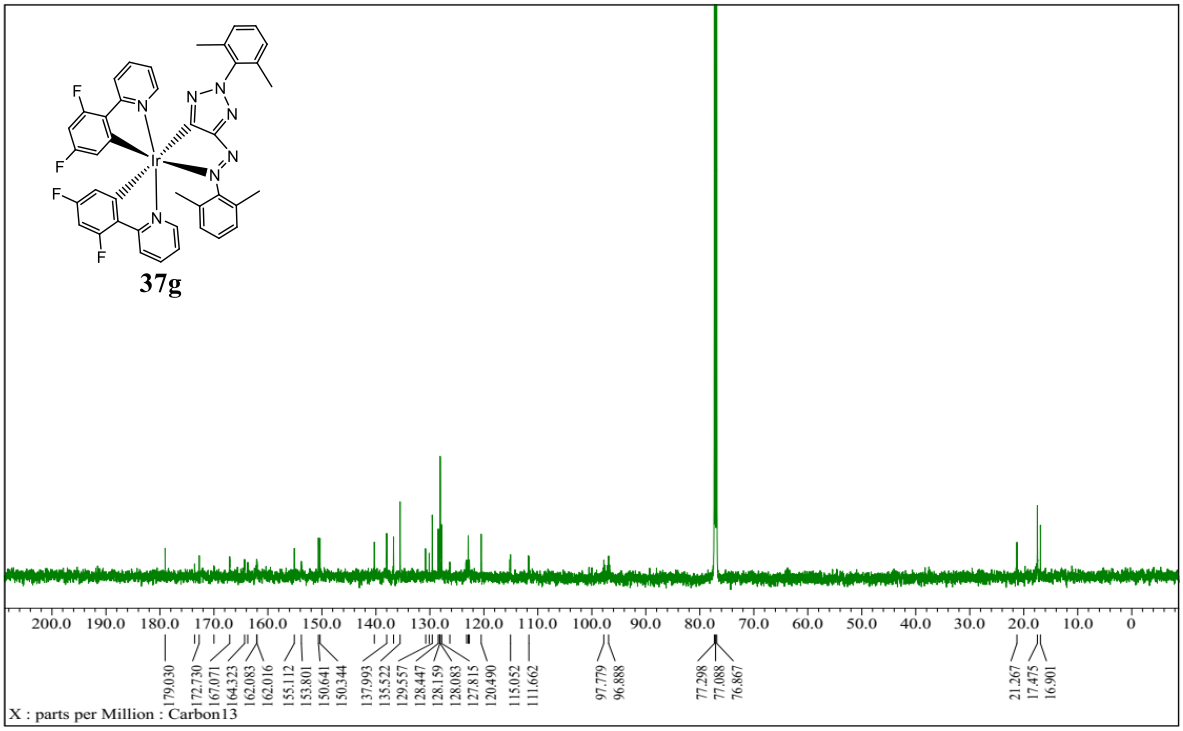

Figure S57. $^{13}C\{^{1}H\}$ NMR spectrum of **2a**, recorded at 151 MHz in $CDCl_3$.

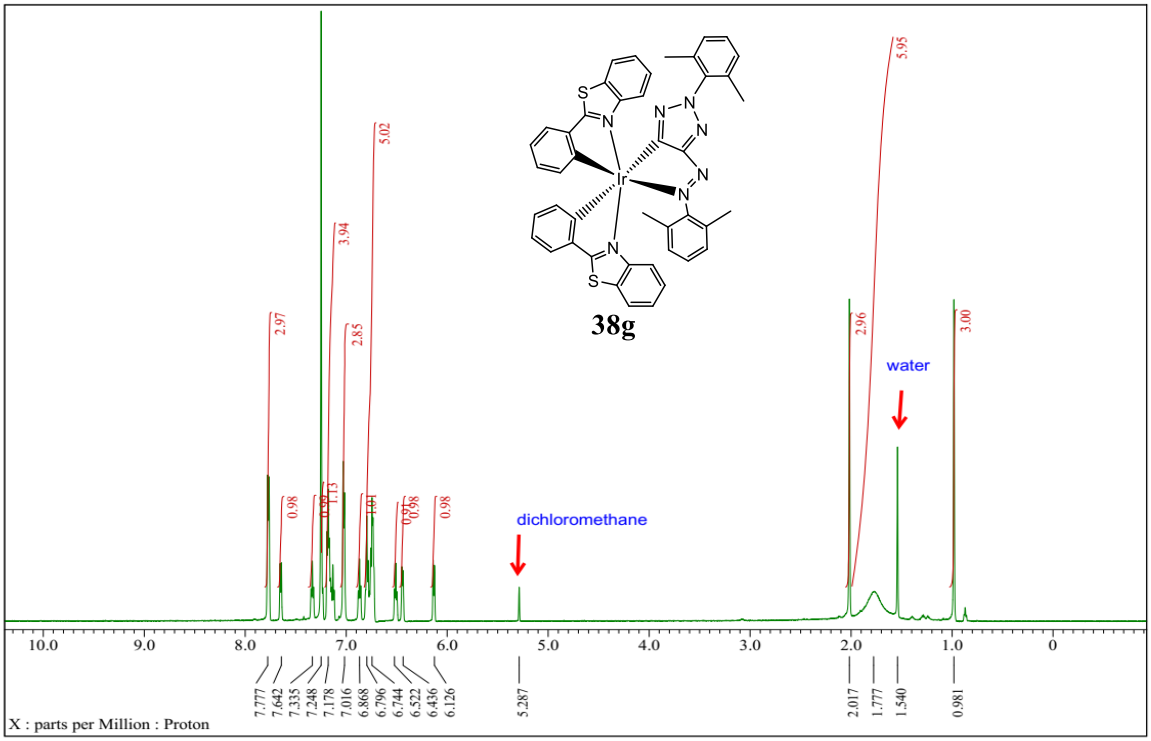

Figure S58. ^{1}H NMR spectrum of **38g**, recorded at 600 MHz in $CDCl_3$.

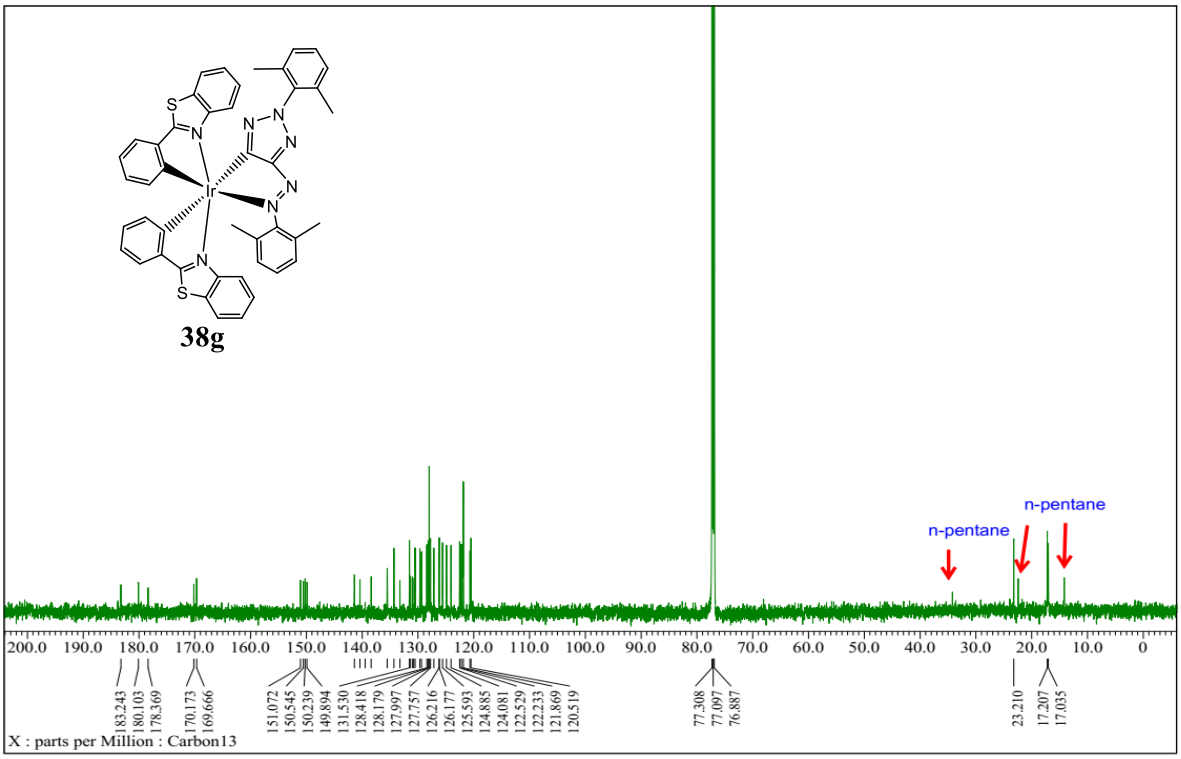

Figure S59. $^{13}C\{^{1}H\}$ NMR spectrum of **38g**, recorded at 151 MHz in $CDCl_3$.

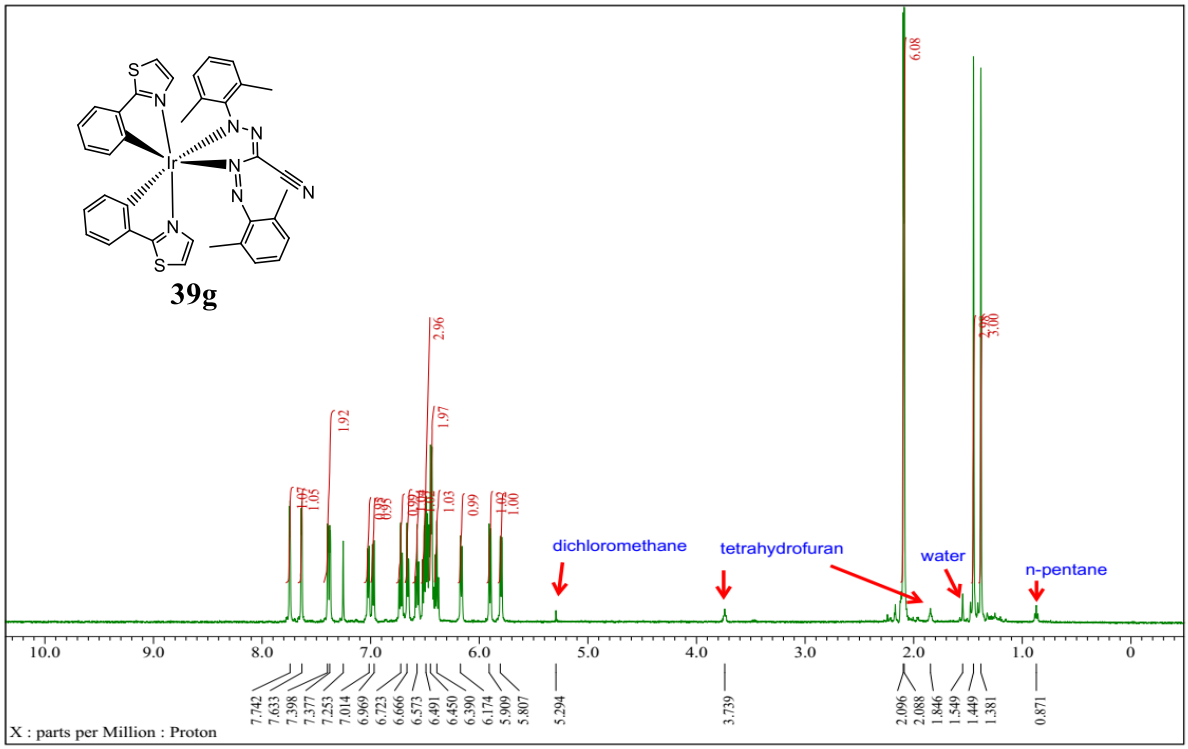

Figure S60. ^{1}H NMR spectrum of **39g**, recorded at 500 MHz in $CDCl_3$.

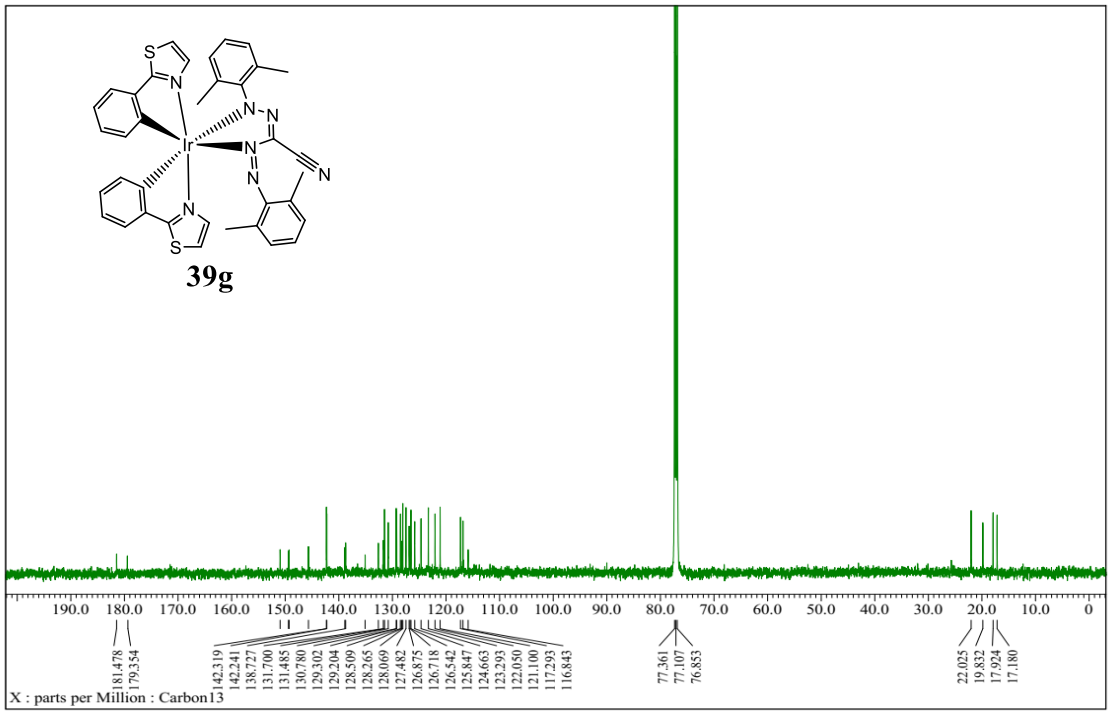

Figure S61. $^{13}C\{^{1}H\}$ NMR spectrum of **39g**, recorded at 126 MHz in $CDCl_3$.

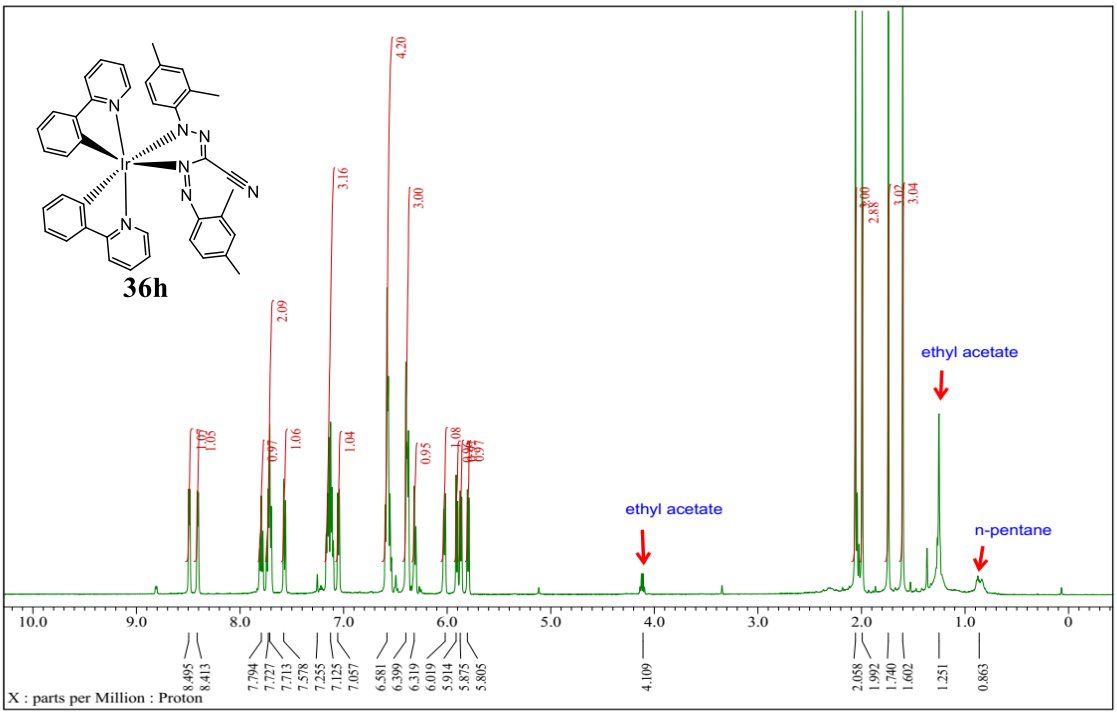

Figure S62. ^{1}H NMR spectrum of **36h**, recorded at 500 MHz in $CDCl_3$.

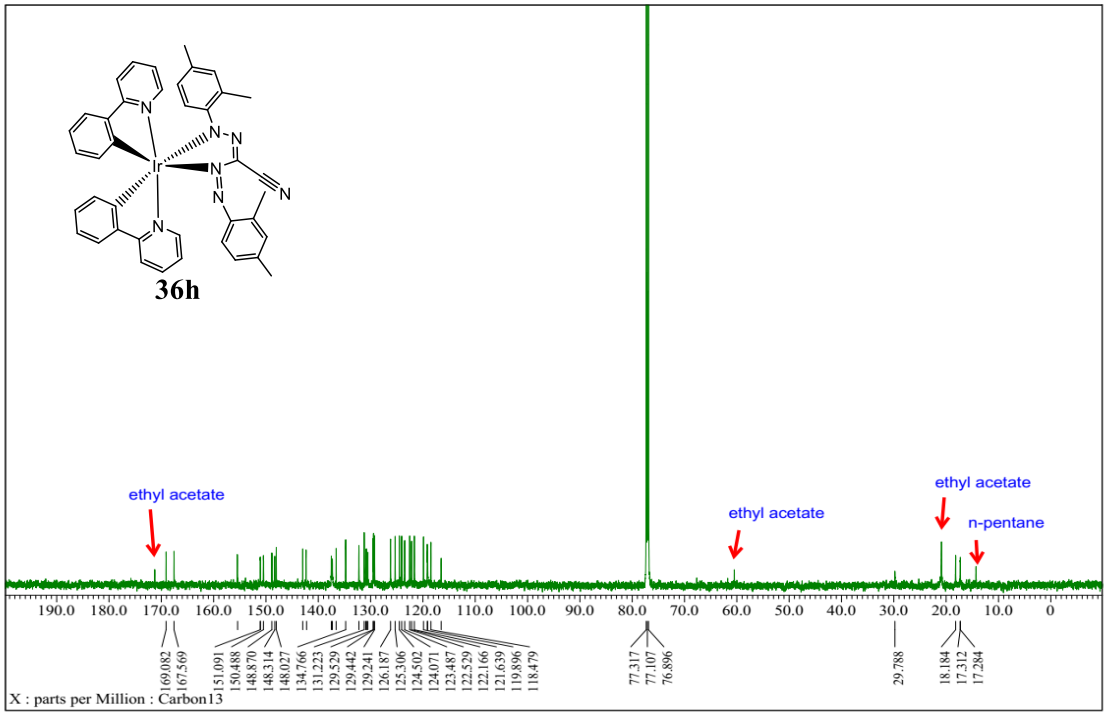

Figure S63. $^{13}C\{^{1}H\}$ NMR spectrum of **36h**, recorded at 151 MHz in $CDCl_3$.

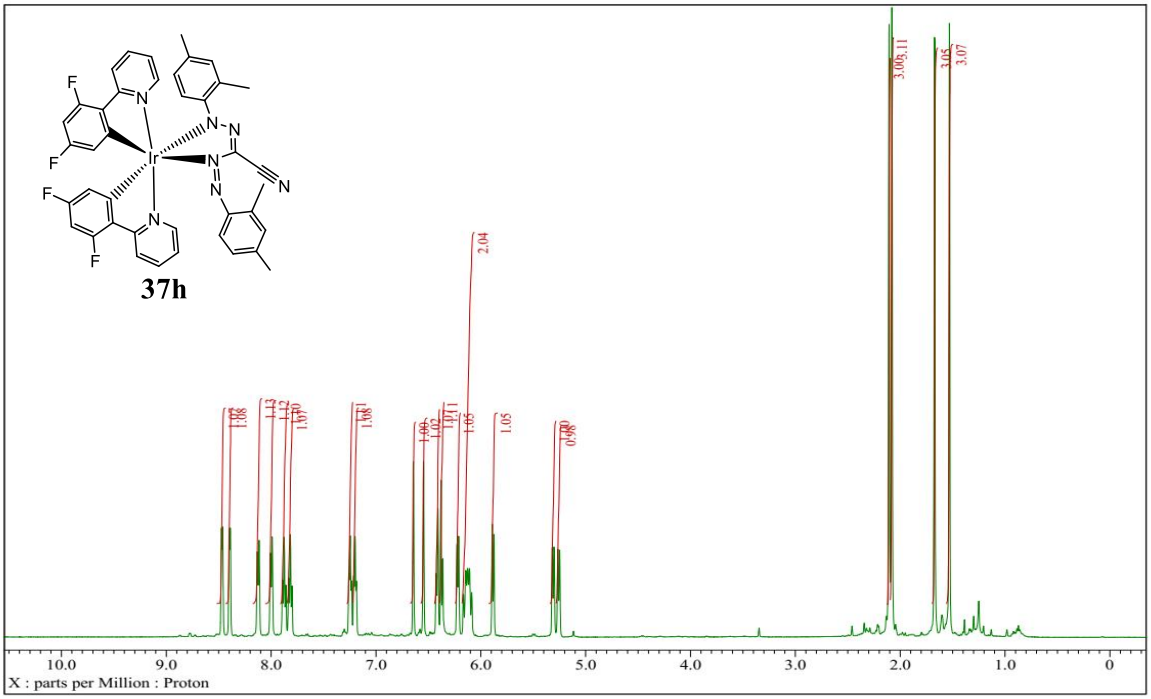

Figure S64. ^{1}H NMR spectrum of **37h**, recorded at 500 MHz in $CDCl_3$.

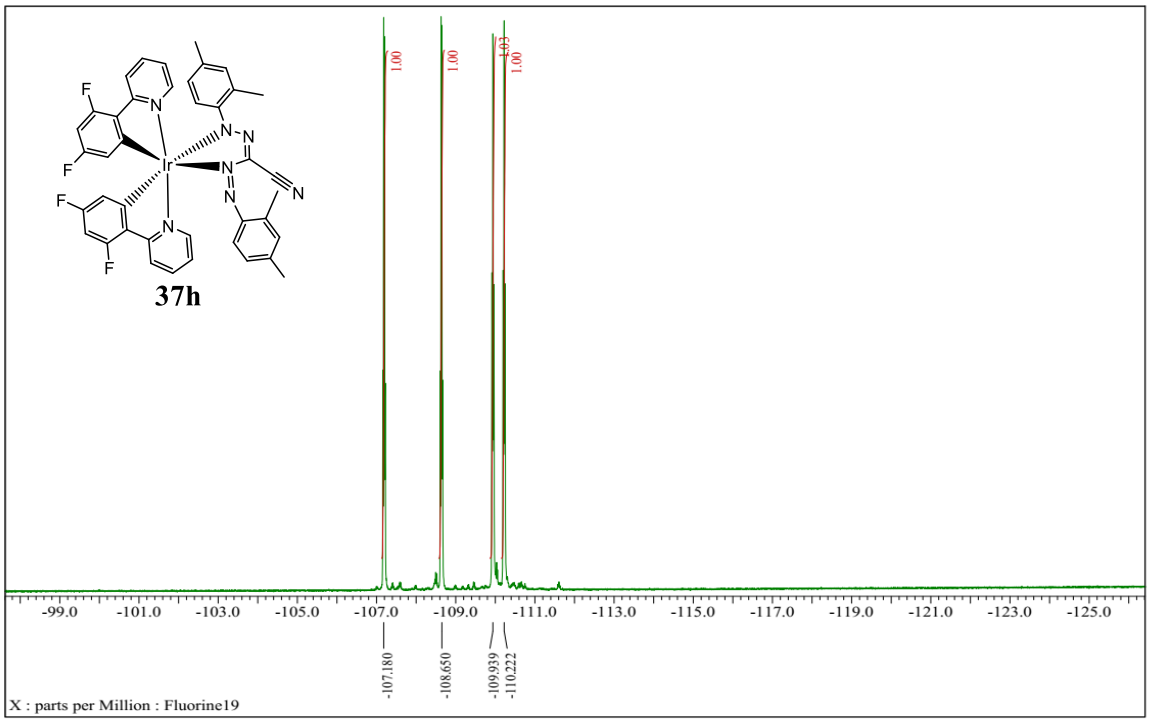

Figure S65. ^{19}F NMR spectrum of **37h**, recorded at 470 MHz in $CDCl_3$.

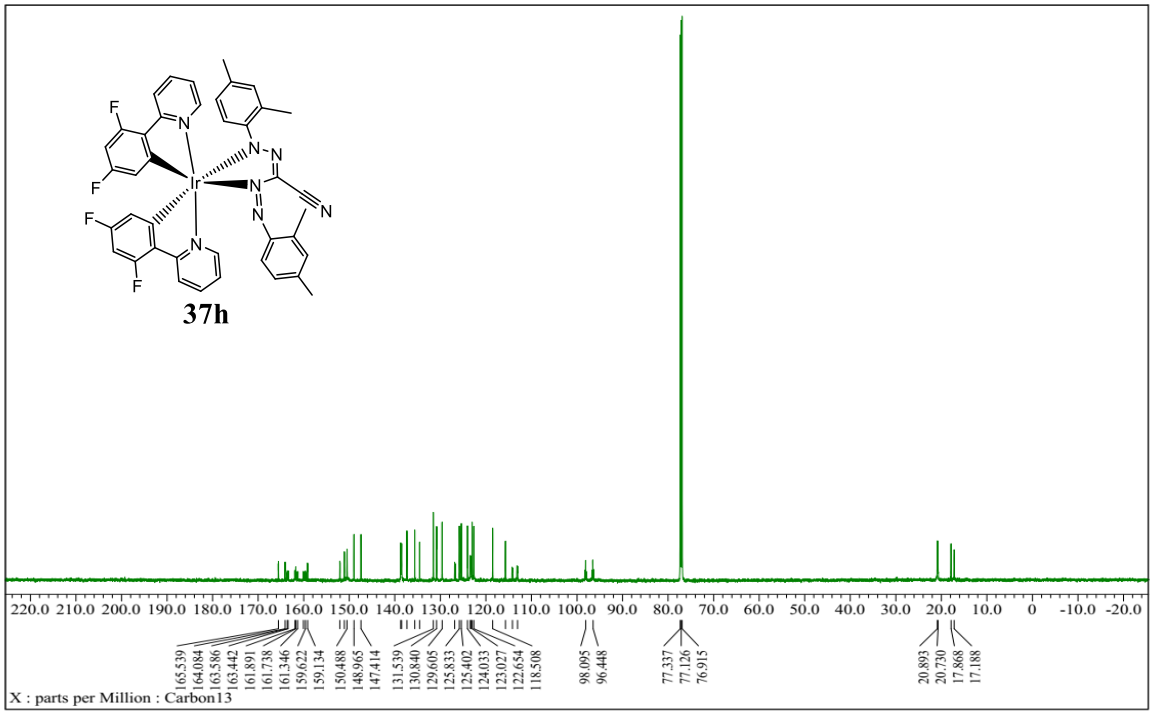

Figure S66. $^{13}C\{^1H\}$ NMR spectrum of **37h**, recorded at 151 MHz in $CDCl_3$.

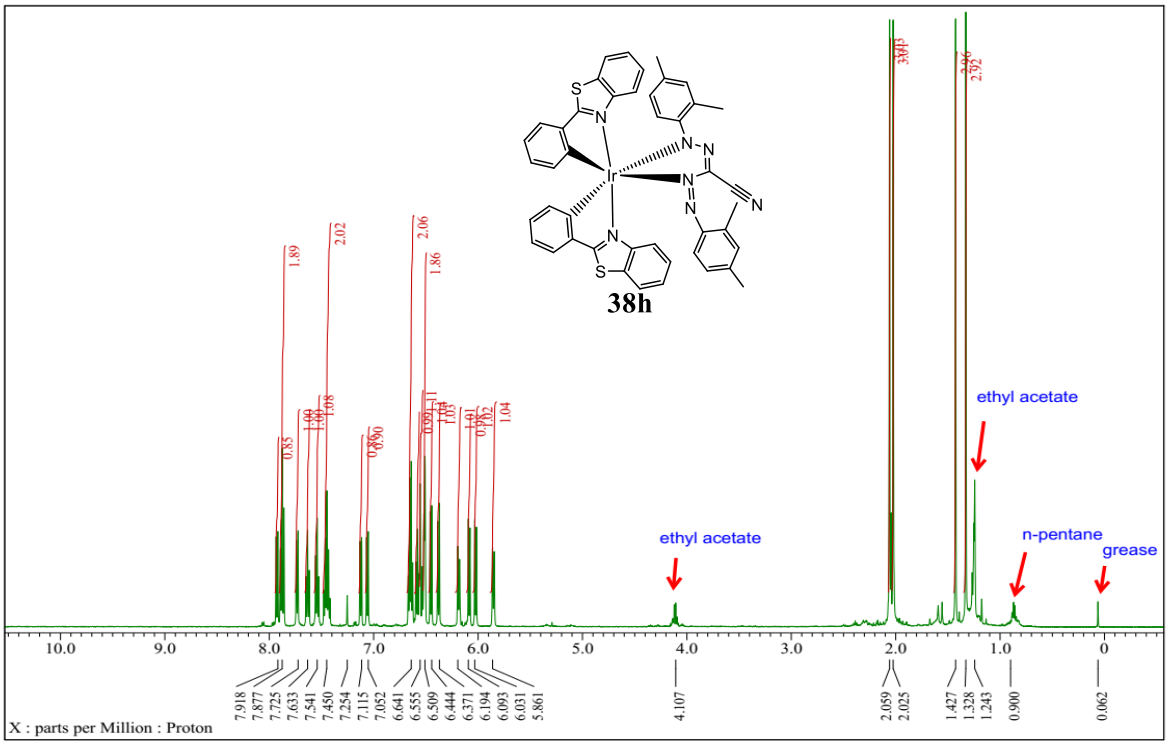

Figure S67. ^{1}H NMR spectrum of **38h**, recorded at 500 MHz in $CDCl_3$.

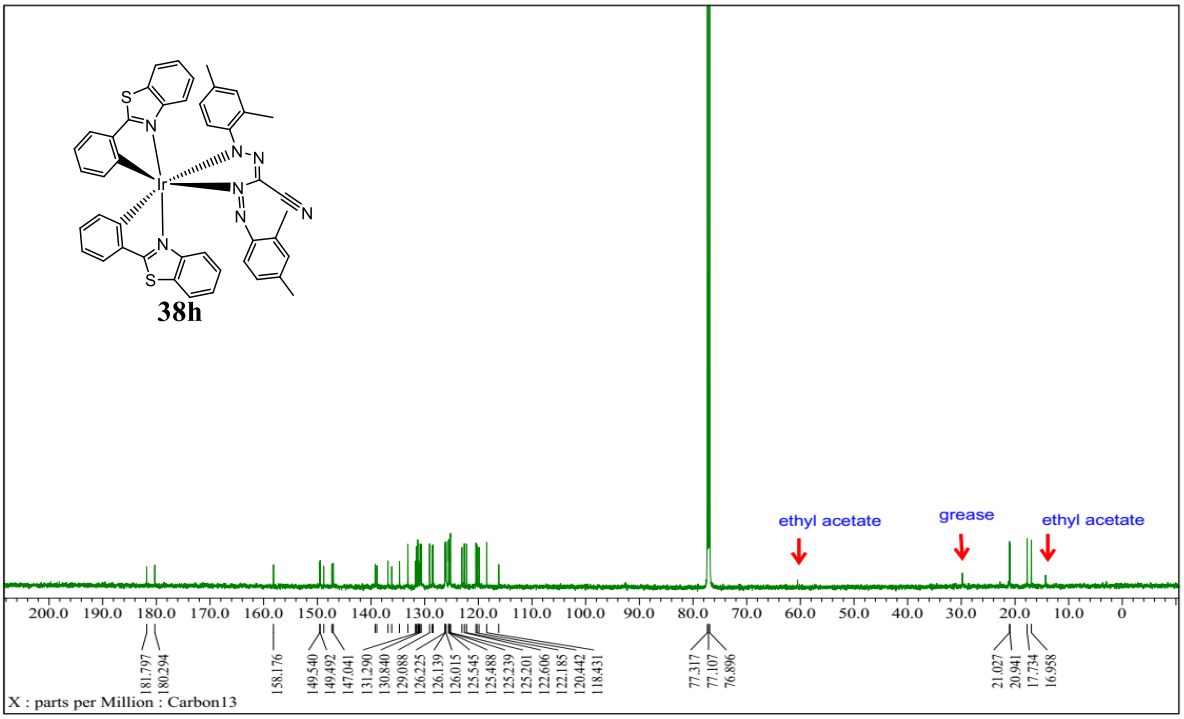

Figure S68. $^{13}C\{^{1}H\}$ NMR spectrum of **38h**, recorded at 151 MHz in $CDCl_3$.

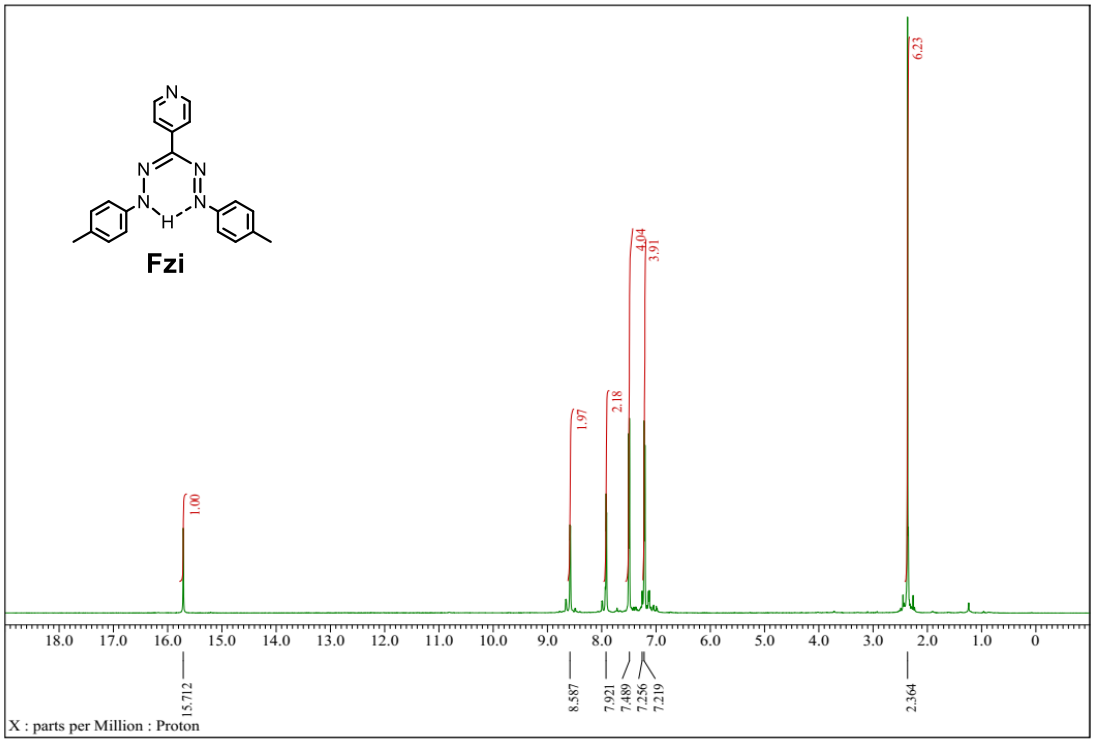

Figure S69. ^{1}H NMR spectrum of **Fzi**, recorded at 500 MHz in $CDCl_3$.

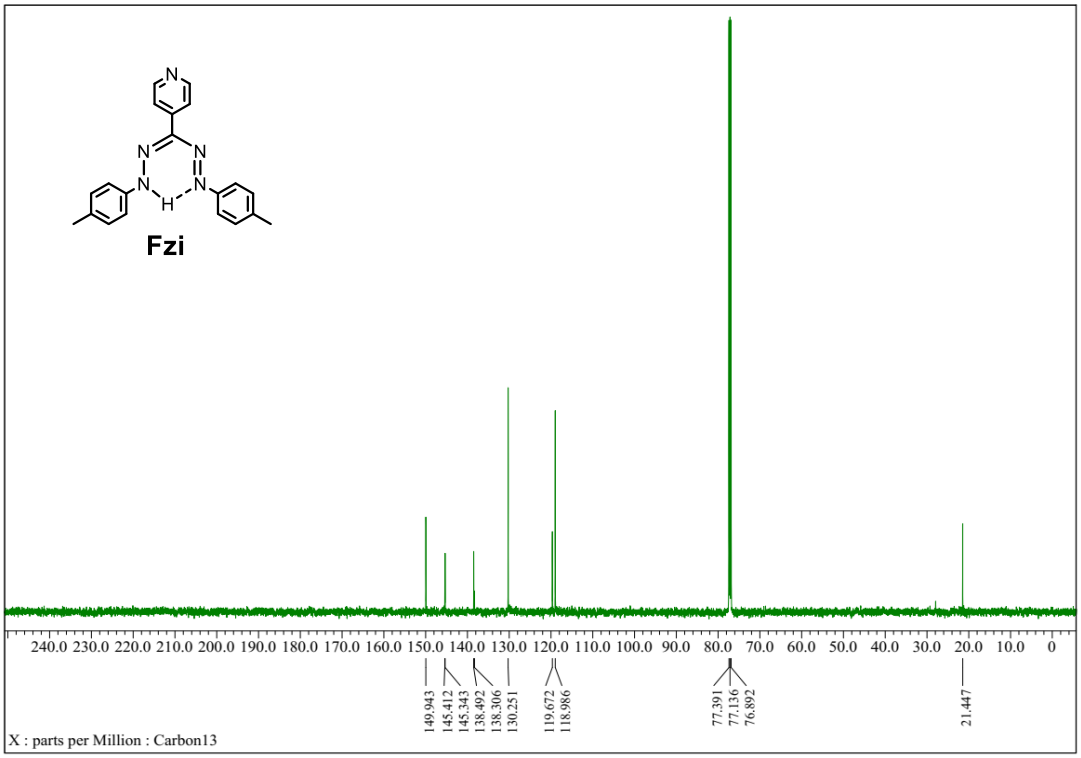

Figure S70. $^{13}C\{^{1}H\}$ NMR spectrum of **Fzi**, recorded at 126 MHz in $CDCl_3$.

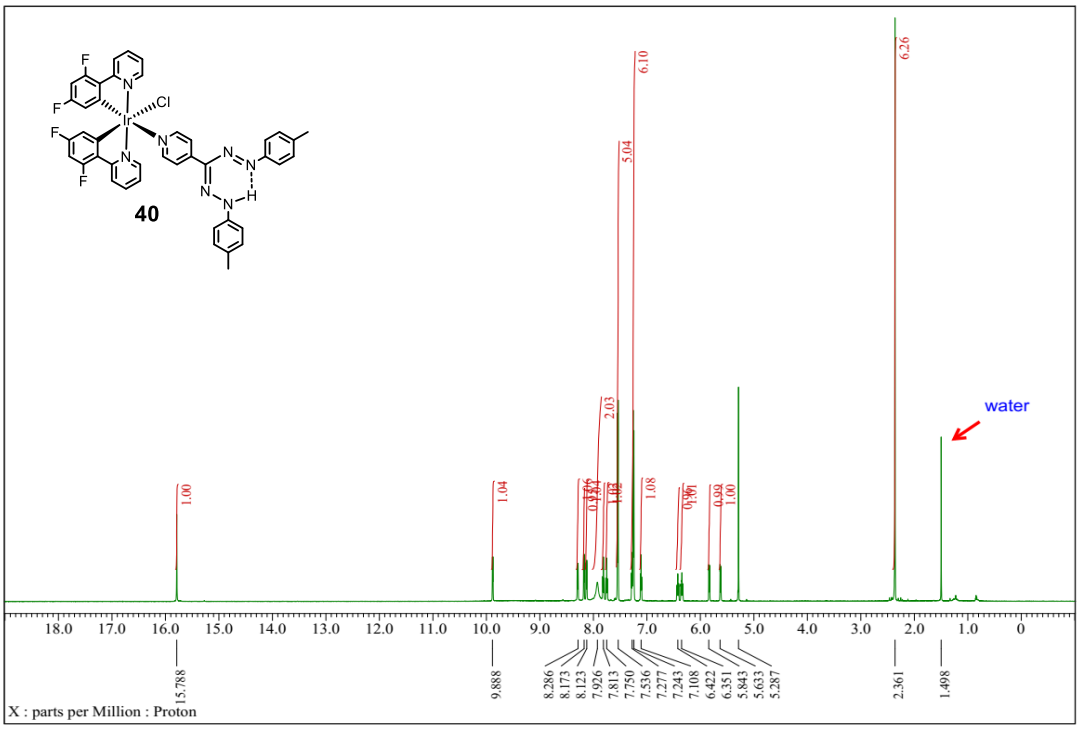

Figure S71. ^{1}H NMR spectrum of complex **40**, recorded at 600 MHz in CD_2Cl_2.

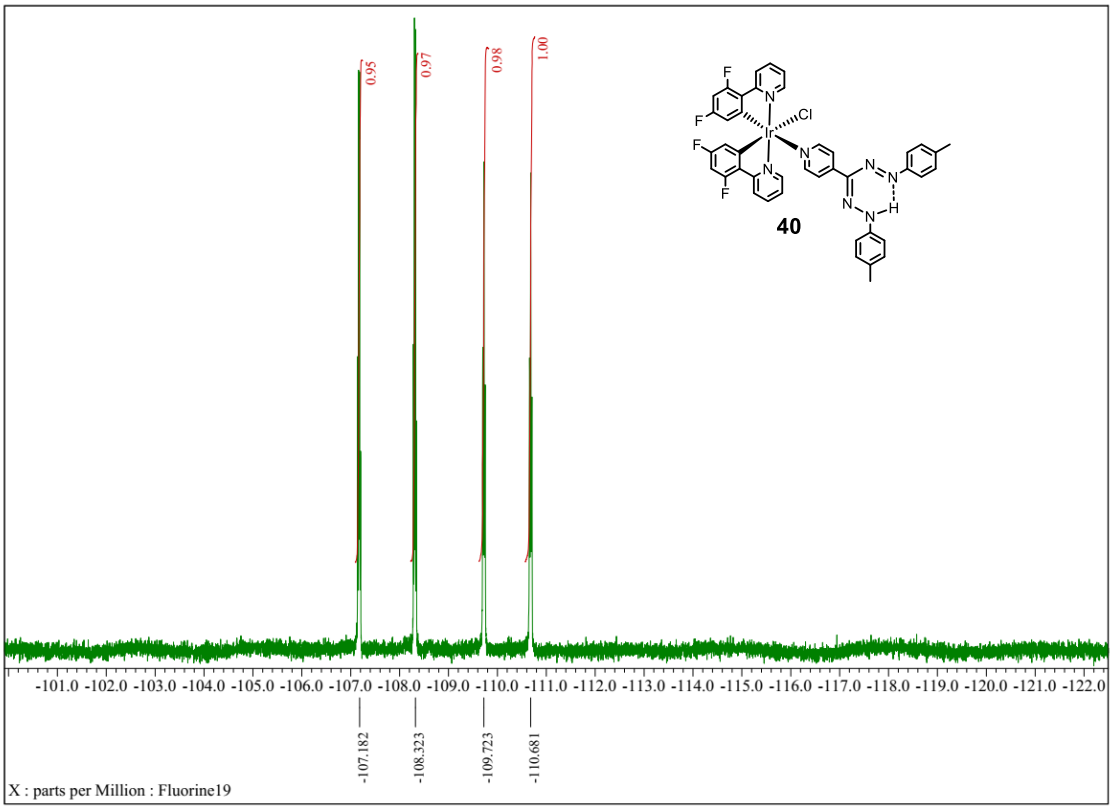

Figure S72. ^{19}F NMR spectrum of complex **40**, recorded at 470 MHz in $CDCl_3$.

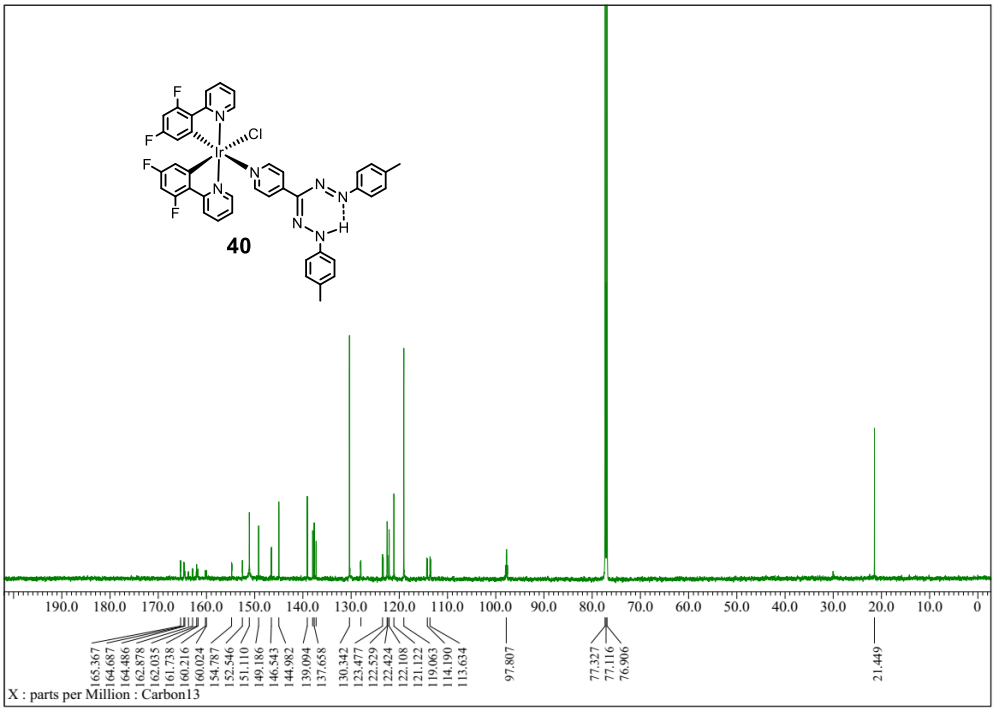

Figure S73. $^{13}C\{^{1}H\}$ NMR spectrum of complex **40**, recorded at 151 MHz in $CDCl_3$.

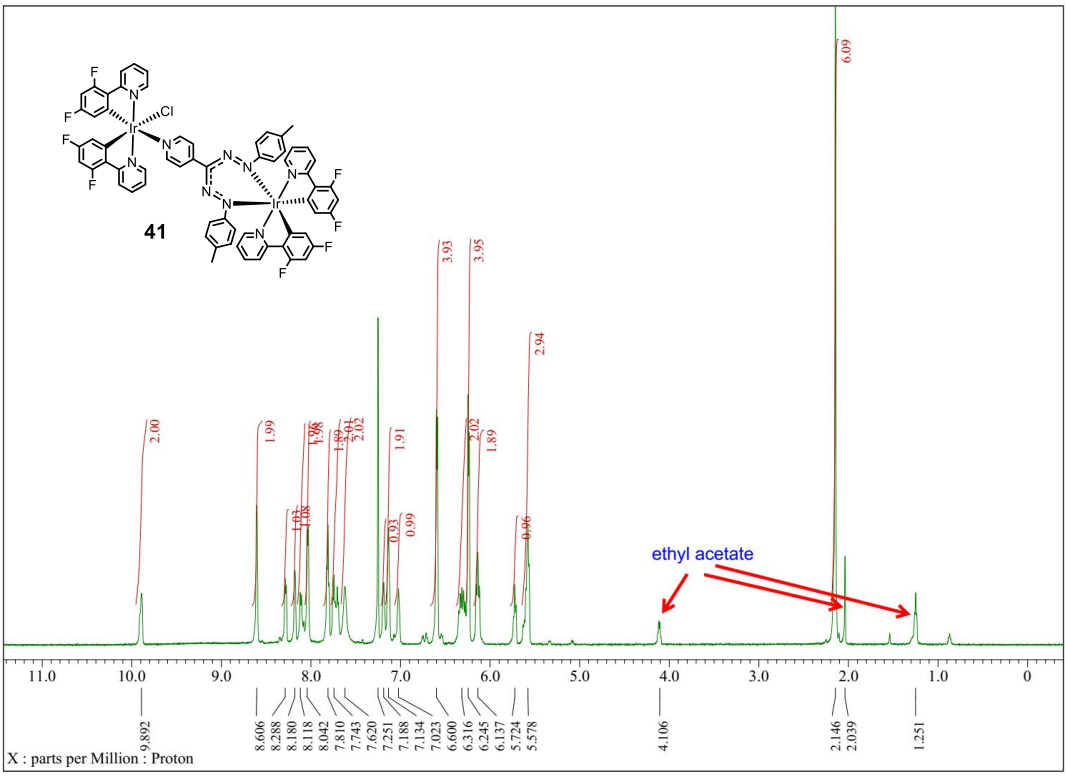

Figure S74. ^{1}H NMR spectrum of complex **41**, recorded at 600 MHz in $CDCl_3$.

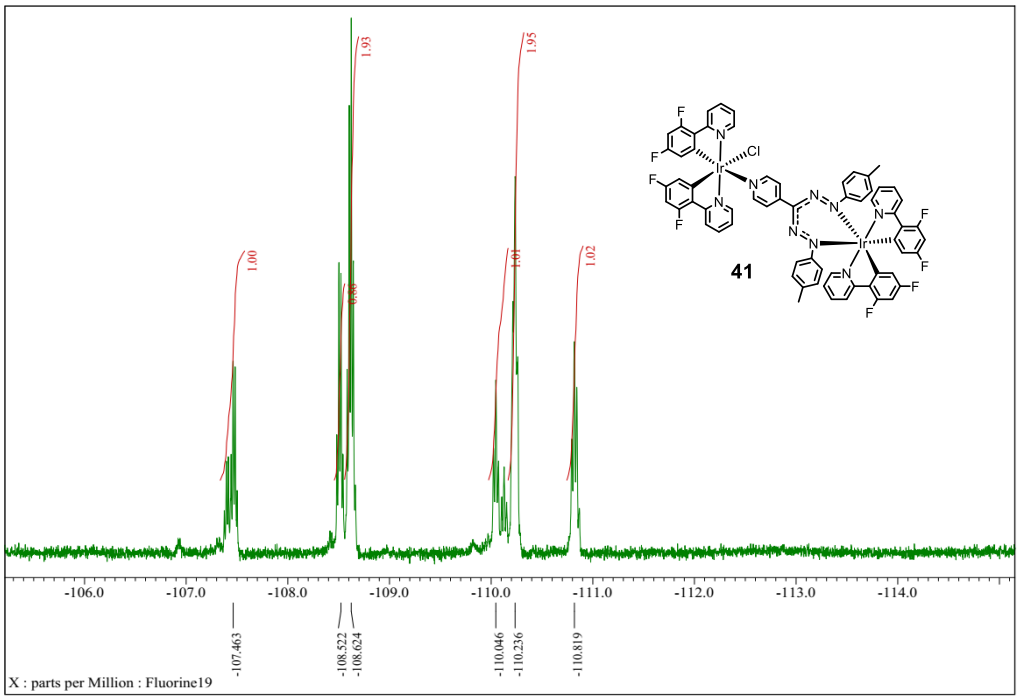

Figure S75.[19]F NMR spectrum of complex **41**, recorded at 470 MHz in $CDCl_3$.

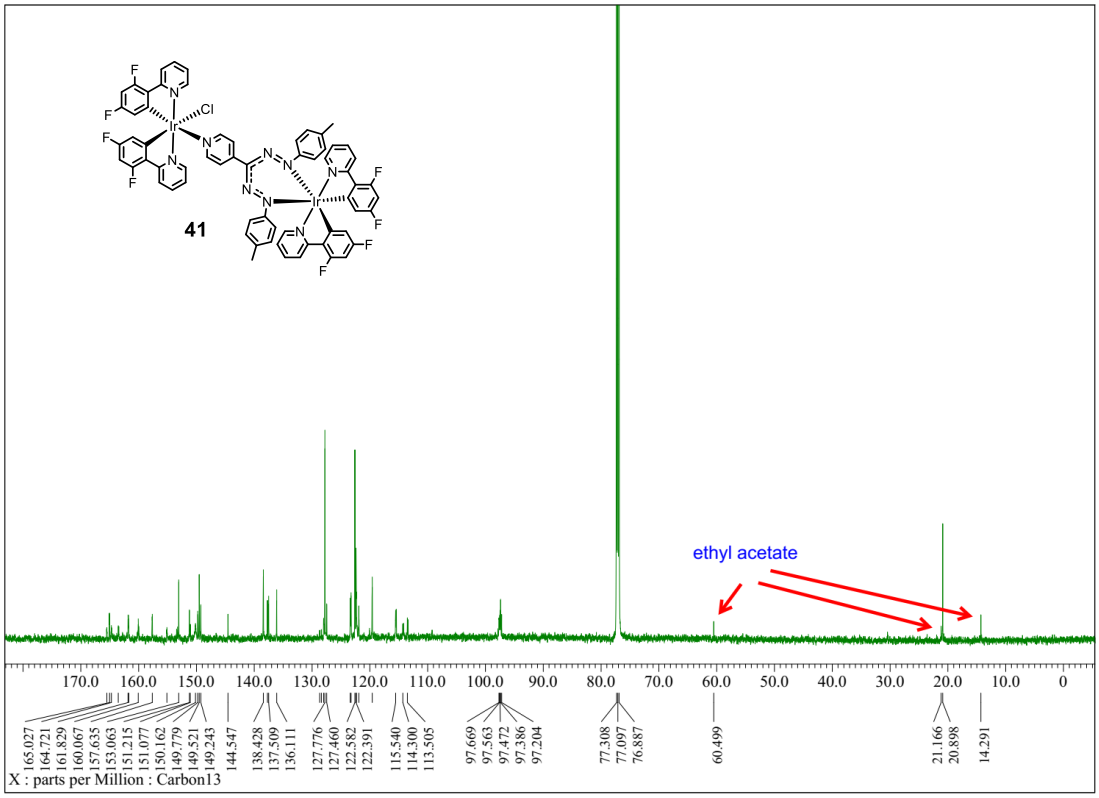

Figure S76. [13]C{[1]H} NMR spectrum of complex **41**, recorded at 151 MHz in $CDCl_3$.

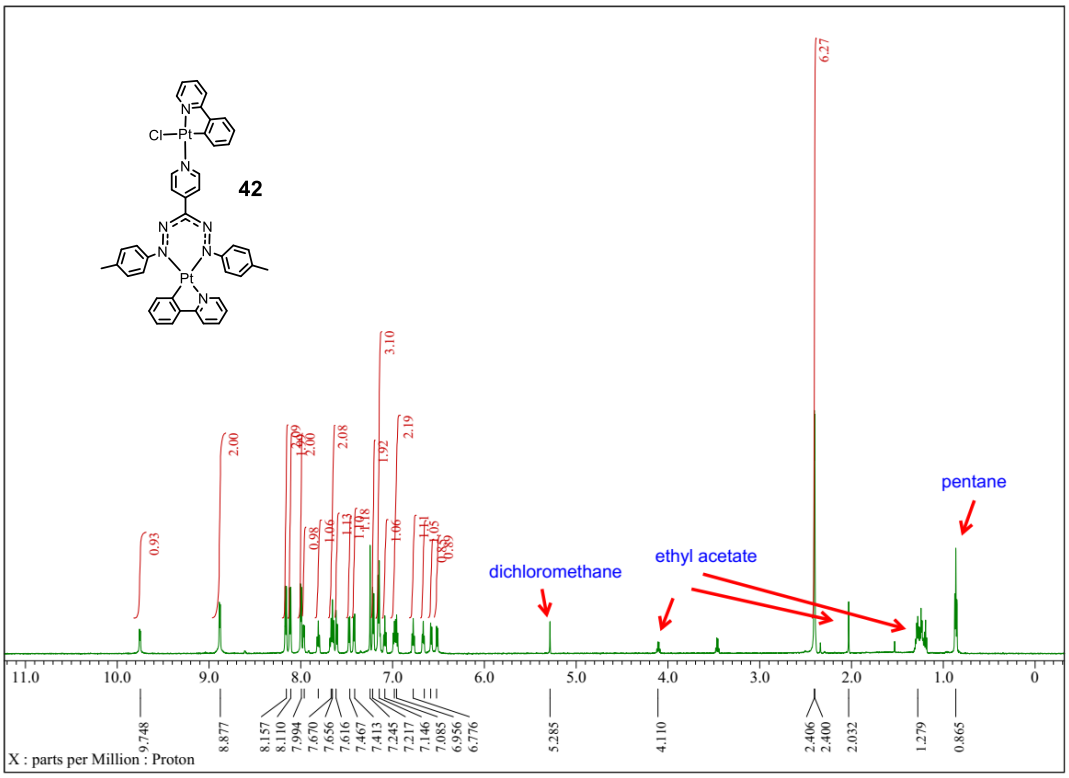

Figure S77. ^{1}H NMR spectrum of complex **42**, recorded at 600 MHz in $CDCl_3$.

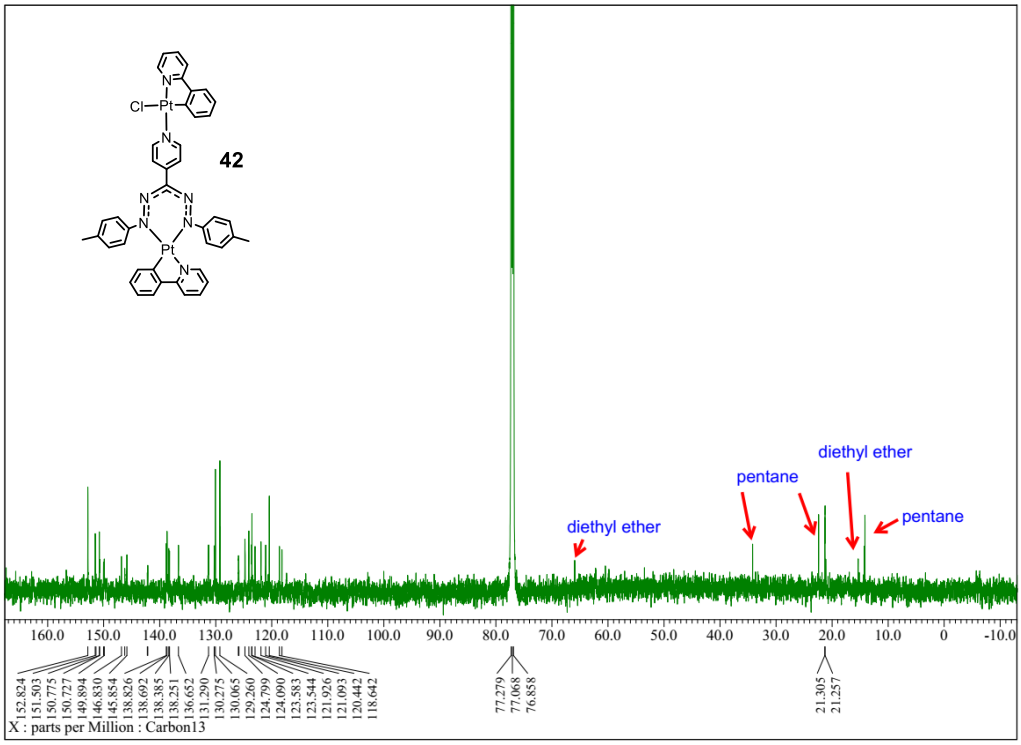

Figure S78. $^{13}C\{^{1}H\}$ NMR spectrum of complex **42**, recorded at 151 MHz in $CDCl_3$.

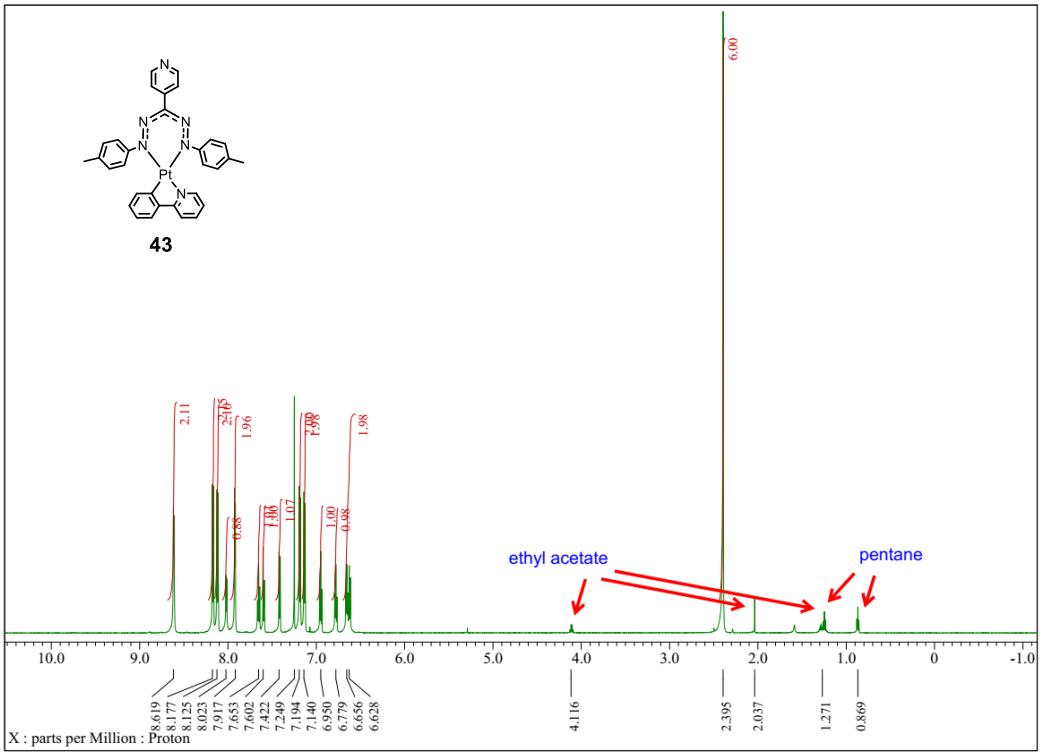

Figure S79. ^{1}H NMR spectrum of complex **43**, recorded at 600 MHz in $CDCl_3$.

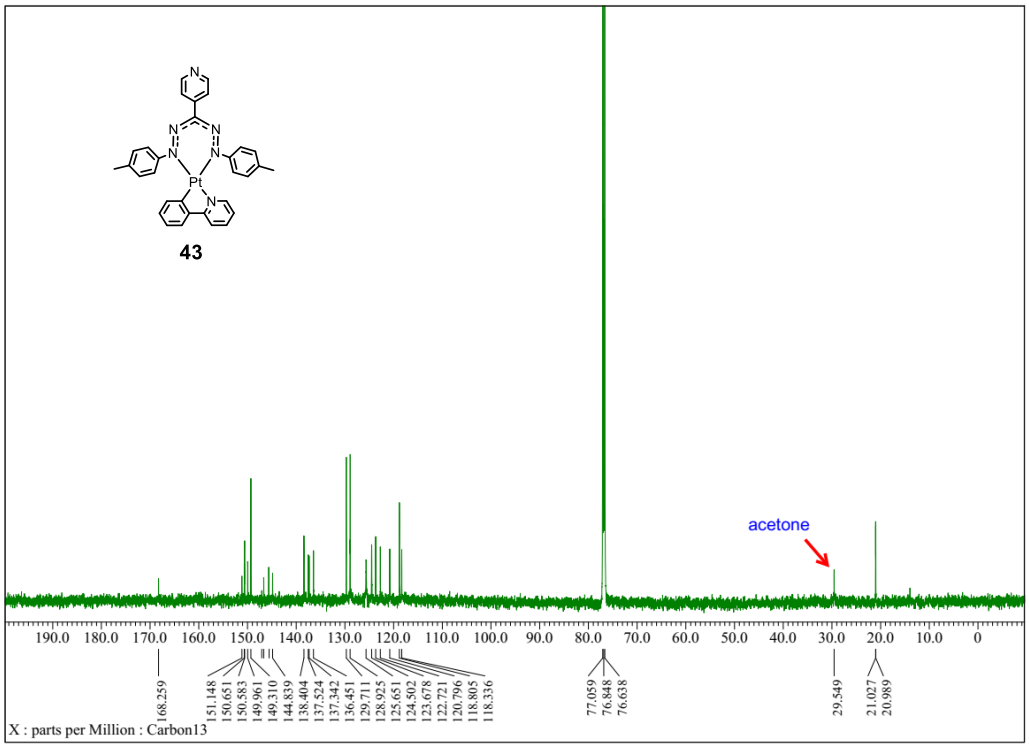

Figure S80. $^{13}C\{^{1}H\}$ NMR spectrum of complex **43**, recorded at 151 MHz in $CDCl_3$.

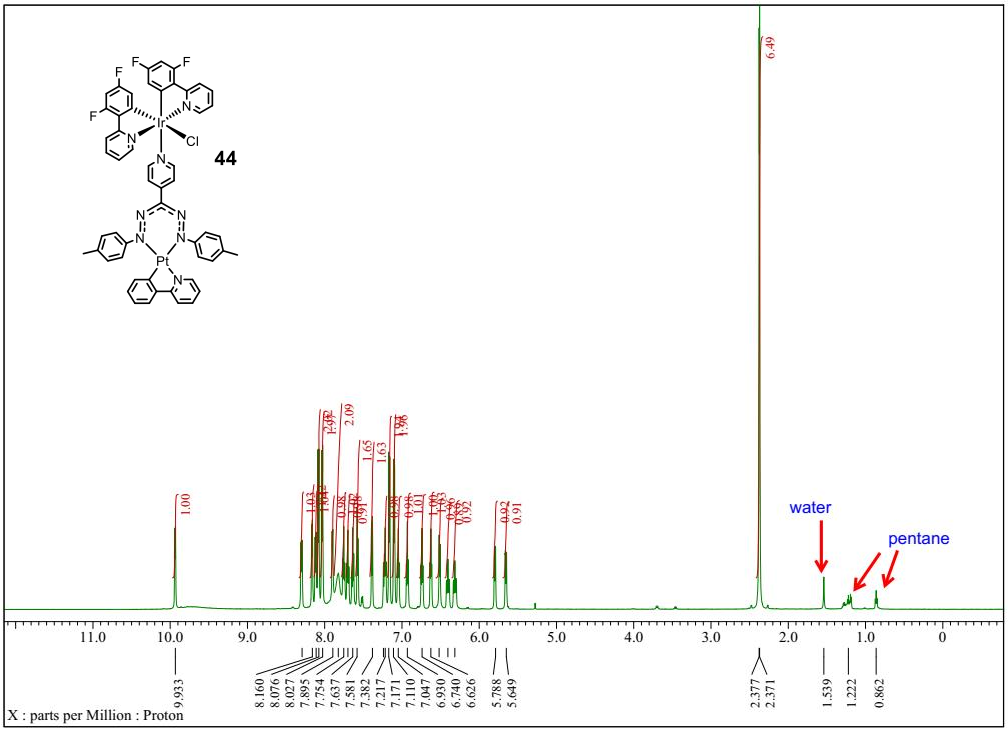

Figure S81. ^{1}H NMR spectrum of complex **44**, recorded at 600 MHz in $CDCl_3$.

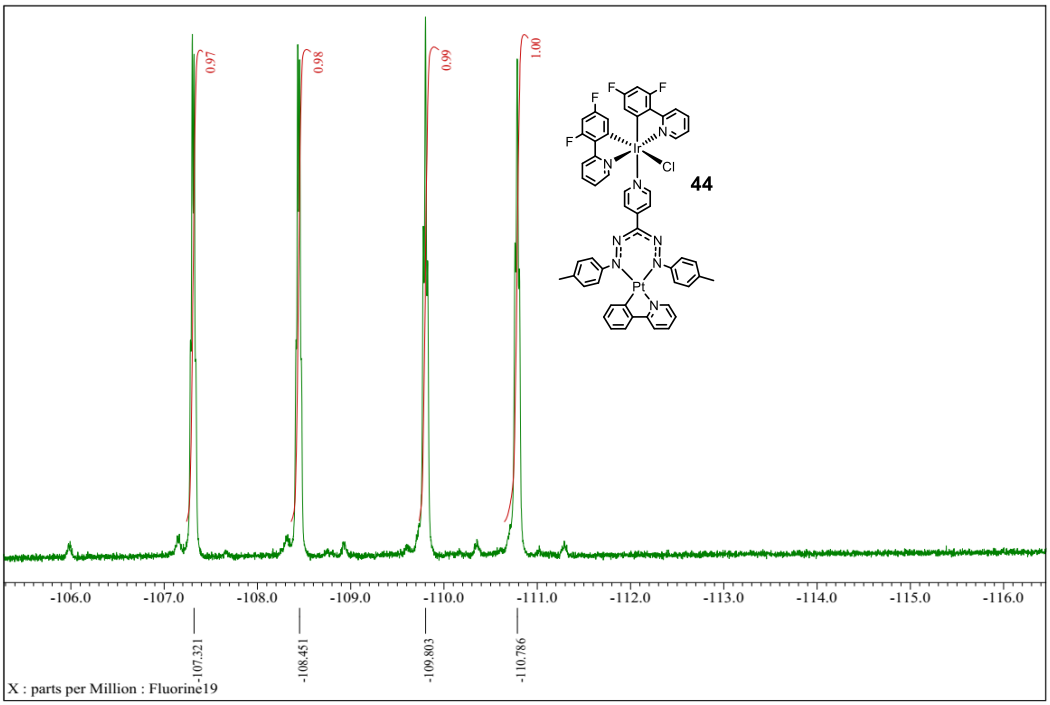

Figure S82. ^{19}F NMR spectrum of complex **44**, recorded at 470 MHz in $CDCl_3$.

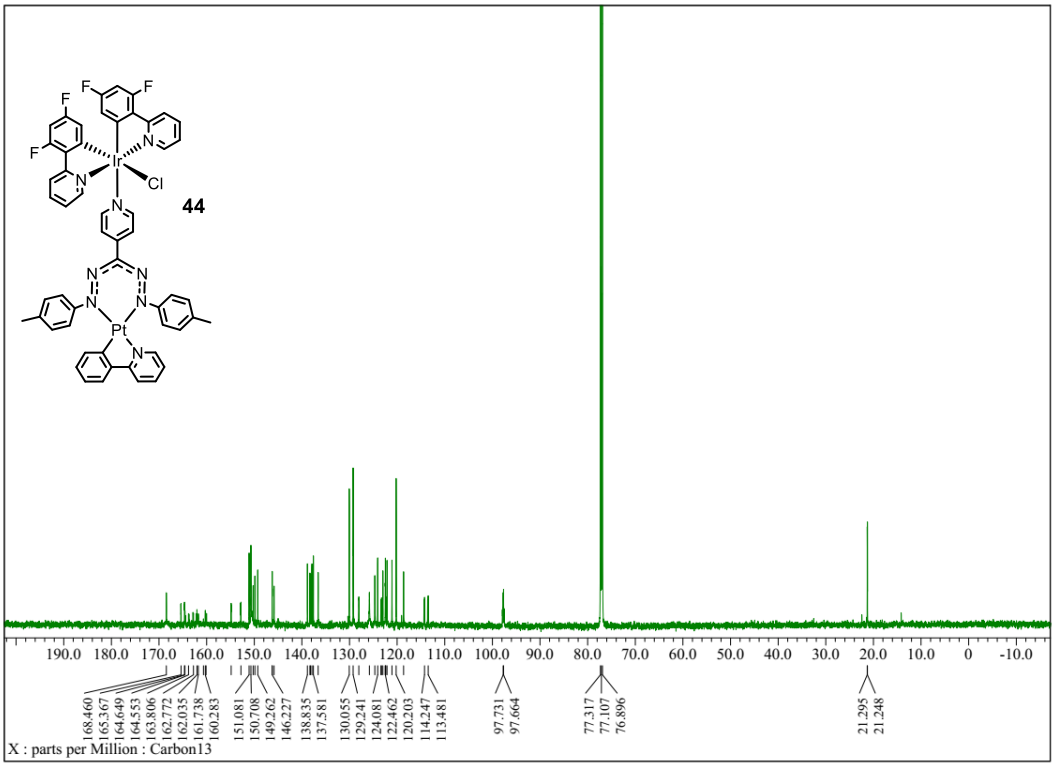

Figure S83. $^{13}C\{^{1}H\}$ NMR spectrum of complex **44**, recorded at 151 MHz in $CDCl_3$.

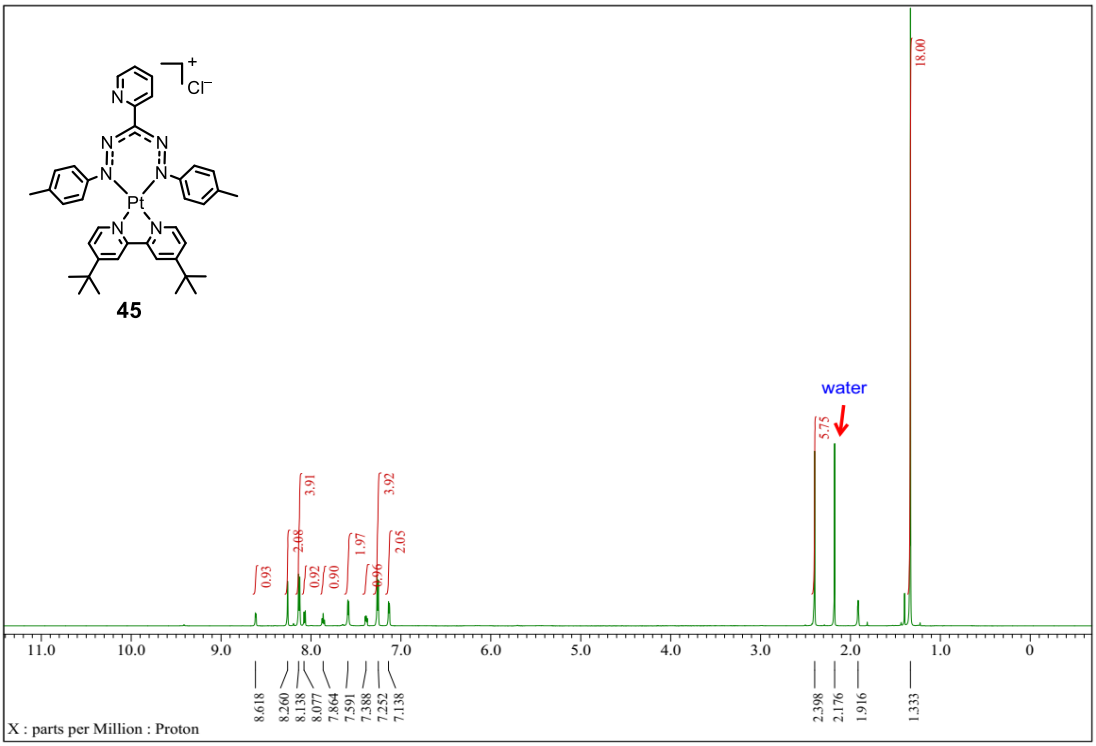

Figure S84. ^{1}H NMR spectrum of complex **45**, recorded at 600 MHz in CD_3CN.

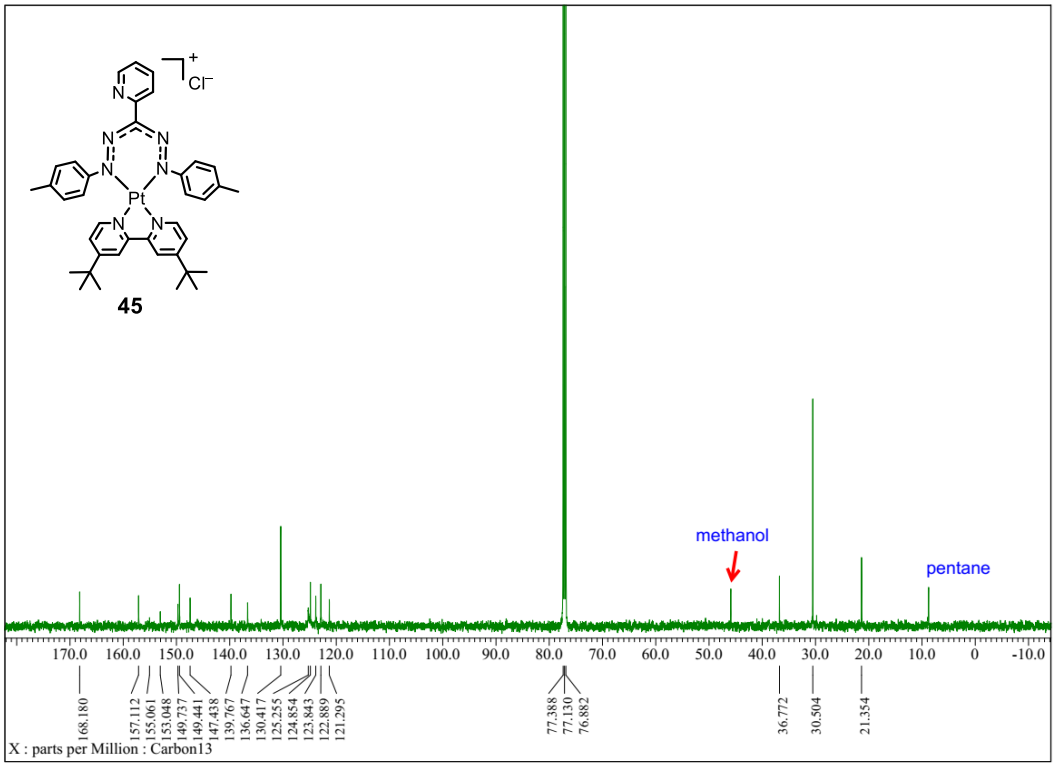

Figure S85. $^{13}C\{^{1}H\}$ NMR spectrum of complex **45**, recorded at 151 MHz in $CDCl_3$.

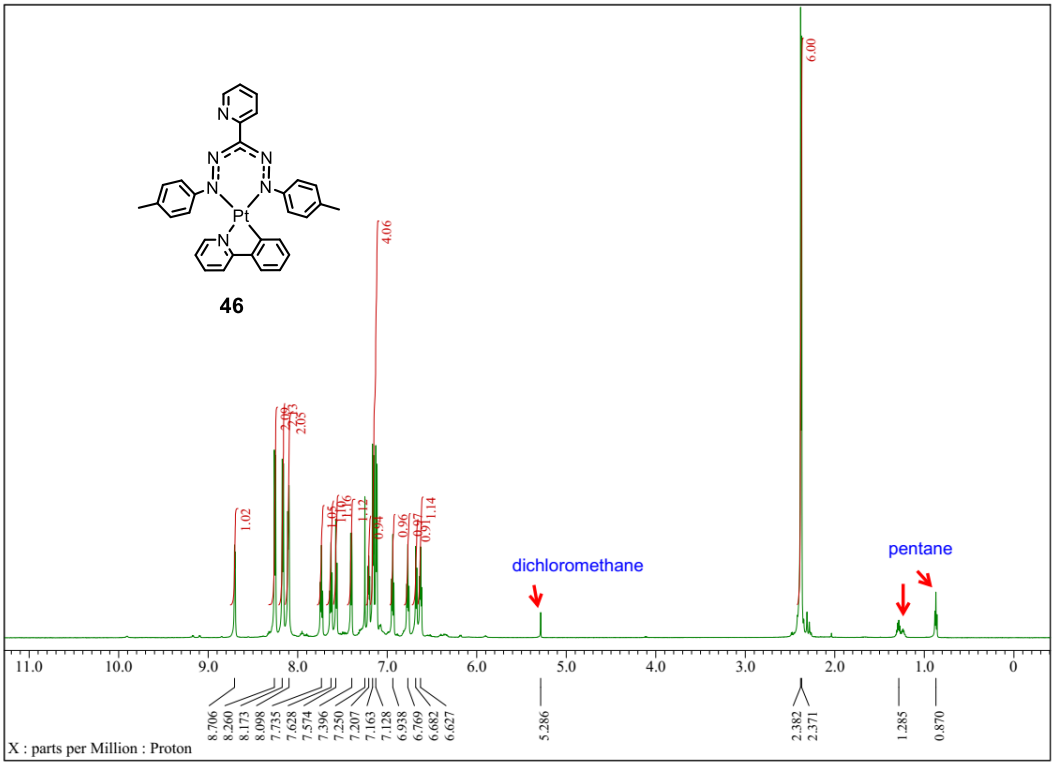

Figure S86. ^{1}H NMR spectrum of complex **46**, recorded at 600 MHz in $CDCl_3$.

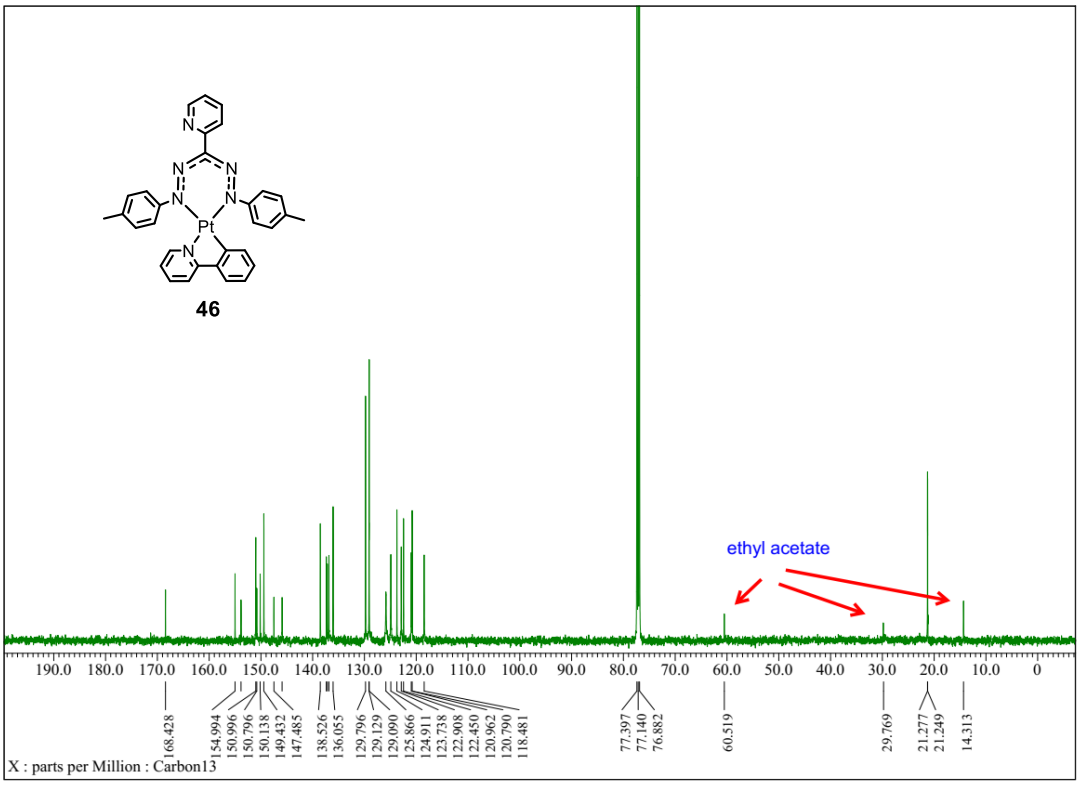

Figure S87. $^{13}C\{^{1}H\}$ NMR spectrum of complex **46**, recorded at 151 MHz in $CDCl_3$.

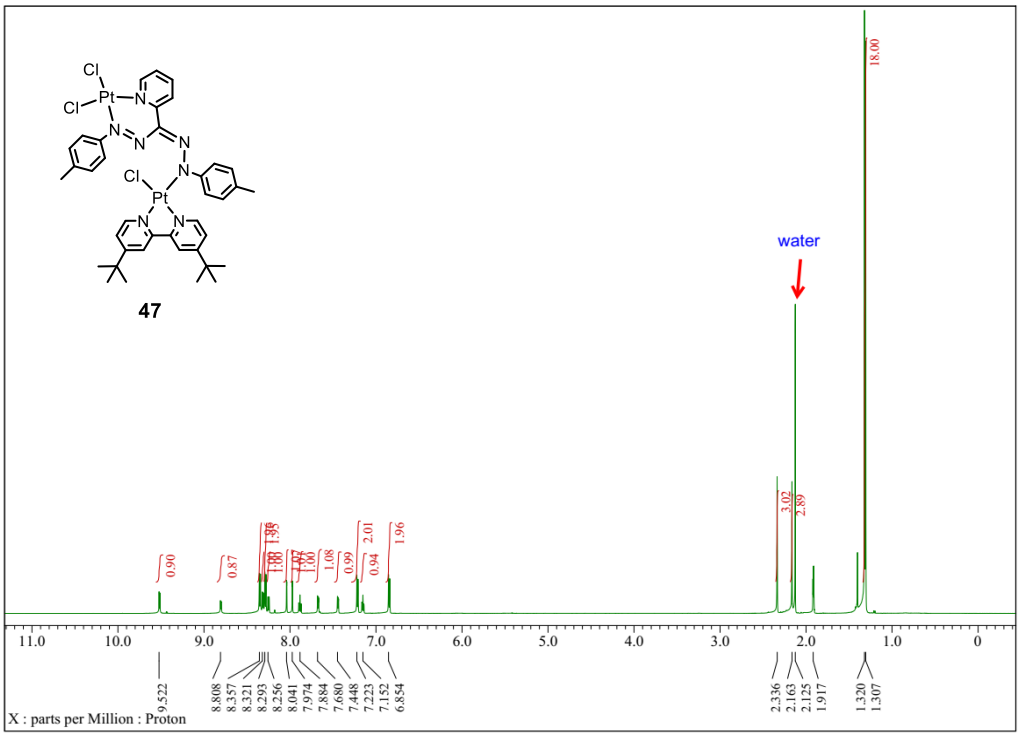

Figure S88. ^{1}H NMR spectrum of complex **47**, recorded at 600 MHz in CD_3CN.

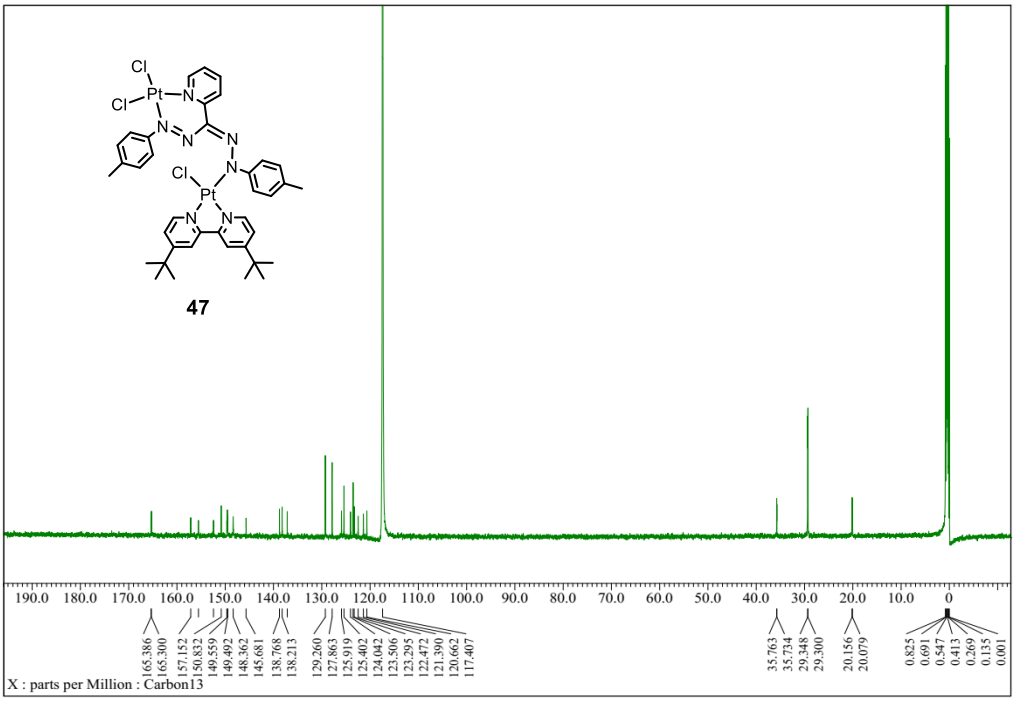

Figure S89. $^{13}C\{^{1}H\}$ NMR spectrum of complex **47**, recorded at 151 MHz in CD_3CN.

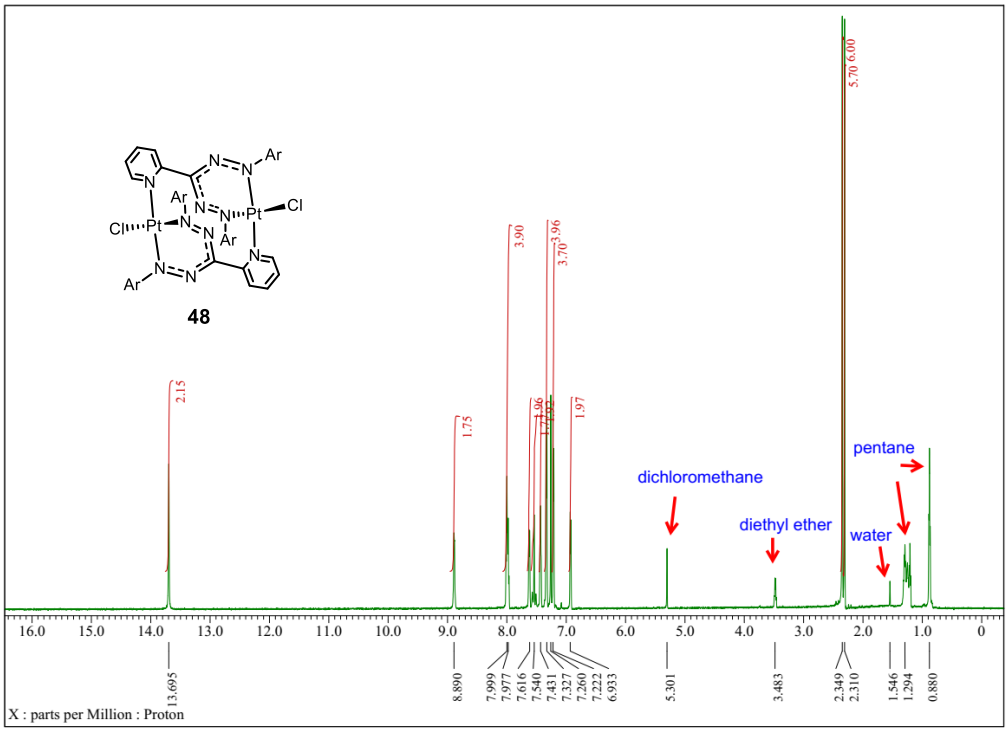

Figure S90. ^{1}H NMR spectrum of complex **48**, recorded at 600 MHz in $CDCl_3$.

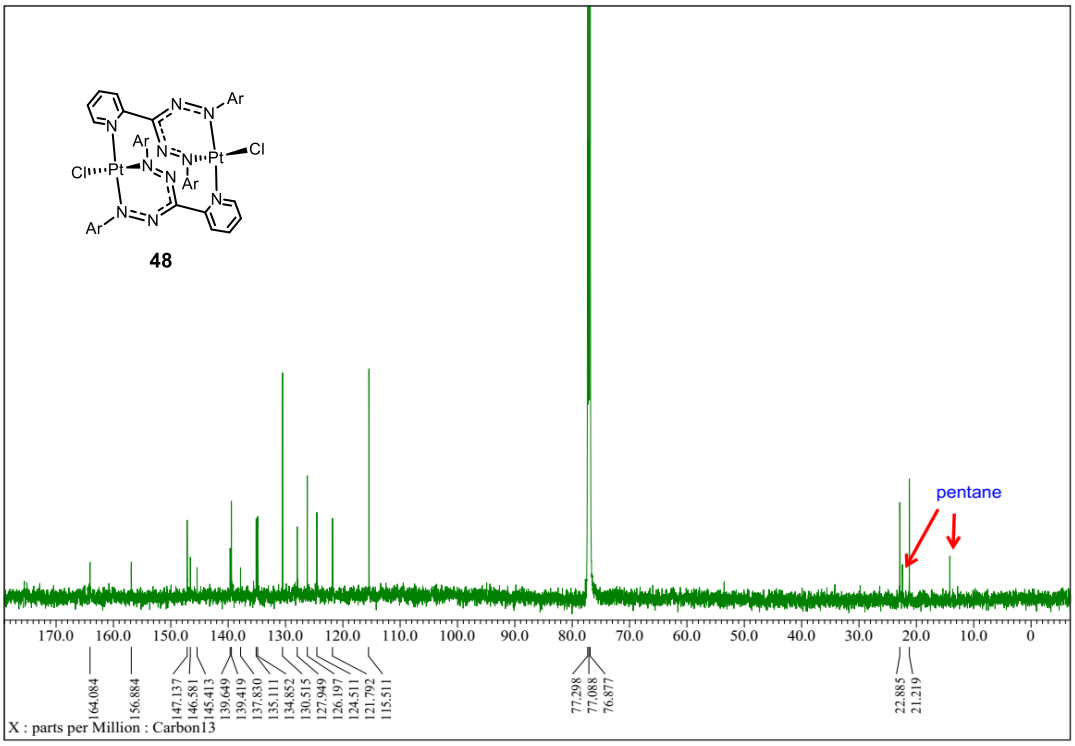

Figure S91. $^{13}C\{^{1}H\}$ NMR spectrum of complex **48**, recorded at 151 MHz in $CDCl_3$.